

Design and Analysis of Advanced Photonic Devices for Electromagnetic Transmission and Sensing

by

Md. Saiful Islam

Master of Science in Electrical & Electronic Engineering
Islamic University of Technology, 2016

Bachelor of Science in Electronics & Telecommunication Engineering
Rajshahi University of Engineering & Technology, 2012

Thesis submitted for the degree of

Doctor of Philosophy

in

Electrical and Electronic Engineering,
Faculty of Engineering,
Computer and Mathematical Sciences
The University of Adelaide, Australia

July, 2021

Supervisors:

Prof. Derek Abbott, School of Electrical & Electronic Engineering

A/Prof. Brian W.-H. Ng, School of Electrical & Electronic Engineering

Candidate:

Md. Saiful Islam

[Researcher Profile](#)

[Google Scholar](#)

[Researchgate](#)

[Publons](#)

[ORCID](#)

[Linkedin](#)

© 2021
Md. Saiful Islam
All Rights Reserved



Dedication: This work is dedicated to my parents (**Md. Gowhar Ali & Kamrun Nahar**) and my wife (**Jakeya Sultana**) for their constant support and patience throughout my academic life. The work is also dedicated to my principal supervisor **Prof. Derek Abbott** for his constant support, and guidance throughout the PhD journey.

Abstract

In this thesis, we report the investigation of advanced photonic devices for electromagnetic transmission and biochemical sensing in the terahertz and optical regimes. The choice of material for designing a terahertz device is deemed to be one of the most crucial factors. First, we consider materials that are frequently used in making terahertz devices. We experimentally demonstrate the optical, thermal, and chemical properties of various chosen glasses, polymers, and resin to select the optimal material for terahertz.

Second, we perform a broad review on terahertz optical fibres—this includes various fibre categories, their guiding mechanisms, fabrication methodologies, possible experimental methodologies, and applications.

Third, we analyse and demonstrate the design of various fibre structures for terahertz transmission and sensing, and then perform experiments on a hollow core antiresonant fibre. We demonstrate successful fabrication of an asymmetrical Zeonex fibre using a novel fabrication method. This is carried out by using a tabletop horizontal extruder designed for producing polymer filaments. The fabricated fibre is then experimentally investigated for terahertz transmission and gas sensing.

Fourth, we study optical fibre based surface plasmon resonance biosensors for operation in the optical regime. Theoretical studies are undertaken to obtain the best possible sensor in consideration of performance, experimental feasibility, and fabrication. One of the optimized sensors is then fabricated as a possible candidate for possible real-world sensing applications.

Finally, we study metasurface planar devices for achieving high sensitivity and quality factor in the terahertz regime. We first demonstrate a tunable graphene metasurface that can achieve multi-band absorption and high refractometric sensing. Later, we demonstrate on an all-dielectric metasurface that reports highest Q-factor in the terahertz regime. We fabricate and experiment on the dielectric metasurface and find good agreement with the simulation.

Statement of Originality

I certify that this work contains no material which has been accepted for the award of any other degree or diploma in my name, in any university or other tertiary institution and, to the best of my knowledge and belief, contains no material previously published or written by another person, except where due reference has been made in the text.

In addition, I certify that no part of this work will, in the future, be used in a submission in my name, for any other degree or diploma in any university or other tertiary institution without the prior approval of the University of Adelaide and where applicable, any partner institution responsible for the joint-award of this degree.

I give permission for the digital version of my thesis to be made available on the web, via the University's digital research repository, the Library Search and also through web search engines, unless permission has been granted by the University to restrict access for a period of time.

I acknowledge the support I have received for my research through the provision of ECMS Divisional Scholarship and full fee Scholarship.

Signature

19/07/2021

Date

Acknowledgments

I would like to take the opportunity to express my gratitude to all those people whose support, skills, friendship and encouragement have helped me to complete this thesis successfully. First of all, I would like to convey special thanks to my supervisors, Prof. Derek Abbott and A/Prof. Brian Wai-Him Ng. Their encouraging attitude has been valuable throughout my candidature, and helped me to grow as an engineer and research scientist. I have learned many positive and life time skills from them, which cannot be summarized in a few lines. However, I would like to highlight the ones that have inspired me the most. There is nothing defined as impossible in Derek's world. Any result of my work is treated as a major discovery by his enthusiasm and readiness for discussion. Derek's passion about research has driven me towards my limits and consequently better outcomes. Both Derek and Brian's feedback on my research caused me to look at problems differently.

My thesis has been an exceptionally rewarding and memorable journey. During this journey I have worked with many engineers, scientists, and technicians, who have broadened my view and approach to tackle problems. Special thanks to Prof. Cristiano Monteiro de Barros Cordeiro, University of Campinas, Brazil, for his continuous support and feedback regarding the material characterization, and fibre based transmission and sensing work. I would like to thank Prof. Heike Ebendorff-Heidepriem, deputy director of Institute for Photonics and Advanced Sensing (IPAS) from School of Chemistry and Physics at University of Adelaide, for her assistance and guidance on the fiber fabrication process, and Prof. Dusan Losic from School of Chemical Engineering & Advanced Materials, The University of Adelaide, Australia, for providing the required lab access for thermal and chemical analysis of different materials and fruitful discussion regarding various experiments. I specially thank Prof. Sharath Sriram of RMIT University, Australia for the metasurface fabrication support.

I acknowledge the guidance and support from Dr Alex Dinovitser who helped me carrying out the experiments correctly. He spent a lot of time with me in the lab carrying out the experimental analysis together. Based on my requirements he made a number

Acknowledgments

of devices to support my experiments. Besides, he is the person with whom I discussed every issue throughout the journey. Alex also supported me in checking and commenting on my research papers.

I acknowledge informative discussions with Dr Julker Nine of School of Chemical Engineering & Advanced Materials, The University of Adelaide, Australia, Dr Zohreh Vafapour from John Hopkins University, USA, Dr Alice L. S. Cruz from Braz Cubas University, Brazil, and Alson K. L. Ng of IPAS, Adelaide.

Thanks goes to all of my internal and external collaborators, Dr Rajib Ahmed of Stanford University, USA, Dr Rifat Ahmed from Australian National University, Australia, Aditi Upadhyay of RMIT University, Lucy Peng of IPAS, Prof. S. M. Abdur Razzak from Rajshahi University of Engineering & Technology, Bangladesh, Prof. Mohammad Faisal from Bangladesh University of Engineering & Technology, Bangladesh, Prof. Mohammad Rakibul Islam from Islamic University of Technology, Bangladesh, Kawsar Ahmed from Mawlana Bhashani Science & Technology University, Bangladesh, and Dr Shilun Feng from Nanyang Technological University, Singapore.

Much vital support was provided by the administrative staff of the School of Electrical and Electronic Engineering. Thanks are due to staff who keep the machine of the department running, including: Sharyn Liersch, Jodie Schluter, Sanaz Orandi, Franca Guest, and Laura McNamara.

Thanks go to my friends and colleagues from the University of Adelaide who always encouraged me for a bright future. Thanks to Mr Henry Ho for T-ray laboratory hardware and experimental assistance.

I greatly acknowledge the support from the Australian Research Council (grant no. DP170104984), Sao Paulo Research Foundation (FAPESP) under grant 2018/10409, the ARC Research Hub for Graphene enabled industry transformation, funding under industrial transformation research hub IH150100003, support from Optofab node of the Australian National Fabrication Facility (ANFF) supported by the Commonwealth and South Australian State Government.

I am grateful to the Australian Government, the University of Adelaide, and Faculty of Engineering, Computer & Mathematical Sciences (ECMS) for the ECMS Divisional Scholarship award in 2017, as well as to the School of Electrical and Electronic Engineering of University of Adelaide for providing travel funding. I would like to thank the committee members who awarded me the Frank Perry Traveling Award to attend the 45th IRMMW-THz 2020 at Buffalo, USA.

At last but not the least, I would like to sincerely thank my wife, Jakeya Sultana for encouraging me throughout the whole journey, and my parents, Md. Gowhar Ali and Kamrun Nahar, for their endless and tremendous support, encouragement, and generous patience.

Md. Saiful Islam

Thesis Conventions

The following conventions have been adopted in this Thesis:

Typesetting

This thesis is typeset using the L^AT_EX2e software. TEXnic Center is used as an effective interface to L^AT_EX.

Referencing

Harvard style is used for referencing and citation in this thesis.

Spelling

Australian English spelling is adopted, as defined by the Macquarie English Dictionary Dictionary (1982).

System of units

The units comply with the international system of units recommended in an Australian Standard: As ISO 1000–1998 (Standards Australia Committee ME/71, Quantities, Units and Conversions 1998).

Physical constants

The physical constants comply with a recommendation by the Committee on Data for Science and Technology: CODATA Mohr *et al.* (2008).

Frequency band definition

We will consider T-rays as lying in the 0.1–10 THz band as argued by Abbott and Zhang (2007). T-rays have frequencies that correspond to the so-called terahertz-gap. Thus in the field, when we refer to terahertz radiation this is an alternative term for T-rays. In this context, the term terahertz radiation is understood as meaning radiation in the terahertz-gap or T-rays and the word terahertz is not to be confused with the units of terahertz that spans three decades from 10^{12} Hz. The visible light has a wavelength ranges from 380 nm to 750 nm, and the mid-IR ends at around 40 μm .

Publications

Journal Articles

- **M. S. Islam**, J. Sultana, J. Osario, B. W.-H. Ng, F. Benabid, H. E. Heidepriem, D. Abbott, and C. M. B. Cordeiro, "Single-step tabletop fabrication for terahertz specialty optical fibre sensor," *Advanced Photonics Research*, (Under review), 2021.
- Z. Vafapour, H. Ghahraloud, A. Keshavarz, **M. S. Islam**, A. Rashidi, M. Dutta, and M. A. Stroschio, "The potential of refractive index nanobiosensing using a multi-band optically tuned perfect light metamaterial absorber," *IEEE Sensors Journal*, vol. 21, no. 12, pp. 13786–13793, 2021.
- **M. S. Islam**, C. M. B. Cordeiro, M. Franco, J. Sultana, A. Cruz, and D. Abbott, "Terahertz optical fibers [Invited]," *Optics Express*, vol. 28, no. 1, pp. 16089–16117, 2020.
- J. Sultana, **M. S. Islam**, C. M. B. Cordeiro, M. S. Habib, M. Kaushik, A. Dinovitser, B. W.-H. Ng, H. E. Heidepriem, and D. Abbott, "Hollow core inhibited coupled antiresonant terahertz fiber: A numerical and experimental study," *IEEE Transaction on Terahertz Science & Technology*, vol. 11, no. 3, pp. 245–260, 2021.
- **M. S. Islam**, J. Sultana, C. M. B. Cordeiro, M. J. Nine, A. L. S. Cruz, A. Dinovitser, B. W.-H. Ng, H. E. Heidepriem, D. Losic, and D. Abbott, "Experimental study on glass and polymers: Determining the optimal material for potential use in terahertz technology," *IEEE Access*, vol. 8, pp. 97204–97214, 2020.
- J. Sultana, **M. S. Islam**, C. M. B. Cordeiro, A. Dinovitser, M. Kaushik, B. W.-H. Ng, and D. Abbott, "Exploring low loss and single-mode in antiresonant tube lattice terahertz fibers," *IEEE Access*, vol. 8, pp. 113309–113317, 2020.
- **M. S. Islam**, J. Sultana, M. Biabanifard, M. J. Nine, Z. Vafapour, C. M. B. Cordeiro, A. Dinovitser, B. W.-H. Ng, and D. Abbott, "Tunable localized surface plasmon graphene metasurface for multiband superabsorption and terahertz sensing," *Carbon*, vol. 158, pp. 559–567, 2020.

- *J. Sultana, **M. S. Islam**, M. S. Habib, A. Dinovitser, M. Kaushik, B. W.-H. Ng, and D. Abbott, "Linearity and nonlinearity in hollow-core antiresonant fiber sensors in the terahertz regime," *IEEE Instrumentation and Measurement Magazine*, (Accepted for publication on 25th May, 2020).
- M. A. Mollah, and **M. S. Islam**, "Novel single hole exposed-suspended core localized surface plasmon resonance sensor," *IEEE Sensors Journal*, vol. 21, no. 3, pp. 2813–2820, 2021.
- I. M. Ankan, M. A. Mollah, J. Sultana, and **M. S. Islam**, "Negative curvature hollow-core anti-resonant fiber for terahertz sensing," *Appl. Opt.*, vol. 59, no. 28, pp. 8519–8525, 2020.
- J. Sultana, **M. S. Islam**, C. M. B. Cordeiro, A. Dinovitser, M. Kaushik, B. W.-H. Ng, and D. Abbott, "Terahertz hollow core antiresonant fiber with metamaterial cladding," *Fibers*, vol. 8, no. 2, Art. No. 14, 2020.
- *M. Dorraki, **M. S Islam**, A. Allison, and D. Abbott, "Parameter identification using moment of velocity," *Royal Society Open Science*, vol. 6, no. 11, Art. No. 190671, 2019.
- *Z. Lei, Y. Sun, Y. A. Nanekaran, S. Yang, **M. S Islam**, H. Lei, D. Zhang, "A novel data-driven robust framework based on machine learning and knowledge graph for disease classification," *Future Generation Computer Systems*, vol. 102, pp. 534–548, 2020.
- **M. S. Islam**, Cristiano. M. B. Cordeiro, J. Sultana, A. A. Rifat, R. Ahmed, S. Feng, A. Dinovitser, B. W.-H. Ng, and D. Abbott, "A hi-bi ultra-sensitive surface plasmon resonance fiber sensor," *IEEE Access*, vol. 7, no. 21, pp. 7908–79094, 2019.
- **M. S. Islam**, J. Sultana, A. A. Rifat, M. S. Habib, A. Dinovitser, B. W.-H. Ng, and D. Abbott, "Localized surface plasmon resonance biosensor: an improved technique for SERS response intensification," *Opt. Lett.*, vol. 44, no. 5, pp. 1134–1137, 2019.
- F. Haider, R. A. Aoni, R. Ahmed, **M. S. Islam**, and A. E. Miroschnichenko, "Propagation controlled photonic crystal fiber-based plasmonic sensor via scaled-down approach," *IEEE Sensors Journal*, vol. 19, no. 3, pp. 962–969, 2019.

-
- K. Ahmed, F. Ahmed, S. Roy, B. K. Paul, M. N. Aktar, D. Vigneswaran, and **M. S. Islam**, "Refractive index-based blood components sensing in terahertz spectrum," *IEEE Sensors Journal*, vol. 19, no. 9, pp. 3368–3375, 2019.
 - M. R. Islam, M. F. Kabir, T. Khandokar, and **M. S. Islam**, "A novel hollow core terahertz refractometric sensor," *Sens. & Bio-Sens. Res.*, vol. 25, Art. No. 100295, 2019.
 - J. Sultana, M. R. Islam, M. Faisal, K. Md. Abu Talha, and **M. S. Islam**, "Design and analysis of a Zeonex based diamond-shaped core kagome lattice photonic crystal fiber for T-ray wave transmission," *Opt. Fiber Technol.*, vol. 47, pp. 55–60, 2019.
 - **M. S. Islam**, J. Sultana, A. A. Rifat, A. Dinovitser, B. W.-H. Ng, and D. Abbott, "Dual-polarized highly sensitive plasmonic sensor in the visible to near-IR spectrum," *Optics Express*, vol. 26, no. 21, pp. 30347–30361, 2018.
 - **M. S. Islam**, J. Sultana, K. Ahmed, A. Dinovitser, B. W.-H. Ng, and D. Abbott, "Zeonex based asymmetrical terahertz photonic crystal fiber for multichannel communication and polarization maintaining applications," *Appl. Optics*, vol. 57, no. 4, pp. 666–672, 2018.
 - **M. S. Islam**, J. Sultana, K. Ahmed, A. Dinovitser, B. W.-H. Ng, and D. Abbott, "A novel Zeonex based oligoporous-core photonic crystal fiber for polarization preserving terahertz applications," *Optics Communications*, vol. 413, no. 15, pp. 242–248, 2018.
 - J. Sultana, **M. S. Islam**, M. R. Islam, and D. Abbott, "High numerical aperture, highly birefringent novel photonic crystal fibre for medical imaging applications," *Electronics Letters*, vol. 54, no. 2, pp. 61–62, 2018.
 - J. Sultana, **M. S. Islam**, M. R. Islam, and D. Abbott, "Highly birefringent elliptical core photonic crystal fiber for terahertz application," *Optics Communications*, vol. 407, no. 15, pp. 92–96, 2018.
 - J. Sultana, **M. S. Islam**, K. Ahmed, A. Dinovitser, B. W.-H. Ng, and D. Abbott, "Terahertz detection of alcohol using photonic crystal fiber sensor," *Appl. Optics*, vol. 57, no. 10, pp. 2426–2433, 2018.

- **M. S. Islam**, B. W.-H. Ng, and D. Abbott, "Porous-core photonic crystal fibers guide polarization preserving terahertz waves," *Laser Focus World*, vol. 54, no. 5, 2018.
- **M. S. Islam**, J. Sultana, M. Faisal, M. R. Islam, A. Dinovitser, B. W.-H. Ng, and D. Abbott, "A modified hexagonal photonic crystal fiber for terahertz applications," *Optical Materials*, vol. 79, pp. 336–339, 2018.
- **M. S. Islam**, J. Sultana, R. A. Roni, A. Dinovitser, B. W.-H. Ng, and D. Abbott, "Terahertz sensing in a hollow core photonic crystal fiber," *IEEE Sensors Journal*, vol. 18, no. 10, pp. 4073–4080, 2018.
- **M. S. Islam**, J. Sultana, K. Ahmed, A. Dinovitser, M. R. Islam, B. W.-H. Ng, and D. Abbott, "Sensing of toxic chemicals using polarized photonic crystal fiber in the terahertz region," *Optics Communications*, vol. 426, pp. 341–347, 2018.
- **M. S. Islam**, J. Sultana, K. Ahmed, A. Dinovitser, B. W.-H. Ng, and D. Abbott, "A novel approach for spectroscopic chemical identification using photonic crystal fiber in the terahertz regime," *IEEE Sensors Journal*, vol. 18, no. 2, pp. 575–582, 2018.
- **M. S. Islam**, J. Sultana, M. Dorraki, J. Atai, M. R. Islam, A. Dinovitser, B. W.-H. Ng, and D. Abbott, "Low loss and low dispersion hybrid core photonic crystal fiber for terahertz propagation," *Phot. Net. Comm.*, vol. 35, no. 3, pp. 364–373, 2018.
- **M. S. Islam**, J. Sultana, K. Ahmed, A. Dinovitser, B. W.-H. Ng, and D. Abbott, "Design and characterization of a low-loss, dispersion-flattened photonic crystal fiber for T-ray wave propagation," *Optik - International Journal for Light and Electron Optics*, vol. 145, pp. 398–406, 2018.

Conference Papers

- **M. S. Islam**, A. Upadhyay, R. T. Ako, J. Sultana, B. W. H-Ng, M. Bhaskaran, S. Sri-ram, and D. Abbott, "Terahertz ultrahigh-Q metasurface enabled by out-of-plane asymmetry," *46th Int. Conf. on Infra. Milli. & Terahertz Waves*, 2021. (Accepted, May 2021).

-
- **M. S. Islam**, B. W.-H. Ng, and D. Abbott, "Terahertz ultrahigh-Q metasurface enabled by out-of-plane asymmetry," *45th Int. Conf. on Infra. Milli. & Terahertz Waves*, 2020. DOI: 10.1109/IRMMW-THz46771.2020.9370414.
 - **M. S. Islam**, B. W.-H. Ng, and D. Abbott, "Broadband characterization of glass and polymer materials using THz-TDS," *44th Int. Conf. on Infra. Milli. & Terahertz Waves*, 2019. DOI: 10.1109/IRMMW-THz.2019.8874013.
 - **M. S. Islam**, B. W.-H. Ng, and D. Abbott, "Electrically tunable graphene metasurface for multiband superabsorption and terahertz sensing," *44th Int. Conf. on Infra. Milli. & Terahertz Waves*, 2019. DOI: 10.1109/IRMMW-THz.2019.8873851.
 - J. Sultana, **M. S. Islam**, C. M. B. Cordeiro, A. L. S. Cruz, A. Dinovitser, B. W.-H. Ng, and D. Abbott, "Novel hollow-core anti-resonant terahertz fiber with metamaterial cladding," *44th Int. Conf. on Infra. Milli. & Terahertz Waves*, 2019. DOI: 10.1109/IRMMW-THz.2019.8873836.
 - J. Sultana, **M. S. Islam**, C. M. B. Cordeiro, A. L. S. Cruz, A. Dinovitser, B. W.-H. Ng, and D. Abbott, "Five-capillary cladded low loss anti-resonant terahertz fiber," *44th Int. Conf. on Infra. Milli. & Terahertz Waves*, 2019. DOI: 10.1109/IRMMW-THz.2019.8874476.
 - **M. S. Islam**, B. W.-H. Ng, and D. Abbott, "A gold coated plasmonic sensor for biomedical and biochemical analyte detection," *43rd Int. Conf. on Infra. Milli. & Terahertz Waves*, 2018. DOI: 10.1109/IRMMW-THz.2018.8510018.
 - **M. S. Islam**, J. Sultana, A. Dinovitser, K. Ahmed, M. R. Islam, M. Faisal, B. W.-H. Ng, and D. Abbott, "A novel Zeonex based photonic sensor for alcohol detection in beverages," *IEEE International Conference on Telecommunication and Photonics (ICTP)*, 2018. DOI: 10.1109/ICTP.2017.8285905.

***All publications indicated with an asterisk resulted from side projects not directly related to this thesis.**

Contents

Abstract	v
Statement of Originality	vii
Acknowledgments	ix
Thesis Conventions	xiii
Publications	xv
Contents	xxi
List of Figures	xxvii
List of Tables	xxxix
Chapter 1. Introduction	1
1.1 Terahertz radiation or T-rays	2
1.2 Application of T-rays	3
1.3 Thesis outline	5
1.4 Summary of original contribution	8
Chapter 2. Experimental study on glass and polymers: materials for terahertz	11
2.1 Introduction	12
2.2 Sample preparation	15
2.3 Experimental setup	16
2.4 Signal averaging and phase unwrapping	18
2.5 Mathematical expressions to extract optical properties from THz-TDS data	20
2.6 Dielectric and optical properties of measured samples	22
2.7 Chemical and thermal stability of polymers	25
2.8 Conclusion	28

Chapter 3. Terahertz optical fibres	29
3.1 Introduction	30
3.2 Terahertz optical fibre types and guiding mechanisms	32
3.2.1 Hollow-core waveguides having single and hybrid cladding	41
3.2.2 Drilling	48
3.2.3 Stack and draw	48
3.2.4 Preform-molding/fibre-inflation technique	50
3.2.5 Extrusion	50
3.2.6 3D Printing	51
3.2.7 Transmission and communication	55
3.2.8 Sensing	56
3.2.9 Fibre-based terahertz imaging	58
3.3 Future work	59
3.4 Conclusion	61
Chapter 4. Terahertz waveguide: concepts and modelling	63
4.1 Key contributions to terahertz waveguides	64
4.1.1 Design, simulation, and signal processing methodology	64
4.1.2 Synopsis of the numerical method	64
4.2 Waveguides for terahertz transmission	67
4.2.1 A modified hexagonal photonic crystal fibre	67
4.2.2 Zeonex based asymmetrical terahertz photonic crystal fibre	73
4.2.3 Other proposed waveguides for low loss terahertz transmission	78
4.3 Terahertz waveguides for sensing applications	80
4.3.1 A novel approach for spectroscopic chemical identification	80
4.3.2 Terahertz sensing in a hollow-core photonic crystal fibre	83
4.3.3 Mechanism of terahertz sensing and requirements of a birefringent fibre	90
4.4 Summary	91
Chapter 5. Tabletop fabrication for terahertz specialty optical fibre sensor	93

5.1	Introduction	94
5.1.1	Fibre design	96
5.1.2	Fibre fabrication	97
5.2	Fibre characterization	100
5.2.1	Loss measurement and simulation	100
5.2.2	Dispersion and sensing measurements	104
5.3	Discussion	106
Chapter 6. Surface plasmon resonance biosensor		107
6.1	Localized surface plasmon resonance biosensor	108
6.1.1	Introduction	108
6.1.2	Design methodology, simulation, and optimization	109
6.1.3	Results and discussion	111
6.2	A hi-bi ultra-sensitive SPR fibre sensor	119
6.2.1	Introduction	119
6.2.2	Modelling and theoretical analysis of the sensor	122
6.2.3	Sensor performance analysis	127
6.3	An exposed core localized SPR biosensor	137
6.3.1	Introduction	137
6.3.2	Geometric structure and numerical modelling of the proposed PCF-LSPR sensor	139
6.3.3	Performance analysis of the proposed sensor	141
6.4	Fabrication and coating	148
6.5	Conclusion	149
Chapter 7. Electrically tunable graphene metasurface		151
7.1	Tunable graphene metasurface	152
7.1.1	Introduction	152
7.1.2	Design, simulation and fabrication methodology	155
7.1.3	Parameter optimization-genetic algorithm	157
7.1.4	Transmission line theory and equivalent circuit modelling of the proposed device	158

7.1.5	Results and discussion	159
7.1.6	Mechanism of plasmon enhancement and multiband superabsorption	161
7.1.7	Dynamically tunable property enabled by graphene	163
7.1.8	Wide angle of incidence	165
7.1.9	Characterization of the proposed device considering fabrication tolerances	166
7.1.10	Application to refractive index sensing	166
7.2	Conclusion	170
Chapter 8. Bound states in the continuum for guided terahertz plasmons		171
8.1	High-Q guided terahertz plasmons	172
8.1.1	Introduction	172
8.1.2	Design, simulation, optimization, and fabrication methodology .	175
8.1.3	Step by step fabrication procedure	176
8.1.4	Equivalent circuit modelling and mathematical expressions . . .	177
8.2	Results and discussion	179
8.2.1	Mechanism behind plasmon enhancement and sharp resonance .	180
8.2.2	Performance considering the germanium length and thickness variation	181
8.2.3	Performance considering the fabrication imperfections	182
8.2.4	Angle dependence of the metasurface	182
8.2.5	Application in sensing	183
8.3	Fabrication of the all-dielectric metasurface	187
8.4	Experiment on the metasurface	190
8.5	Conclusion	191
Chapter 9. Conclusion and future remarks		193
9.1	Thesis overview	194
9.2	Chapter 2: Experimental analysis of glasses and polymers: materials for terahertz	194
9.2.1	Aim	194

9.2.2	Methodology	194
9.2.3	Results	195
9.2.4	Future direction	195
9.3	Chapter 3: Terahertz optical fibre	196
9.3.1	Aim	196
9.3.2	Methodology	196
9.3.3	Results	196
9.3.4	Future direction	197
9.4	Chapter 4: Terahertz waveguides: modelling and analysis	198
9.4.1	Aim	198
9.4.2	Methodology	199
9.4.3	Results	199
9.4.4	Future direction	199
9.5	Chapter 5: Tabletop fabrication for terahertz specialty optical fibre sensor	200
9.5.1	Aim	200
9.5.2	Methodology	200
9.5.3	Results	200
9.5.4	Future direction	201
9.6	Chapter 6: Surface plasmon resonance biosensor	201
9.6.1	Aim	201
9.6.2	Methodology	201
9.6.3	Results	202
9.6.4	Future direction	202
9.7	Chapter 7: Electrically tuneable graphene metasurface	202
9.7.1	Aim	202
9.7.2	Methodology	203
9.7.3	Results	203
9.7.4	Future direction	203
9.8	Chapter 8: Bound states in the continuum for guided terahertz plasmons	204
9.8.1	Aim	204
9.8.2	Methodology	204
9.8.3	Results	204
9.8.4	Future direction	204

Appendix A. Terahertz experiment setups	207
A.1 Terahertz setup for material characterization	208
A.2 Experiment setup for terahertz fibre characterization	209
A.3 Experiment setup for terahertz metasurface characterization	210
Appendix B. Simulation procedure in COMSOL Multiphysics	213
B.1 Simulation tools	213
B.2 Finite element method	213
B.3 COMSOL multiphysics	214
B.3.1 Step A: Model wizard.mph	214
B.3.2 Step B: Model builder	217
Appendix C. MATLAB Code	223
C.1 Matlab Code for obtaining optical properties of Graphene, BP, and optical fibre	223
Bibliography	233
Glossary	267
List of abbreviations	269
Index	273
Biography	277
Scientific genealogy	279

List of Figures

1.1	Electromagnetic spectrum.	3
1.2	Thesis outline.	5
<hr/>		
2.1	Methodologies of preparing smoothed surfaced Zeonex samples	13
2.2	Experimental setup.	15
2.3	Effect of nitrogen, signal averaging and phase unwrapping.	17
2.4	Phase angle and refractive index.	18
2.5	Spectral response and transmittance	19
2.6	Measured refractive index and dielectric constants of the materials.	22
2.7	Absorption coefficient and dielectric loss of the measured samples.	23
2.8	Chemical stability analysis.	25
2.9	Thermal stability analysis.	26
<hr/>		
3.1	Representative sketches of terahertz optical fibres.	34
3.2	Optical fibre categories.	35
3.3	Absorption loss as a function of core diameter and porosity.	37
3.4	Suspended-core terahertz fibres.	38
3.5	Hollow-core terahertz fibre based on antiresonant effect.	40
3.6	Hollow-core terahertz Bragg fibre	41
3.7	Hollow core terahertz waveguides with metallic wires and coating.	42
3.8	Terahertz optical fibre fabrication methods.	49
3.9	Characterization methods of terahertz optical fibre.	52
3.10	Low losses terahertz optical fibres.	54
3.11	Application of terahertz optical fibre in sensing and imaging.	55
3.12	Schematic of the all-terahertz fibre scanning near-field microscope.	58

List of Figures

4.1	Development of hexagonal PCF for terahertz transmission.	70
4.2	Development of asymmetrical terahertz waveguide.	74
4.3	Terahertz waveguides for low loss terahertz transmission.	79
4.4	Asymmetric porous waveguide for transmission and sensing.	81
4.5	Development of hollow waveguide sensor.	86
<hr/>		
5.1	Schematic diagram and typical loss of the specialty fibre.	96
5.2	Table-top fabrication procedure.	98
5.3	Representative images of the fabricated samples.	99
5.4	The experimental setup to measure the fabricated fibres.	100
5.5	Transmission spectra: measured and simulated.	101
5.6	Experimental total attenuation (red curves) and simulated loss (dashed blue curves), and sensitivity.	103
<hr/>		
6.1	Schematic and mode field characteristics of the LSPR biosensor.	110
6.2	Loss and sensitivity for metallic thickness variation.	111
6.3	Loss and sensitivity for geometric optimization.	113
6.4	Loss and sensitivity for analyte property variation.	114
6.5	Sensing performance of the optimized LSPR bisensor.	116
6.6	Schematic cross section and propagation modes of the hi-bi sensor.	123
6.7	Optimizing the plasmonic materials of the sensor.	128
6.8	Optical field distribution at fundamental core mode.	129
6.9	Confinement loss and amplitude sensitivity.	131
6.10	The wavelength dependent dispersion relation.	132
6.11	Resonance wavelength vs dielectric RI.	134
6.12	3D view of the proposed sensor where light impinges at the center of the fibre.	140
6.13	Dispersion relation of the exposed core fibre.	142
6.14	Optimization of geometric parameters.	143
6.15	Loss and sensitivity regarding outer dielectric.	143

6.16	Loss and sensing performance of the optimized fibre sensor.	144
6.17	Resonance wavelength and sensor length with the variation of RI.	145
6.18	FOM and FWHM with RI variation.	147
6.19	Fabrication and coating of the exposed core fibre.	148

7.1	Schematic of the electrically tunable graphene metasurface.	154
7.2	Equivalent circuit model of the metasurface.	158
7.3	Performance of the metasurface in terms of reflection, transmission, and absorbtion.	160
7.4	Mode field patterns of the proposed metasurface.	160
7.5	Magnetic field patterns of the metasurface.	161
7.6	Effect of graphene sheet on the metasurface performance	162
7.7	Effect on resonance frequency	162
7.8	Frequency tunability of the metasurface	163
7.9	Effect of graphene chemical potential	164
7.10	Angle dependence of the graphene metasurface	165
7.11	Performance variation considering fabrication tolerance	166
7.12	Performance of the metasurface as a sensor	167
7.13	Performance of the metasurface by changing dielectric properties	167
7.14	Linearity of the sensor	168
7.15	FWHM of the metasurface	168

8.1	Schematic of the all dielectric metasurface reflector.	174
8.2	Step by step fabrication procedure of the proposed metasurface.	176
8.3	Equivalent circuit modelling	178
8.4	Performance in consideration to reflection, transmission, and absorption of the all dielectric metasurface	180
8.5	Mode field patterns of the high-Q metasurface	180
8.6	Performance by varying the Ge resonator	181
8.7	Performance variation by considering the fabrication tolerance	183

List of Figures

8.8	Angle dependencies of the all dielectric metasurface	184
8.9	Performance as a sensor of the all dielectric metasurface	185
8.10	Linearity and Q -factor	186
8.11	Schematic of the structure contains elliptical resonator.	188
8.12	Step-by-step fabrication method	188
8.13	SEM images of the fabricated samples	189
8.14	Experimental setup for reflection measurement	189
8.15	Experimental outcome of the fabricated metasurface	190
<hr/>		
A.1	Schematic of experimental set-up	208
A.2	The experimental setup for fibres transmission measurement	209
A.3	The experimental setup for humid air sensing	210
A.4	The experimental setup for metasurface reflection measurement.	211
<hr/>		
B.1	Step by step COMSOL Simulation procedure.	215
B.2	Parameters setup in COMSOL simulation.	218
B.3	Material definition in COMSOL.	220
B.4	Mesh definition in COMSOL.	221

List of Tables

2.1	Optical properties of selected materials	24
2.2	Measured thermal properties of selected materials.	26
3.1	Terahertz optical fibres main features.	45
3.2	Selected experimentally demonstrated terahertz optical fibres.	46
3.3	Selected numerically studied terahertz optical fibres.	47
4.1	Comparison of obtained result between the proposed PCF with prior PCFs	72
4.2	Comparison between the obtained result of the proposed PCF with other PCF's	78
4.3	Comparison of the proposed PC-PCF sensor with prior PCF sensors for ethanol detection.	82
4.4	Comparison of sensing performance with global parameter variation of the hollow core PCF	89
4.5	Comparison of characteristics between the proposed sensor and prior sensor	89
5.1	Dimensions of the fabricated fibres.	100
6.1	Performance analysis of the proposed sensor by varying the dielectric RI	132
6.2	Comparison of performance of the proposed sensor with prior sensors having practical sensing approach.	133
6.3	Comparison of the proposed exposed core sensor with prior SPR sensors.	146
7.1	Comparison of the proposed multi-band device with prior reported de- vices.	169
8.1	Properties of the proposed high- Q device at optimum design parame- ters obtained by genetic algorithm.	186
8.2	Comparison of the proposed metasurface with prior reported metasur- faces.	187

Introduction

TERAHERTZ or T-ray radiation is situated between the electronics and photonics domains, or approximately between microwaves and the far-infrared, where microwaves lie around the present upper frequency limit of electronics, and far-infrared marks the lower frequency limit of optics. Traditionally, it has been a largely unexplored region of the electromagnetic spectrum. The technology for this region is still under development despite potential applications in spectroscopy, sensing, and communication. The advent of terahertz time-domain spectroscopy (THz-TDS) paves the way for further investigation and research on this frequency band. The optical regime on the other hand is a well developed regime as compared to terahertz. This introductory chapter offers a brief description of T-rays and outlines the structure of the thesis, the chapter contents, and the original contributions.

1.1 Terahertz radiation or T-rays

In the electromagnetic spectrum, the terahertz frequency band is usually defined within the range 0.1 THz to 10 THz (Sakai 2005, Abbott and Zhang 2007) although some researchers prefer to narrow it down to 0.3–3.0 THz (Siegel 2002, Woolard *et al.* 2005). A broad view of the electromagnetic spectrum and a schematic of its application areas is shown in Fig. 1.1(a), where an expanded view near the T-ray band is shown in Fig. 1.1(b). As can be seen, Fig. 1.1(b) indicates the overlapping of the T-ray band with the longer wavelength end of the EHF band, shorter wavelength end of the far infrared (FIR) band. It indicates that the EHF band ends at around 300 GHz or 0.3 THz whereas the T-ray band starts from 0.1 THz, and at the other end the FIR band starts from 1.0 THz whereas terahertz ends at 10 THz. The overlapping between two frequency bands is not usual and a precedence already exists—for example there is overlap between the x-ray and gamma ray bands. Researchers in the field specify terahertz using different units, however in this thesis we use THz as a spectral unit. The other forms of expressing terahertz are as follows:

- Frequency: $f = 0.1\text{--}10$ THz
- Angular frequency: $\omega = 2\pi f = 0.628\text{--}62.8$ rad/s
- Time: $t = 1/f = 0.1\text{--}10$ ps
- Wavelength: $\lambda = c/f = 30\ \mu\text{m}\text{--}3$ mm
- Wavenumber: $\bar{k} = 1/\lambda = 3.3\text{--}333$ cm⁻¹
- Photon energy: $hf = \hbar\omega = 410\ \mu\text{eV}\text{--}41$ meV

where, c and $h = 2\pi\hbar$ indicate the speed of light in free space and Planck's constant respectively.

Compared with other frequency ranges, the development of terahertz technology is largely lagging behind mainly due to lack of available materials/devices for effectively manipulating terahertz waves. The number of commercial products operating in the terahertz range are negligible compared with the overwhelming number of products in other frequency bands, such as microwaves and optics. However, terahertz waves are potentially important for many applications with societal impact.

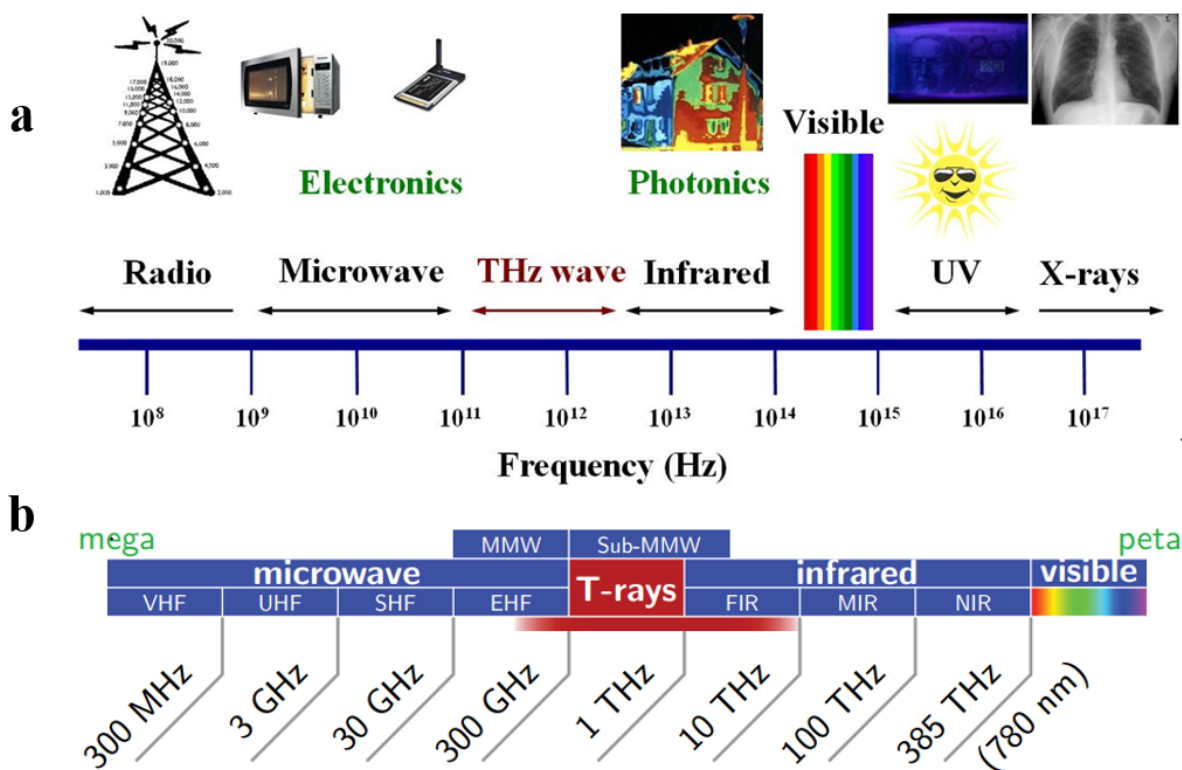


Figure 1.1. Electromagnetic spectrum. (a) Broad-view of electromagnetic spectrum showing the T-ray band and its neighboring electronics and photonics band. (b) Expanded view of the neighborhood of the T-ray band, indicating the lower and upper ends of the T-ray band overlaps the EHF and FIR bands, respectively. After Withayachumnankul (2009), Woolard *et al.* (2005).

1.2 Application of T-rays

At terahertz frequencies electromagnetic radiation interacts strongly with systems that have characteristic lifetimes in the picosecond range and/or energies in the meV range. Examples of such systems include bound electrical charges (Cole *et al.* 2001), free charge plasmas (Huber *et al.* 2001), strongly confined charge plasmas (Cooke *et al.* 2006), transient molecular dipoles (Beard *et al.* 2002), phonons in crystalline solids (Schall *et al.* 2001), hydrogen bonds in chemicals (Walther *et al.* 2003), intermolecular forces in liquids (Ronne *et al.* 1997), and biological matter (Whitmire *et al.* 2003).

The T-ray frequency band has the potential for various significant applications including but not limited to astronomy, security screening, biological and medical spectroscopy, non destructive evaluation, sensing, and communications (Zhao *et al.* 2019,

1.2 Application of T-rays

He *et al.* 2016, Ma *et al.* 2018a, Deng *et al.* 2019, Xu and Lam 2010, Withayachumnankul *et al.* 2018, Islam *et al.* 2017a, Islam *et al.* 2018j, Islam *et al.* 2018f, O'Hara *et al.* 2019, Chen *et al.* 2018c, Islam *et al.* 2020d, Keshavarz and Vafapour 2019). Owing to its penetration property through non-polar, dry, and nonmetallic materials such as wood, ceramics, paper, plastics, and fabrics, T-rays have significant application in the areas of surveillance imaging and quality control of products where contraband items can be concealed beneath physical layers such as clothing or packing materials (Federici *et al.* 2005, Tonouchi 2007). A number of studies have also shown the application of the T-ray band for material characterization (Islam *et al.* 2019e, Islam *et al.* 2020b, Ferguson and Zhang 2002, Beard *et al.* 2001, Grischkowsky *et al.* 1990, Nafaty and Miles 2007, Shi *et al.* 2019, Anthony *et al.* 2011a, Bolivar *et al.* 2003, Cunningham *et al.* 2011, Chang *et al.* 2017).

Moreover, various molecules, explosives, and drugs have spectral fingerprints, in the T-ray band, which offer advantages for T-ray spectroscopy and sensing (Woolard *et al.* 2005, Shen *et al.* 2005, Leahy-Hoppa *et al.* 2007, Kemp 2011). Although water absorbs a significant amount of T-ray energy and this is considered as one of the main limitations for terahertz applications, T-rays are suitable for sensing the hydration level in biological tissue—of great interest in the detection of skin cancer (Pickwell *et al.* 2004, Woodward *et al.* 2002). The strong absorption of T-rays by water molecules makes it suitable for sensing the hydration level in biological tissue. Moreover, the non-ionizing and non-invasive nature T-rays lend their applicability to medical and dental diagnostics that pose minimal or no health risk for human imaging when applied at low power levels (Han *et al.* 2000, Löffler *et al.* 2001, Mittleman *et al.* 1997, Smye *et al.* 2001).

T-ray characteristics are also desirable for various short-range communication systems mostly with large bandwidth—this has become feasible via significant recent development of high power T-ray sources (Hirata *et al.* 2006, Hirata *et al.* 2009, Koenig *et al.* 2013).

In Section 1.3, the structure of the thesis and the content of each chapter are summarized. This is followed by Section 1.4, where the original contribution of this research is highlighted.

Background	Chapter 1	Introduction
Material	Chapter 2	Experimental analysis on glass and polymers: materials for terahertz
Terahertz optical fibre	Chapter 3	Terahertz optical fiber
	Chapter 4	Terahertz waveguide: concepts and modelling
	Chapter 5	Tabletop fabrication for terahertz specialty optical fibre sensor
Visible to mid-IR fiber	Chapter 6	Surface plasmon resonance biosensor
Terahertz metasurface	Chapter 7	Electrically tuneable graphene metasurface
	Chapter 8	Bound states in the continuum for guided terahertz plasmons
Summary	Chapter 9	Conclusion and future remarks

Figure 1.2. Thesis outline. The thesis is composed of nine chapters where the original contributions are from chapter 2 to chapter 8. Chapter 9 provides an overall summary and future direction of the thesis.

1.3 Thesis outline

As outlined in Fig. 1.2, the thesis encompasses nine chapters. The original contributions of this thesis are provided in Chapters 2 to 8. The fundamentals necessary for understanding the main idea of each chapter are provided in the respective chapters. In Chapter 9 the summary of the thesis, the aim of each chapter, the methodology, the results, and the future directions are presented. The detailed description for each chapter of the thesis is as follows:

Chapter 1: Introduction provides a detail overview of terahertz spectrum and its applications, the structure of the thesis, a detailed discussion of the original contribution, and motivation of the work in this thesis are outlined.

Chapter 2: Experimental analysis of glasses and polymers: materials for terahertz. The thesis is mostly based on using different materials to make various advanced terahertz devices. Therefore from the outset, we choose to characterize various polymers and glasses useful for terahertz applications. The optical properties are characterized

1.3 Thesis outline

by THz-TDS while the thermal and chemical dependencies are also studied to identify the thermal and chemical stability of those materials. Based on the results of the optical, thermal, and chemical analysis the optimal materials to be used for terahertz technology are determined and discussed in this chapter.

Chapter 3: Terahertz optical fibre provides a brief review of the guiding mechanisms, the fabrication methodologies, the characterization methods, and the applications of terahertz waveguides. Various optical fibre types such as tube fibres, solid core fibre, hollow-core photonic bandgap, antiresonant fibres, porous-core fibres, metamaterial-based fibres, and their guiding mechanisms are studied in this chapter. The past and present trends in fabrication methods, including drilling, stacking, extrusion, and 3D printing, are elaborated. Fibre characterization methods including different optics for terahertz time-domain spectroscopy (THz-TDS) setups are reviewed and application areas including short-distance data transmission, imaging, sensing, and spectroscopy are discussed.

Chapter 4: Terahertz waveguide: concept and modelling. In this chapter various categories of terahertz fibre are designed, simulated, and analyzed to get an optimal fibre for terahertz guidance and sensing. Transmission properties such as effective material loss, core power fraction, confinement loss, effective area, birefringence, and dispersion are analyzed to choose optimal fibres for transmission and polarization preserving applications.

Chapter 5: Tabletop fabrication for terahertz specialty optical fibre sensor. In this chapter a hollow-hexagonal photonic crystal fibre is studied for transmission and gas sensing. The fibre design and simulation are carried out using COMSOL multiphysics software. Analytical analysis is carried out to validate the simulation result. An efficient, simple, and cost-effective method of fabricating asymmetric complex polymer fibres are used to fabricate the fibre. The experimental analysis of the fibre is also carried out using the TAS7400TS Advantest terahertz system. A promising result is found for short distance low loss data transmission and environmental gas sensing.

Chapter 6: Surface plasmon resonance biosensor. This chapter includes the study of surface plasmon and localized surface plasmon based fibre sensors in the optical

(visible to mid-IR) regime. Novel plasmonic sensors are designed and simulated using COMSOL multiphysics simulation software. One of the optimized fibre is then fabricated and coated by gold and graphene to be used for practical bio-sensing applications.

Chapter 7: Electrically tuneable graphene metasurface. The previous chapters are all based on transmission and sensing using optical fibre, while in this chapter a plasmonic metasurface is demonstrated for multi-band super-absorption and terahertz sensing. The design and simulation of the graphene metasurface is carried out using Finite Element Method (FEM) based software, CST microwave studio where a genetic algorithm (GA) is used to optimize the geometric parameters, and metasurface tunability is achieved via an external gate voltage on the graphene. This graphene absorber shows promising sensing capability with high linearity.

Chapter 8: Bound states in the continuum for guided terahertz plasmons. In this chapter, two different asymmetrical all-dielectric high-Q terahertz metasurface is studied that demonstrates high quality factor, remarkably narrow full width at half maxima (FWHM), high sensitivity, and high figure of merit (FOM). One of the high-Q metasurfaces is fabricated, and experimental validation is carried out using THz-TDS.

Chapter 9: Conclusion and future work. In this chapter we summarise the major outcomes, and the author's main contribution. It also contains a recommendations for future possible studies.

The appendices at the end provide supporting information and technical details. Appendix A describes the experiment set-ups used to characterize optical fibres and metasurfaces. Appendix B provides the step-by-step simulation procedure using COMSOL multiphysics simulation software. Appendix C includes data processing algorithms. It contains MATLAB codes to extract the frequency-dependent dielectric parameters, refractive index and absorption coefficient, of bulk material and fibre from the THz-TDS measurements. Appendix C also includes the algorithm for obtaining the plasma and collision frequency in graphene and black phosphorus.

1.4 Summary of original contribution

The thesis contains multidisciplinary studies and involves several original contributions in the field of fibre-based terahertz transmission and sensing, sensing in the optical regime, material characterization, graphene metasurfaces, and all-dielectric metasurfaces.

Spectroscopic analysis of various glasses and polymers that are most commonly used for terahertz devices is performed. The polymer pellets are obtained from Zeon corporation, Japan, to make circular disks of Zeonex, and Topas. The Teflon, PMMA, HDPE, silica, and BK7 are from IPAS, Adelaide, and the UV-resin from the University of Campinas, Brazil. For all the samples we carry out surface polishing using silicon carbide (SiC) sandpaper of different grit sizes, performing final polishing using a water-based diamond suspension. The spectroscopic analysis of all the materials is carried out using terahertz time-domain spectroscopy (THz-TDS). These give the refractive index, permittivity, loss tangent, absorption coefficient, and transmittance of the measured samples. We find that polymers show improved performance in consideration of loss and transmittance at terahertz. Further, we carry out stability analysis of the materials in the thermal and chemical environments. We use a thermal analyzer, TA Instruments (Q-500, Tokyo, Japan), to carry out the thermogravimetric analysis. Besides, we carry out the chemical stability testing of the low loss materials. We use a mechanical shaker and expose the materials to a highly acidic, saline, and basic solution. From all of these analyses, we determine that the Topas and Zeonex are best suited for terahertz applications. The content of this chapter is published in *45th International Conference on Infrared, Millimeter, and Terahertz Waves (45th IRMMW-THz)* (Islam *et al.* 2019e) and at *IEEE Access* (Islam *et al.* 2020b).

This thesis also demonstrates the design, simulation, fabrication, and experiment of terahertz optical fibre for terahertz transmission and sensing. We propose novel low loss and highly birefringent terahertz waveguides and published related articles in the *IEEE Sensors Journal* (Islam *et al.* 2017a, Islam *et al.* 2018j), *Applied Optics* (Islam *et al.* 2018d), *Optical Materials* (Islam *et al.* 2018h), and in *Optics Communications* (Islam *et al.* 2018f). In this thesis we use either kagome cladding with an asymmetric core created

by placing asymmetric rectangular air holes (Islam *et al.* 2017a), asymmetric hollow-core created by rectangular tubes (Islam *et al.* 2018j), or asymmetrical core created by elliptical air holes (Islam *et al.* 2018h). We design a hollow-core antiresonant waveguide, fabricated by a novel tabletop simple fabrication method. The fabrication steps consist of metal printing of the preform and then use of a horizontal extruder to fabricate the fibre structure. Note that using this fabrication method any type of fibre structure can be fabricated. To our knowledge, this is the first terahertz fibre fabrication using the method. Four different dimensions of the fibre are fabricated and the experiments are carried out in the ARC National T-ray Facility lab of the University of Adelaide. We also use the fibre for gas sensing. The simulation, analytical and experimental results show close agreement. The manuscript is submitted for publication at *Advanced Photonics Research* (Islam *et al.* 2021).

Besides working on terahertz transmission and sensing, we also work on making optical fibre-based sensors that operate in the optical (visible to mid-infrared) regime. Due to the plasmonic effect created by metal coating on the fibre surface we create surface plasmon and localized surface plasmon resonance based sensors for biochemical and analyte detection. The content of these studies are published at the *43rd IRMMW-THz 2018* conference (Islam *et al.* 2018e), *Optics Express* (Islam *et al.* 2018i), *IEEE Access* (Islam *et al.* 2019b), *Optics Letter* (Islam *et al.* 2019d), *JOSA B* (Islam *et al.* 2019c), and *IEEE Sensors Journal* (Mollah and Islam 2020). Considering the fabrication feasibility, the studies (Islam *et al.* 2018e, Islam *et al.* 2018i, Islam *et al.* 2019b, Islam *et al.* 2019d, Islam *et al.* 2019c, Mollah and Islam 2020).

Besides demonstrating the development of fibre-based optical devices, this thesis also shows our work on advanced metasurface based terahertz devices. In the first instance, we propose a graphene-based tunable multiband super-absorber. We design a multilayered graphene-based absorber that can consecutively achieve multiple absorption bands. The absorption frequencies are tunable by graphene chemical potential. Changing the graphene chemical potential changes the operating frequency. We further show that the proposed tunable metasurface is applicable for terahertz sensing. The content of this work is published at the *IRMMW-THz-2019* conference and

1.4 Summary of original contribution

Carbon (Islam *et al.* 2019f, Islam *et al.* 2020d).

Moreover we design a Bound States in the Continuum (BIC) enabled all-dielectric terahertz metasurface for achieving high Q-factor and Figure of Merit (FOM) based device in the terahertz frequency range. The designed metasurface results in significantly improved performance as compared to the metasurfaces reported in the literature. The content of this work is published at the *IRMMW-THz-2020* conference (Islam *et al.* 2020c) and further extended version is submitted for publication in a journal. Note that, both studies are designed and simulated using the CST microwave studio suite software where parametric optimization is carried out using a genetic algorithm. A further all-dielectric metasurface is fabricated in collaboration with RMIT, and then tested using THz-TDS, where the experimental outcome shows close agreement with the simulation result. This experimental study is in preparation for further submission to a journal.

In the next chapter we show the experimental analysis of various materials including glasses, polymers, and resin to find out the optimal material for terahertz application. The optical, thermal, and chemical analysis of the materials are carried out and following standard signal processing technique the refractive index, permittivity, absorption coefficient, loss tangent, temperature dependent, and chemical stabilities of selected materials are discussed.

Experimental study on glass and polymers: materials for terahertz

THE optical properties of polymers and glasses useful for terahertz applications are experimentally characterized using terahertz time-domain spectroscopy (THz-TDS). A standard system setup utilizing transmission spectroscopy is used to measure different optical properties of materials including refractive index, relative permittivity, loss tangent, absorption coefficient, and transmittance. The thermal and chemical dependencies of materials are also studied to identify the appropriate materials for given terahertz applications. The selected materials can then be utilized for applications such as in waveguides, filters, lenses, polarization preserving devices, metamaterials, absorbers, and sensors in the terahertz frequency range.

2.1 Introduction

The terahertz spectrum (0.1–10 THz) is considered as one of the least explored segments in the electromagnetic spectrum due to the lack of powerful terahertz sources and efficient detectors. However, the recent technological advancements in optics and electronics, advances in terahertz systems utilizing mode-locked femtosecond fibre lasers, together with advances in emitters and receivers, have led to progress in this field (Ferguson and Zhang 2002). The use of terahertz transmission mode has a number of significant applications spectroscopy (Zhao *et al.* 2019), lenses (He *et al.* 2016), security (Ma *et al.* 2018a), bio-imaging (Xu and Lam 2010), photonic crystals for communication and sensing (Withayachumnankul *et al.* 2018, Islam *et al.* 2017a, Islam *et al.* 2018f), high bandwidth communications (O'Hara *et al.* 2019) and biological sensing (Chen *et al.* 2018c, Islam *et al.* 2020d, Keshavarz and Vafapour 2019). One of the emerging applications of terahertz spectroscopy is to characterize the optical properties of a wide variety of materials such as semiconductors, ceramics, chemical mixtures, gases, lubricating oils, glasses and polymers (Ferguson and Zhang 2002, Beard *et al.* 2001). There are particular advantages of using terahertz for material characterization. First, terahertz spectroscopy typically covers a very wide bandwidth and a large number of materials have spectral fingerprints within this frequency range.

Second, terahertz spatial resolution is higher than microwaves because of its shorter wavelength, and finally, many dry non-polar materials are transparent to terahertz, making *in situ* characterization through packaging materials an attractive possibility (Bolivar *et al.* 2003).

Many materials were previously studied using far-infrared Fourier Transform Spectroscopy (FTS) where continuous wave (CW) non-coherent sources were used instead of the picosecond pulsed coherent sources in THz-TDS. There are a number of important aspects where THz-TDS differs from FTS that lends THz-TDS some significant advantages. The measurements typically carried out with THz-TDS utilize a pump-probe configuration, where amplitude and phase are acquired simultaneously. The pump-probe detection scheme also has improved signal to noise ratio (up to 60 dB or 10^6 in power) compared to about 300 typically obtained using FTS (Bolivar *et al.* 2003).

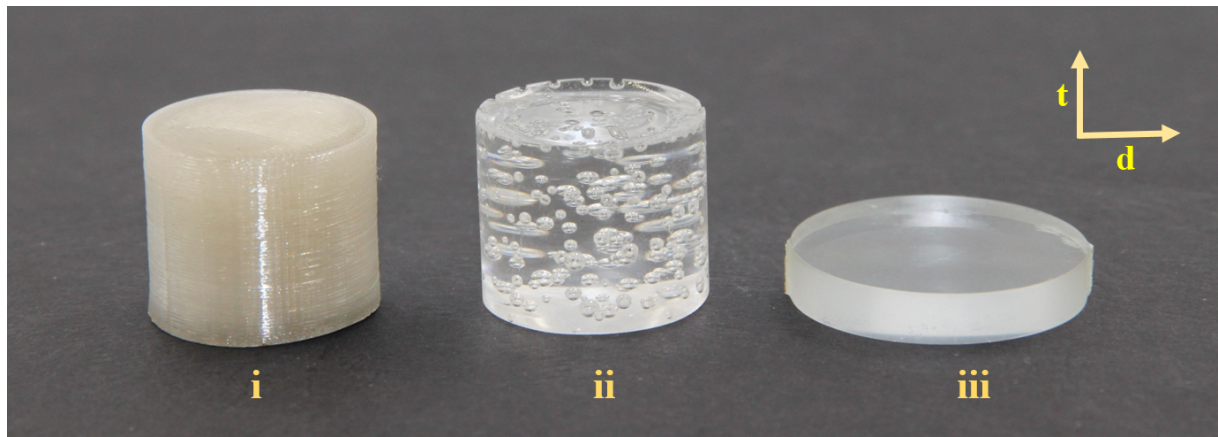


Figure 2.1. Methodologies of preparing smoothed surfaced Zeonex samples. (i) prepared using a 3D printer where the surface is rough containing ridges that potentially scatter the time domain signal, (ii) made using furnace at a temperature of 200°C for 24 hours, containing air bubbles, (iii) transparent sample without air bubbles inside, furnace at 200°C for 48 hours and polished with silicon carbide (SiC) sandpaper of different grit sizes. The d and t in the figure indicate the diameter and thickness of the samples which are 10mm×10mm for (i), 10mm×12mm for (ii), and 10mm×3mm for (iii), Islam *et al.* (2020b).

Note that for material characterization, the absorption coefficient and refractive index are directly related to the transmitted signal amplitude and phase that are readily obtained using THz-TDS whereas FTS is only able to provide a field intensity measurement that can only provide the absorption coefficient, and refractive index can only be obtained indirectly by resorting to the Kramers-Kronig relation with reduced accuracy. Moreover, the high dynamic range of THz-TDS allows transmission studies of highly absorptive materials.

Measurement using THz-TDS falls into two distinct categories, one is to identify or differentiate substances contained in a material, and another is to characterize the optical and dielectric properties of materials. In 1990, a study on different highly resistive dielectrics and semiconductors including sapphire, quartz, silicon, germanium, gallium arsenide, etc. were carried out using far infrared, time-domain spectroscopy (Grischkowsky *et al.* 1990). The refractive index and power absorption coefficients were measured within the frequency range of 0.2 to 2.0 THz.

2.1 Introduction

Anthony *et al.* (2011a) performed an analysis on Zeonex based microstructured fibre where the reported refractive index and absorption coefficients are 1.519 and 0.19 cm^{-1} respectively. Naftaly and Miles (2007) carried out a study on polymers, oils and glasses. However, they did not consider some important terahertz materials such as Zeonex, Topas, Teflon, PMMA, Duran and UV-resins, that are now commonly employed in various terahertz applications. In their analysis, Naftaly *et al.* showed that PMMA and HDPE achieve a refractive index of 1.61 and 1.54, where the reported absorption coefficients of these materials are 7.5 and 0.225 cm^{-1} , respectively.

Recently, Shi *et al.* (2019) performed an optical and electrical characterization on PMMA for the application of broadband absorbers. In 2012, an experiment on different polymer materials was also carried out (Fedulova *et al.* 2012), where a refractive index of 1.61, and 1.54 for PMMA and HDPE having corresponding absorption coefficients of 7.5, and 0.225 cm^{-1} respectively were obtained. Using transmission spectroscopy and S-parameters, Chang *et al.* also carried out studies on polymers at low (0.75–1.6 THz) frequencies. Cunningham *et al.* (2011) also studied various polymers, however, they did not consider Zeonex, UV-resin nor any of the glasses. In a 2014 spectroscopic study of common polymers, the authors did not consider some important terahertz materials such as Zeonex and HDPE (D'Angelo *et al.* 2014). Moreover, they did not consider glasses for characterization. Recently, in 2018, Pickwell-MacPherson's group carried out research on transparent, highly absorptive and conductive samples. In that work, they developed a fibre-based terahertz ellipsometer that provides excellent robustness on samples with different properties. Recently, a fundamental study of THz-TDS measurements were carried out, however the authors did not present specific samples for study (Withayachumnankul and Naftaly 2014, Jepsen 2019). More importantly none of the above referenced articles (Naftaly and Miles 2007, Cunningham *et al.* 2011, D'Angelo *et al.* 2014, Withayachumnankul and Naftaly 2014, Jepsen 2019) consider the analysis of the thermal and chemical properties of materials.

Considering the importance of characterizing the optical, thermal and chemical properties of polymers, glasses and UV-resins, in this thesis we introduce a combined characterization approach aimed at assisting the selection of the most appropriate materials for various terahertz applications. A comprehensive range of characterization methods is selected to provide the thermal range, chemical stability, absorption coefficients,

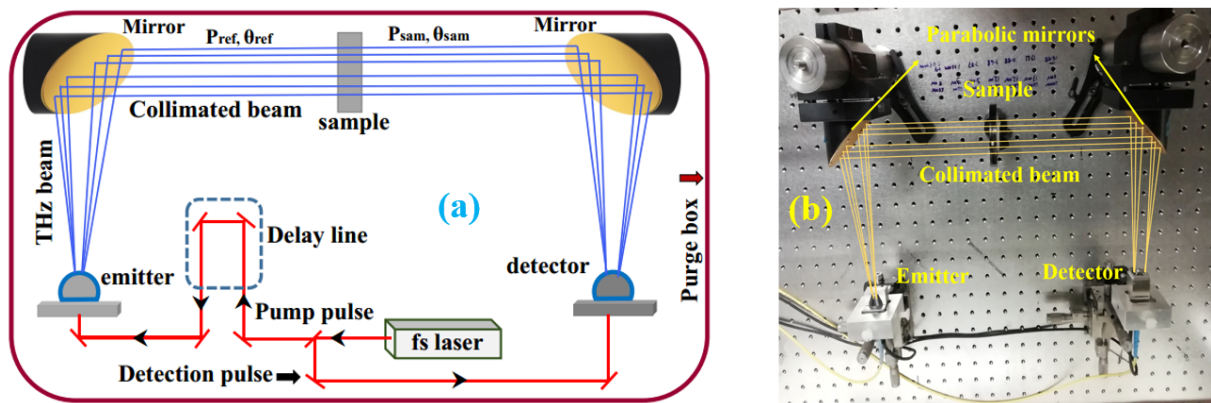


Figure 2.2. Experimental setup. (a) Schematic of experimental set-up of the enclosed THz-TDS system with a purge box filled with nitrogen, two parabolic mirrors creating a parallel beam where a sample holder is used to hold the sample, the reference signal is obtained by removing the samples whereas the sampled signal is obtained when a sample is in place as shown in the photograph, (b) the actual set-up Islam *et al.* (2020b).

transparency and loss properties for this purpose. The methods used for characterization are presented in the experimental section showing the experimental set-up and theoretical aspects of the required calculation. Finally, an overall performance analysis is carried out, together with a concise summary of material properties in the conclusion.

The studied glasses and polymers in this manuscript are commonly used for making different terahertz devices including waveguides (Islam *et al.* 2017d, Islam *et al.* 2016a), sensors, filters (Li *et al.* 2018a, Pavanello *et al.* 2013), lenses, metamaterials (He 2015) and metasurfaces (Ako *et al.* 2020, Islam *et al.* 2020d) for different applications in the terahertz frequency range. Some UV-resins for example can be used in stereolithography (SLA) 3D printers making them an interesting material for building terahertz waveguides (Argyros 2013, Cruz *et al.* 2018).

2.2 Sample preparation

Samples of Topas 5013 L-10 and Zeonex 480R are prepared from raw pellets. Initially, filaments of those materials are made using a Filabot EX2 filament Extruder and used for 3D printing of the samples. Fused Deposition Modelling (FDM) for 3D printing technology with high printing resolution is used to fabricate the samples, however, the outcomes are not satisfactory as there are numerous ridges on the surface, see

2.3 Experimental setup

Fig. 2.1(i), which potentially scatter the terahertz beam. Moreover, the fabricated samples are not optically transparent, with almost zero transmission measured using THz-TDS due to numerous air voids.

In the second trial we put the pellets inside a metal holder placed into a furnace at 200°C. After 24 hours, the small voids coalesce into larger air bubbles, shown in Fig. 2.1(ii). The air bubbles in the sample also scatter the terahertz beam and are therefore also unsuitable for material characterization. We further place the samples inside the furnace for another 24 hours, which removes all of the air bubbles. The samples are then cooled down and removed from the holder, and then cut and polished to make both the surfaces flat, smooth and parallel.

The polishing is graded using progressively finer silicon carbide (SiC) sandpaper, of grit sizes 120, 240, 320, 400, 800, 1200 and 2500 μm respectively. The samples are then given a final polish and smoothed using water based diamond suspension of 3 μm particle size. The polished and smoothed sample is shown in Fig. 2.1(iii). The sample of UV-resin is made using Stereolithography (SLA) 3D printing technology and polished before the experiment. Note that all other samples are cut and polished using the same procedure and all the measured samples have similar thickness of around 3 mm. Note that, the pellets of Topas and Zeonex are obtained from Zeon corporation, Japan. The UV-resin is prepared in Brazil, the sample of Teflon, PMMA, and HDPE are provided by the National T-ray facility lab, University of Adelaide. All the glass samples are supplied by the Institute for Photonics and Advanced Sensing (IPAS), University of Adelaide, Australia.

2.3 Experimental setup

The experimental setup and schematic are shown in Fig. 2.2 (a) and Fig. 2.2 (b). This uses a dual-channel ultrashort pulse laser, Advantest TAS7400TS, with a pulse width of ≤ 50 fs (using 1.5m fibre), employing a simple configuration for fibre-coupled, free space terahertz generation and detection. The laser center wavelength, output power, and repetition rate is 1550 nm, ≥ 20 mW, and 50 MHz respectively. In a phase modulated measurement method, the system time resolution is 2 fs, frequency resolution 1.9 GHz, scan range 524 ps, throughput 200 ms/scan and frequency accuracy

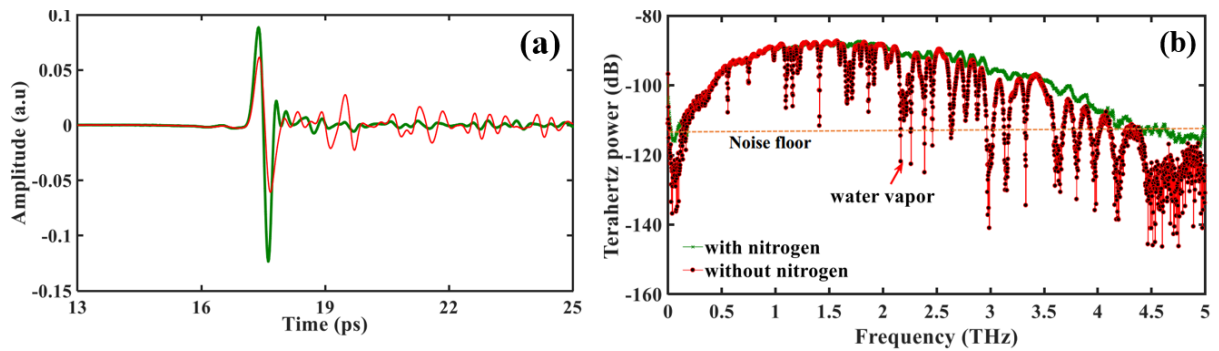


Figure 2.3. Effect of nitrogen, signal averaging and phase unwrapping. (a) Time-domain amplitude (a.u) and (b) power (dB), with and without dry nitrogen environment and signal averaging in the time domain. The red lines in the figures indicate signal without a nitrogen environment and averaging, whereas green lines indicate signal with nitrogen environment and averaging, Islam *et al.* (2020b).

is ± 10 GHz. The phase modulation measurement method relies on the difference in phase (arrival time) due to changes in wave path. The mechanical strain or thermal expansion of samples changes the optical path length and therefore cause changes in phase. This phases of reference and sample are then required to obtain the optical properties of the sample. The terahertz receiver Advantest model TAS1230 is fabricated with a photo-conductive antenna coupled to a hyper-hemispherical silicon lens in a fibre pigtailed compact housing.

The transmitter utilizes the Cherenkov (Auston *et al.* 1984) effect where the femtosecond optical pulse propagates through an electro-optic crystal with a second-order non-linearity. The Advantest model TAS1130 transmitter with a lithium niobate crystal waveguide has a bandwidth of 0.5 to 7 THz (Advantest 2021). Two off-axis gold-coated parabolic mirrors (Edmund optics) with an effective focal length of 150 mm are used to create a parallel collimated beam for spectroscopy. To ensure the beam passing through the sample, we insert an iris of diameter less than the sample diameter. The reason for this standard setup is to obtain more averaged data from the measurements. In consideration to sample dimension, different types of sample holders were utilized to constrain the measurement to the sample and ensure consistent results. The system was enclosed with a custom made purge box and the performance with and without dry nitrogen are shown in Fig. 2.3 (a-b). It can be seen that without nitrogen and averaging

2.4 Signal averaging and phase unwrapping

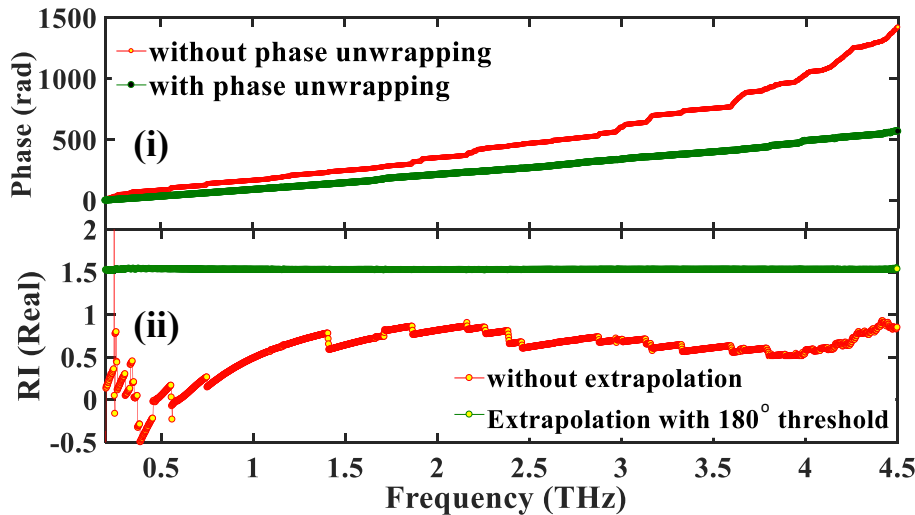


Figure 2.4. Phase angle and refractive index. (i) The phase of the transfer function, obtained from the measurement of a Zeonex sample, is unwrapped with and without phase extrapolation. (ii) The index of refraction is determined by using the phases in (i). The reported value of the RI of Zeonex at terahertz frequencies is around 1.529, Islam *et al.* (2020b).

(red) the terahertz amplitude, Fig. 2.3 (a), is comparatively reduced than in nitrogen environment and signal averaging (green). Moreover, for the spectrum, Fig. 2.3 (b), sharp water vapour lines are experienced, which is reduced in the nitrogen environment.

2.4 Signal averaging and phase unwrapping

The post-processing of THz-TDS data is followed by signal averaging and phase unwrapping. Random noise in measurements can be reduced by repeated multiple measurements. Signal averaging in the time domain, increases the signal strength relative to noise. Therefore, by averaging a set of replicated measurements, the signal to noise ratio (SNR) increases as a function of the square root of the number of ensembles (Withayachumnankul and Naftaly 2014). In our case, we repeat the measurement having 2048 number of sample scanning. The result is depicted in Fig. 2.3 (a) and Fig. 2.3 (b) where signal amplitude and power are shown with signal averaging.

Phase unwrapping is a vital step for correct characterization of the optical constants of samples. The phase spectrum can be obtained from the transfer function that wraps around with an abrupt jump from $-\pi$ to π . This indicates that whenever the absolute

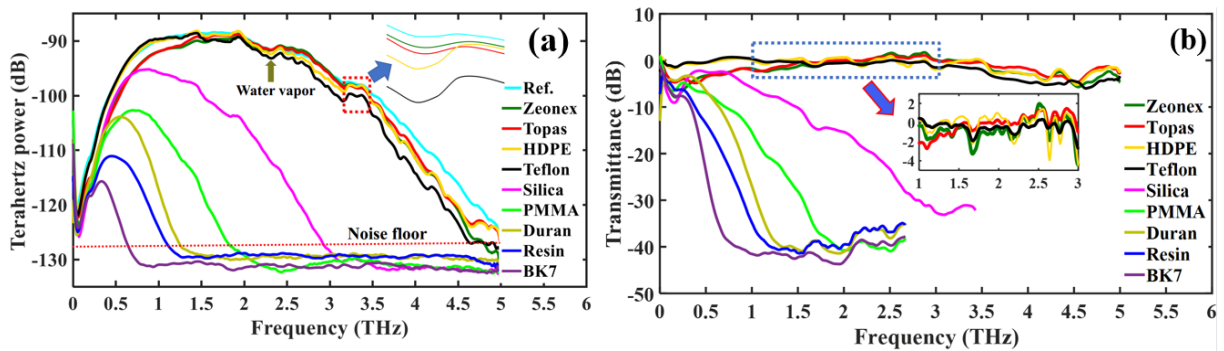


Figure 2.5. Spectral response and transmittance's of the measured polymers and glasses. (a) The received power spectrum of reference (background), Zeonex, Topas, HDPE, Teflon, Silica, PMMA, BK7, Duran, and UV-resin, (b) The terahertz transmittance's of the same materials, Islam *et al.* (2020b).

value of the phase is greater than π , it will jump by 2π . Phase jumps create discontinuity artifacts in the phase spectrum, leading to the incorrect characterization of optical properties. Phase unwrapping solves the phase wrapping problem. We choose a phase unwrap threshold of π and start unwrapping from 0.1 THz because at lower frequencies, errors in phase unwrapping can occur due to noise (Withayachumnankul and Naftaly 2014, Jepsen 2019).

The difference of phase of a transfer function obtained from a Zeonex sample by means of phase unwrapping and without phase unwrapping is shown in Fig. 2.4(i). This indicates that the phase extrapolation reduces phase jumps, making it suitable for correct sample characterization, even at very low frequencies. A complication of perfect phase unwrapping occurs at low and high frequencies where the noise plagues the amplitude and phase data, resulting in false unwrapping. Starting from noisy low frequencies, phase unwrapping causes error to propagate towards the phase at high frequencies. As a solution, an adaptive unwrapping procedure is followed that discards the phase at low frequencies. The missing phase profile at low frequencies is then extrapolated from high frequency unwrapped phases (Withayachumnankul and Naftaly 2014). With phase unwrapped, the refractive index of Zeonex is characterized, as shown in Fig. 2.4(ii). This illustrates the large error in the refractive index without unwrapping, while phase extrapolated by 180° corrects the refractive index measurement of Zeonex to the expected correct value of 1.529.

2.5 Mathematical expressions to extract optical properties from THz-TDS data

The received power spectrum, transmittance, absorption coefficient, phase shift, refractive index, dielectric loss and permittivity are calculated using the following expressions (Advantest 2021)

$$P_{\text{linear}}(\omega) = |\tilde{F}(\omega)|^2 \quad (2.1)$$

where $P_{\text{linear}}(\omega)$ indicates power spectrum, $|\tilde{F}(\omega)| = \sqrt{\text{Re}(\tilde{F}(\omega))^2 + \text{Im}(\tilde{F}(\omega))^2}$ represents the FFT complex data and magnitude respectively. Now, the linear transmittance can be found from the below equation

$$T_{\text{linear}}(\omega) = \frac{P_{\text{sam}}(\omega)}{P_{\text{ref}}(\omega)} \times 100 \quad (2.2)$$

where $T_{\text{linear}}(\omega)$ indicates the transmittance, and $P_{\text{ref}}(\omega)$ and $P_{\text{sam}}(\omega)$ represents the reference and sample power spectrum.

The absorption coefficient of a sample can be represented as (Naftaly and Miles 2007),

$$\alpha_{\omega} = \frac{2\omega k(\omega)}{c} \quad (2.3)$$

where, α_{ω} represents the absorption coefficient [m^{-1}], $k(\omega)$ represents the extinction coefficient, ω represents the angular frequency, [$\text{rad}/10^{-12}\text{s}$], and c represents the speed of light, [m/s].

The phase shift between the sampled and referenced signal can be denoted by,

$$\phi(\omega) = \theta_{\text{sam}}(\omega) - \theta_{\text{ref}}(\omega) \quad (2.4)$$

where $\phi(\omega)$, [rad], represents the phase shifts, $\theta_{\text{sam}}(\omega)$ and $\theta_{\text{ref}}(\omega)$ represents the sample and reference phases respectively (Withayachumnankul and Naftaly 2014).

Furthermore, the refractive index $n(\omega)$ and extinction coefficient $k(\omega)$ of a sample can be represented as,

$$n(\omega) = 1 + \frac{c\phi(\omega)}{d\omega} + \frac{c}{d\omega} \text{Arg} \left[\tilde{t}_{\text{as}}(\omega)\tilde{t}_{\text{sa}}(\omega) \times \sum_{l=0}^m \left((\tilde{r}_{\text{sa}}(\omega))^2 \exp \left[-i \frac{2\tilde{n}(\omega)d\omega}{c} \right] \right)^l \right]. \quad (2.5)$$

Now, the refractive index $n(\omega)$ and extinction coefficient $k(\omega)$ of a sample can be represented as,

$$k(\omega) = -\frac{c}{2d\omega} \ln \left[\frac{T_{\text{linear}}(\omega)}{\left| \tilde{t}_{\text{as}}(\omega) \tilde{t}_{\text{sa}}(\omega) \times \sum_{l=0}^m \left((\tilde{r}_{\text{sa}}(\omega))^2 \exp \left[-i \frac{2\tilde{n}(\omega)d\omega}{c} \right] \right) \right|^2} \times \frac{1}{100} \right] \quad (2.6)$$

where $n(\omega)$ and $k(\omega)$ represent the refractive index and the extinction coefficients respectively, $\tilde{t}_{\text{sa}}(\omega) = \tilde{t}_{\text{as}}(\omega) = \frac{2}{\tilde{n}(\omega) + 1}$, $\tilde{r}_{\text{sa}}(\omega) = \tilde{r}_{\text{as}}(\omega) = \frac{\tilde{n}(\omega) - 1}{\tilde{n}(\omega) + 1}$, d represents the sample thickness, $\tilde{n}(\omega) = n(\omega) - ik(\omega)$ indicates the complex index of refraction, $\arg[\cdot] = \tan^{-1}(y/x)$ denotes the deflection angle, m indicates the number of multiple reflections. The deflection angle term can be neglected for thicker samples and therefore we use a simplified form of Eqn. 2.5 to obtain the refractive indices, Eqn. 2.7.

In simplified form, neglecting the deflection angle, the refractive index and extinction coefficient can be written as (Naftaly and Miles 2007, Withayachumnankul and Naftaly 2014)

$$n(\omega) = 1 + \frac{c\phi(\omega)}{d\omega}, \quad (2.7)$$

$$k(\omega) = -\frac{c}{d\omega} \left\{ \ln \left[\frac{4n(\omega)}{[n(\omega) + 1]^2} \right] - \ln |T_{\text{linear}}(\omega)| \right\}. \quad (2.8)$$

Using the refractive index, the permittivity and the dielectric loss tangent can then be calculated by,

$$\varepsilon_1(\omega) = n(\omega)^2 - k(\omega)^2 \quad (2.9)$$

$$\varepsilon_2(\omega) = 2n(\omega)k(\omega) \quad (2.10)$$

where $\varepsilon_1(\omega)$ and $\varepsilon_2(\omega)$ represents the permittivity and dielectric loss tangent respectively, (Advantest 2021).

2.6 Dielectric and optical properties of measured samples

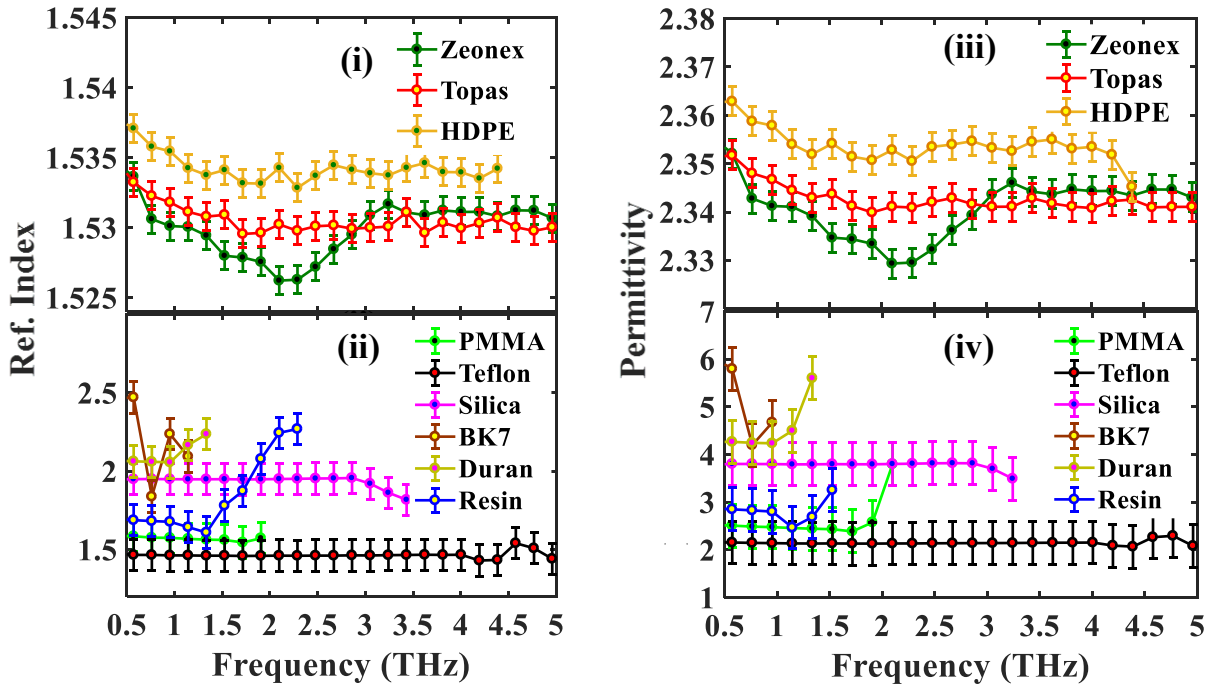


Figure 2.6. Measured refractive index and dielectric constants of the materials. (Refractive indices (i–ii), and dielectric constants (iii–iv) of the measured polymers and glasses, Islam *et al.* (2020b).

2.6 Dielectric and optical properties of measured samples

At terahertz frequencies, the dielectric and optical properties including the refractive index, dielectric constant, bandwidth, absorption coefficient, dielectric loss, and transmittance of the samples is illustrated and discussed in this section. The measured terahertz power (dB) passing through various samples is shown in Fig. 2.5 (a). The system is purged and the measurements are carried out in a nitrogen environment. As compared to Fig. 2.3 (b) (without nitrogen), we see that the water vapour peaks are significantly reduced in nitrogen environment, Fig. 2.5 (a). We see that a similar transmission bandwidth is obtained for Zeonex, Topas, HDPE, and Teflon where a comparatively lower transmission bandwidth is achieved for PMMA. From the glasses, the FS-300 silica shows better power transmission over other measured glasses such as BK7 and Duran. The FS-300 silica, BK7, and Duran achieve a transmission bandwidth of around 2.5 THz, 0.75 THz, and 1.1 THz respectively, while the UV-resin exhibits the narrowest power transmission bandwidth of all polymers at around 0.9 THz. Fig. 2.5 (a) illustrates the water vapour peaks from the measurement environment and the nature of the samples itself that can be reduced by flushing the measurement system with dry nitrogen, and storing the samples in a dry environment.

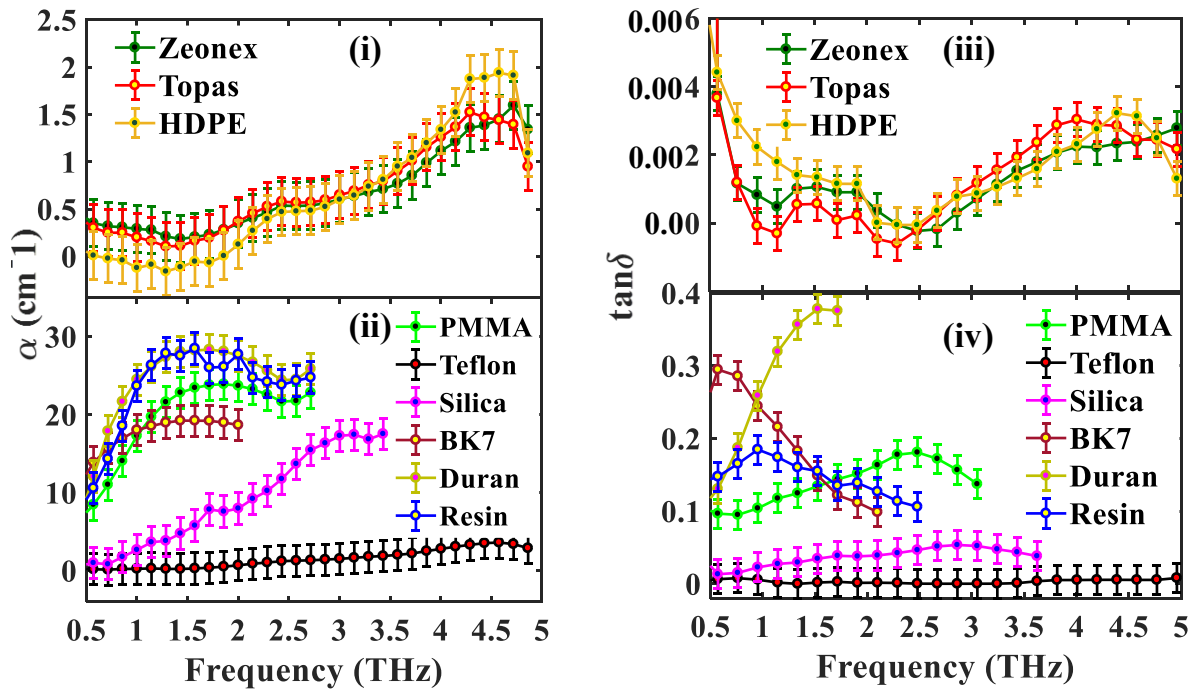


Figure 2.7. Absorption coefficient and dielectric loss of the measured samples. (i-ii) Absorption coefficients, and (iii-iv) dielectric loss tangents of the measured polymers and glasses showing low absorption coefficients for the polymers than the glasses and UV-resin, Islam *et al.* (2020b).

The transmittance of the materials is calculated using Eqn. 2.2 and illustrated in Fig. 2.5 (b), showing the low terahertz transmittance for BK7, UV-resin, Duran and silica, and better transmittances for Zeonex, Topas, Teflon, and HDPE. Therefore, a high-frequency application that requires high transparency, should utilize the Zeonex, Topas, HDPE and Teflon materials wherever their mechanical and thermal properties may allow this.

Using the time delays of measured samples, the associated phases are extracted. This data, together with the phases and extinction coefficients, enables the calculation of refractive indices and relative permittivities, as illustrated in Fig. 2.6 (i-ii) and Fig. 2.6 (iii-iv). The average refractive index of the measured Zeonex, Topas, HDPE, PMMA, Teflon, silica, BK7, Duran, and resin are 1.529, 1.531, 1.535, 1.584, 1.466, 1.943, 2.46, 2.06, and 1.69 respectively. The relative permittivities has a square relation with the refractive index. The measured properties are compared with the literature (Beard *et al.* 2001, Naftaly and Miles 2007, Bolivar *et al.* 2003, Cunningham *et al.* 2011), shown in Tab. 2.1, which are perfectly matched.

2.6 Dielectric and optical properties of measured samples

Sample	n	n (Published)	Relative permittivities	$\tan\delta$	α (cm^{-1})	α (cm^{-1}) published
Zeonex	1.529	1.519	2.34	0.006	0.184	0.19
Topas	1.531	1.53	2.343	0.007	0.20	0.15, 0.25
PMMA	1.584	1.61, 1.57	2.50	0.10	4.40	7.5, 9.25
HDPE	1.535	1.54, 1.36	2.36	0.005	0.22	0.225, 1.66
Teflon	1.466	1.45, 1.42	2.15	0.008	0.26	0.25, 0.6
TPX	-	1.455	2.11	-	-	0.4
PP	-	1.48	2.19	-	-	0.29
Silica	1.943	1.96	3.78	0.045	1.98	3.5, 3.8
BK7	2.46	2.52	6.05	0.21	11	15
Duran	2.06	–	4.05	0.25	15	–
UV-resin	1.69	–	2.86	0.15	16	–

Table 2.1. Optical properties of selected materials. Comparative study of refractive indices, relative permittivities, loss tangents, and absorption coefficients of the measured samples with the literature. After, Anthony *et al.* (2011a), Fedulova *et al.* (2012), Cunningham *et al.* (2011), Naftaly and Miles (2007), Podzorov and Gallot (2008), Kitai *et al.* (2017), Sanjuan and Tocho (2012).

The absorption coefficients and dielectric loss tangents of the measured samples are illustrated in Fig. 2.7 (i–ii) and Fig. 2.7 (iii–iv). These are higher for all the glasses, PMMA and UV-resin than for Zeonex, Topas, HDPE, and Teflon. However, Fig. 2.7 also illustrate that the absorption coefficient and loss tangent for HDPE and Teflon are relatively higher at high frequencies than Zeonex and Topas. The obtained average absorption coefficients and loss tangents are summarized in Tab. 2.1 and compared with the literature. Note that Topas and Zeonex show almost similar properties all over the frequency of interests. The unwanted peaks in the absorption spectrum are due to the remained water vapour present during measurements.

In Tab. 2.1 we combine the properties including refractive indices, relative permittivities, loss tangents and absorption coefficients of the measured glasses and polymers. These properties are then compared with the literature and it can be seen that they are in good agreement.

In addition to searching for the low loss materials from the studied glasses and polymers, it is also necessary to characterize their thermal and chemical stability. Therefore besides the optical properties, we also determine the thermal and chemical properties

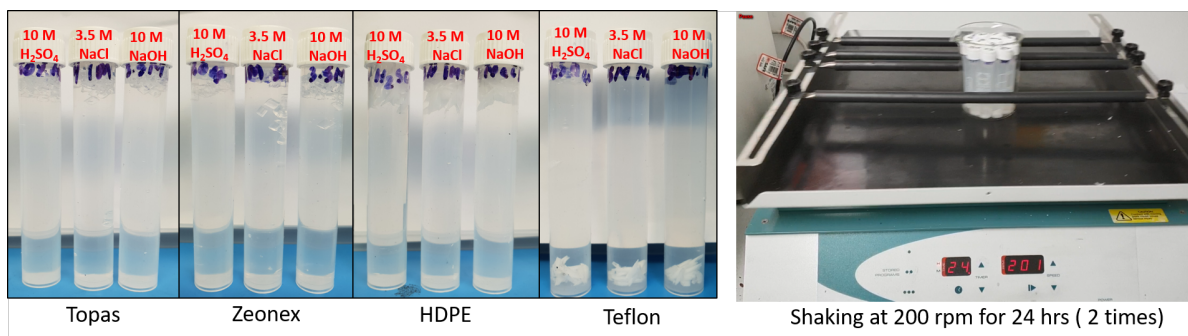


Figure 2.8. Chemical stability analysis. Chemical stability testing of Topas, Zeonex, HDPE and Teflon over acidic, salinic, and basic environments, Islam *et al.* (2020b).

of the low loss polymers to determine suitable materials that are applicable for harsh and hostile environments.

2.7 Chemical and thermal stability of polymers

To measure the chemical stability, as in Fig. 2.8, 0.5 g of each material was exposed to 10 ml of highly acidic (low pH) H₂SO₄ (10 M) solution, saline NaCl (3.5 M) solution, and basic (high pH) NaOH (10 M) solution (here, M indicates molar concentration). These solutions were agitated by a mechanical shaker at 200 rpm for 24 hrs to observe any effect of a chemical attack on the materials. No physical changes were observed in the first 24 hrs, thus the agitation was continued for another round of 24 hrs. Finally, the materials were taken out and dried at room temperature followed by a mass measurement. No significant mass change ($\pm 1.5\%$) was found for any of these four materials and this demonstrates the extreme chemical stability of these materials against acidic and saline environments.

In order to characterize the thermal stability of the selected materials (Topas, Zeonex, HDPE, Teflon), the thermogravimetric (TG) and derivative thermogravimetric (DTG) analysis were carried out using non-isothermal thermogravimetric analysis setup, TA Instruments (Q-500, Tokyo, Japan). The thermal analyser was temperature calibrated between experiments using the Curie point of nickel as a reference. The experiment was performed under a nitrogen environment at a purge rate of 60 ml/min. For each polymer, samples of approximately 40 mg was heated upto 800°C at a heating rate of 5°C/min. Based on the heating rate, the onset temperature and peak temperature may vary, however, for simplicity we consider a heating rate of 5°C/min. The TG

2.7 Chemical and thermal stability of polymers

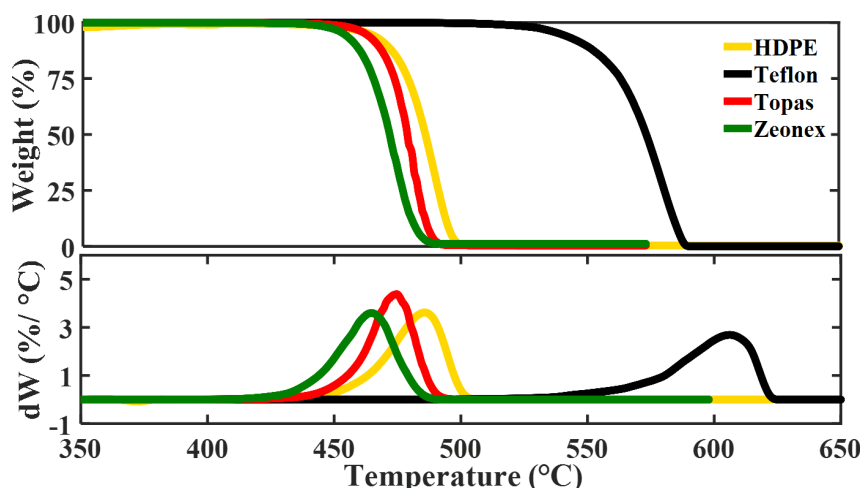


Figure 2.9. Thermal stability analysis. Percentage of weight loss and derivative of weight loss of HDPE, Topas, Teflon, and Zeonex as a function of temperature variation, Islam *et al.* (2020b).

Sample	Onset Temperature (°C)	Peak Temperature (°C)	ΔT (°C)
HDPE	468	485	17
Teflon	580	610	30
Topas	460	476	16
Zeonex	443	463	20

Table 2.2. Measured thermal properties of selected materials. The onset temperature, peak temperature, and the difference between onset and peak temperature of HDPE, Teflon, Topas and Zeonex at a heating rate of 5°C/min.

and DTG curves for HDPE, Teflon, Topas and Zeonex are illustrated in Fig. 2.9 where the DTG plot shows a peak weight loss from where the peak temperature degradation (T_p) can be determined. The onset temperature degradation (T_{onset}) is the point at which the material starts to degrade or disintegrate while the peak temperature is a point at which the degradation rate reaches at its maximum. The detailed thermal characteristics of the samples including the weight loss temperatures, T_p and T_{onset} is shown in Tab. 2.2.

According to Tab. 2.2 and Fig. 2.9 we find that the Teflon has highest thermal stability among the experimented samples and starts losing its weight due to evaporation from around 525°C and ended up at around 620°C. While the other three materials HDPE, Topas, and Zeonex have shown similar thermal characteristics and start losing weight from 440°C and ending up of around 480 to 500°C. Fig. 2.9 also illustrates that all the

samples lose their weight after a particular temperature is attained, and the obtained results are aligned with a previous thermal study of Topas and HDPE (Liu *et al.* 2003).

Though Teflon has the best thermal stability, it shows higher absorption loss and dielectric loss tangent at high frequencies compared to Zeonex, Topas and HDPE. Teflon is a fairly heat resistant and excellent anti-friction polymer that enables its use in mechanical units without additional lubrication. High loss materials such as PMMA, silica, BK7, Duran, resin, etc. also have high refractive indices that can be used for thinner metamaterial or metasurface designs. Moreover, crystalline materials such as silicon, germanium, sapphire and quartz demonstrate low transmittance at terahertz due to reflection losses. The absorption coefficients of these materials are around 0.5 cm^{-1} (Rogalin *et al.* 2018, Dai *et al.* 2004). Because of the high refractive index and desired physiochemical properties, these crystalline materials are widely used in manufacturing substrates with high-quality interference mirrors for high reflection coefficients.

As demonstrated in Fig. 2.9, HDPE shows improved thermal stability over Zeonex or Topas, however, HDPE has higher absorption loss. Similar to Teflon, HDPE exhibits an increasing loss trend at higher frequencies. The thin HDPE films are used for manufacturing terahertz polarizers and windows for Golay cells. The absorption coefficient, dielectric loss tangent, transmittance and thermal stability of Zeonex and Topas are almost identical, with a linear trend in optical characteristics, observed at higher terahertz frequencies. The absorption coefficient and loss tangent of Zeonex and Topas are extremely low and that also comes with higher transmittance than any other measured samples. Other polymers such as polypropylenes (PP) and polymethylpentene (TPX) show potential for terahertz applications however both have higher absorption coefficients (0.29 cm^{-1} @ 1.0 THz for PP, and ($\sim 0.4 \text{ cm}^{-1}$ @ 1.0 THz, for TPX) (Podzorov and Gallot 2008, Kitai *et al.* 2017) than Topas and Zeonex.

Low loss TPX is a strong material and can mechanically be converted into lenses and windows, exhibiting excellent optical properties for serving as an ideal substitute for picarin (tsurupica) in the manufacture of lenses. Picarin is commercially less accessible and more expensive (Fedulova *et al.* 2012). However, based on transparency and

2.8 Conclusion

absorption coefficients, the Zeonex and Topas are considered superior to TPX. Therefore, in consideration of absorption coefficients, transparency, dielectric loss tangents and thermal and chemical stability of polymer materials, Zeonex and Topas can be considered as desirable for applications in terahertz technology. These applications include terahertz lenses, modulators, filters, metamaterials, metasurfaces and terahertz sensors.

2.8 Conclusion

The optical, chemical and thermal properties of glasses and polymers are investigated to select the optimal materials for applications in terahertz technology. The THz-TDS and TGA analyses are carried out for obtaining optical and thermal properties whereas the experiments of chemical properties are carried out in acidic, salinic and basic environments. Optical, thermal and chemical investigations show that the materials are highly chemically and thermally stable. However, considering the absorption coefficients, transmittances and loss tangents, both Zeonex and Topas are found to be best suited for terahertz applications.

In the following chapter, a comprehensive review of terahertz optical fibres is carried out. Different optical fibre categories made by various materials are discussed. The guiding mechanisms, fabrication methodologies, experimental methodologies, and application of terahertz optical fibres are also addressed.

Terahertz optical fibres

TERAHERTZ optical fibres are essential for developing the full potential of complex terahertz systems. In this chapter, we review the guiding mechanisms, the fabrication methodologies, the characterization methods, and the applications of terahertz waveguides. We examine various optical fibre types including tube fibres, solid core fibre, hollow-core photonic bandgap, antiresonant fibres, porous-core fibres, metamaterial-based fibres, and their guiding mechanisms. The optimal materials for terahertz applications are discussed. The past and present trends of fabrication methods, including drilling, stacking, extrusion and 3D printing, are elaborated. Fibre characterization methods including different optics for terahertz time-domain spectroscopy (THz-TDS) setups are reviewed and application areas including short-distance data transmission, imaging, sensing, and spectroscopy are also discussed.

3.1 Introduction

The advance of terahertz technology and the growing interest in applications have increased the demand for developing new sources, detectors, waveguides, and other components for efficient control of terahertz waves. Low loss and low dispersion waveguides represent one of the critical technologies for a new generation of terahertz systems. The focus on terahertz has increased because of the recent availability of convenient sources and detectors, bridging the so-called “terahertz gap” that was traditionally due to the lack of practical, low-cost and efficient components. The new frontier includes exciting applications such as non-destructive testing (NDT), label-free and non-invasive molecular detection, detection of DNA hybridization, pharmaceutical drug testing, and broadband short-range communications (Gallot *et al.* 2000, Atakaramians *et al.* 2013, Siegel 2002, Islam *et al.* 2018f, Islam *et al.* 2017d, Islam *et al.* 2016a, Islam *et al.* 2018d, Sultana *et al.* 2018b, Islam *et al.* 2016c, Islam *et al.* 2017b, Islam *et al.* 2018h). Terahertz also has potential for biomedical spectroscopy with a photon energy that is lower than that of mid-IR radiation, yet with stronger polar molecular interactions than microwave radiation (Yang *et al.* 2018c, Reyes-Vera *et al.* 2018, Habib *et al.* 2018, Paul *et al.* 2018, Habib and Anower 2019, Wang *et al.* 2019, Rana *et al.* 2018, Xiao *et al.* 2018a, Nazarov *et al.* 2018, Yan *et al.* 2018, Sultana *et al.* 2017b, Mittleman *et al.* 1998, Gerecht *et al.* 2011, Lin *et al.* 2008, Pickwell and Wallace 2006, Islam *et al.* 2017a, Islam *et al.* 2019f, Islam *et al.* 2020d, Islam *et al.* 2018j, Williams 2007, Chan *et al.* 2007).

Moreover, it is in demand for defence and security screening as it can easily penetrate plastics, cardboard and clothing (Tsydynzhapov *et al.* 2018). Despite all the potential applications, terahertz is still in the development phase because most present terahertz systems are bulky and typically depend on free-space transmission. Whilst the availability of sources and detectors has enabled recent work in this area, other components remain primitive in comparison to their optics counterparts (i.e., designed for visible and infrared).

Terahertz radiation is highly sensitive to the atmosphere due to water vapour content. The free space transmission of terahertz experiences various undesirable losses

due to the coupling with atmospheric components that significantly reduces the transmission efficiency. Therefore, in order to upgrade some terahertz systems, it is necessary to build up low loss waveguides. As a primary solution, prior studies have proposed several waveguides including metallic wires, parallel plates, dielectric tubes with metal coating, polystyrene foams, sub-wavelength fibres, Bragg fibres, hollow-core fibres, porous-core fibres, and antiresonant terahertz fibres (Jeon *et al.* 2005, Gallot *et al.* 2000, McGowan *et al.* 1999, Wang and Mittleman 2004, Yudasari *et al.* 2014, Agrawal 2012, Poli *et al.* 2007, Knight *et al.* 1998, Vincetti and Setti 2010, Beravat *et al.* 2016, Russell 2003, Knight 2003, Cerqueira Jr 2010, Argyros and Pla 2007, G er ome *et al.* 2010, Couny and Benabid 2006, Couny *et al.* 2007, Yu and Knight 2016, Wei *et al.* 2017, Russell *et al.* 2017, Argyros 2013, Barh *et al.* 2015, Atakaramians *et al.* 2009a, Chen *et al.* 2013, Hassani *et al.* 2008, Bao *et al.* 2012, Kaijage *et al.* 2013, Aming *et al.* 2016, Sultana *et al.* 2018b, Atakaramians *et al.* 2009b, Cruz *et al.* 2013c, Faisal and Islam 2018, Rana *et al.* 2016, Mei *et al.* 2019, Vincetti 2009a, Cruz *et al.* 2018, Anthony *et al.* 2011b, Yang *et al.* 2016, Lai *et al.* 2010, Bao *et al.* 2015, Zhu *et al.* 2019, Hasanuzzaman *et al.* 2018, Cruz *et al.* 2015, Cruz *et al.* 2017, Sultana *et al.* 2019c, Sultana *et al.* 2019a, Sultana *et al.* 2020, Dupuis *et al.* 2011, Cruz *et al.* 2015, Harrington *et al.* 2004, Atakaramians *et al.* 2013, Markov *et al.* 2012, Markov *et al.* 2014, Yang *et al.* 2019b). Metal wires were proposed in the early days of terahertz technology development (Jeon *et al.* 2005, Gallot *et al.* 2000, McGowan *et al.* 1999).

Single metal wire can operate as a waveguide for terahertz pulses with reduced dispersion and low attenuation (Wang and Mittleman 2004, Atakaramians *et al.* 2013). However, the coupling of the free-space terahertz beam to the metal wire-guided mode is very ineffective, since the fundamental mode of metal wire waveguide is radially polarized while the photoconductive antennas produce linearly polarized terahertz signal (Wang and Mittleman 2004). Two-wire waveguides gained attention with low loss and improved coupling properties (Atakaramians *et al.* 2013), however, not practical for real-world applications. In spite of metallic wires possessing desirable propagation characteristics, the most promising device for guiding terahertz is a dielectric waveguide and its principal category is the terahertz optical fibre. Since the introduction of the solid dielectric rod, there are now a large number of proposed designs for terahertz optical fibres—the most advanced designs are based on the concept of speciality optical fibres (Atakaramians *et al.* 2013). Terahertz optical fibres have, for example, the potential to be designed to allow waveguiding through air and much deeper control of

3.2 Terahertz optical fibre types and guiding mechanisms

the waveguide optical properties such as loss, birefringence, dispersion, transmittance bands, modal areas, etc.

In this chapter, we aim to combine the recent development of terahertz optical fibres with different geometries and guiding mechanisms, the background materials, the fabrication techniques, measurement techniques, and potential applications.

3.2 Terahertz optical fibre types and guiding mechanisms

In this section, the main advances in the development of terahertz waveguides are summarized. A large variety of terahertz waveguide concepts have been proposed in the last two decades and, usually, are based on metal wires and dielectric waveguides. As a classical optical fibre, the terahertz wave propagation in dielectric waveguides can be supported by the following physical mechanisms: the total internal reflection effect (TIR) (Agrawal 2012), the modified total internal reflection (mTIR) (Poli *et al.* 2007) in microstructured fibres (or Photonic Crystal fibre-PCF), the photonic bandgap effect (PBG) (Knight *et al.* 1998), the antiresonant effect with inhibited coupling of core and cladding modes (Vincetti and Setti 2010) and the topological channel effect in helically twisted structures (Beravat *et al.* 2016). The TIR and mTIR effects are related to the refractive index contrast between core and cladding of an optical fibre, allowing the fibre to propagate electromagnetic waves at the high index core. The mTIR is essentially the same TIR physical effect and is present when the cladding is a microstructured region with lower refractive index material formed by low index inclusions (usually air holes) in the background fibre material (Russell 2003). The PBG effect in microstructured optical fibres leads to a condition where the electromagnetic wave is not allowed to propagate in the transverse directions but is able to propagate longitudinally at a defect region (Knight *et al.* 1998). The defect region is a perturbation in the periodic microstructure of the cladding and defines the fibre core region (Knight *et al.* 1998). In this condition, the electromagnetic wave can be guided via an “out-of-plane” photonic bandgap and low loss longitudinal transmission occurs in spectral bands where the two-dimension microstructured lattice exhibits forbidden wavelengths for transverse electromagnetic waves (Knight *et al.* 1998, Russell 2003, Knight 2003). These narrow spectral bands depend on the periodic cladding structure, geometry, and refractive index contrast between the background material and the low index periodic inclusions in

the microstructured cladding (Russell 2003, Knight 2003). The PBG effect allows wave propagation in hollow-core waveguides that opens the possibility of applications in telecommunications and sensing (Russell 2003, Knight 2003, Cerqueira Jr 2010).

Some hollow-core PCFs have a cladding microstructure with a high air filling factor (thin webs between large air-holes). This lattice structure is called *kagome* and it does not support the PBG effect. An optical fibre with kagome cladding lattice exhibits a lower density of photonic states and, in this situation, core and cladding modes can co-exist without coupling (Atakaramians *et al.* 2013), (Argyros and Pla 2007, G er ome *et al.* 2010, Couny and Benabid 2006, Couny *et al.* 2007) (guidance based on inhibited coupling). The probability of coupling between core and cladding modes depends on the match of their effective indexes and their spatial mode overlap (Argyros and Pla 2007). The low density of cladding modes is a critical condition, reducing the probability of core and cladding mode coupling. This opens the possibility of low loss core guidance in wide spectral range in *kagome* lattice fibres (Couny *et al.* 2007).

In such structures, the cladding is formed by a complex lattice of air-holes with high filling factor, and the fibre core is surrounded by a thin dielectric ring (Cerqueira Jr 2010, Argyros and Pla 2007, G er ome *et al.* 2010, Couny and Benabid 2006, Couny *et al.* 2007). If we consider simplifying this structure to a thin dielectric ring surrounding the hollow-core, this is called a tube fibre (or pipe fibre). Like a kagome structure, the very low density of modes supported by the ring reduces the probability of coupling in core and cladding modes (inhibited coupling). In fact, it is possible to analyze the guidance condition in the tube fibre considering the structure as an antiresonant reflecting optical waveguide (ARROW) (G er ome *et al.* 2010). As a double-layered Fabry-P erot resonator, at the antiresonant wavelengths the constructive interference occurs inside the hollow-core supporting terahertz transmission, and at the resonant wavelengths the light couples to lossy modes inside the dielectric ring (Cerqueira Jr 2010, Argyros and Pla 2007, G er ome *et al.* 2010, Couny and Benabid 2006).

This guidance mechanism is known as the *antiresonant* effect with inhibited coupling and has been explored in terahertz waveguide design with low loss and wideband transmission. A new guidance effect was recently demonstrated in coreless PCF with

3.2 Terahertz optical fibre types and guiding mechanisms

a helical twist (Beravat *et al.* 2016). The twisted structure presents a topological channel that creates favorable guidance conditions. The helical twist causes a quadratic increase in the optical path as a function of fibres radius and twist rate, impacting more strongly the effective indexes of cladding modes with field distribution far from the fibre centre. As a result, a helical twist causes a decoupling (or an inhibited coupling) between modes with field close to the fibre center from modes with field far from the fibre center. The result is a waveguide with low confinement loss, even when the structure is a coreless microstructured fibre (Beravat *et al.* 2016, Russell *et al.* 2017). Fig. 3.1 presents one example of terahertz optical fibre structure to each possible guidance mechanism.

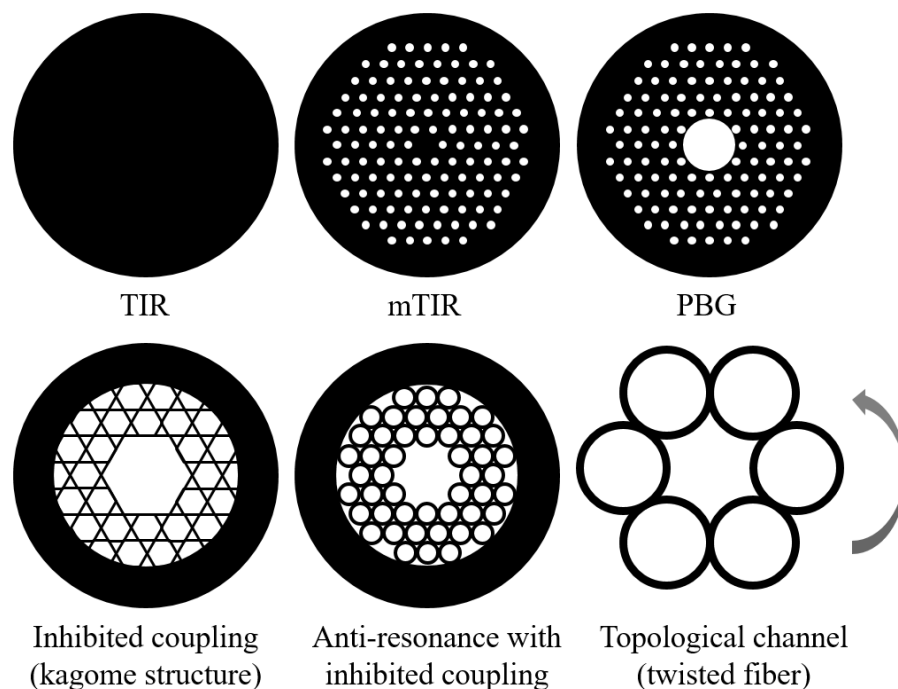


Figure 3.1. Terahertz optical fibres. Representative sketches of terahertz optical fibres with corresponding guidance mechanism indicated (Islam *et al.* 2020a).

Terahertz optical fibres have been proposed in the literature building upon the developments in speciality optical fibres (Atakaramians *et al.* 2013, Argyros 2013, Barh *et al.* 2015). The designs have explored almost all the guidance mechanisms already applied in photonics. The main categories of terahertz optical fibres are: solid rod fibre (or microwire fibre) (Atakaramians *et al.* 2013, Argyros 2013), porous fibre (Argyros 2013, Barh *et al.* 2015, Atakaramians *et al.* 2009a, Chen *et al.* 2013, Hassani *et al.* 2008), porous-core fibre (Bao *et al.* 2012, Kaijage *et al.* 2013, Aming *et al.* 2016), slotted core fibre (Sultana *et al.* 2018b, Atakaramians *et al.* 2009b, Cruz *et al.* 2013c, Faisal and Islam 2018),

suspended core fibre (Rana *et al.* 2016, Mei *et al.* 2019), hollow-core fibre (Vincetti 2009a, Cruz *et al.* 2018, Anthony *et al.* 2011b, Yang *et al.* 2016, Lai *et al.* 2010), hollow-core fibre based on anti-resonances and inhibited coupling mechanism (Vincetti and Setti 2010, Bao *et al.* 2015, Zhu *et al.* 2019, Hasanuzzaman *et al.* 2018, Cruz *et al.* 2015, Cruz *et al.* 2017, Sultana *et al.* 2019c, Sultana *et al.* 2019a) Bragg fibre (Hassani *et al.* 2008, Zhu *et al.* 2019, Dupuis *et al.* 2011, Cruz *et al.* 2015), porous fibre with embedded metallic wires (Yudasari *et al.* 2014, Harrington *et al.* 2004, Atakaramians *et al.* 2013, Markov *et al.* 2014), and helically twisted fibre (Stefani *et al.* 2018). Fig. 3.2 presents the variety of terahertz optical fibres presented in the literature, where black and white colors represent the dielectric material and the air region, respectively.

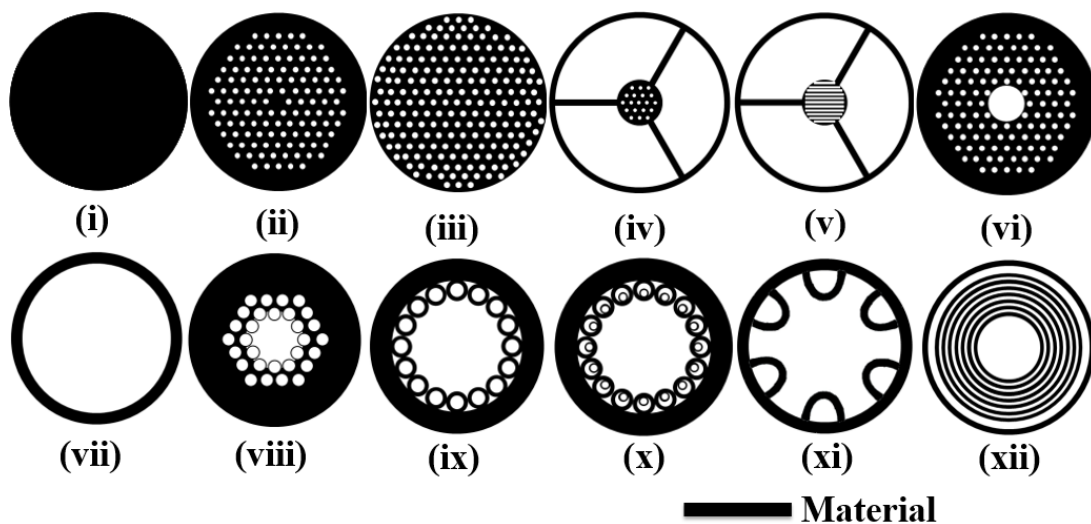


Figure 3.2. Optical fibre categories. (i) Solid rod fibre, (ii) Microstructured optical fibre, (iii) Porous fibre, (iv) Suspended porous-core fibre, (v) Suspended slotted core fibre, (vi) Hollow-core bandgap fibre, (vii) Hollow-core tube fibre, (viii) Hollow-core fibre with negative curvature, (ix) Hollow-core fibre based on anti-resonances and inhibited coupling, (x) Hollow-core nested antiresonant nodeless fibre, (xi) 3D printed hollow-core fibre based on anti-resonances and inhibited coupling, and (xii) Bragg fibre (Islam *et al.* 2020a).

The main problem in the development of terahertz optical fibres is the strong absorption of terahertz in dielectric (polymers or vitreous) materials. The high absorption loss demands specialized designs to achieve the desired properties for terahertz optical fibres. A solid rod fibre, the most straightforward terahertz fibre, has high confinement of modal power in the dielectric material, resulting in very high absorption loss. Microstructured solid core terahertz fibres have a similar issue resulting

3.2 Terahertz optical fibre types and guiding mechanisms

in high absorption losses. However, a coreless porous terahertz fibre with subwavelength air-holes, can reduce the absorption loss by adjusting the fraction of modal power at the air (air-holes plus air-cladding) and at the dielectric background material (Chen *et al.* 2013, Hassani *et al.* 2008). Porous terahertz fibres reaching 85% of modal core power fraction were also demonstrated in Argyros (2013), Barh *et al.* (2015), Atakaramians *et al.* (2009a), Chen *et al.* (2013), Hassani *et al.* (2008), resulting in reduced propagation losses.

Porous-core terahertz fibres are those in which a dielectric core has a microstructure of sub-wavelength air-holes and the surrounding cladding is built with larger air-holes (Bao *et al.* 2012, Kaijage *et al.* 2013, Aming *et al.* 2016, Hasanuzzaman *et al.* 2015). Porous-core terahertz fibre provides high confinement with low loss terahertz propagation. However, some designs add extra effort to prepare the fibre preform by including air-holes with very different diameters to build the micro-structured core and cladding regions. This kind of porous-core terahertz fibre was proposed in (Kaijage *et al.* 2013, Aming *et al.* 2016) leading to high power confinement at the porous-core region (40%–50%) and propagation losses of about 0.07 cm^{-1} . Porous-core fibre design based on the PGB effect allows the use of similar air-hole diameters. This approach was firstly demonstrated in terahertz fibres built with cyclic olefin copolymer (COC–TOPAS) operating at 0.75–1.05 THz with losses lower than 1.5 dB/cm (Bao *et al.* 2012). An even more difficult design was proposed in a porous-core fibre with elliptical air-holes that was proposed to obtain high birefringence of about 0.119 and low-loss propagation of 0.0689 cm^{-1} at the 1.0 THz (Hasanuzzaman *et al.* 2015). In general, a core porosity of 50% to 60% allows reduction of the absorption loss to 45% and 38% of the bulk material loss, respectively (Kaijage *et al.* 2013).

An alternative design to porous-core terahertz fibre is the slotted-core terahertz fibre developed with the purpose of providing high birefringence of about 0.02 to 0.075 at 1 THz (Sultana *et al.* 2018b, Atakaramians *et al.* 2009b, Cruz *et al.* 2013c, Faisal and Islam 2018) and low loss below 0.06 cm^{-1} (Sultana *et al.* 2018b, Islam *et al.* 2015). Basically, fibre core has high porosity due to the inclusion of rectangular or elliptical slots filled with air (Sultana *et al.* 2018b, Atakaramians *et al.* 2009b, Cruz *et al.* 2013c, Faisal and Islam 2018). Slotted-core fibres were only numerically studied because the extra challenge of preparing the fibre preform and integrating rectangular or elliptical slots at the

core region into a cladding with circular air-hole macrostructure (Sultana *et al.* 2018b, Atakaramians *et al.* 2009b, Cruz *et al.* 2013c, Faisal and Islam 2018, Islam *et al.* 2015). Note that Fig. 3.3(a–d) present examples of porous-core and slotted-core terahertz optical fibre designs and their material absorption loss as function of core-diameter and porosity (Kaijage *et al.* 2013, Islam *et al.* 2015). Slotted-core terahertz fibres have the potential to result very low propagation losses, but experimental demonstration must be presented.

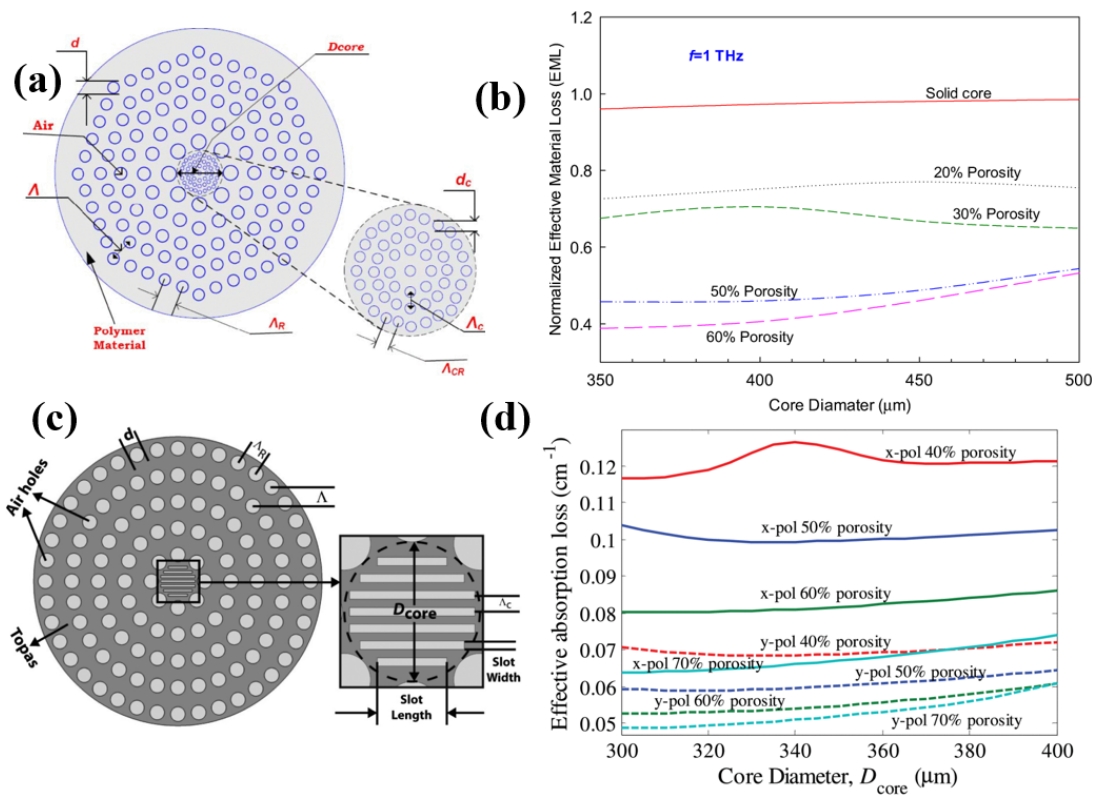


Figure 3.3. Porous-core and slotted-core terahertz optical fibre designs and absorption loss as function of core diameter and porosity. (a)-(b) Microstructured porous-core terahertz fibre design and its absorption loss (Kaijage *et al.* 2013). (c)-(d) Slotted-core terahertz fibre design and its absorption loss (Islam *et al.* 2015, Islam *et al.* 2020a).

An optimized design of porous terahertz fibre, or suspended core terahertz fibre can reduce the absorption loss to less than 1/10 of the bulk material loss. However, considering the high absorption losses of dielectric materials, a hollow-core fibre seems to be a more effective option. Based on the established hollow-core fibres for phonics applications in the optical regime, hollow-core terahertz fibres have been proposed based on

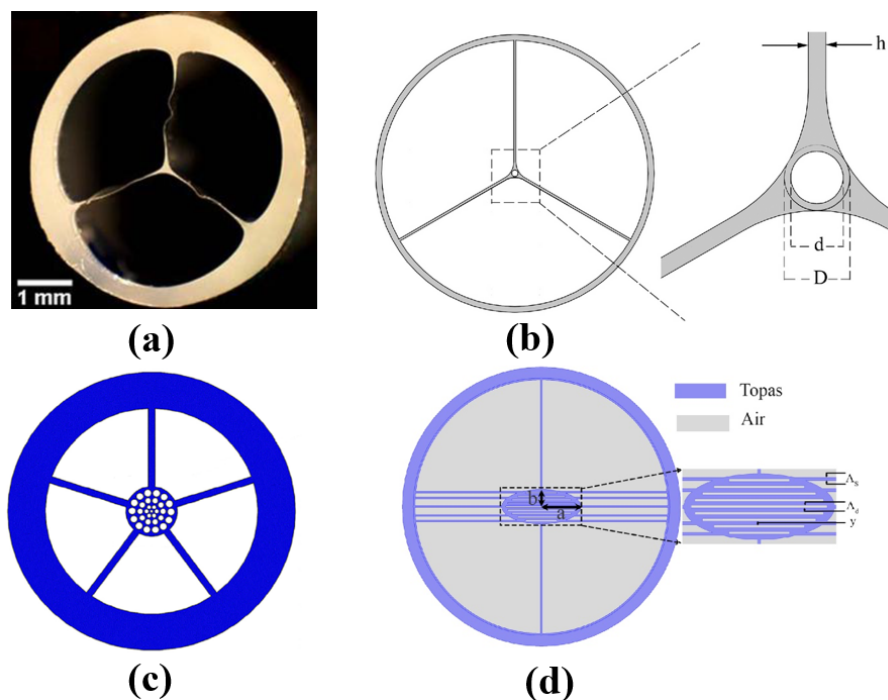


Figure 3.4. Suspended-core terahertz fibres. (a) Subwavelength core (Mei *et al.* 2019), (b) Hollow-core (Jiang *et al.* 2013), (c) Graded porous-core (Mei *et al.* 2019), (d) Slotted-core (Faisal and Islam 2018).

different guiding mechanisms: the band-gap effect, low cladding mode density in fibres with kagome structure and the antiresonant effect (Vincetti and Setti 2010, Vincetti 2009a, Cruz *et al.* 2018, Anthony *et al.* 2011b, Yang *et al.* 2016, Lai *et al.* 2010, Bao *et al.* 2015, Zhu *et al.* 2019, Hasanuzzaman *et al.* 2018, Cruz *et al.* 2015, Cruz *et al.* 2017).

Hollow-core terahertz fibres, based on kagome structures, were demonstrated with remarkable low absorption losses of 0.6 cm^{-1} over 0.65–1.0 THz (Anthony *et al.* 2011b) and 0.02 cm^{-1} over 0.2–1.0 THz, with minimum of 0.002 cm^{-1} at 0.75 THz (Yang *et al.* 2016). The kagome terahertz fibre presented in Anthony *et al.* (2011b) was fabricated by the stack and draw technique and resulted in single-mode operation with propagation loss about twenty times lower than the loss of polymer PMMA used as manufacture material. The hollow-core kagome structure presented in Yang *et al.* (2016) was manufactured by 3D printing leading to broadband propagation (above 0.4 THz) and enables mechanical splicing by connecting separated parts without any additional alignment issue. Fig. 3.4 (a-d) present both kagome based hollow-core fibres and their spectral

propagation losses (Anthony *et al.* 2011b, Yang *et al.* 2016). These hollow-core structures are representative of two most promising fabrication techniques applied to terahertz optical fibre manufacture. The first technique (stack and draw) allows obtaining flexible single-mode waveguides and the second technique (additive manufacturing by 3D printing in polymer) open the possibility to fabricate special designs that are impossible to be prepared with any other manufacturing technique.

Despite the efficacy of low-loss PBG and kagome based hollow-core terahertz fibres, a simpler design is possible and has been explored for terahertz wave propagation. Antiresonant hollow-core terahertz fibres (tube terahertz fibres) enable wave propagation with extremely low absorption losses of 0.0005 cm^{-1} at 1.0 THz (Lai *et al.* 2010, Bao *et al.* 2015) over large bandwidths. An antiresonant waveguide can be formed by just one dielectric tube or a design based on connected tubes as presented in Fig. 3.5(a) and 3.5(c). These waveguides present wider transmission bands than that of PBG based hollow-core terahertz fibres. Figs. 3.5(b) and 3.5(d) present the attenuation constant and loss coefficient to the single tube waveguide and tube lattice waveguide, respectively (Lai *et al.* 2010, Vincetti and Setti 2013).

Besides the search of appropriated designs to obtain low loss terahertz propagation, the another very important parameter to enable broadband terahertz transmission is the chromatic dispersion of terahertz optical fibres. A very simple antiresonant terahertz fibre, based on just one dielectric tube with absorptive cladding, might provide low loss $0.05\text{--}0.5 \text{ cm}^{-1}$ and low dispersion propagation ($|\beta_2| < 10 \text{ ps/THz/cm}$) in the 0.3–1.0 THz range (Bao *et al.* 2015). The authors demonstrated that an absorptive material, placed outside the dielectric tube, reduces the slope of dispersion curves especially in the vicinity of resonant loss maxima, what causes a strong reduction in the group velocity dispersion (GVD), reduction of bending losses, remains $< 0.2 \text{ cm}^{-1}$ for bending radii down to 10 cm, and propagation bandwidth much larger than the classical ARROW waveguide (Bao *et al.* 2015).

Another possible design of hollow-core fibre is the Bragg terahertz fibre that consists of a hollow-core surrounded by circular concentric rings of high and low refractive indexes (Bragg reflector). In this category of fibre, usually the fibre core is much larger than the operating wavelength what ensures high coupling efficiency with different

3.2 Terahertz optical fibre types and guiding mechanisms

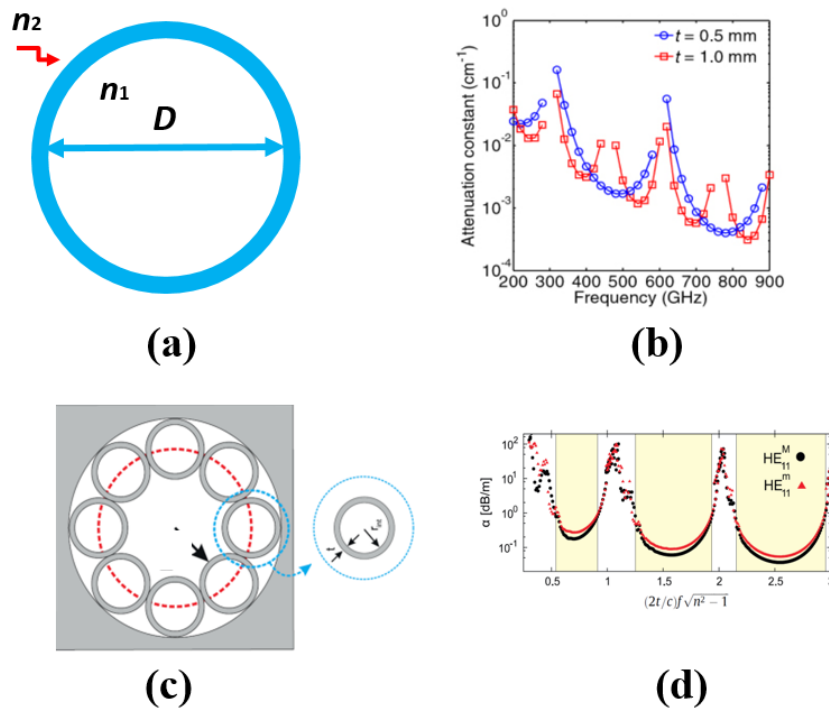


Figure 3.5. Hollow-core terahertz fibre based on antiresonant effect. (a-b) Simplest dielectric tube terahertz waveguide (Lai *et al.* 2010), (c-d) Negative curvature hollow-core tube lattice terahertz waveguide (Vincetti and Setti 2013, Islam *et al.* 2020a).

terahertz sources (Hassani *et al.* 2008). Few studies about Bragg terahertz fibres are available in the literature (Hassani *et al.* 2008, Dupuis *et al.* 2011, Cruz *et al.* 2015), but the numerical and experimental results demonstrate transmission from 0.2–2.0 THz and loss of 0.1 cm^{-1} to 1.0 THz (Dupuis *et al.* 2011, Cruz *et al.* 2015). The Fig. 3.6 (a-b) present a terahertz Bragg fibre design, manufactured by rolling two different polymer films, and its spectral transmission loss, respectively (Dupuis *et al.* 2011). This design and manufacture process has the advantage of simplicity, cost effective, besides enable flexible waveguides and propagation from 0.2–2.0 THz. The Fig. 3.6 (c-d) show a 3D printed terahertz Bragg fibre, with diameter core of 7.2 mm, and its spectral transmission loss, respectively (Cruz *et al.* 2015). The 3D printed Bragg fibres using low-cost printers, as presented in Cruz *et al.* (2015), simple to fabricate, but the low spatial printing resolution and the use of only one printing material limits the designs in their ability to achieve the operation in the Bragg regime. An alternative can be to fill the air gap with a liquid polymer or another dielectric where the high-index contrast leads to omnidirectional reflection.

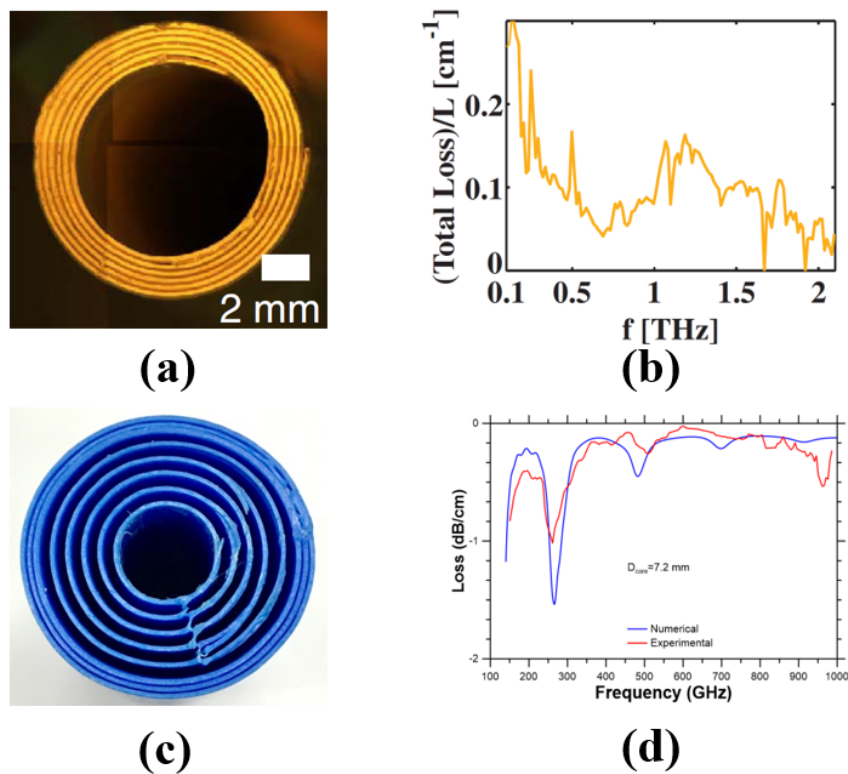


Figure 3.6. Hollow-core terahertz Bragg fibre, design and its spectral transmission loss. (a)-(b) Manufactured by rolling two polymer layers (Dupuis *et al.* 2011), (c)-(d) Fabricated by 3D printing (Cruz *et al.* 2015, Islam *et al.* 2020a).

An alternative design of hollow-core terahertz fibre is a hybrid terahertz fibre that is based on porous fibre with embedded metallic wires (Yudasari *et al.* 2014, Sultana *et al.* 2019a, Harrington *et al.* 2004, Markov *et al.* 2014). Further details about terahertz fibres with embedded wires will be presented in the next section.

A new frontier of terahertz fibre optic development is the proposal of helically twisted hollow-core terahertz fibres. Considering the new features demonstrated by this category of fibres in photonic applications, there is a significant opportunity to develop devices to manipulate terahertz modes with circular polarization and modes with orbital angular momentum (OAM) (Stefani *et al.* 2018).

3.2.1 Hollow-core waveguides having single and hybrid cladding

In this section, various hollow-core metallic single and hybrid clad waveguides are discussed. The single clad waveguide refers to a structure with a single layer of material (metal or polymer), Fig. 3.7(i); whereas hybrid clad (metamaterial) waveguides

3.2 Terahertz optical fibre types and guiding mechanisms

contain a minimum of two different materials, creating conjugate layers, Fig. 3.7(ii-viii) (Yudasari *et al.* 2014, Sultana *et al.* 2019a, Harrington *et al.* 2004, Markov *et al.* 2014). The net idea is to combine the low-loss, low-dispersion terahertz propagation properties of metal wires/sheet based waveguides with the mechanical robustness of porous terahertz fibres.

Hollow-core single-clad metallic pipe waveguides

McGowan *et al.* (1999) reported the first experimental investigation on a long circular stainless-steel hollow pipe waveguide. The next year, Gallot *et al.* (2000) extended the idea by reporting a brass circular hollow waveguide. In all of these cases, the terahertz transmission is limited not only by the high loss of the metal but also by group velocity dispersion of the guided waves. Hidaka *et al.* (2005) developed a flexible, hollow terahertz waveguide and compared the results by using both polymer (ferroelectric polyvinylidene fluoride, i.e. PVDF) and metal (copper). An improved loss performance was found by using the polymer than the copper. Alongside the ohmic losses, the inner surface roughness (Hidaka *et al.* 2005) introduced from the washing process and inconsistency of the waveguide cross-section (Gallot *et al.* 2000) introduced from extrusion over the length are the main limitations of the metal waveguides.

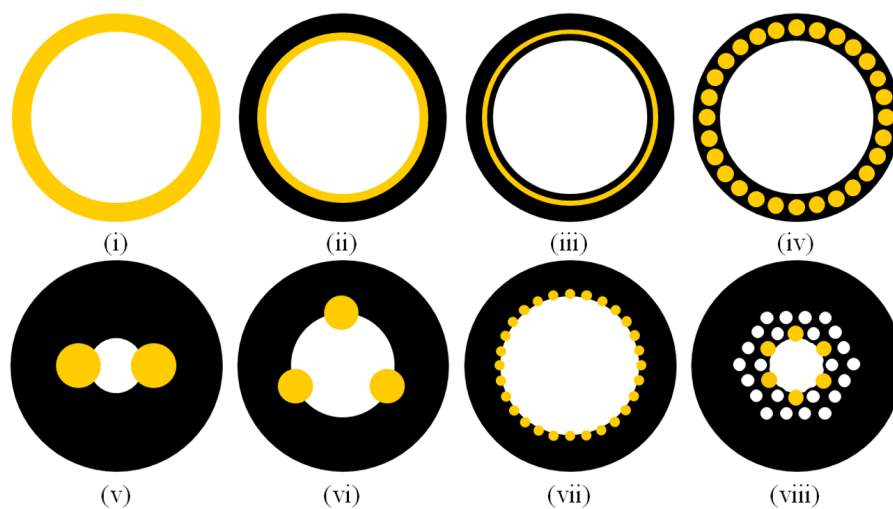


Figure 3.7. Hollow core terahertz waveguides with metallic wires and coating. (i) Single metallic cladded waveguide, (ii-iii) Hybrid cladded waveguide, (iv) Metamaterial cladding (Li *et al.* 2016a), (v) Two-wire dielectric cladding (Markov *et al.* 2012, Atakaramians *et al.* 2013, Markov *et al.* 2014); (vi) Three wire dielectric cladding (Yudasari *et al.* 2014), (vii-viii) Cladding with multiple metal wire inclusions (Yudasari *et al.* 2014, Atakaramians *et al.* 2013, Li *et al.* 2016a), (Islam *et al.* 2020a).

Hollow-core metamaterial waveguides

Hybrid-clad also known as metamaterial waveguide refers to the waveguides having a minimum of two different layers of materials. Each layer has different functionalities, for example, the use of polymer as a supporting tube (Harrington *et al.* 2004) can introduce the flexibility to deposit metal on polymer inner surface. The inner thin metal layer serves as a reflector and maintains the optical properties. Harrington *et al.* (2004) adapted metal coating idea using liquid-phase chemistry method from the mid-IR region and applied it to the terahertz spectrum. The ejection of a thin metal layer of correct optimal thickness inside and/or outside of the transparent polymer is the main concept of liquid-phase chemistry method. However, this method possesses complex procedures and limits the coating diameter and length. Various hybrid cladded waveguides are shown in Fig. 3.7.

A 3D printed porous fibre with embedded metallic wires was reported in Yudasari *et al.* (2014) reaching low-loss absorption coefficients of $0.05\text{--}0.4\text{ cm}^{-1}$ and close to zero dispersion, Fig. 3.7(vii). A challenge of embedded metal wire design is the careful maintenance of inter-wire gaps along the fibre length, because any variation of this distance can increase the radiation losses significantly (Markov *et al.* 2014). Atakaramians *et al.* (2013) analysed two-wire and four-wire configuration of metamaterial waveguide. The reported power loss was 0.3 cm^{-1} for the two-wire fibre, and 0.5 cm^{-1} for the four-wire fibre. To obtain the desired wire-based hybrid cladding geometries, the dielectric waveguide preform can be made first and then metal wires can be inserted manually (Yudasari *et al.* 2014).

The dielectric coating on metal is another type of metamaterial waveguide that facilitates the transmission over a metallic tube waveguide. For example, polystyrene coated metal enhances the reflectivity of the metal via an interference effect and the metal acts as a mirror. An experimental characterization on a silver/polystyrene-coated hollow glass waveguide (Bowden *et al.* 2007, Bowden *et al.* 2008a) shown that the transmission loss reduces to 0.95 dB/m , in contrast to the high loss of $3.5\text{--}5.0\text{ dB/m}$ for the metal-only waveguides. This is due to the low extinction coefficient (Matsuura and Takeda 2008) and low dielectric absorption (Tang *et al.* 2009) of the dielectric loaded waveguide. A drawback of introducing the dielectric layer in a metallic waveguide

3.2 Terahertz optical fibre types and guiding mechanisms

is that the dielectric coating introduces interference peaks, which limits the bandwidth of operation (Matsuura and Takeda 2008). Thus, the thickness of the dielectric should be optimized in such a way that a low transmission loss window can be located in the desired frequency region. The addition of a thin dielectric layer of an oversized waveguide can reduce losses but enlarging the core size increases the number of modes so that modal coupling and modal dispersion become problematic. A single layer of subwavelength metal wires with optimal thickness is sufficient to provide the required guidance through hollow-core with dielectric cladding environment (Li *et al.* 2016a). The waveguide reported by Li *et al.* was fabricated using co-drawing technique (Tuniz *et al.* 2012) with indium wires and Zeonex. Within the single-mode window, the propagation loss of their waveguide is as low as 0.28 dB/cm.

For the wire-based hybrid clad hollow waveguide, the dominant guided mode is a HE_{11} -like mode (Atakaramians *et al.* 2013, Yudasari *et al.* 2014). It should be noted that coated dielectric layer thickness plays an important role in defining the dominant mode between HE_{11} and TE_{01} . It is found that for correct optimal thickness the dominant mode for the dielectric coated metal waveguide is the HE_{11} mode (Bowden *et al.* 2007, Bowden *et al.* 2008b, Matsuura and Takeda 2008, Tang *et al.* 2009). The loaded dielectric film reduces the loss of TM mode, which is higher for the metal waveguide. This results in the dominant mode for the dielectric loaded waveguide to be the HE_{11} mode with a lower attenuation constant.

Tab. 3.1 summarizes the main features of terahertz optical fibre categories and address selected works representing the advances in terahertz dielectric waveguides development.

Tab. 3.2 presents selected experimentally demonstrated terahertz optical fibres with description of fibre category, background material, core diameter, effective material loss (EML in cm^{-1}) or confinement loss (CL in dB/cm), and dispersion (GVD). The materials are: Polystyrene (PE), polypropylene (PP), polymethyl methacrylate (PMMA), polytetrafluoroethylene or teflon (PTFE), cyclic olefin copolymer (COC), cyclo-olefin polymer (COP), VeroWhitePlus (photopolymer), Somos EvoLve 128 (photopolymer), acrylonitrile butadiene styrene (ABS), polylactic acid (PLA), high-density polyethylene (HDPE), silica (SiO_2), arsenic sulfide (As_2S_3), and high resistivity silicon (HRS).

Terahertz fibre cat.	Highlights	Concerns	Extra comments
Solid core	Design simplicity, ease of manufacture.	High absorption and bending losses, High dispersion (GVD).	Tapered subwavelength fibre to evanescent field sensing, can be flexible.
Porous	Average absorption loss and design and manufacture complexity, mechanical robustness.	High bending loss, high dispersion (GVD), multimode guidance.	Tapered subwavelength fibre to evanescent field sensing.
PCF	Mechanical robustness, average design and manufacture complexity, single-mode guidance.	High absorption and bending loss.	Solid, porous or slotted core
Suspended core	Reduced absorption loss, Isolated fibre core, High evanescent field into the air cladding, Single-mode guidance.	Design and manufacture with average complexity.	Solid, porous or slotted core Special design to guide with near-zero dispersion.
PBG and kagome hollow-core	Reduced absorption and bending losses, Low dispersion.	Design and manufacture complexity, Reduced manufacturing tolerance, Multimode guidance, Large outer diameter.	Bandgap guidance of PBG fibre, wideband guidance of kagome fibre, terahertz signal well coupled to large core diameters.
Antiresonant	Low absorption loss, Design simplicity, Ease of manufacture.	Weak mechanical robustness, Multimode guidance.	Single tube fibre, absorptive cladding, terahertz signal well coupled to large core diameters, possible manufacture with 3D printing.
Bragg	Reduced absorption loss, Isolated fibre core.	Average manufacture complexity, Reduced manufacturing tolerance, Multimode guidance.	Possible manufacture with 3D printing, terahertz signal well coupled to large core diameters.
Hollow-core with hybrid metallic-dielectric cladding	Low absorption loss, High field confinement in a wide frequency range.	Design and manufacture with high complexity, Reduced manufacturing tolerance.	Low-loss air-bound ARROW modes at high frequencies, close-to-zero dispersion with two-wire configuration, Plasmonic modes at lower frequencies, possible use of embedded metal wires or layers in different fibre designs.

Table 3.1. Terahertz optical fibres main features. Indicating the fibre categories and its features.

3.2 Terahertz optical fibre types and guiding mechanisms

Terahertz fibre cat.	Material	Core diameter (μm)	Loss (EML or CL)	Dispersion
Solid core	PE	200	0.01 cm^{-1} at 0.3 THz	-
Solid core	PS, COP	1600×1600	0.3 cm^{-1} (PS) and 0.04 cm^{-1} (0.12 THz)	-
Porous	Silica	182	1.2-2.0 dB/cm (0.4-0.6 THz)	-
Porous	PE	350	0.01 cm^{-1} at 0.3 THz	-
Porous	PTFE	430	$< 0.27 \text{ cm}^{-1}$ (0.1-1.0 THz)	-
PCF	COC	870, 4200	0.09 cm^{-1} (0.35-0.65 THz)	1 ps/THz/cm
Suspended	PE	150	0.02 cm^{-1} (0.28-0.48 THz)	-
Kagome	PMMA	1600, 2200	0.8 cm^{-1} (0.75-1.0 THz)	-
Kagome	VeroWhite	9000	0.02 cm^{-1} (0.2-1.0 THz)	-
Antiresonant	PTFE	2100	0.05 dB/cm	-
Antiresonant	Resin	9000×4500	0.005 cm^{-1}	-
Antiresonant	Resin	5000	0.11 cm^{-1} (0.2-1.0 THz)	-
Bragg	ABS	7200	0.52 dB/cm (0.35 THz)	-
Bragg	PMMA	4500	0.12 cm^{-1} (0.18 THz)	-
Hybrid (metal)	COC	2000	0.2 cm^{-1} (0.85 THz)	5 ps/THz/cm (0.65-1.05 THz)

Table 3.2. Selected experimentally demonstrated terahertz optical fibres. Indicating the material used, the fibre dimension, and optical properties. After Han *et al.* (2002), Guo *et al.* (2019), Nagel *et al.* (2006), Dupuis *et al.* (2009), Leea *et al.* (2019), Nielsen *et al.* (2009), Mei *et al.* (2019), Anthony *et al.* (2011b), Yang *et al.* (2016), Vincetti and Setti (2013), Yang *et al.* (2019a), Yang *et al.* (2020), Cruz *et al.* (2015), Li *et al.* (2017b), Atakaramians *et al.* (2013).

Tab. 3.3 presents selected numerically studied terahertz optical fibres with description of fibre category, background material, core diameter, effective material loss (EML in cm^{-1}) or propagation loss (dB/cm), and dispersion (GVD).

Fabrication constraints are crucial when designing and developing a new polymer optical fibre. Polymers are considered as the most efficient material for manufacturing terahertz waveguides as they can show low loss and flat dispersion properties in the terahertz regime. The fabrication processes of terahertz polymer fibres are adapted from the microstructured optical fibre. In general, the microstructured optical fibres can be fabricated by drilling, stacking and drawing, extrusion, casting/molding and

Terahertz fibre cat.	Material	Core diameter (μm)	Loss (EML or CL)	Dispersion (ps/THz/cm)
Porous	COC	560, 600, 760	0.007 cm^{-1} (0.2 THz)	-
Porous	PMMA	400	0.01 cm^{-1} (0.2 THz)	-
PCF porous core	COC	350–500	$0.1\text{--}0.2 \text{ cm}^{-1}$ (0.7–1.2 THz)	-
PCF porous core	COC	350	0.07 cm^{-1} (1.0 THz)	-
PCF porous core	HRS	100	0.04 cm^{-1} (0.9–1.0 THz)	0.6
PCF slotted core	COC	350	0.07 cm^{-1} (1.0 THz)	4
PCF porous core	COC	300–450	0.053 cm^{-1} (1.0 THz)	-
Suspended porous core	COC	432	$0.01\text{--}0.1 \text{ cm}^{-1}$ (0.35 – 1.0 THz)	0.14
Suspended slotted core	COC	320	0.39 dB/cm (0.95 THz)	0.5)
Kagome porous core	COC	300	0.029 cm^{-1} (1.30 THz)	0.49
Kagome porous core	COP	250–350	0.04 cm^{-1} (1.0 THz)	0.98 ± 0.09
PBG	PTFE, HDPE	882	0.01 dB/cm (0.9–1.1 THz)	-
PBG	COP	1500×2034	0.01 cm^{-1} (0.82–1.05 THz)	0.16–1.12
Antiresonant	PMMA	7000, 9000	$0.0007\text{--}0.004 \text{ cm}^{-1}$ (0.7 THz)	-
Antiresonant	PTFE	2100	0.05 dB/cm	-
Hybrid (metal)	PE	200	0.64 cm^{-1} (> 1.514 THz)	2-3
Hybrid	COC	1000	0.25 dB/cm (0.3–0.46 THz)	-
Hybrid (Metamaterial)	COP	3000	0.01 dB/cm (1.0 THz)	-

Table 3.3. Selected numerically studied terahertz optical fibres. Showing the fibre categories and optical properties. After Atakaramians *et al.* (2009b), Atakaramians *et al.* (2008), Chen *et al.* (2013), Kaijage *et al.* (2013), Rana *et al.* (2016), Yang *et al.* (2018c), Faisal and Islam (2018), Vincetti (2009a), Mei *et al.* (2019), Vincetti (2009b), Rana *et al.* (2018), Sultana *et al.* (2019b), Vincetti (2009a), Xiao *et al.* (2018a), Lai *et al.* (2010), Vincetti and Setti (2013), Markov and Skorobogatiy (2013), Li *et al.* (2016b), Sultana *et al.* (2020).

3.2 Terahertz optical fibre types and guiding mechanisms

solvent deposition, and 3D printing. In this section, we discuss the methodology of these fabrication methods and point out a few practical examples of the same.

3.2.2 Drilling

The drilling method is widely used to fabricate microstructured and photonic crystal preforms with circular holes. Such preforms need to be subsequently drawn to optical fibres to guide visible and infrared signals. The computer numerical controlled (CNC) drilling machine offers the ability to fabricate complex structured preforms with high precision (Barton *et al.* 2004). It should be noted the need to optimize the drilling parameters such as cutting speed, spindle speed and depth of cut to avoid air hole surface roughness or polymer melting due to high drilling temperature.

A detailed drilling procedure has been discussed in Arrospide *et al.* (2018). The size of the drill imposes a limitation on the maximum length of the preform and determines the number of holes that can be drilled (Barton *et al.* 2004). To control the system temperature and hole deformation, a liquid coolant is required during drilling. Also, the drill bit has a very short lifetime and frequent replacement makes the whole fabrication process complex and time-consuming. Drilling is not suitable for porous-core and antiresonant fibre because of its geometrical complexity. It is also difficult to maintain the mechanical strength of a thin wall between adjacent air holes in fibre structures with a high air filling fraction (Barton *et al.* 2004). A possible geometry is a Bragg fibre with a larger central hole and small holes forming the concentric layers, Fig. 3.8 (a).

3.2.3 Stack and draw

Stacking is another approach for creating hole patterns in a preform (Talataisong *et al.* 2019, Han *et al.* 2002, Goto *et al.* 2004, Cho *et al.* 2008, Lu *et al.* 2008, Liu and Tam 2017). A number of polymer capillaries are stacked manually and bundled together with a polymer jacket to prepare the final preform. The microstructured layers of a suitable preform are fastened together with ordinary thin plastic tubes. A wide range of complex structures with different hole patterns has been made using passive or active pressure. This freedom allows changing the shape of originally circular holes like shown in Fig. 3.8 (b), (Anthony *et al.* 2011b, Dupuis *et al.* 2009, Setti *et al.* 2013).

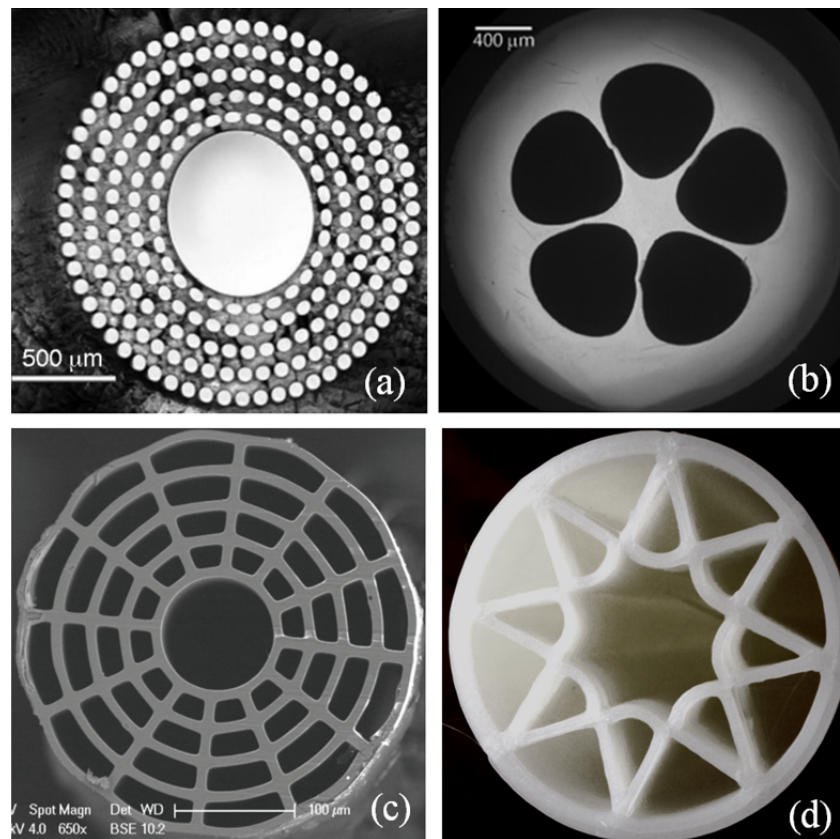


Figure 3.8. Terahertz optical fibre fabrication methods. Various geometries of optical fibre fabricated by, (a) Drilling (Nielsen *et al.* 2009, Anthony *et al.* 2011a, Bao *et al.* 2012, Ponseca Jr *et al.* 2008); (b) Stack and draw (Talataisong *et al.* 2019, Han *et al.* 2002, Goto *et al.* 2004, Cho *et al.* 2008, Lu *et al.* 2008, Liu and Tam 2017); (c) Sacrificial-polymer method (Dupuis *et al.* 2009, Dupuis *et al.* 2010), preforming/molding/fibre-inflation technique (Zhang *et al.* 2006, Dupuis *et al.* 2010), and extrusion (Atakaramians *et al.* 2009a); (d) 3D printing (Van Putten *et al.* 2018, Wu *et al.* 2008, Wu *et al.* 2011, Sultana *et al.* 2019c, Yang *et al.* 2019b), Islam *et al.* (2020a).

Stacking is the most common method for fabricating the preforms for hollow-core fibre and porous fibre with high air proportion. The handmade stacking is very labour-intensive and time-consuming for mass production. However, the limitation in the preform length and drawbacks of drill bit imposed by the drilling method can be overcome by this technique. The maximum achieved porosity with stacking is 8–18% (Dupuis *et al.* 2009). A more detailed stacking procedure has been discussed in Arrospeide *et al.* (2018).

3.2 Terahertz optical fibre types and guiding mechanisms

The sacrificial polymer technique is a subtraction process, where the sacrificial rods are stacked in the microstructured mold without touching and co-drawn with polyethylene granules (Dupuis *et al.* 2009, Dupuis *et al.* 2010). The advantage of this technique is that complete hole may collapse during drawing and can be removed as the preform contains no holes. The PMMA rods are dissolved in tetrahydrofuran (THF), and the air holes reveal in the fibre. The sacrificial material should have a higher glass transition temperature than casting material. A microstructured sub-wavelength fibre with 29–45% porosity has been possible to fabricate with a fibre length of several meters (Dupuis *et al.* 2009, Dupuis *et al.* 2010).

3.2.4 Preform-molding/fibre-inflation technique

Molding is a procedure where the fibre preform is cast in a microstructured mold. The microstructured mold features a special structured alignment to assemble a number of polytetrafluoroethylenes coated alloy steel wires (Zhang *et al.* 2006) or bottom end sealed silica capillaries (Dupuis *et al.* 2010). The bundle of steel wires/silica capillaries is placed in the bottom end sealed of a large diameter of a quartz tube to enable pressurization in the preform. The tube is filled with polymer granules and placed into a furnace to melt it. Upon cooling, the steel wires/solid rods are removed from the solidified cast preform. The air holes in resultant preform are pressurized to prevent the complete hole collapse during drawing, and the sufficient air pressure inflates the holes with maximum porosity of 86% (Dupuis *et al.* 2010). The molding technique is suitable for the arbitrary shapes and size in hole patterns by varying the mold structure and arrangement (Zhang *et al.* 2006). A drawback of this approach is that the deformation of the porous cross-section can happen with unusual pressurization.

3.2.5 Extrusion

Extrusion is a common technique to fabricate either the polymer preforms or directly fibre from a billet or from granules. The extrusion dies exit geometry defines the fibre cross-section. Extrusion technique has been applied in microstructured fibre designs named as spider web porous fibre (Atakaramians *et al.* 2009a), rectangular porous fibre (Atakaramians *et al.* 2009a), including antiresonant fibre. The obtainable porosity using extrusion are 57% and 65% (Atakaramians *et al.* 2009a). The critical step in extrusion is designing and machining the dies. A new die (or an intensive cleaning process)

is required for each extrusion, making the fabrication technique expensive and time-consuming. An interesting characteristic is that, different fibre structures can be fabricated using the extrusion technique. Fig. 3.8(c) shows various fibres fabricated using the sacrificial-polymer, preform-molding, and extrusion technique.

3.2.6 3D Printing

Note that 3D printing is a well established and comparatively easier method of fabricating terahertz optical fibres. The most widely used 3D printing techniques are stereo lithography (SLA)—uses a laser scanner to solidify the liquid resin which are photocurable (Li *et al.* 2017b), fused filament method (FDM)—uses a nozzle to soften Zeonex, Topas, PMMA, PC, PE, ABS, Nylon (Van Putten *et al.* 2018), polymer jetting technique—uses UV lamps on print heads to cure acrylic polymer and water-soluble polymer layer (Wu *et al.* 2008, Wu *et al.* 2011), each of which are suited to a range of terahertz fibre fabrication techniques. An example of an FDM 3D printing sample is shown in Fig. 3.8(d). The 3D printing process allows preparation in a single-stage process, forming complex fibre geometries without any further processing or drawing. The 3D printing technique allows for rapid prototyping of fibre designs as the fabrication cycle is significantly shorter. The limitation of 3D printing technology is that the choice of material needs to be compromised for improved surface roughness. The use of FDM has the ability to use many different polymers. That comes, however, with higher surface roughness. The SLA technique can improve surface roughness but the choice of material is restricted.

In this section, two most commonly used measurement systems such as terahertz time-domain spectroscopy (THz-TDS), and continuous-wave (CW) terahertz spectroscopy are discussed as the tool for terahertz waveguide characterization. In THz-TDS, coherent detection of time-domain signal can directly measure the transient electric field that is then Fourier transformed to provide the properties of the sample under study as a function of the frequency. A basic linear THz-TDS consists of a terahertz source (emitter) and terahertz detector, pumped by a femtosecond laser system where terahertz optics (mirrors/lenses) are optional. The three different THz-TDS setups are explored in this review, as illustrated in Fig. 3.9, and capable of transmission mode measurement.

3.2 Terahertz optical fibre types and guiding mechanisms

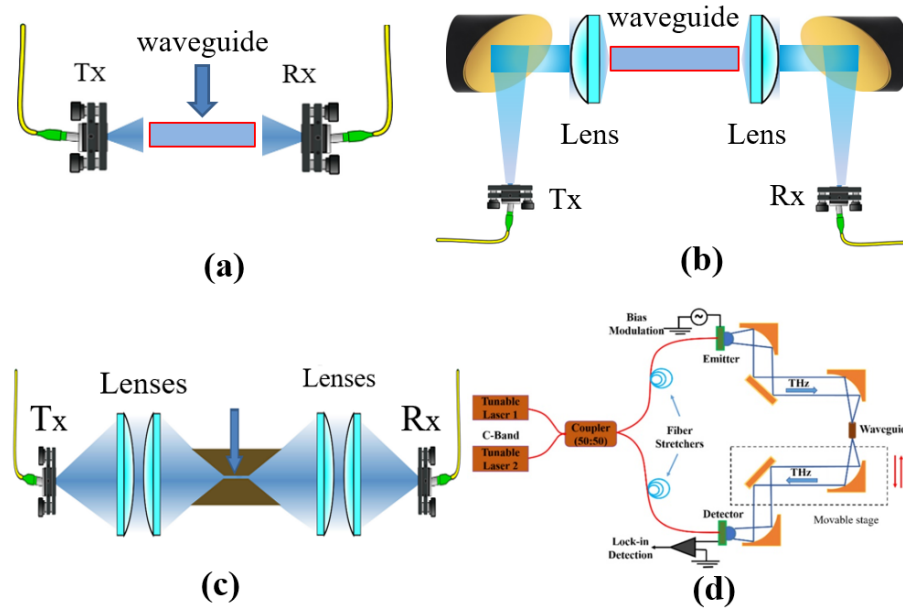


Figure 3.9. Characterization methods of terahertz optical fibre. (a) THz-TDS setup where the waveguide placed in between emitter and detector (Atakaramians *et al.* 2009a, Van Putten *et al.* 2018); (b) THz-TDS setup by using high resistive silicon lenses (McGowan *et al.* 1999, Wu *et al.* 2011, Lai *et al.* 2010), (c) a four lens setup of THz-TDS (Peretti *et al.* 2018), (d) a CW-THz setup (Ma *et al.* 2017), (Islam *et al.* 2020a).

In the first setup, the input and output faces of waveguide are directly positioned inline to the emitter and detector-Fig. 3.9(a). In this case, the terahertz pulse is directly propagate towards the core of the fibre that is then received by the detector. The emitter and detector are the fixed components for the THz-TDS, where the path length between them is altered according to the waveguide length, (Atakaramians *et al.* 2009a, Van Putten *et al.* 2018). Generally, large core fibres can be excited directly by solely using the transmitter and receiver, where additional lenses are not required.

An alternative approach for waveguide characterization is using mirrors and hyper-spherical silicon/polymer lenses at the front and end interface of the waveguide, 3.9(b). This kind of setup is generally necessary in order to achieve smaller beam size and strong beam coupling with the waveguide. As an example, McGowan *et al.* (1999), Gallot *et al.* (2000), Atakaramians *et al.* (2013), Anthony *et al.* (2011a), Ponseca Jr *et al.* (2008), Wu *et al.* (2011), Lai *et al.* (2010), use this method of waveguide characterizations where smaller beam size was required. A similar kind of beam size can be achieved by using four lenses (silicon/polymer) as shown in Fig. 3.9(c). The lenses in this case

need to be positioned and optimized according to their focal length (Peretti *et al.* 2018).

Note that CW-THz is another commonly used system for waveguide characterization, Fig. 3.9(d). The setup shown in Fig. 3.9(d) has two distributed feedback lasers that has slightly different center wavelength. The wavelengths are equally distributed to the emitter and detector arm by the 50:50 coupler. The fibre stretchers in this CW-THz system create additional path delay and cancel the phase noise.

Generally, there are two different methods for waveguide characterization. In the first method, measurements of the same sample with different lengths can be carried out by inserting and removing them in the setup (McGowan *et al.* 1999, Gallot *et al.* 2000, Li *et al.* 2016a). This method of measurement introduces a coupling loss that varies from measurement to measurement as every time a sample is inserted the beams needed to be re-alignment. Another approach is the cut-back technique, where the waveguide entrance is kept fixed on the setup while the sample has its length shortened and the transmission power measured (Harrington *et al.* 2004, Bowden *et al.* 2008b, Bowden *et al.* 2007). The use of the cutback method is limited to fibres that can be easily cut without being moved out from the characterization setup.

Over the last few years, THz-TDS has become a reliable and commercially available product, however, the high cost of the femtosecond lasers needed to excite the photoconductive antenna hinders their widespread use for commercial applications (Yu *et al.* 2019, Kohlhaas *et al.* 2017). One of the advantage of the CW-THz system is their high spectral resolution that depends on laser linewidth. Moreover, the full CW-THz system can be driven by laser diodes that makes the system much more compact and inexpensive (Yu *et al.* 2019, Kohlhaas *et al.* 2017).

Here and in the previous sections, the types of terahertz optical fibres, their guiding mechanisms, suitable materials for terahertz guidance, possible fabrication, and characterization methods were discussed. On a general note, we find that loss is a significant issue for terahertz wave propagation, which can be significantly reduced by optimal choice of fibre geometry and background material. One of the main hurdles in the field is the imperfect fabrication of terahertz fibres. For example, 3D printing

3.2 Terahertz optical fibre types and guiding mechanisms

technology can produce complex fibre structures but, in general, with non-ideal materials and/or with high surface roughness and low transparency. Other processes can be time-consuming or require multiple steps. Some fibres can also be very thick (many mm in diameter) reducing its flexibility or be very fragile making it difficult the cleaving process of a high-quality surface. A practical consequence is an extra effort in doing a cut-back loss measurement and getting reliable experimental coupling and transmission loss data.

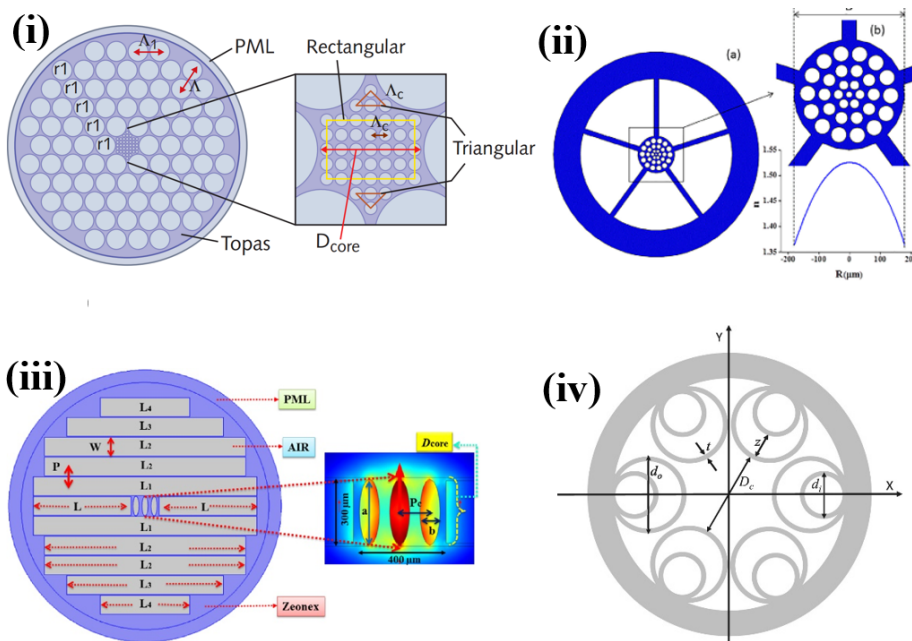


Figure 3.10. Low losses Terahertz optical fibres. (i) PCF like fibre with microstructured core (Islam *et al.* 2018a). (ii) Graded-index core fibre (Mei *et al.* 2019). (iii) Asymmetrical terahertz fibre (Islam *et al.* 2018d). (iv) Antiresonant terahertz fibre (Hasanuzzaman *et al.* 2018), (Islam *et al.* 2020a).

The field of terahertz optical fibres is still in development. The main applications of terahertz fibres include short-distance data transmission, sensing, and imaging. For propagation, terahertz fibres must present low losses, low dispersion, and in some cases, have mechanical flexibility. The principal issue in the realization of these fibres is high absorption loss of most materials in the terahertz regime, which implies increased fibre transmission loss. While negligible loss materials are not available, one method to overcome and control the losses is via optimization of fibre design. In sensing applications, fibres are used to increase the interaction of terahertz power with the analyte, leading to sensors with higher sensitivity. This interaction may occur outside the fibre, as in rod fibres, or the core of a hollow-core fibre. The use of hollow-core fibres goes

beyond refractive index analyses, and has been employed for real-time monitoring and molecular concentration sensors. Moreover, imaging systems employ terahertz fibres as probes to deliver and collect signal for biological sensing, for example. All these mentioned applications depend on low loss fibres, thus research effort for overcoming these material losses are critical for real-world applications and continued improvement is expected over the coming years.

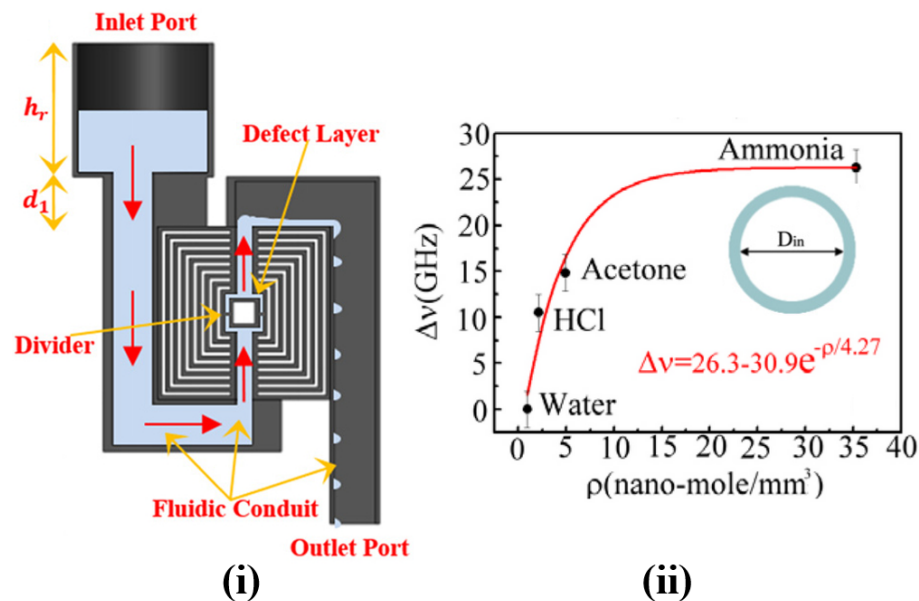


Figure 3.11. Application of terahertz optical fibre in sensing and imaging. (i) Micro-fluid sensor based on 3D printed Bragg fibre (Mei *et al.* 2019, Li *et al.* 2017b); (ii) Sensitivity of the pipe sensor to different samples: water, HCl, acetone and ammonia (You *et al.* 2012), (Islam *et al.* 2020a).

3.2.7 Transmission and communication

The primary use of terahertz optical fibres is to transport T-waves with minimal influence of the external medium. Since the 2000s, significant effort has been carried out in the development of low loss and low dispersion terahertz waveguides to improve fibre transmission properties. The first circular dielectric terahertz waveguide was a solid polymeric rod which guided terahertz waves with an attenuation constant of 0.01 cm^{-1} (Chen *et al.* 2006). To date, several studies have proposed low loss waveguides optimization of fibre design and improved choice of available fabrication materials (Hassani *et al.* 2008, Kaijage *et al.* 2013, Mei *et al.* 2019, Chen and Chen 2010).

3.2 Terahertz optical fibre types and guiding mechanisms

A recent study (Islam *et al.* 2018a) presented a combination of a porous-core circular PCF fabricated with the low loss material, Topas. In this case, 52% of the power fraction was present in the microstructured core region, which reduces the overlap between the terahertz modal power and the host material. This effect leads to an effective material loss (EML) of 0.034 cm^{-1} and an ultra-flattened dispersion variation of 0.09 ps/THz/cm , Fig. 3.10(i). This numerical approach also showed guiding characteristics such as single mode propagation and birefringence. Generally, these propagation characteristics are required for transmission and communication applications. In 2019, a suspended graded-index porous-core fibre was proposed (Mei *et al.* 2019), Fig. 3.10(ii). The guiding mechanism is based on TIR, and the numerical where numerical investigation shows that by introducing a graded-index in the fibre core an extremely flat dispersion of $0.14 \pm 0.07 \text{ ps/THz/cm}$ and an intermodal dispersion of $0.0152 \pm 0.0004 \text{ ps/THz/cm}$ are achieved. These dispersion values were found over 0.75 to 1.0 THz when the fibre core diameter is $432 \mu\text{m}$. An asymmetrical terahertz fibre was also reported (Islam *et al.* 2018d), Fig. 3.10(iii), with a high fibre birefringence of 0.063, an EML of 0.06 cm^{-1} and nearly zero dispersion flattened property of $\pm 0.02 \text{ ps/THz/cm}$. The antiresonant hollow-core terahertz fibre (Hasanuzzaman *et al.* 2018), Fig. 3.10(iv), is also a promising candidate for low loss terahertz transmission. An investigation on this type of fibre shows a loss of 0.05 dB/m and 600 GHz wide dispersion flattened bandwidth (Hasanuzzaman *et al.* 2018). Based on the results above, it is possible to find out a promising path to guide terahertz waves in short and long distances. Although these designs were investigated only numerically, the authors rely on the available fabrication methods discussed in Section 4 for practical applications.

3.2.8 Sensing

As in the optics regime, terahertz fibres can also be used for sensing applications to detect substances as liquids, vapors, solid particles or thin material layers. Terahertz rod fibres, or subwavelength rod fibres, for example, guide electromagnetic waves with a frequency dependent high power fraction due to the infinite air cladding. The evanescent field is sensitive to changes in the cladding refractive index, shifting the waveguide dispersion curve. As an example, in 2009, a liquid sensor based on a polystyrene wire was demonstrated (You *et al.* 2009). In the experiment, water and alcohol were readily distinguished and a variation of 58% in the dispersion curve between those two liquids was observed. Moreover, melamine and polyethylene alcohol solutions

were investigated. It was observed that by increasing the melamine and PE concentrations from 0 ppm to 100 ppm, a change in the dispersion curve occurred up to the solution saturation limit, 80 ppm for melamine and 40 ppm for PE (You *et al.* 2009). The sensor was able to detect variations of 20 ppm in the solution concentration, equivalent to refractive index changes of 0.01. Also, based on a solid core fibre, a numerical study showed an interferometric fibre sensor for terahertz frequencies (Cruz *et al.* 2013b). The sensor was formed by a Singlemode-Multimode-Singlemode structure, and the operation principle was based on multimodal interference in the multimode fibre. A sensitivity of 5 GHz/RIU over a refractive index range of 1.4–1.5 was obtained. Apart from the chemical sensors listed, several sensing schemes based on Bragg gratings have also been proposed for strain sensing (Hefferman *et al.* 2015), distributed sensing (Chen *et al.* 2015), and thickness monitoring (Yan *et al.* 2013).

Terahertz Bragg fibres also have been used as sensors (Cao *et al.* 2019, Li *et al.* 2017b). Cao *et al.* (2019) showed an interesting result regarding a 3D printed terahertz Bragg fibre as a resonant fluidic sensor. There, a modal analysis for the rectangular Bragg fibre, Fig. 3.11(i), was numerically studied with a defective layer located in the reflective Bragg structure. This layer simulates the region filled by the fluid analyte to be characterized. The spectral changes in the resonant absorption peaks were investigated as a function of fluid RI using a continuous-wave terahertz spectroscopy system. A sensitivity of 110 GHz/RIU was achieved, Fig. 3.11(ii). A study by Li *et al.* (2017b) showed the application of a 3D printed terahertz Bragg fibre as a powder and thin-film sensor with sensitivity close to 0.1 GHz/ μm .

Hollow-core fibres and hollow-tubes present resonant characteristics in its spectral transmission. Many sensors in the optical and terahertz regimes have been proposed based on antiresonant mechanism. The resonant peaks present in the waveguide spectral transmission are sensitive to refractive-index variations inside and outside the core, leading to shifts in their resonant frequency. For powder and vapor detection, for example, a glass tube waveguide was presented by You *et al.* (2012), where, the hollow-tube was filled with ammonia, acetone, HCl, and water separately. The changes in

3.2 Terahertz optical fibre types and guiding mechanisms

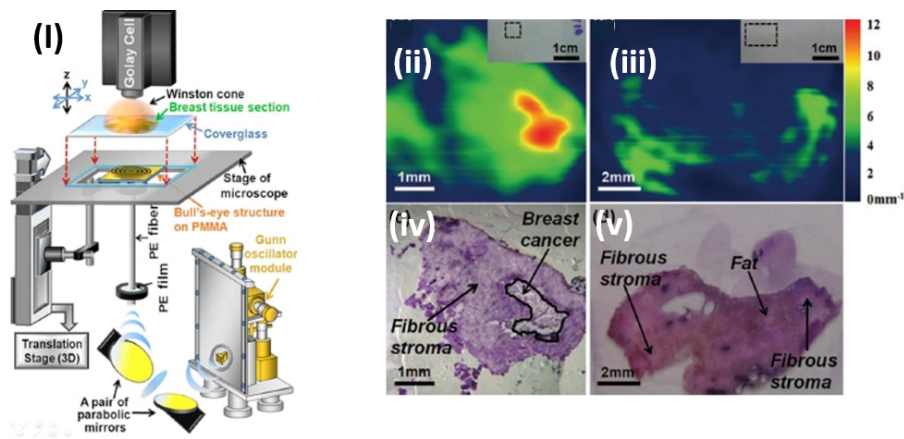


Figure 3.12. Schematic of the all-terahertz fibre scanning near-field microscope. Here, (ii) and (iii) are terahertz near-field absorption coefficient images of the breast tissue sections, cancerous and normal samples, respectively. Also, (iv) and (v) are photomicrographs of the corresponding breast tissue, (Islam *et al.* 2020a).

the tube spectral transmission showed a limit of molecular density around $1.6 \text{ nano-mole/mm}^3$ and sensitivity around 22.2 GHz/RIU . Other work (You *et al.* 2010) demonstrated a hollow-tube based sensor to analyse subwavelength-thick molecular overlayers in the fibre core. The lowest thickness detectable was about $2.9 \mu\text{m}$ of aqueous concentrations of carboxy polymethylene powder (carbopol) (You *et al.* 2010). Plasmonic fibre (Hassani and Skorobogatiy 2008), sapphire fibre (Katyba *et al.* 2018) and a large number of numerical studies have shown promising fibre designs for sensing of alcohol and petroleum derivatives (Sultana *et al.* 2018a, Islam *et al.* 2018j), chemical agents (Sultana *et al.* 2018a, Islam *et al.* 2018j, Ahmed *et al.* 2019, Islam *et al.* 2017a, Islam *et al.* 2018j), for example, but further practical results on fibre sensing applications are still needed.

3.2.9 Fibre-based terahertz imaging

A considerable number of terahertz imaging and spectroscopy systems were demonstrated over the last twenty years (Islam *et al.* 2018a, Mei *et al.* 2019, Mittleman *et al.* 1999, Mittleman 2018). Among the different approaches to near-field imaging, fibre-scanning systems have been proposed as a powerful non-destructive testing option, investigation of concealed objects, and endoscopy (Mittleman 2018). Lu *et al.* (2008)

proposed a terahertz scanner using a subwavelength plastic fibre as a probe. The imaging system consisted of a polyethylene solid core fibre, a continuous wave Gunn oscillator, and a Golay cell. In this system, one end of the fibre was free to move, and the other end was fixed. This configuration was suitable for scanning a $6 \times 6 \text{ cm}^2$ area, and allowed measuring the terahertz transmission through transparent samples, such as dry seahorses and fish, and concealed objects, Fig. 3.12.

A study on fibre based terahertz near field microscopy was carried out to diagnose breast tumors (Chen *et al.* 2011b) where the bulls eye corrugated structure designed to enhance the spatial resolution. This imaging system was capable of being interconnected with an optical microscope, and samples were able to be observed simultaneously, where images of cancerous cells and healthy tissues could also be distinguished. Based on the same principle, equivalent systems were used to diagnose breast tumors and liver cancer in Chen *et al.* (2011b), Hua *et al.* (2013). A fibre based *in-vivo* detection system of breast cancer was also reported where the system has the ability to detect cancer before it was evident with other techniques (Chen *et al.* 2011a). Their study indicates that the system has the potential to be used in a pre-clinical investigation of cancer, and other applications in terahertz microscopy. Other fibres as metamaterial fibres (Tuniz *et al.* 2013) and sapphire fibres (Katyba *et al.* 2019) have also been studied as potential subdiffraction imaging probes for terahertz near-field systems.

3.3 Future work

Free-space terahertz wave propagation is still widely used, but terahertz waveguides and, in particular, optical fibres are gaining increasing attention. Their importance is related to the concept of developing complex terahertz configurations that potentially combine sources and detectors with a reliable and simple way of terahertz transmission. Many materials and optical fibre geometries have been studied and analysed and most promising results indicate the use of low loss polymers to manufacture fibres where most of the transmitted power can be guided in air. Antiresonant fibres stand out among other hollow-core fibres, due to their robustness to fabrication tolerances, geometrical simplicity, and hence fabrication feasibility. Combining simplicity and low attenuation with high bandwidth, single-mode guidance, and low dispersion is, for most applications, the main target. fibres possessing composite cladding, with

3.3 Future work

metamaterial inclusion, better confine the terahertz signal (Li *et al.* 2016a), and fibres with helically twisted to guide modes with orbital angular momentum are two of the most exciting directions for actual and near future investigations.

Different manufacturing techniques are being used to produce such fibres, but 3D printing technology represents a clear advantage in terms of cost, time, easiness, and potential for manufacture of speciality fibres (Cruz *et al.* 2018) already integrated with other components required for a particular application. The use of filaments, made of low loss polymers, is required, but they are not always available commercially. Another clear drawback is the poor surface roughness of 3D printed fibres when low-cost desktop printers are used. It should be noted that sophisticated 3D printers able to produce higher quality samples usually require proprietary filaments preventing the direct usage of special polymers. Post-processing a 3D printed fibre is likely an excellent strategy to enhance its quality (roughness, layers adhesion, transparency, etc.). Here we can include the concept already applied to produce 3D printed fibres for the optical and infrared regime (Talataisong *et al.* 2018), i.e., printing a fibre preform and subsequently drawing it to a fibre stage. Extrusion is another powerful technique that is likely to be applied to mass production of high-quality specially designed THz optical fibres. There, the whole fibre cross-section can be produced simultaneously (Atakaramians *et al.* 2009a)—different from 3D printing or stacking-and-draw, for example. Simple and complex waveguides can be obtained by carefully designing the extrusion die, ram speed and furnace temperature profile. Extrusion of fibre projects with intrinsic low confinement loss due mostly air guidance, and while using low terahertz loss materials, is an interesting route to be wider explored.

Due to their large overall dimensions, with external diameters as big as 10 mm in some situations (Yang *et al.* 2016, Lai *et al.* 2009), some terahertz fibres are not mechanically flexible and this reduces the practical interest in applications requiring long waveguide lengths. Investigating ways of producing flexible fibres via selection of the required mechanical properties the fibre material and the fibre geometry (such as fibres with high air filling fraction and thin external jackets), as well as studying waveguide curvature loss will help develop this field further. Combining special coatings such as graphene (Mittendorff *et al.* 2017) could extend the functionalities of terahertz fibres

and will likely be a hot topic in this vibrant research area.

Terahertz waves have been demonstrated as promising technology to non intrusive analysis in biological, medical, chemical, and industrial applications. However, compact, portable, cost effective and robust devices need to be developed. In this scenario, the terahertz optical fibres, usually fabricated in short lengths, represent a challenge and a great opportunity to make such devices a reality.

3.4 Conclusion

The work on terahertz optical fibre discussed throughout this chapter combines, the analysis of suitable materials that can be used to make a low loss terahertz optical fibre; a comprehensive review of various geometry including the micro-structured photonic crystal fibre, the hollow-core fibre, the antiresonant fibre and the metamaterial-based fibres; the guiding mechanism of each type of fibres; an analysis of different methodology of fibre fabrication and characterization; and finally an outline of suitable application areas with further directions of future work.

From the analysis of various glasses and polymers, it has been found that polymers perform better as compared to glasses. From the polymers, the Zeonex, Topas, TPX, Teflon and HDPE show comparatively lower absorption losses and therefore suitable to be considered as a building material of terahertz optical fibre.

Various geometries of terahertz optical fibres including their guiding mechanisms have been reviewed and discussed. This fibre includes the hollow pipe waveguides (polymers/metals), microstructured optical fibres including hollow-core and porous-core, the hollow-core photonic bandgap fibres and the antiresonant terahertz fibres. From the discussion, it can be noted that every fibre has some advantages and disadvantages and there is a trade-off between low loss, bandwidth and fabrication feasibility. For example, hollow-core fibre can provide low loss terahertz guidance and comparatively simple fabrication at the expense of low bandwidth of operation. On the other hand, porous fibre can provide larger bandwidth but with higher loss and increased fabrication complexity as compared to hollow-core fibres. Metamaterial-based waveguides

3.4 Conclusion

are still in their infancy by comparison.

The various fabrication methodologies discussed in the manuscript indicate the possibilities of fabricating various geometries of terahertz optical fibres. For example, as discussed in section 6, the drilling method is suitable for fabricating circular hole patterns only, whereas the extrusion and 3D printing technique can fabricate any type of complex and asymmetric fibre geometries. The most common method for terahertz fibre characterization is the use of THz-TDS where different optics setups can be used to focus signal onto the fibre core. Among the various terahertz applications short-range high throughput transmission, gas, and chemical sensing and imaging show significant promise.

The following chapter shows our original contribution to terahertz transmission and sensing using micro-structured optical fibre. We describe design mechanism, simulation, and signal processing methodology of different symmetrical and asymmetrical terahertz fibre to show both the loss, dispersion, sensing, and other polarization maintaining applications.

Terahertz waveguide: concepts and modelling

IN previous chapters we discussed material characterization, and performed a brief review of terahertz optical fibres including the guiding mechanisms, fabrication methodologies, and experimental procedures. In this chapter, we show our contribution to modelling and analysis on terahertz waveguides and sensors. Here, we briefly discuss our proposed waveguides applicable for terahertz transmission and sensing. We also discuss the mechanism of chemical and gas sensing using terahertz optical fibre.

4.1 Key contributions to terahertz waveguides

After a brief literature review of terahertz waveguides, fabrication methods, and potential applications we find that there is still a lack of suitable waveguides applicable to low loss terahertz transmission, polarization preserving applications, and sensing. Therefore, we propose novel symmetric and asymmetric waveguide structures to achieve low transmission loss, high birefringence, near-zero dispersion, high core power fraction, and high relative sensitivity.

4.1.1 Design, simulation, and signal processing methodology

The design and simulation of all our contributed waveguides are carried out using the full vector Finite Element Method (FEM) method based on commercially available software COMSOL multiphysics. The *Electromagnetic Waves, emw* solver with a *Physics-controlled mesh* sequence having an *Extremely fine* mesh element size is used to get high accuracy output from the simulation software. A perfectly matched layer (PML) boundary condition is considered at the outer surface to make the computational region finite. In all of our waveguide design we choose either Topas (COC) or Zeonex (COP) because of their remarkable properties at terahertz, the details of materials are better described in Chapter 2 of this thesis.

4.1.2 Synopsis of the numerical method

In a terahertz waveguide, there are few limiting factors such as effective material loss (EML), confinement loss, bending loss, and scattering loss that limits the transmission and efficient detection of analytes. The EML of a PCF can be calculated by the equation,

$$\alpha_{\text{eff}} = \sqrt{\frac{\epsilon_0}{\mu_0}} \left(\frac{\int_{\text{mat}} n_{\text{mat}} |E|^2 \alpha_{\text{mat}} dA}{\left| \int_{\text{all}} S_z dA \right|} \right) \quad (4.1)$$

where, ϵ_0 and μ_0 represent the permittivity and permeability in free space, α_{mat} and n_{mat} indicate the bulk material loss and the RI of Zeonex, S_z implies the z-component of Poynting vector $S_z = \frac{1}{2}(\mathbf{E} \times \mathbf{H}^*)_z$, here, \mathbf{E} is the electric field component and \mathbf{H}^* is the magnetic field component (Islam *et al.* 2017a).

Confinement loss of an optical link is another important parameter that specifies the radiation leakage from the waveguide. It depends upon the core porosity as well as the number of hollow rings used in the cladding (Sultana *et al.* 2017a). Note that leakage of useful light occurs from the core to the cladding. The amount of light leakage determines the confinement loss that can be calculated using the imaginary part of the complex refractive index using the equation,

$$L_c = \left(\frac{4\pi f}{c} \right) \text{Im}(n_{\text{eff}}), \text{ cm}^{-1} \quad (4.2)$$

where, L_c indicates the confinement loss, f specifies the operating frequency, and $\text{Im}(n_{\text{eff}})$ represents the imaginary part of the effective refractive index (Sultana *et al.* 2017a).

To ensure single mode operation of a circular cored PCF the normalized frequency or V-parameter is usually analysed. V-parameter of a fibre can be calculated by,

$$V = \frac{2\pi r f}{c} \sqrt{n_{\text{co}}^2 - n_{\text{cl}}^2} \leq 2.405 \quad (4.3)$$

where, n_{co} and n_{cl} are the refractive indexes of the core and cladding respectively. The value of n_{co} is equal to the effective refractive index (n_{eff}) of the porous core. The value of n_{cl} should be more than 1 (Islam *et al.* 2017d) as the cladding not only consists of air but also on the used background material. Here, r defines the core radius (Islam *et al.* 2017d).

In order to use a PCF in a multi-channel communication link the dispersion characteristics should be as flat as possible. If the fibre has flattened dispersion properties, several signals from the source arrive at the destination nearly simultaneously. In our calculation only the waveguide dispersion has been considered while the material dispersion is neglected because the selected materials used to design our waveguides has negligible dispersion (Sultana *et al.* 2017a). The dispersion parameter of a fibre can be calculated using the equation,

$$\beta_2 = \frac{2}{c} \frac{dn_{\text{eff}}}{d\omega} + \frac{\omega}{c} \frac{d^2 n_{\text{eff}}}{d\omega^2}, \text{ ps/THz/cm}. \quad (4.4)$$

Here, β_2 indicates the dispersion, c indicates the speed of light, and ω represents the radian frequency (Islam *et al.* 2016a).

4.1 Key contributions to terahertz waveguides

The area covered by the mode fields inside the core region can quantitatively be measured by the term effective area. The effective area of a fibre can be calculated by,

$$A_{\text{eff}} = \frac{[\int I(r)rdr]^2}{[\int I^2(r)dr]^2} \quad (4.5)$$

where, $I(r) = |E_t|^2$ represents the amount of transverse electric field spreading in the PCF (Islam *et al.* 2016a).

For broad sensing application a wide numerical aperture (NA) is desirable and is achieved when the refractive index difference between the core and cladding of a PCF can be made larger. The NA can be quantified by the following equation,

$$\text{NA} = \frac{1}{\sqrt{1 + \frac{\pi A_{\text{eff}} f^2}{c^2}}} \quad (4.6)$$

where, A_{eff} represents the effective area of a PCF (Chowdhury *et al.* 2017).

To understand the performance of a PCF into sensing applications, it is important to calculate the relative sensitivity. Sensitivity is a measure of the amount of interaction of light with the material and can be expressed as,

$$R = \frac{n_r}{n_{\text{eff}}} \times P \quad (4.7)$$

where, R is defined as the relative sensitivity, n_r is refractive index of the chemical need to be detected, n_{eff} represents the effective refractive index, and P represents the percentage of interaction of light with the chemicals in the core holes to be sensed (Islam *et al.* 2017a).

According to Poynting's theorem the equation of calculating the fraction of power present in the core holes can be defined as,

$$P = \frac{\int_{\text{sample}} \text{Re}(E_x H_y - E_y H_x) dx dy}{\int_{\text{total}} \text{Re}(E_x H_y - E_y H_x) dx dy} \times 100 \quad (4.8)$$

where, E_x , E_y and H_x , H_y are the transverse electric and magnetic field of the guided mode respectively. The integration of the numerator is carried out for the samples to be sensed in the core region and the integration of the denominator is performed over

the whole fibre region (Cordeiro *et al.* 2006).

Preserving the polarization state of a PCF is important in consideration to sensing applications; eliminating the polarization mode dispersion (PMD), as well as stabilizing the operation of optical devices. Birefringence is a measure of the polarization states of a fibre that is defined as the refractive index difference between the polarization modes. It can be calculated by the following equation,

$$B = |n_x - n_y| \quad (4.9)$$

here, B indicates the birefringence, n_x represents the mode index in the x -polarization mode and n_y represents the mode index in the y -polarization mode (Islam *et al.* 2017a).

4.2 Waveguides for terahertz transmission

In this section, we discuss our reported waveguides as an application in terahertz transmission. Our goal is not only to achieve low loss but also high birefringence, and low and flat dispersion. For creating birefringence it is important to have asymmetry among the polarization modes, therefore we use either elliptical, rectangular, or circular air holes structured in a way so that it can create birefringence. There is a trade-off between the loss and the birefringence when one increases another decrease or vice versa.

4.2.1 A modified hexagonal photonic crystal fibre

We present a Zeonex based highly birefringent and dispersion flattened porous core photonic crystal fibre (PC-PCF) for polarization preserving applications in the terahertz region. In order to facilitate the birefringence, an array of elliptical shaped air holes surrounded by porous cladding is introduced. The porous cladding comprises circular air-holes in a modified hexagonal arrangement. The transmission characteristics of the proposed PCF are investigated using a full-vector finite element method with perfectly matched layer (PML) absorbing boundary conditions. Simulation results show a high birefringence of 0.086 and an ultra-flattened dispersion variation of ± 0.03 ps/THz/cm at optimal design parameters. Besides, a number of other important wave-guiding properties including frequency dependence of the effective material

4.2 Waveguides for terahertz transmission

loss (EML), confinement loss, and effective area are also investigated to assess the fibre's effectiveness as a terahertz waveguide.

Highly birefringent and dispersion flattened terahertz optical waveguides have drawn growing interest nowadays as alternatives to free-space transmission. Since the terahertz region is situated between the technologically well-developed microwave and infra-red regions, it is amenable to generation and detection techniques from both fields. Terahertz waves also enable a wider bandwidth than microwave frequencies, making it a superior candidate for high-speed short-range communications, and sensing, especially for label-free and non-invasive molecular detection. However, the practical implementation of terahertz is limited because most of the terahertz transmission systems are bulky and mostly dependent on free space for wave propagation. In the case of free space propagation, many undesirable losses can be introduced due to coupling with other components, transporting and managing terahertz beams, etc. As a primary solution, prior studies have proposed several waveguides including parallel plates, metallic wires, metal-coated dielectric tubes, polystyrene foams, sub-wavelength polymer fibres, Bragg fibres, and hollow-core fibres (Islam *et al.* 2017d, Islam *et al.* 2016a, Wang and Mittleman 2004). These all possess shortcomings due to higher absorption loss, higher coupling loss, lower power fraction, and higher bending loss. As an improvement, porous core PCF (Chen *et al.* 2013, Atakaramians *et al.* 2009b, Atakaramians *et al.* 2009a, Hasanuzzaman *et al.* 2016, Islam *et al.* 2016b) has gained considerable attention because of its versatility in enabling desired waveguide properties. Note that a PCF's geometrical parameters such as core diameter, core air hole size, and shape, the distance between air holes, the frequency can be tuned and optimized to obtain desired properties that enable low loss, controllable chromatic dispersion, high birefringence, and large modal effective area.

Several studies considered micro-structured porous core fibres for operation in the terahertz band. Atakaramians *et al.* (2009b), Atakaramians *et al.* (2009a) experimentally characterized porous core PCFs of different geometries. Using Topas as the background material, they obtained a low birefringence with high dispersion variation in the terahertz frequency band. Later studies examined a dual air hole unit based PCF and showed a moderate birefringence of 0.033 (Hasanuzzaman *et al.* 2016). Next, without significant improvement in birefringence, dual asymmetrical based PCF's were

also proposed (Islam *et al.* 2016b, Islam *et al.* 2018d). Furthermore, Wu *et al.* (2016) proposed a PCF and obtained a low birefringence with high dispersion variation. Recently, for further improvement of birefringence and dispersion properties, we proposed a PCF that consists of a regular hexagonal cladding with many elliptical air holes in the core (Sultana *et al.* 2018b). By considering a large length of elliptical-shaped air holes, we obtained a high birefringence of 0.086 with dispersion flatness of ± 0.07 ps/THz/cm in the terahertz frequency range. However, such a central elliptical air hole of the PCF almost crosses the core boundary and further adds to the fabrication challenge.

Considering all of the aforementioned issues (Atakaramians *et al.* 2009b, Atakaramians *et al.* 2009a, Hasanuzzaman *et al.* 2016, Islam *et al.* 2016b, Islam *et al.* 2018d) and limitations realized from our previous publication on highly birefringent PCF (Islam *et al.* 2018f) the motivation here is to design a highly birefringent, dispersion flattened fibre that eases the fabrication challenge. The novelty is introduced by applying elliptical-shaped micro-array based air holes inside a modified hexagonal lattice. The research goal is to achieve a fabrication friendly PCF with high birefringence and negligible dispersion variation.

As shown in Fig. 4.1(a), the air hole diameters (d) in the cladding region are all equal. The core region consists of an array of nine elliptical air holes. The elliptical air holes are used in order to create asymmetry in both the x and y polarization modes. This is because, as the asymmetry of a PCF increases, the birefringence also increases. Moreover, we create asymmetry in the cladding region by removing two air holes from the first ring of it. In Fig. 4.1(a), D_{core} indicates the area of the core region, a and b indicate the length and width of the elliptical air holes. The air filling fraction (AFF) at the cladding region is maximized to 0.94 because further increase tends to overlap the air holes that leads to fabrication difficulties. The pitch distance in horizontal and vertical directions of the core region is defined as p_c and p_{c_1} . The total fibre diameter is 3.2 mm. Cyclo-olefin Polymer (COP) commercially named as Zeonex is chosen as the bulk material because of its unique suitable optical characteristics in terahertz .

The electric field distribution of the proposed fibre at 1.1 THz frequency is shown in Fig. 4.1(b–g). For x -polarization the effective refractive index for the fundamental

4.2 Waveguides for terahertz transmission

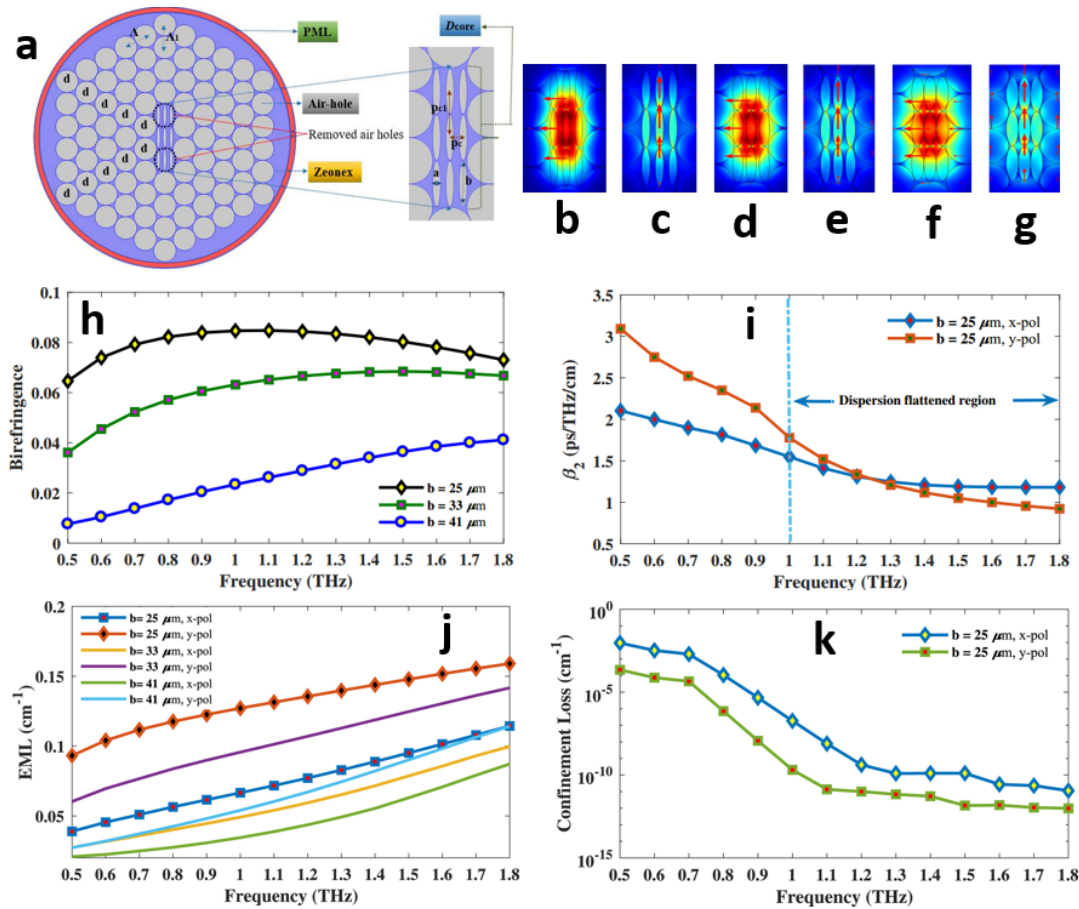


Figure 4.1. Development of Hexagonal PCF for terahertz transmission. (a) Schematic of the proposed structure. (b) E- field distribution for core air hole width of (b) 25 μm , x-pol (c) 25 μm , y-pol (d) 33 μm , x-pol (e) 33 μm , y-pol (f) 41 μm , x-pol (g) 41 μm , y-pol. (h) Birefringence, (i) Dispersion, (j) effective material loss, (k) and confinement loss, as a function of frequency (Islam *et al.* 2018h).

mode is 1.179 and as the core structure is asymmetric the waveguide will have a different refractive index in the y -polarization. The refractive index of the y -polarization is 1.265. The E-field distribution of the PCF indicates that some other modes can be present in the waveguide but for those modes the light pulse will propagate outside the core area (Islam *et al.* 2017a). So, when light is launched at the center of the PCF only the fundamental modes will get excited, resulting in single mode operation.

From Fig. 4.1(h) it can be observed that birefringence increases with core air hole width reduction where maximum birefringence is obtained at $b = 25 \mu\text{m}$. The one reason is, as core air hole width reduces the refractive index difference between the x and y polarization mode increases. The other reason is that, at higher b the mode field starts to

de-localize from the core and starts penetrating through the cladding. It is observed that the highest birefringence of 0.086 is obtained at 1.1 THz and then starts decreasing with further increase of frequency. This happens because at higher frequencies than 1.1 THz the scattering behaviour of a PCF increases but at the same time the incremental rate of refractive index difference of the orthogonal polarization modes decreases. Thus, we choose 1.1 THz as optimum design condition of the PCF. Please note that, we cannot reduce the b value further than $b = 25 \mu\text{m}$ because that causes the fibre to be converted into solid core that will significantly increase the EML. Therefore, we choose $b = 25 \mu\text{m}$ as optimum where the birefringence is highest as compared to other b values. PCF with such highly birefringent property have potential for application in sensing, filtering and medical imaging applications.

Fig. 4.1(i) indicate the characteristics of dispersion with respect to frequency and other optimum design parameters. It can be observed that the dispersion at x -polarization is more flat than the dispersion of y -polarization therefore we choose x -polarization as optimum. At x -polarization an ultra-flattened dispersion variation of $\pm 0.03 \text{ ps/THz/cm}$ is obtained at a bandwidth of 800 GHz. Note that, a flattened dispersion profile of a PCF allows multi chromatic signals to travel with nearly equal group delay.

At different elliptical air hole width (b), the amount of EML with respect to frequency for both x and y -polarization is characterized and shown in Fig. 4.1(j). It can be seen that the EML in y -polarization is larger than x -polarization and from Fig. 4.1(b–g) it can be seen that there may be a significant amount of scattering loss in the y -polarization, and this is another reason of choosing x -polarization as an optimum design parameter. It can also be observed that EML decreases when b increases because such increase of b decreases the amount of material from the core. Fig. 4.1(j) indicate that EML increases linearly with frequency that meets the theoretical equation of calculating bulk material absorption loss of a fibre, $\alpha(\nu) = \nu^2 + 0.63\nu - 0.13$, dB/cm, where ν is the normalized frequency (Islam *et al.* 2017d). At optimum design parameters the obtained EML is 0.065 cm^{-1} that is better than previously reported (Chen *et al.* 2013, Hasanuz-zaman *et al.* 2016) highly birefringent PCFs.

Fig. 4.1(k) shows the characteristics of confinement loss with respect to frequency. It can be seen that confinement loss decreases with the increase of frequency. This is

4.2 Waveguides for terahertz transmission

because, as frequency increases the mode fields begins to confine more strongly in the porous core region. At optimal design parameters, the obtained confinement loss is $3.8 \times 10^{-9} \text{ cm}^{-1}$ that is lower compared to optical waveguides (Chen *et al.* 2013, Atakaramians *et al.* 2009b, Atakaramians *et al.* 2009a, Hasanuzzaman *et al.* 2016, Islam *et al.* 2016b, Sultana *et al.* 2018b, Woyessa *et al.* 2017). A terahertz PCF with such low confinement loss is suitable for terahertz functional applications, mainly in terahertz integration systems.

Reference	Material	Birefringence	Disp. (ps/THz/cm)	CL, (cm^{-1})
(Atakaramians <i>et al.</i> 2009b)	Topas	0.026	± 0.07	-
(Atakaramians <i>et al.</i> 2009a)	Topas	0.012	—	—
(Islam <i>et al.</i> 2016b)	Topas	0.045	± 0.26	0.08
(Islam <i>et al.</i> 2018d)	Zeonex	0.063	± 0.02	5.45×10^{-13}
(Wu <i>et al.</i> 2016)	Topas	0.03	± 0.4	4.34×10^{-4}
This Thesis	Zeonex	0.086	± 0.03	3.8×10^{-9}

Table 4.1. Comparison of obtained result between the proposed PCF with prior PCFs. Showing the material used, and other optical properties.

Table 4.1 shows the characteristics comparison of the proposed PCF with prior PCFs. It can be observed from the obtained characteristics of the proposed PCF that, it shows improved optical characteristics including birefringence, dispersion, and transmission losses over prior PCFs that is desirable for efficient transmission as well as polarization preserving applications of terahertz waves.

In this particular research work, a single mode PCF with high birefringence and negligible dispersion flatness has been designed and analysed for terahertz wave guidance. To attain high birefringence, the symmetry between the x and y polarization mode has been broken using elliptical structured air holes. The designed waveguide shows an ultra-high birefringence of 0.086 at 1.1 THz and an ultra flattened dispersion variation of ± 0.03 ps/THz/cm within a broad spectrum. In addition, low EML of 0.065 cm^{-1} and negligible confinement loss of $3.8 \times 10^{-9} \text{ cm}^{-1}$ has also been obtained at optimal design conditions. Photonic crystal fibre with such highly birefringent and low loss

property is suitable for polarization preserving, sensing, filtering and short distance faster transmission of terahertz waves. Moreover, the near zero flattened dispersion property is suitable for multichannel communication application where the chromatic signals have nearly equal pulse spreading. It is expected that existing fabrication technologies can be used to produce this PCF for industrial applications.

4.2.2 Zeonex based asymmetrical terahertz photonic crystal fibre

We report on the design, in-depth analysis, and characterization of a novel elliptical array of core-based photonic crystal fibre (PCF) for multichannel communication and polarization-maintaining applications of terahertz waves. The asymmetrical structure of air holes both in core and cladding makes the birefringence higher and the compact geometrical structure, as well as different size of cladding air holes, makes the dispersion properties flat. The simulated results show a near-zero dispersion flattened properties of ± 0.02 ps/THz/cm, high birefringence of 0.063, low effective material loss (EML) of 0.06 cm^{-1} , and negligible confinement loss of $5.45 \times 10^{-13} \text{ cm}^{-1}$ in the terahertz frequency range. Additionally, the core power fraction, effective area, physical attributes, and fabrication possibilities of the fibre are discussed. With such attractive waveguiding properties the proposed terahertz PCF can potentially be applied in efficient and convenient transmission of terahertz waves.

To use fibre efficiently in multichannel communication and polarization-maintaining applications, numerous PCF have been proposed in recent years (Sultana *et al.* 2017a, Islam *et al.* 2018a, Islam *et al.* 2016a, Islam *et al.* 2016c, Islam *et al.* 2017b). In 2009, an experimental study on dispersion properties of a porous core fibre was investigated by Atakaramians *et al.* (2009c). They also investigated different shapes of PCF structure including circular and rectangular shaped to obtain the characteristics of birefringence and dispersion (Atakaramians *et al.* 2009b). Later, to obtain high birefringence and flat dispersion a slotted core circular cladded PCF was proposed (Islam *et al.* 2015). They obtained a high birefringence of 0.075, but with a high dispersion variation of ± 0.5 ps/THz/cm. An oligo-porous core PCF with asymmetric hexagonal lattice was also proposed by Wu *et al.* (2016), however it failed to improve birefringence and the dispersion property of the fibre. Recently, Luo *et al.* (2017) proposed a square lattice PCF for flattened dispersion and high birefringence. They obtained a birefringence

4.2 Waveguides for terahertz transmission

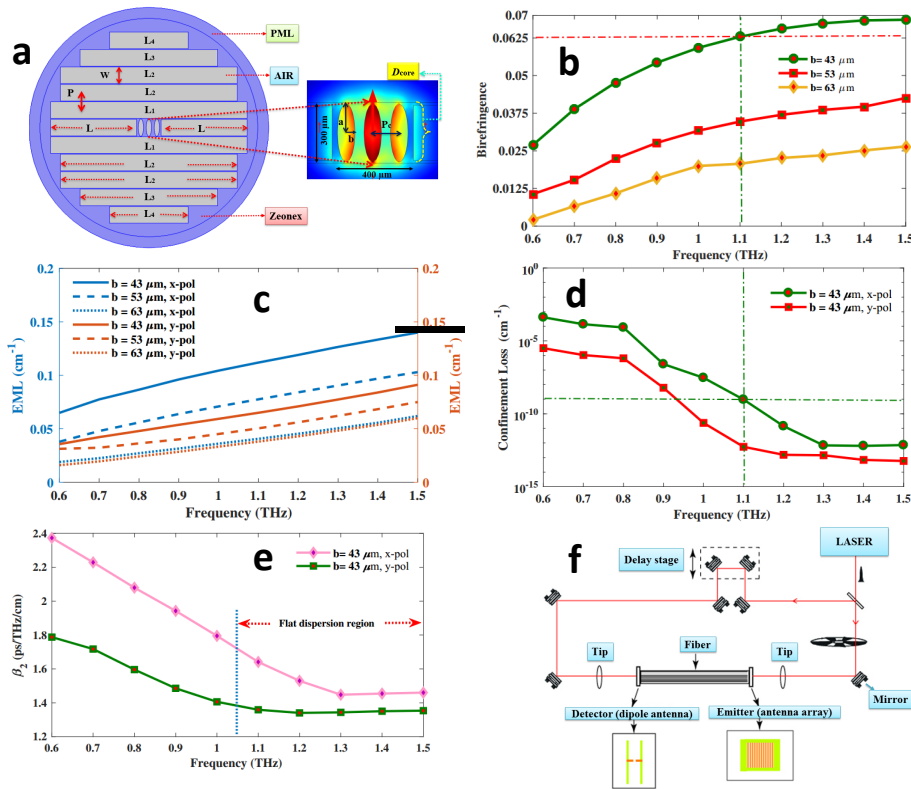


Figure 4.2. Development of asymmetrical terahertz waveguide. Schematic and mode field pattern of the proposed structure, (a). Birefringence for ellipse minor axis variation, (b). Effective material loss (EML) at different minor axis length of elliptical air holes (b) at both x - and y -polarization modes, (c). Confinement loss at both x - and y -polarization modes, (d). Dispersion variation for x - and y -polarization modes, (e). Experimental set-up procedure of the proposed PCF using THz-TDS, (f), (Islam *et al.* 2018d).

of 0.063 with dispersion variation of ± 0.12 for x -polarization mode and ± 0.08 for y -polarization mode. Therefore, after analysing the literature for flattened dispersion and highly birefringent fibre it is found that there is a large scope for PCF improvement in case of dispersion variation and birefringence. Hence, we propose a novel PCF consisting of rectangular-shaped air hole based cladding and an elliptical array of air hole based core. The research aim is to flatten the dispersion and increase the birefringence with the reduction of confinement loss. One of the greatest advantages of the proposed PCF is its extraordinary simplicity and thus feasible to fabricate using the state of the art fabrication technology. The proposed PCF structure combines an array of elliptical air holes in the core with a slotted cladding structure, where asymmetries in both the core and cladding are utilized to increase the birefringence.

In the cladding region of Fig. 4.2(a), the rectangular slot lengths are defined as L , L_1 , L_2 , L_3 and L_4 in above and below as well as both side of the core. The defined lengths are $1200 \mu\text{m}$, $3000 \mu\text{m}$, $2700 \mu\text{m}$, $2000 \mu\text{m}$ and $1000 \mu\text{m}$ respectively. Here, W and P indicates the slot width and pitch distance, centre to centre distance between air holes, which are same for each rectangular air holes. Considering the fabrication difficulties, the pitch P and slot width W are fixed at $280 \mu\text{m}$ and $270 \mu\text{m}$ respectively.

The core region of the PCF is defined as D_{core} . The major axis length and minor axis length of the elliptical-shaped air holes inside D_{core} are defined as a and b . Considering the fabrication conditions we fixed a maximum major axis length of $142 \mu\text{m}$ and by doing such we were able to increase the index difference between the polarization modes and thus increases the birefringence. However, we varied the minor axis length of b to investigate the fibre characteristics in b . The maximum allowable minor axis length is $63 \mu\text{m}$ and further increase may overlap the air holes and create fabrication difficulties. Therefore, the core pitch distance of P_c was set to $65 \mu\text{m}$ to allow sufficient distance between the elliptical air holes. In our proposed PCF the core length is $400 \mu\text{m}$ while the core width is $300 \mu\text{m}$. The total fibre diameter including the PML is 3.9 mm .

Birefringence is an important parameter for polarization-maintaining terahertz applications. It mainly depends upon the air hole structures of the fibre. The more asymmetry can be made in the x and y polarization mode, the higher the birefringence. The birefringence property is characterized by different minor axis length (b) of elliptical air holes that are shown in Fig. 4.2(b). We have seen that birefringence increases with the reduction of b . It is also seen that birefringence increases with the increase of frequency. As the core air hole width decreases, the index difference between the x and y -polarization mode increases that causes the increment of birefringence.

The EML as a function of frequency and different (b) is shown in Fig. 4.2(c). It is observed that EML decreases with an increase of (b). The increase of (b) increases the amount of air and reduces the amount of material from the core that causes the EML to be reduced. It is also observed that EML increases with the increase of frequency. This phenomenon is true because it meets the theoretical consequences of calculating material absorption loss concerning frequency. The empirical equation of calculating EML is given by $\alpha(\nu) = \nu^2 + 0.63\nu - 0.13, \text{ cm}^{-1}$. It can also be seen that the EML

4.2 Waveguides for terahertz transmission

in y polarization mode is lesser than the x polarization mode because from the mode profile it can be observed that in y polarization less amount of light is transferred to the cladding region and background material and a major portion of the signal passing through core air holes.

Confinement loss of a fibre determines the length of signal transmission in a terahertz optical waveguide. It depends upon the core porosity and the number of rings used in the cladding. The characteristics of confinement loss with the variation of frequency are demonstrated in Fig. 4.2(d). It can be observed that confinement loss is decreasing concerning frequency. This is because at higher frequencies the mode fields confine more tightly into the core region and hence the confinement loss reduces. At optimal design conditions, the obtained confinement loss is $5.45 \times 10^{-13} \text{ cm}^{-1}$ which is trivial as compared to the obtained EML.

In optical communication systems, multiplexing techniques came into existence to increase the information-carrying capacity of a channel. However, the main limiting factors are dispersion and fibre nonlinearity. In a conventional silica-based fibre, dispersion increases with wavelength, and thus different optical channels suffer different amounts of pulse broadening. One of the solutions is to use a dispersion compensator in reshaping the signals but it requires repeaters after a particular distance (Babita and Rastogi 2013). To overcome these difficulties fibres with low finite dispersion and negligible dispersion flatness are required. The flat dispersion property helps the number of input signals of a multichannel communication system to be transmitted through the fibre with minimum pulse broadening and thus increases the channel capacity.

In designing the PCF our main motivation was to flatten the dispersion property. Dispersion originates from the waveguide structure, as well as from the material itself. Zeonex exhibits negligible material dispersion in the terahertz frequency range therefore the effect of material dispersion was ignored. Hence we calculated the waveguide dispersion that mainly depends on the geometrical structure of the fibre. In Fig. 4.2(e) the dispersion variation of the proposed PCF with respect to frequency is shown. It is seen that there is a broad difference between the x and y polarization mode. This is true because the PCF structure is asymmetrical so the characteristics difference will be larger. We have seen that for x and y -polarization modes the dispersion variations

are ± 0.45 ps/THz/cm and ± 0.23 ps/THz/cm for the frequency range of 0.6–1.5 THz. However, we choose the bandwidth 1.05–1.5 THz in the y -polarization mode as the operating band because in that region the dispersion variation is ± 0.02 ps/THz/cm that is the lowest for any proposed terahertz PCF. Note that the obtained dispersion value is suitable for multichannel communication applications, as dispersion limits information rate.

It is important to mention the fabrication possibilities of a PCF. The proposed fibre consists of an elliptical array of the core inside a slotted air hole based lattice. Note that an extrusion technique for slotted structured air holes has already been carried out by Atakaramians *et al.* (2009a), Atakaramians *et al.* (2009b). Besides, the elliptical-shaped air holes are fabricated by Issa *et al.* (2004). Moreover, using methyl methacrylate (MMA) monomer polymerization method Liu *et al.* (2011) fabricated elliptical-shaped air holes. A recently published article on PCF mentioned that the elliptical-shaped air holes can be fabricated easily using the existing fabrication technique (Sultana *et al.* 2018b). Besides, micro-structured polymer optical fibre with asymmetric air holes are feasible to fabricate with the 3D printing technology (Ebendorff-Heidepriem and Monro 2007, Ebendorff-Heidepriem *et al.* 2014).

The experimental characterization procedure for all types of terahertz fibres is shown in Fig. 4.2(f). Using terahertz time-domain spectroscopy (THz-TDS) the terahertz properties of fibres can be characterized (Atakaramians *et al.* 2009c, Atakaramians *et al.* 2009a). A mode-locked Ti: sapphire laser can be used to drive the emitter and detector of the THz-TDS. The emitter can be a photoconductive antenna array (Wächter *et al.* 2007) while the detector can be a dipole antenna. The fabricated fibre can be placed between the emitter and the detector. The fibre tip needs to be placed close to the emitter and detector. Here, the delay stage is used to enable sampling of terahertz pulses in the time domain.

Tab. 4.2 shows a comparison of characteristics between the proposed PCF and previously proposed terahertz PCFs. It is clearly observable that, the proposed PCF achieves better terahertz characteristics than the prior PCFs.

A novel Zeonex based near-zero dispersion flattened and highly birefringent PCF is designed and analysed for possible application in the terahertz frequency band. The

4.2 Waveguides for terahertz transmission

References	THz	Dispersion (ps/THz/cm)	Birefringence	EML (cm ⁻¹)	CL (cm ⁻¹)
(Islam <i>et al.</i> 2015)	1	±0.5	0.075	0.07	0.034
(Hasan <i>et al.</i> 2016)	1	±1.42	0.048	0.085	4.40 × 10 ⁻⁴
(Islam <i>et al.</i> 2016b)	1	0.98 ± 0.39	0.045	0.08	-
(Wu <i>et al.</i> 2016)	3	0.2 – 1	0.03	0.06	4.34 × 10 ⁻⁴
(Islam <i>et al.</i> 2016b)	0.7	±0.55	10 ⁻²	0.07	4.34
(Rana <i>et al.</i> 2017)	0.5	±0.5	–	0.0103	3.8
(Luo <i>et al.</i> 2017)	1	±0.12	0.063	0.081	3.6 × 10 ⁻²
This paper	1.1	±0.02	0.063	0.06	5.45 × 10 ⁻¹³

Table 4.2. PCF comparison. Our proposed PCF is compared against pre-existing PCFs in the literature demonstrating improved optical performance.

proposed fibre shows two promising properties one is near zero flat dispersion and the other is high birefringence. The obtained near-zero dispersion flattened characteristics of ±0.02 ps/THz/cm is suitable for multichannel communication application where different optical pulse experiences nearly equal pulse broadening. Moreover, the high birefringent of 0.063 and low loss characteristics of the PCF is suitable for polarization preserving applications, especially for long-distance sensing and filtering. The commercial deployment of the fibre is easy as it is feasible to fabricate with the existing fabrication technology. Therefore, it is anticipated that the proposed PCF will create a new window for next-generation terahertz research.

4.2.3 Other proposed waveguides for low loss terahertz transmission

In this section we focus on our other proposed waveguide that are mostly based on arrangement of circular shaped air holes. The cross section of the waveguide structures

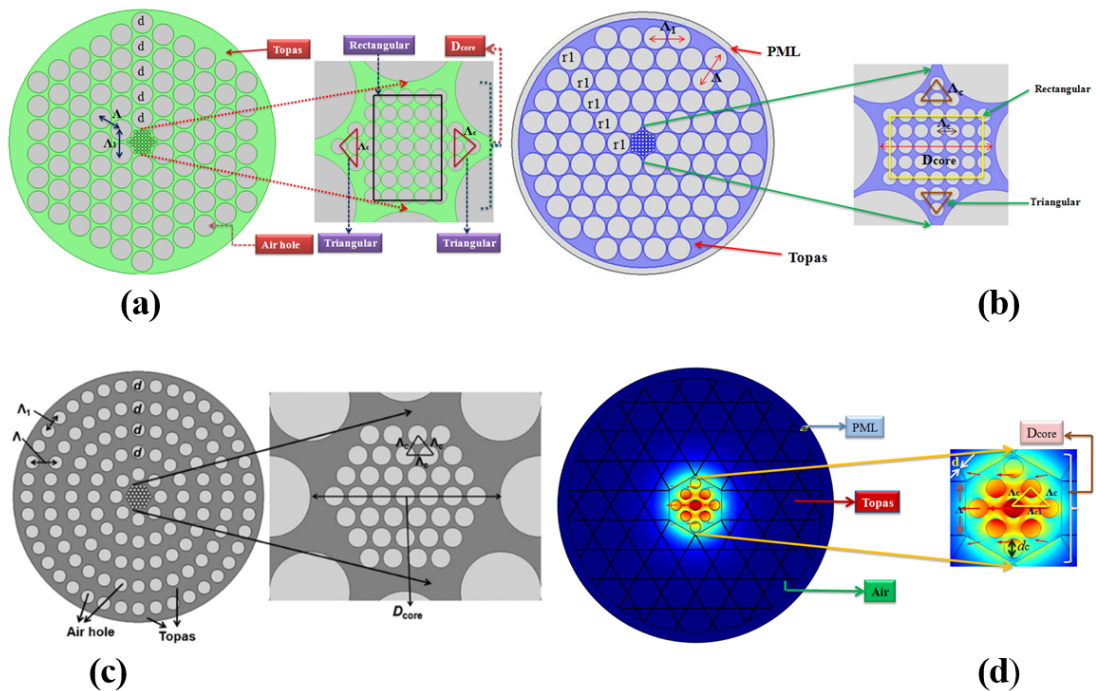


Figure 4.3. Terahertz waveguides for low loss terahertz transmission. Photonic crystal fibre (PCF) proposed to reduce transmission loss of electromagnetic (and especially terahertz) waves include a hybrid core in a regular hexagonal cladding (a), a hybrid core in a modified hexagonal cladding (b), a rotated hexagonal core in a circular cladding (c), and a diamond-shaped core in a kagome cladding (d), (Islam *et al.* 2018g, Islam *et al.* 2018b, Islam *et al.* 2018h).

are shown in Fig. 4.3.

Dramatic reduction of the material absorption loss caused by the bulk material used in the background of a PCF is possible through (a) a hexagonal cladding and hybrid structured core; (b) a modified hexagonal cladding in which the air holes from each edge are removed, reducing loss and improving birefringence; (c) a circular-clad PCF waveguide with rotated hexagonal core; and (d) a kagome-clad PCF that reduces confinement loss 3–4X more than other competing PCF structures. The latter kagome configuration reduces loss by a factor of 3–4X more than the other reported cladding structures. The reason being that kagome cladding has the ability to constrict more light inside the core and restrict light from going further towards the cladding.

4.3 Terahertz waveguides for sensing applications

In this section, we demonstrate that terahertz optical fibres can be used as a chemical sensor. Two sensor geometry is broadly discussed. One is based on kagome cladding with a rectangular array of core and the other is based on a rectangular air hole-based hollow sensor. In the end, we also discussed the mechanism of how a terahertz optical fibre can be used as a sensor.

4.3.1 A novel approach for spectroscopic chemical identification

In a kagome-based waveguide design we show that the terahertz optical fibres can be used as a sensor, the schematic, and achieved results are shown in Fig. 4.4. We choose a kagome structure in the cladding due to superior transmission bandwidth as well as very low confinement loss in a broad frequency range (Hossain and Namihira 2014) over Bragg fibre (Wang *et al.* 2011). In various PCF sensors, it is important yet challenging to preserve the polarization state (Ademgil and Haxha 2015) because of sensitivity increases for highly polarized fibre. It is difficult to maintain the polarization states in circular-shaped air holes in the core due to various factors as mentioned in (Sharma *et al.* 2013). Therefore, to preserve the polarization state effectively, it is necessary to apply asymmetric air holes in the PCF. Several PC-PCF with asymmetric structured air holes were proposed (Ademgil and Haxha 2015, Paul *et al.* 2017a) earlier but none of them achieved high birefringence with high relative sensitivity. Keeping that in mind, we propose rectangular structured air holes inside the core with kagome cladding. The rectangular structure is responsible for increasing the birefringence and the compact geometry of the PC-PCF facilitates high sensitivity as well as flat dispersion characteristics.

The schematic of the proposed kagome based asymmetric fibre structure, the intensity of signal interaction with the analytes (water, ethanol & benzene), relative sensitivity, and other fibre properties is shown in Fig. 4.4(a-f). It can be seen that terahertz strongly interacts with the liquid inside the core holes. To characterize the modal characteristics, we can observe the light propagation for both x and y polarization modes. It can be seen that only the fundamental modes propagate through the core area. However, as the waveguide structure is asymmetric, this will produce both birefringence and modes that result in light propagated outside the core area (Rana *et al.* 2017). So when

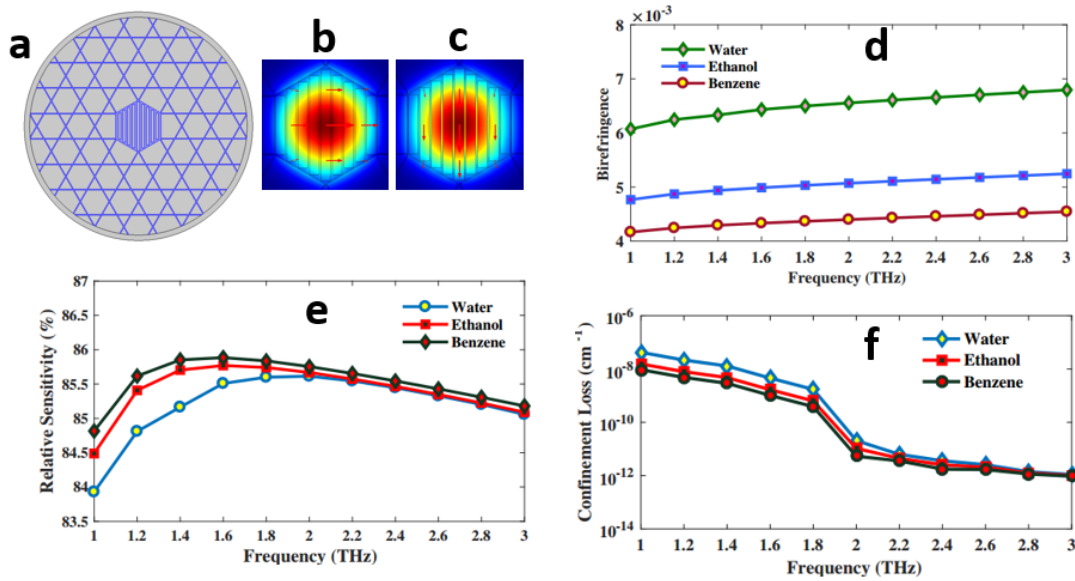


Figure 4.4. Asymmetric porous waveguide for transmission and sensing. Schematic of the proposed structure, (a). Mode field propagation in x-direction (b), and in y-direction (c). Birefringence (d), relative sensitivity (e), and confinement loss (f) as a function of frequency for the analyte of water, ethanol, and benzene respectively (Islam *et al.* 2017a).

a light pulse emerges at the center of the waveguide only the fundamental modes will be excited and the proposed PCF sensor will operate in the single-mode condition.

The birefringence obtained from the fibre structure for different analyte solution is shown in Fig. 4.4(d) which indicate that because of the asymmetric fibre structure the birefringence is higher. This can be helpful for terahertz sensing, the reason of why a birefringent fibre is required for terahertz sensing is discussed in the later Section 4.3.3.

The relative sensitivity, that obtained from core power fraction, and effective refractive indices of the waveguide are investigated for both x and y polarization. The detail of sensing performances is discussed in the published paper (Islam *et al.* 2017a). From where it can be seen that sensitivity in the y -polarization mode increases than the x -polarization because light interacts more strongly in the y -polarized mode than the x -polarization. Confirmation of this is seen in Fig. 4.4(b-c) where it is observed that the interaction of light and analytes is better in y -polarization mode than the x -polarization mode. The relative sensitivity obtained for the y -polarization for water, ethanol, and benzene is 85.6%, 85.7%, and 85.9% respectively. To the best of our knowledge, at the

4.3 Terahertz waveguides for sensing applications

time the paper was published this was the highest relative sensitivity obtained for any kind of sensor proposed for chemical sensing application in the terahertz frequency range.

The property of confinement loss to the frequency at optimum design parameters is shown in Fig. 4.4(f). It can be observed that confinement loss decreases with the increase of frequency. The interaction of the evanescent field with the sensing chemicals increases with frequency and thus the confinement loss decrease. The obtained confinement loss for water, ethanol and benzene are $4.5 \times 10^{-9} \text{ cm}^{-1}$, $1.7 \times 10^{-9} \text{ cm}^{-1}$, and $1.02 \times 10^{-9} \text{ cm}^{-1}$ respectively.

Reference	Operating Region	Relative Sens.(%)	Dispersion (ps/THz/cm)	CL (cm^{-1})	Birefringence
(Ademgil 2014)	1.5 μm	25.1	-	1.3×10^{-4}	-
(Ademgil and Haxha 2015)	1.5 μm	23.75	-	5.5×10^{-5}	-
(Arif <i>et al.</i> 2016)	1.33 μm	48.5	-	10^{-9}	-
(Paul <i>et al.</i> 2017b)	1.33 μm	67.66	-	7.5×10^{-12}	-
(Asaduzzaman and Ahmed 2017)	1.33 μm	29.25	-	1.76×10^{-9}	-
(Arif and Biddut 2017)	1.3 μm	53.35	-	3.7×10^{-11}	0.0028
This Thesis	1.6 THz	85.7	0.47 ± 0.265	1.7×10^{-9}	0.005

Table 4.3. PCF sensor comparison. Comparison of the proposed PC-PCF sensor with prior PCF sensors for ethanol detection at terahertz.

In Tab. 4.3 a comparison of characteristics of the proposed PC-PCF sensor with other prior sensors for liquid (ethanol) detection is shown. It is seen that the sensitivity of the proposed PC-PCF increased largely with negligible confinement loss, flattened dispersion, and high birefringence.

Fabrication is an important consideration of a fibre design in which the practical application of a PCF is dependent. As our proposed PC-PCF comprises an asymmetrical structure so capillary stacking and sol-gel are not suitable to fabricate the proposed

fibre as they can only be used to fabricate circular-shaped microstructured air holes. However, it is worthwhile to note that, kagome lattice PC-PCF with asymmetrical rectangular structured hole based core has already been fabricated by Atakaramians *et al.* (2009a). Moreover, kagome lattice PCF with different complex structures have also been fabricated by the Max Plank Institute. The 3D printing technology (Ebendorff-Heidepriem *et al.* 2014) for manufacturing the extrusion dies paves the way for fabricating highly asymmetric structures of PCF. Moreover, for sensing and photochemistry applications a kagome lattice PCF including some other complex PCF structures has been fabricated by Cubillas *et al.* (2013). Therefore, by employing the existing PCF fabrication technologies the proposed PCF is feasible.

A kagome lattice slotted core micro-structured PC-PCF based chemical fibre sensor is proposed for terahertz sensing applications. Using Topas as the base material, with the simulation results showing an ultra-high relative sensitivity of 85.6%, 85.7%, and 85.9% and ultra-low confinement loss of $4.5 \times 10^{-9} \text{ cm}^{-1}$, $1.7 \times 10^{-9} \text{ cm}^{-1}$, and $1.02 \times 10^{-9} \text{ cm}^{-1}$ for water, ethanol and benzene respectively in the terahertz frequency range. Moreover, near-zero flat dispersion, high birefringence, high effective area, and large numerical aperture has also been obtained for optimal design parameters. Besides, the proposed PC-PCF sensor is realizable using the existing fabrication technology. Thus, it is expected that with such remarkable sensing properties the proposed PC-PCF-based sensor opens a new window for further terahertz sensor research and paves the way for chemical sensing and other biological applications.

4.3.2 Terahertz sensing in a hollow-core photonic crystal fibre

A terahertz sensor based on a hollow-core photonic crystal fibre (HC-PCF) has been shown here for chemical analyte detection in the terahertz frequency range. The Zeonex based asymmetrical hollow core is filled with an analyte and surrounded by several asymmetrical rectangular air holes bounded by a perfectly matched layer (PML) with absorbing boundary conditions. The performance of the proposed sensor is numerically investigated by using finite element method (FEM) based COMSOL software. It is found that a hollow core provides a high relative sensitivity as well as low transmission loss. Moreover, simplicity in design facilitates manufacturability and making it practical for many different biological and industrial applications.

4.3 Terahertz waveguides for sensing applications

In recent years, there has been significant interest in the design and fabrication of photonic crystal fibre (PCF) because of its diverse applications. It has much interest due to novel light guidance properties and the potential for interaction of light with gases or liquids. Note that PCFs are not only applicable for communication but also sensing applications. After much innovation, PCF based sensors are maturing nowadays due to their compact size, acceptable cost, robustness, and ability to perform in hostile environments such as in high electromagnetic and high chemical exposed fields (Wolfbeis and Weidgans 2006). Major applications of PCF based sensors include sensing of vapours and gases, chemical sensing and medical analysis, monitoring of industrial production, marine and environmental analysis, bioprocess control, and in automotive control.

Among different types of PCF such as solid core, hollow core, and porous core we choose a hollow core for sensing applications as it allows a greater analyte volume inside its core area compared to other core types. Moreover, the guided mode in a hollow-core fibre is strongly confined in the core area that greatly reduces the effect of the background material in the waveguiding properties of the fibre (Shephard *et al.* 2005, Roberts *et al.* 2005). Note that, the air in our air hole core is displaced by a liquid analyte for sensing purposes. Precise and accurate chemical detection is of importance because of its significant applications in the medical and food industries.

Several sensing approaches have been previously used for chemical analyte detection. Using a hydrothermal process Jiaqiang *et al.* (2006) proposed a ZnO nanorods for chemical analyte detection. However, the problem was that their proposed method required a very high temperature that limits the practicability of a sensor. Jepsen *et al.* (2007), Jepsen *et al.* (2008), using reflection mode terahertz time-domain spectroscopy proposed a method to detect chemical analytes. However, obtaining terahertz spectra using that method was challenging. Terahertz time-domain spectroscopy of alcohol in fuel oils was proposed by Arik *et al.* (2013). An optical fibre-based sensor coated with polypyrrole-polyethylene oxide (PPO) material was also investigated to detect volatile compounds such as ammonia, triethylamine, methanol, ethanol, and acetone vapors (Bagchi *et al.* 2017).

Besides, considering the advantages of PCF, a number of sensors with different core-cladding structures was reported previously (Monro *et al.* 2001, Pinto and Lopez-Amo 2012, Ademgil 2014, Ademgil and Haxha 2015, Arif *et al.* 2016, Paul *et al.* 2017a). However, all these sensors operate in the infrared or mid-infrared region and failed to achieve a sensitivity of more than 74%. Recently, the terahertz region has gained attention because of emerging applications in the field of sensing (Walther *et al.* 2010, Fischer *et al.* 2005a), spectroscopy (Zhang and Grischkowsky 2004), investigation of DNA, RNA, and proteins (Markelz *et al.* 2000, Fischer *et al.* 2005b, Markelz *et al.* 2007), biotechnology (Nagel *et al.* 2002), detection of intraoperative breast cancer and colon cancer (Drukteinis *et al.* 2013), diagnosis of skin cancer (Rahman *et al.* 2016), and measurement of HIV load viruses (Shafiee *et al.* 2014). Thus, considering the applications of terahertz we recently proposed a PCF based sensor for chemical analyte detection (Islam *et al.* 2017a). Using a porous core structure in a complex kagome lattice we obtained a relative sensitivity of about 86%. However, the problem with such a PCF structure is the difficulty in fabrication. Thus, there is the motivation for a more fabrication friendly PCF design with increased relative sensitivity in the terahertz band.

Therefore, considering the facts mentioned in Monro *et al.* (2001), Pinto and Lopez-Amo (2012), Ademgil (2014), Ademgil and Haxha (2015), Arif *et al.* (2016), Paul *et al.* (2017a), Islam *et al.* (2017a) and as a possible solution we propose a hollow core PCF based terahertz sensor for chemical analyte detection. In a Zeonex (Cyclo Olefin Polymer) substrate we introduce an asymmetrical air hole structure both in the core and cladding.

Physical insight of the proposed sensor

The cross-section of the designed hollow-core (HC) PCF terahertz sensor is shown in Fig. 4.5(a). Hollow-core fibres are advantageous for sensing applications as the sample under test located in the core can interact with incoming light simultaneously. A hollow core provides lower effective material loss (EML), as well as a higher core power fraction than porous core as the core in an HC-PCF, is only filled with the target analyte instead of bulk material (Islam *et al.* 2017a). Note that it is a challenging task to maintain the polarization state of a PCF, as sensing performance depends on a highly polarized fibre (Emiliyanov *et al.* 2013). High birefringence (i.e. index difference between the polarization modes) can be obtained from the asymmetrical PCF structure that has not been achieved by previously reported sensors

4.3 Terahertz waveguides for sensing applications

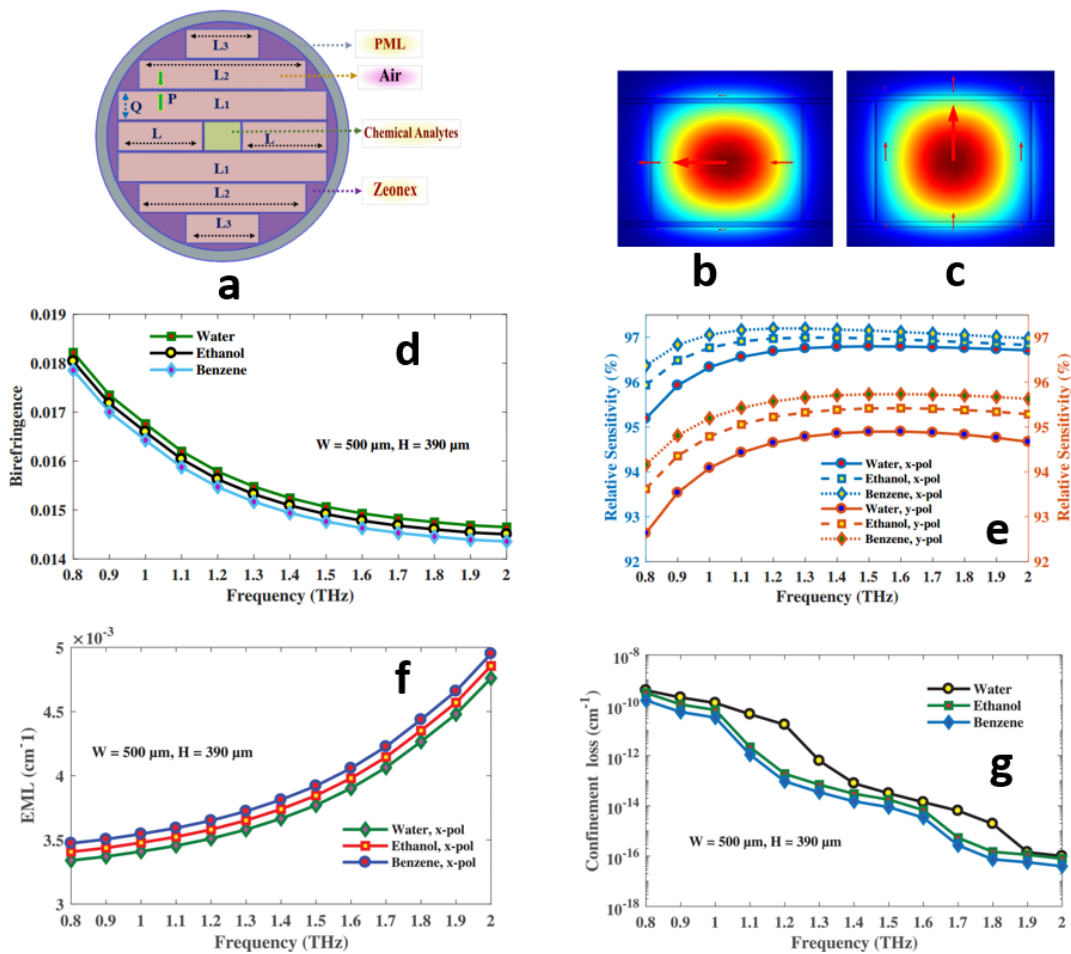


Figure 4.5. Development of hollow waveguide sensor. Schematic of the proposed structure, (a). Mode field propagation in x-direction (b), and in y-direction (c). Birefringence (d), relative sensitivity (e), and confinement loss (f) as a function of frequency for the analyte of water, ethanol, and benzene respectively.

(Monro *et al.* 2001, Emiliyanov *et al.* 2013). Here, the proposed rectangular hollow core is surrounded by an asymmetrical rectangular cladding that provides increased birefringence with improved sensing performance.

The core region consists of a single asymmetrical air hole that defined it as a hollow core. The width and height of the hollow core structure are defined as W and H respectively. A perfectly matched layer (PML) absorbing boundary is given at the outer part of the cladding. The PML boundary condition itself acts as an anti-reflecting layer that absorbs outgoing waves of the PCF (Islam *et al.* 2018f). It is worthwhile to mention that instead of using air in the hollow core region we use different chemical analytes such as water, ethanol, and benzene with refractive index (RI) of 1.33, 1.354, and 1.366

respectively (Islam *et al.* 2017a).

In a PCF based sensor light can be guided either by photonic bandgap (PBG) or by the modified total internal reflection (MTIR) effect. The photonic bandgap mode in a PCF operates when the RI of the cladding is greater than that of the core. On the other hand, the MTIR effect comes into operation when the core RI is greater than that of cladding. In the proposed sensor we used analytes with a high RI, thus the light-guiding mechanism of our proposed sensor is the MTIR mode.

The intensity of light interaction with matter (water, ethanol, and benzene) is shown in Fig. 4.5(b–c). It can be seen that for both the polarization mode the light is well guided inside the core.

Sensitivity of a terahertz PCF is totally dependent on the intensity of light-matter interaction. This rely on the absorption coefficient at a particular frequency. According to the Beer-Lambert law it can be defined as (Ademgil 2014, Ademgil and Haxha 2015, Arif *et al.* 2016),

$$I(f) = I_0(f) \exp[-r\alpha_m l_c] \quad (4.10)$$

where $I(f)$ represents the intensity of light with the presence of analyte needs to be sensed and $I_0(f)$ is the intensity without the presence of an analyte. Here, r , α_m , l_c , and f represent the relative sensitivity, absorption coefficient, channel length and the operating frequency respectively.

As shown in Arif *et al.* (2016), the absorbance of the chemicals to be sensed can be found by,

$$A = \log\left(\frac{I}{I_0}\right) = -r\alpha_m l_c. \quad (4.11)$$

The property of birefringence for different analyte variation is shown in Fig. 4.5(d). It can be seen that birefringence reduces with frequency increase. The reason is that, as the frequency increases the index difference between the polarization modes also decreases. At optimum design parameters, the obtained birefringence for water, ethanol,

4.3 Terahertz waveguides for sensing applications

and benzene are 0.15, 0.17, and 0.19 respectively. Please note that it is potentially possible to increase the birefringence further by reducing either W or H but that will significantly reduce the relative sensitivity.

Fig. 4.5(e) shows the variation of the relative sensitivity of water, ethanol, and benzene with respect to frequency. It can be seen that relative sensitivity increases up to a certain frequency and then decreases slightly. This is because, as frequency increases, the effective RI of the guided mode increases but the core power fraction does not increase after a particular frequency.

In a terahertz sensor, there are few limiting factors such as effective material loss (EML), confinement loss, bending loss, and scattering loss that limits the efficient detection of analytes. Among these, the major loss mechanism is EML that occurs due to the used background material and can be reduced by using air holes inside the core region. Another reason for choosing the hollow core is that it can largely reduce the amount of background material from the core and thus helps to reduce the EML.

The characteristics of EML with respect to frequency with different analyte variation is shown in Fig. 4.5(f). It can be seen that EML increases with a frequency increase that meets the theoretical condition of calculating EML (Islam *et al.* 2018f). It can be seen from Fig. 4.5(f) that the EML at optimum design conditions is extremely low and lowest than ever proposed by any PCF based waveguide.

Fig. 4.5(f) indicates the variation of confinement loss for different analytes with respect to frequency. It is observed that confinement loss reduces with frequency increase because increment of frequency causes the mode fields to constrict more strictly in the hollow core region and thus the confinement loss reduces. It can be seen that the obtained confinement loss for water ($6.22 \times 10^{-13} \text{ cm}^{-1}$), ethanol ($6.95 \times 10^{-14} \text{ cm}^{-1}$) and benzene ($3.48 \times 10^{-14} \text{ cm}^{-1}$) is negligible as compared to the obtained EML.

The obtained relative sensitivity of water, ethanol, and benzene for different W and H is compared in Table 4.4. It can be seen from Table 4.4 that, highest relative sensitivity is obtained for benzene with a maximum W and H . The reason is that at maximum W and H the hollow core can load the maximum amount of analyte into it. Another

W and H	Operating frequency	Sensitivity of water (%)	Sensitivity of ethanol (%)	Sensitivity of Benzene (%)
497 μm and 387 μm	1.5 THz	95.6	95.9	96.2
500 μm and 390 μm	1.5 THz	96.4	96.6	97.2
503 μm and 393 μm	1.5 THz	97.6	97.9	98.2

Table 4.4. Effect of fibre geometries on sensing. The effect of performance variation with global parameter variation of the hollow core PCF sensor.

reason for obtaining the highest sensitivity with benzene is its higher RI compared to other used analytes.

Reference	Operating Region	Relative Sens. (%)	EML (cm^{-1})	CL (cm^{-1})	Birefringence
(Ademgil and Haxha 2015)	1.5 μm	23.75	-	5.5×10^{-5}	-
(Paul <i>et al.</i> 2017b)	1.33 μm	67.66	-	7.5×10^{-12}	-
(Islam <i>et al.</i> 2017a)	1.6 THz	85.7	-	1.7×10^{-9}	0.005
This thesis	1.4 THz	96.8	0.0035	6.9×10^{-14}	0.0154

Table 4.5. Performance comparison with other reported sensors. Comparison of characteristics between the proposed hollow core sensor and prior sensor for chemical (ethanol for example) analyte detection.

Considering ethanol as the chemical analyte, Table 4.5 shows the comparison of different characteristics of the proposed PCF and prior PCF. It can be observed that the PCF has the highest possible sensitivity because of the hollow core. Moreover, besides high birefringence, the proposed PCF based terahertz sensor also demonstrate extremely low EML and negligible confinement loss than obtained by prior PCFs (Ademgil 2014, Ademgil and Haxha 2015, Arif *et al.* 2016, Paul *et al.* 2017a, Islam *et al.* 2017a).

4.3 Terahertz waveguides for sensing applications

A hollow-core photonic crystal fibre is designed and analysed for chemical analyte detection in the terahertz frequency range. Using Zeonex as the substrate and at optimal design conditions, simulation results show a high relative sensitivity of 96.69%, 96.97%, and 97.2% for water, ethanol, and benzene respectively. In addition, the sensor shows low EML and negligible confinement loss that is useful for efficient sensing. Moreover, the obtained high birefringence property is suitable to increase the sensing performance. Using the existing fabrication methods the proposed PCF is feasible to fabricate. Therefore, with such remarkable sensing properties and design flexibility, the proposed sensor will open a new window for next-generation terahertz research and can potentially be applicable in different food and biomedical industries.

4.3.3 Mechanism of terahertz sensing and requirements of a birefringent fibre

In the sensor architecture, the fibre itself will work as a sensing element that will be filled with analyte using the capillary action of the analyte and polymer. The low mechanical strength of the fibre is not an issue as only a short length is used for sensing. To ensure the liquid enters only the core and not the cladding, there are various possibilities such as

- slowly feeding the analyte from a fine tip such as a hypodermic needle or
- depositing a layer on one end of the fibre to block analyte entering the cladding.

Now, considering ethanol as the chemical analyte we will describe how to optimize the sensing performance of the proposed chemical sensor and show why the asymmetrical property of the fibre is important for achieving this. Note that measurement uncertainty increases with sample thickness due to terahertz absorption but, if sample thickness is reduced too much, uncertainty also increases due to an insufficient interaction depth—thus there is a trade-off between these extremes and an optimal thickness can be calculated. It has been proven that the optimal sample thickness to minimize measurement uncertainty is $(2/\alpha)$, where α is the absorption coefficient (Withayachumnankul *et al.* 2008). Note that the absorption coefficient for ethanol is in the 20 to 80 cm^{-1} range in the 0.2 to 1.4 THz band (Balakrishnan *et al.* 2009). Let us now consider $\alpha = 20 \text{ cm}^{-1}$ as this will yield the worst-case largest thickness of

$2/\alpha = 2/20 = 0.1 \text{ cm} = 1 \text{ mm}$. This is rather large, however, if we observe Fig. 2 of reference (Withayachumnankul *et al.* 2008) we see that the minima in the uncertainty versus thickness curves are not narrow but reasonably flattened—and so we can see that halving the optimal thickness does not significantly degrade the uncertainty—this allows us to reasonably halve the value of 1 mm and select 0.5 mm. However, when this 0.5 mm sample is then analysed at 1.4 THz the path length of terahertz radiation will now effectively be $0.05 \times 80 = 4$ absorption lengths. This corresponds to a $20 \log(e^{-4}) = -35 \text{ dB}$ attenuation, which is manageable.

Now, fibre-based terahertz heterodyne detection is known to be able to receive power levels as low as $3 \mu\text{W}$ (Nellen *et al.* 2017). This means that the input terahertz power into the fibre must be $> 160 \mu\text{W}$ and this is perfectly achievable. It is well-known that fibre-based heterodyne detection requires the polarization of the local oscillator to be aligned to the polarization being detected at the end of the fibre. To guarantee this alignment, polarization preserving fibres must be used and this is another motivation why we have designed this chemical sensor using an asymmetrical rectangular core.

4.4 Summary

This chapter contains discussion of modelling and analysis of terahertz waveguides and sensors. We show both symmetrical and asymmetrical waveguide structures suitable for low loss, and polarization maintaining applications. The guiding mechanisms of each proposed sensor, the sensing application for various terahertz fibre is also shown.

In the following chapter, we discuss a novel anti-resonant terahertz fibre for terahertz transmission and gas sensing. A novel fabrication procedure is followed and used to fabricate the antiresonant fibre structure. The fabrication technique is suitable for fabricate any kind of complex terahertz fibres. The experimental analysis of the fibre is also carried out and discussed the transmission and gas sensing properties.

Tabletop fabrication for terahertz specialty optical fibre sensor

AMID the search for efficient terahertz transmission and gas sensing, all-polymer terahertz waveguides attract significant interest due to their compactness and capability for providing environmentally robust systems. The high loss within metals and dielectrics in the terahertz range makes it challenging to build low loss, mechanically stable, and broadband terahertz waveguides. In this context, hollow waveguides made of Zeonex are promising candidates for attaining low transmission loss in the terahertz range. Here, we investigate a hollow hexagonal-core fibre (HCF) that exhibits low loss, near-zero dispersion, wide operating bandwidth, and is suitable as an ultra-sensitive gas sensor. Notably, HCF fabrication is carried out by exploiting an efficient low-cost single-step extrusion method. Our experiments demonstrate that the HCF can achieve remarkably low attenuation and near zero flatten dispersion as compared to any other terahertz fibres. The resulting HCFs are easy to handle and have high thermal and chemical stability. These results bring significant advancements for terahertz fibre fabrication, low-loss ultra-fast short-distance terahertz transmission, and sensing in the terahertz spectral domain.

5.1 Introduction

The new frontier of terahertz research contains a significant number of cutting-edge applications, including label-free and non-invasive molecular detection, DNA hybridization probing, pharmaceutical drug testing, and high-speed short-range optical communications (Gallot *et al.* 2000, Atakaramians *et al.* 2013, Siegel 2004, Islam *et al.* 2016a, Islam *et al.* 2018d, Islam *et al.* 2018h). Terahertz technology also has significant potential for biomedical spectroscopy applications due to its ability to probe molecular interactions (Sultana *et al.* 2017b, Mittleman *et al.* 1998, Gerecht *et al.* 2011, Lin *et al.* 2008, Pickwell and Wallace 2006, Islam *et al.* 2017a, Islam *et al.* 2020d, Islam *et al.* 2018j, Williams 2007, Chan *et al.* 2007). Moreover, it can be potentially applied to security screening as it can penetrate plastics, cardboard, and leather (Tsydynzhapov *et al.* 2018). This motivates the interest in advancing terahertz technology as the demand for state-of-the-art terahertz sources, detectors, and waveguides is as pressing as growing.

Whilst free space terahertz propagation has been widely explored, terahertz transmission is profoundly affected by the water vapour present in the atmosphere. Transmission through waveguides is a promising approach, but the low transparency of materials is a significant challenge. Metal waveguides have been primarily considered, but their finite conductivity, inflexibility, and the surface roughness of metals limit their applicability (Jeon *et al.* 2005). To address this issue, the use of dielectric waveguides has gained attention, and encouraging results have been demonstrated. Polymers, such as Topas, Zeonex, Teflon, TPX, and HDPE, have appeared as materials of interest as they present a lower absorption coefficient than other dielectrics and glasses (Islam *et al.* 2019e).

In this context, the use of microstructured optical fibres (MOF) emerges as an efficient approach for obtaining waveguides with adequate loss, birefringence, and dispersion levels. Indeed, the use of MOFs for the terahertz range is a growing trend (Harrington *et al.* 2004, Anthony *et al.* 2013, Bowden *et al.* 2007, Bowden *et al.* 2008b, Bowden *et al.* 2008a, Matsuura and Takeda 2008, Tang *et al.* 2009, Li *et al.* 2016a, Van Putten *et al.* 2018, Stefani *et al.* 2018, Lai *et al.* 2010). Porous-core fibres, for example, have holes within the core region, which lessen the overlap between the optical mode and the waveguide material, allowing a reduction loss levels in the terahertz range (Islam *et al.* 2017d, Islam *et al.* 2016a, Islam *et al.* 2016c, Islam *et al.* 2017b, Markov

and Skorobogatiy 2013, Atakaramians *et al.* 2009a, Chen *et al.* 2013, Hassani *et al.* 2008, Cruz *et al.* 2013a, Bao *et al.* 2012, Kaijage *et al.* 2013, Ahmed *et al.* 2017a, Aming *et al.* 2016). However, despite all the endeavours towards the development of terahertz fibres with solid or porous cores, achieving low loss, low dispersion, broadband transmission, and ease of fabrication remain critical issues.

Hollow-core fibres, otherwise, arise as the most appropriate choice for attaining optimum terahertz beam transmission. It is because, in hollow-core fibres, the modes propagate through a hollow channel with low interaction with the fibre material. Hollow-core fibres can guide light either under photonic bandgap (PBG) (Birks *et al.* 1995) or inhibited coupling (IC) (Couny *et al.* 2007) mechanisms. In PBG fibres, the mode guidance is possible because the cladding microstructure is such that there are no photonic states, within a specific frequency range, to which the core mode can be coupled. Differently, in IC fibres, the core and cladding modes coexist. Low loss propagation is then achieved by robustly minimizing the coupling between core and cladding modes. This coupling inhibition is attained by reducing the spatial overlap between the modes and by obtaining a strong mismatch between their transverse phases (Debord *et al.* 2017, Debord *et al.* 2019).

Indeed, the excellent performance of IC fibre designs, eg. kagome (Maurel *et al.* 2018), tubular (Debord *et al.* 2017, Chafer *et al.* 2019), conjoined-tubes (Gao *et al.* 2018), nested-tubes (Jasion *et al.* 2020), and hybrid kagome-tubular (Amrani *et al.* 2021) lattice designs) working in the visible and infrared spectral ranges has been recently demonstrated in the literature. However, although terahertz hollow-core fibres have been assessed in simulation studies, there are very few reports on experimental results regarding the operation of those fibres in the terahertz range (Anthony *et al.* 2011b). In this context, it is noteworthy that 3D printing technology has appeared as a potentially useful technique for fabricating terahertz fibres (Van Putten *et al.* 2018, Yang *et al.* 2019b, Cruz *et al.* 2018).

One reason is the larger dimensions of MOFs needed for guiding terahertz, compared to MOFs for the visible and IR ranges. The larger dimensions allow direct 3D printing or extrusion of the fibre itself, which is not possible for MOFs in the visible-IR range, where only the preform can be printed and a draw process is necessary to achieve the

5.1 Introduction

small dimensions. Also, terahertz fibres have shorter lengths compared to visible-IR fibres, which also make terahertz fibres more suited for simple fabrication techniques such as 3D printing.

In this chapter, we investigate a specialty hollow-core terahertz fibre fabricated using Zeonex and a direct manufacturing technique based on a horizontal extruder. In addition to its low loss in the terahertz range, Zeonex presents high thermal and chemical stability and low water absorption. The fibre geometry has a hexagonal-shaped hollow-core, which is connected to the outer jacket via six radial struts. The fabrication method employs a recently developed single-step technique (Cordeiro *et al.* 2020), which is here extended to fabricate a terahertz waveguide for the first time. We report the fabrication of fibres with different dimensions, as well as the characterisation and simulation of their loss, dispersion, and gas sensing properties. The results reported herein will potentially contribute to the development of low-loss ultrafast short-distance terahertz transmission and ultra-sensitive gas sensing measurements.

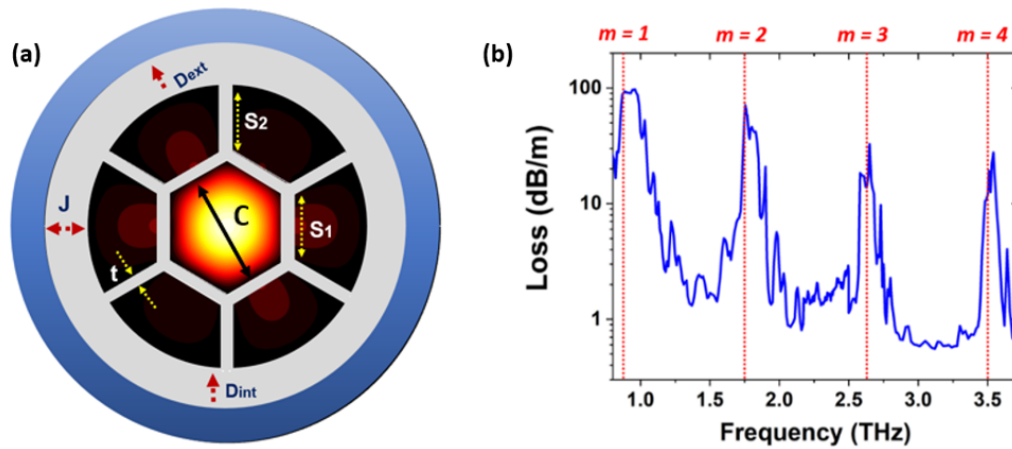


Figure 5.1. Schematic diagram and typical loss of the specialty fibre. (a) Cross-section schematic of the proposed hollow hexagonal-core fibre, where the external blue region indicates the perfectly matched layer (PML) boundary condition. (b) Typical simulated loss spectrum using $S_1 = 1200 \mu\text{m}$, $S_2 = 1170.6 \mu\text{m}$, $t = 148 \mu\text{m}$, and $J = 700 \mu\text{m}$.

5.1.1 Fibre design

Fig. 5.1(a) shows the fibre design we explore herein. It consists of a hollow hexagonal-core fibre (HCF), with Zeonex as the bulk material. In the fibre structure, six radial struts connect the hexagonal core contour to the outer jacket. Here, we denote the

core side length as S_1 and its thickness as t . The radial struts have a length of S_2 . The fibre microstructure is inscribed in a circle with a diameter $D_{\text{int}} = 2 \times (S_1 + S_2)$, and the outer diameter of the fibre is defined as $D_{\text{ext}} = D_{\text{int}} + 2J$, where J is the outer jacket thickness. Previous studies have used similar fibre designs aiming at light transmission through ultraviolet, visible, and infrared wavelengths (Gérôme *et al.* 2010, Hayes *et al.* 2015, Hartung *et al.* 2015), and the realisation of sensing experiments (Tsiminis *et al.* 2016).

The advantage of such a standard waveguide structure is its easy fabrication procedure, which only requires tabletop extruder (Cordeiro *et al.* 2020). In this structure, terahertz waves propagate through the fibre core due to the IC guidance mechanism (Couny *et al.* 2007). It allows obtaining low loss transmission bands where the core mode coupling to the cladding modes is minimized. These low-loss transmission bands are spectrally separated from each other by high-loss narrow bands. The latter are centred at high-loss frequencies, f_{high} , given by Eqn. 5.1, and correspond to resonant coupling between the core mode of interest with the cladding struts. Here, m is the resonance order, c is the speed of light, t is the cladding struts thickness, n_{clad} is the cladding refractive index, and n_{core} is the core refractive index (Debord *et al.* 2017, Debord *et al.* 2019, Setti *et al.* 2013). Fig. 5.1(b) presents a typical loss spectrum of such a structure, which is simulated by using a finite element method-based mode solver, COMSOL Multiphysics. In Fig. 5.1(b), the fibre parameters are $S_1 = 1200 \mu\text{m}$, $S_2 = 1170.6 \mu\text{m}$, $t = 148 \mu\text{m}$, and $J = 700 \mu\text{m}$, similar to one of our fabricated fibres. The Zeonex refractive index is set to ($n = 1.529$) and its absorption coefficient to $\alpha = 0.2 \text{ cm}^{-1}$, as recently measured for planar Zeonex samples (Islam *et al.* 2019e). Note that, the environmental loss that we experience during experiment was not considered in simulation. The high loss frequencies calculated by Eqn. 5.1 appear as dotted vertical lines in Fig. 5.1(b)

$$f_{\text{high}} = \frac{mc}{2t\sqrt{n_{\text{clad}}^2 - n_{\text{co}}^2}}. \quad (5.1)$$

5.1.2 Fibre fabrication

The fabrication of the proposed fibre is carried out by using a tabletop horizontal extruder designed for producing 3D printer filaments (EX2 Filabot). Notably, this is the unique piece of equipment needed for producing the terahertz fibre we describe in this

5.1 Introduction

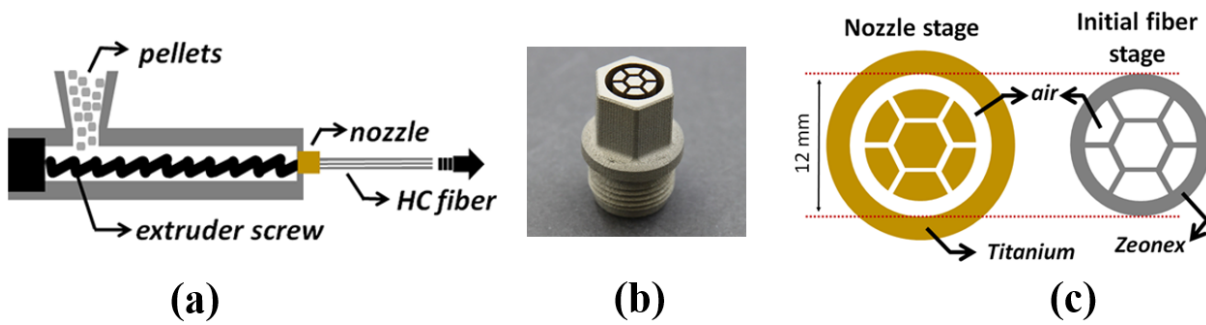


Figure 5.2. Table-top fabrication procedure. (a) Lateral schematic view of the horizontal extruder showing the extruder screw, feeding pellets hopper, specially designed nozzle, and pulled terahertz fibre; (b) Picture of the manufactured nozzle; (c) Top view of the nozzle and fibre with hexagonal shaped core.

paper. The method for obtaining the fibres is represented in Fig. 5.2(a). The operation is based on feeding the extruder screw with polymer pellets via a top hopper while a heating element increases the plastic temperature. A special nozzle, Fig. 5.2(b), is 3D-printed in titanium (Cordeiro *et al.* 2020) and designed to present an external cross-section that defines a solid hexagon linked to an external hollow jacket by six hollow channels, Fig. 5.2(c), left. The air struts in the nozzle are 0.8 mm thick. The internal nozzle diameter measures 12 mm. The internal construction of the nozzle follows a previously developed concept (Ebendorff-Heidepriem and Monro 2007). It allows the nozzle to block the material flow through its exit face in the regions where the fibre holes are designed to be. The fibre that emerges from the nozzle has, therefore, solid struts and a hollow core, Fig. 5.2(c), right. During the fabrication, the extrusion screw rotation speed can be adjusted, and typical values correspond to a material feed rate between 0.05 to 0.1 g/s. Additionally, the temperature is set to 220°C, and the extruded material has an initial external diameter that matches the nozzle's internal diameter, i.e., 12 mm.

As mentioned, Zeonex, a cyclo-olefin polymer (COP), is selected as the fibre material. Beyond its low water absorption, moldability (Setti *et al.* 2013), and favorable chemical resistance (Islam *et al.* 2019e), Zeonex presents low loss in the terahertz frequency range (Islam *et al.* 2019e, Anthony *et al.* 2011a), similar to Teflon, Topas, and HDPE, and considerably better than, for example, PMMA. Here, Zeonex 480R commercial pellets (Product Data Sheet 2015) (with a density of 1.01 g/cm³, glass transition temperature

of 138°C, and water absorption smaller than 0.01%) are selected.

In this work, we target thick fibres with core diameters between 1 mm and 2 mm, and guidance in the 0.5–3.5 THz range. Here, the draw down-ratio of the dimensions of the material emerging from the die exit to the final fibre is quite small (from 12 mm to 5–8 mm typically). To achieve such a small reduction in dimensions, the extruded material is manually pulled at a low rate (few mm/s).

To demonstrate the potential of the technique for producing fibres with different parameters, we report on the fabrication of four fibres, whose geometrical dimensions are presented in Tab. 5.1. The error estimation in the strut thickness, t , is made by considering multiple measurements performed under an optical microscope. Remarkably, such a straightforward fabrication technique can yield fibres with struts within a considerable thickness range, namely between 20 μm and 160 μm . This has been achieved by changing the draw rate while the feed rate has been kept constant. Fig. 5.3 shows representative images of the fabricated fibres.

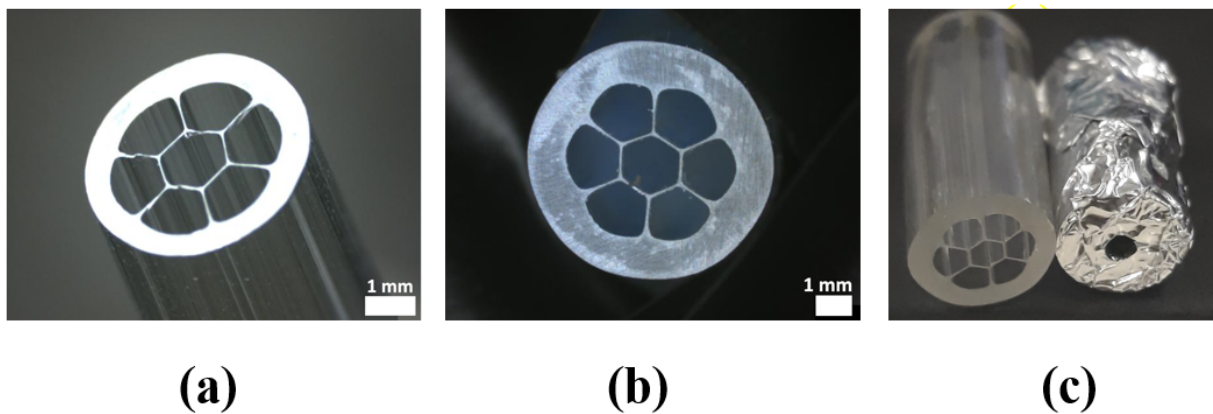


Figure 5.3. Representative images of the fabricated samples. (a) Frontal and (b) lateral view of fibre sample #3. (c) Image of a fibre with an outer diameter of 4.4 mm, a core diameter of 1.2 mm, and struts thickness of 28 μm . The whole fibre is wrapped by aluminium foil just by keeping the core open. This is just to ensure that the signal is only propagating through the core and not through other parts of the fibre.

5.2 Fibre characterization

Fibre type	C (mm)	S (μm)	D _{ext} (mm)	L (mm)
Type-I	2.0	85 \pm 5	7.3	20
Type-II	1.6	65 \pm 10	6.5	40
Type-III	2.2	155 \pm 10	8.0	45
Type-IV	0.6	22 \pm 5	2.0	90

Table 5.1. Dimensions of the fabricated fibres. This include the core diameter (C), the strut thickness (S), total fibre diameter (D_{ext}), and the length of the fibre (L).

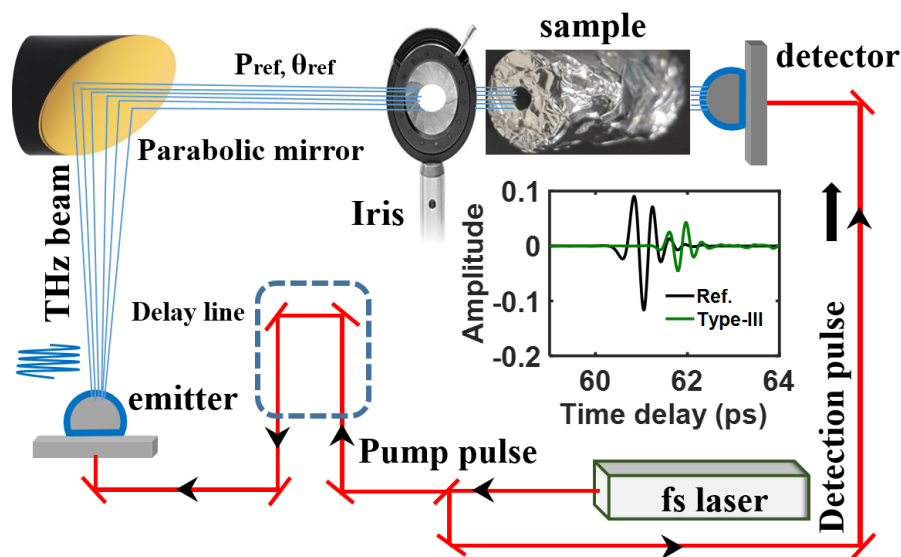


Figure 5.4. The experimental setup to measure the fabricated fibres. It contains a femtosecond (fs) laser, terahertz transmitter, and detector, a parabolic mirror, iris, XYZ translation stage, and the sample. The whole system is enclosed with a purge box containing dry air. The inset shows the terahertz amplitude of the reference and the longer fibre sample.

5.2 Fibre characterization

5.2.1 Loss measurement and simulation

To characterize the fibre performance in the terahertz range, an Advantest TAS7400TS terahertz optical sampling system is used. The system is built with a dual-channel ultrashort pulse laser for free-space terahertz generation and detection (Advantest 2021). In the experiment, depicted in Fig. 5.4, a gold-coated parabolic mirror with a focal length of 100 mm is used to focus the beam towards the waveguide core, and an iris is used to block undesired signals coupling to the core. The fibre waveguide is then placed on a translation stage, and a specially designed 3D-printed fibre holder is used

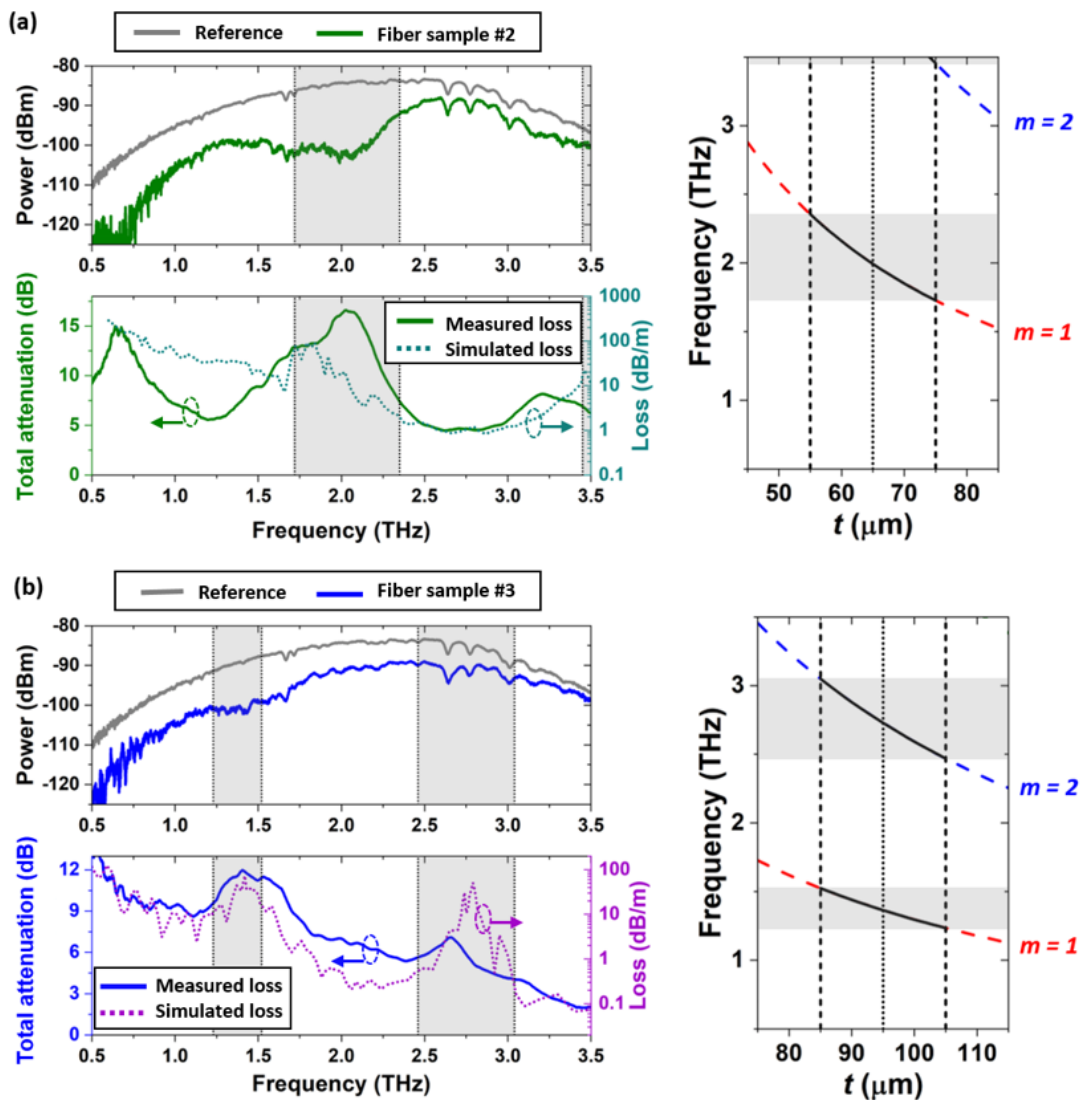


Figure 5.5. Transmission spectra: measured and simulated. (a) Left-hand side top: reference (grey curve) and fibre sample #2 (green curve) measured transmission spectra; left-hand side bottom: total attenuation (solid green curve) and simulated loss (dotted green curve). (b) Left-hand side top: reference (grey curve) and fibre sample #3 (blue curve) measured transmission spectra; left-hand side bottom: total attenuation (solid blue curve) and simulated loss (dotted purple curve). Shaded regions indicate struts resonances, as identified in the plots presented on the right-hand side.

to provide mechanical support. To ensure that the terahertz beam is coupled to the fibre core only, we wrap the waveguide with aluminium foil, while keeping the core region unblocked. The system is enclosed in a custom-made purge box filled with dry air, in order to minimize the presence of water vapor and avoid water-induced absorption. Additionally, care is taken to ensure minimal humidity levels inside the purge box, which was monitored with a hygrometer. Typical reference and sample signals

5.2 Fibre characterization

are presented in the inset in Fig. 5.4.

The loss values of fibre samples #2 and #3 are estimated by using the experimental setup presented in Fig. 5.4. The reference (grey curve) and samples (blue and green curves) transmission spectra are presented on the left-hand side top graphs in Fig. 5.5(a) and Fig. 5.5(b). The reference measurement is carried out without the fibre sample in between the transmitter and receiver, while the sampled signal is taken by placing the fibre samples. The shaded regions indicate the resonances of the microstructure struts, where the high loss occurs. These regions are calculated from Eqn. 5.1 by considering the strut thickness variations, as presented in Tab. 5.1. In the graphs on the right-hand side in Fig. 5.5, we plot Eqn. 5.1 for $m = 1$ and $m = 2$ as a function of the fibre strut thickness to identify the expected high loss regions.

By taking into account the reference and sample spectra, one can calculate the transmission through the fibre sample, $T(\omega) = \frac{P_{\text{sam}}(\omega)}{P_{\text{ref}}(\omega)}$, where $P_{\text{ref}}(\omega)$ and $P_{\text{sam}}(\omega)$ are the reference and sample power spectra, respectively. Thus, one can estimate the total attenuation as $-10 \log T(\omega)$. The resulting values are presented in the bottom left-hand side plots in Fig. 5.5 (left axis). As expected, low loss intervals are observed between the microstructure resonances. For fibre sample #2, the total attenuation figures are measured as 5.6 dB at 1.2 THz and 4.7 dB at 2.7 THz. For fibre sample #3, the total attenuation values are measured to be 9.2 dB at 0.95 THz, 6.2 dB at 2.2 THz, and 2.0 dB at 3.4 THz. The total attenuation of sample #4 is presented in Fig. 5.6(a). Sample #1, on the other hand, could not be measured in our system as its low order resonances are expected to be around 5.9 and 11.8 THz.

Additionally, numerical simulations using the finite element method (FEM) are performed by considering the geometrical parameters of the fabricated fibres. The results are presented in Fig. 5.5 as dotted green and dotted purple curves in the bottom left-hand side plots (right axis). As for the simulations in Fig. 5.1(b), the Zeonex refractive index is taken to be $n = 1.529$, and its absorption coefficient is set to $\alpha = 0.2 \text{ cm}^{-1}$ (Islam *et al.* 2019e). It is seen that minimum loss figures are calculated to be 33.7 dB/m at 1.2 THz and 0.95 dB/m at 2.7 THz for fibre sample #2. For fibre sample #3, loss values of 5.4 dB/m at 0.95 THz, 0.26 dB/m at 2.2 THz, and 0.07 dB/m at 3.4 THz are

calculated. The spectral locations of the resonances are reasonably well-matched, between experimental and simulated results. One source of the discrepancies between measured and simulated data is assumed to be the existence of thickness variations in the struts that demark the core in the fabricated fibres. Further optimization of the fabrication process may reduce such imperfections, allowing to attain fibres with improved microstructures. Due to practical limitations in the current stage of the developed technique, we are unable to perform cutback measurements using the fabricated samples. Thus, our analyses are restricted to the comparison between the total attenuation measured in the experiments (in dB, which includes coupling and transmission loss) and the simulated loss (in dB/m, which accounts for confinement and absorption loss, hence not taking into account the coupling loss).

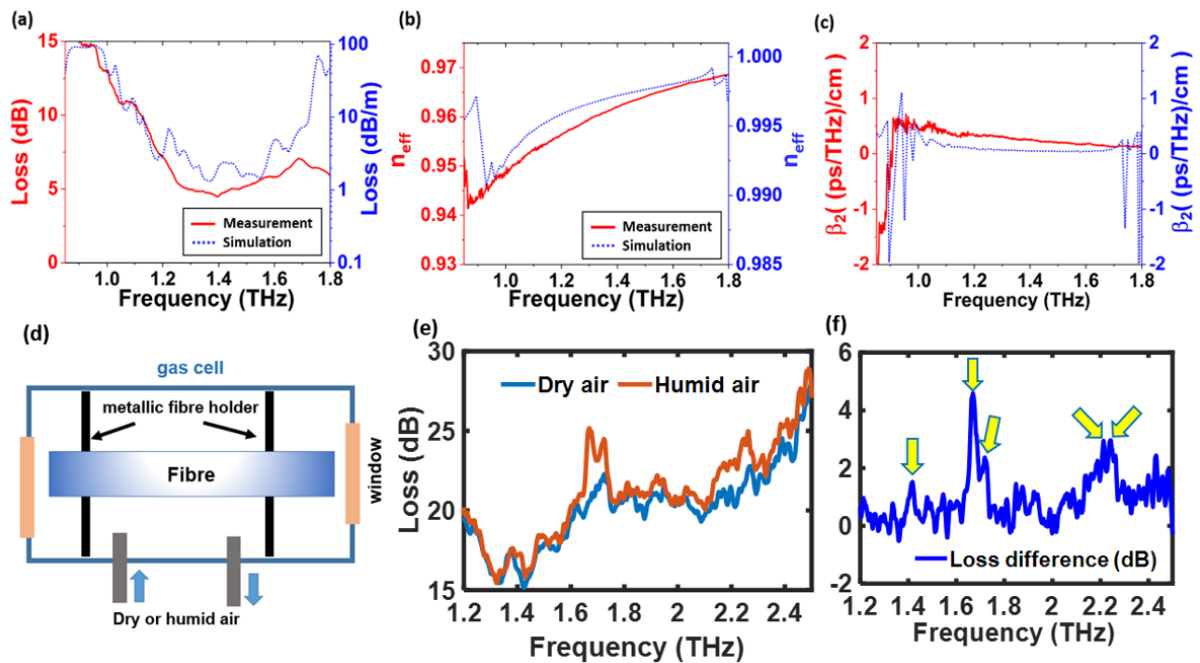


Figure 5.6. Experimental total attenuation (red curves) and simulated loss (dashed blue curves), and sensitivity. (a) Experimental total attenuation (red curves) and simulated loss (dashed blue curves), (b) Effective refractive index, (c) β_2 values for fibre sample #4, (d) Experimental setup for humid air sensing where a vacuum pump is used for continuous flow of humid air. During the measurements, the flow rate through the cell is kept significantly low. The cell contains a tissue wetted by milli-Q water. Two metallic discs are used to hold the fibre straight and block the stray of the terahertz signal coming from outside of the fibre, (e) Experimental loss measurement of a 45 mm long HC-THz fibre filled with dry and humid air from 1.2 to 2.4 THz. (f) Loss difference between data in (e). Water absorption peaks are marked by arrows.

5.2.2 Dispersion and sensing measurements

The time-domain data obtained from the terahertz measurement system can be processed to account for the dispersion properties of the fibres. Thus, fast Fourier transforms (FFTs) can be applied to the obtained time-domain data to retrieve the magnitude and phase in the frequency domain. In this process, the obtained phase is unwrapped between $-\pi$ and $+\pi$ to truncate unwanted noise above this range (Jepsen 2019). The effective refractive index, $n(\omega)$, can be obtained from Eqn. 5.2, where c is the speed of light, l is the fibre length, ω is the angular frequency, and $\phi(\omega)$ represents the phase difference between the reference and sample signals. Additionally, the waveguide dispersion can be quantified from $n(\omega)$ as follows and shown in Eqn. 5.3,

$$n(\omega) = 1 + \frac{c\phi(\omega)}{l d\omega} \quad (5.2)$$

$$\beta_2 = \frac{2}{c} \frac{dn(\omega)}{d\omega} + \frac{\omega}{c} \frac{d^2n(\omega)}{d\omega^2}, \text{ ps/THz/cm.} \quad (5.3)$$

Fibre sample #4 has been used in the dispersion measurements. The fibre loss and the frequency-dependent refractive index derived from the phase data in the terahertz measurements are shown in Fig. 5.6(a) and Fig. 5.6(b), respectively (red curves). Additionally, the simulated loss and effective refractive index values are also shown in Fig. 5.6(a) and Fig. 5.6(b) (dotted blue curves). In Fig. 5.6(b), one sees that experimental and simulated effective refractive index values are in close agreement. The measured values range from 0.948 to 0.967 in the frequency range between 1.0 THz and 1.7 THz. In contrast, the simulated ones range from 0.992 to 0.998 in the same frequency range. Additionally, Fig. 5.6(c) presents the experimental and simulation results for β_2 in fibre sample #4. The obtained β_2 values are remarkably low and flat (values between 0.12 and 0.60 (ps/THz)/cm between 1.0 THz and 1.7 THz) as compared to other experimentally reported low dispersion waveguides (Anthony *et al.* 2011b, Mbonye *et al.* 2009, Mendis and Grischkowsky 2001, Wang and Mittleman 2004, Han *et al.* 2002, Anthony *et al.* 2011a, Anthony *et al.* 2013).

The gas sensing capability of the proposed hollow fibre was verified in a water vapor detection measurement. Here, it is worth mentioning that water vapours have received major attention in research due to their abundance in the atmosphere and as a common absorber for terahertz electromagnetic waves. The undesirable vapour

absorption lines are often referred to as a common impurity in spectroscopic studies. Therefore, water vapour in the atmosphere is one of the most suitable samples in testing the accuracy of the terahertz time-domain spectroscopy (THz-TDS) system (Van Exter *et al.* 1989). Also, the rotational absorption characterization of water vapour is of interest in astronomical and atmospheric measurements (Podobedov *et al.* 2008). The absorption peaks of water and hot water vapours (De Natale *et al.* 1997), for example, have been measured in different frequency ranges via the use of large gas cells (Van Exter *et al.* 1989, Melinger *et al.* 2012, Chevillat and Grischkowsky 1998). Additionally, small amounts of gas in a sealed fibre have been successfully detected by using short and long length fibres (You *et al.* 2012, Katagiri *et al.* 2018). However, there are very few works for water vapour detection using terahertz fibres (Xin *et al.* 2006).

Fig. 5.6(d) exhibits the experimental setup that was employed in such measurements. The hollow-core fibre has been inserted in a gas cell, composed of a plastic jar and two windows, whose atmospheric conditions could be controlled (via the use of a continuous supply of humid air, a flow of nitrogen, and an evacuation system). The air gap between each fibre end and the window was 3 mm and the fibre used in the experiments was 45 mm long. In turn, the gas cell length was 51 mm. The experimental procedure involves measuring the fibre transmittance between 1.2 and 2.4 THz when the fibre is filled with dry nitrogen and when the fibre is filled with humid air at room temperature.

In the measurements, sample #4 has been placed on a metallic holder inside the gas cell and the transmitted signal has been measured when the fibre was in a dry environment and when water vapor was inserted in the gas cell. Fig. 5.6(e) displays the loss of sample #4 when in dry and humid environments. It is seen that the loss is higher for the humid environment, as expected. Moreover, Fig. 5.6(f) presents the difference between the curves in Fig. 5.6(d). This procedure allows identifying the absorption lines at 1.417, 1.669, 1.719, 2.213, and 2.265 THz in a clearer fashion, similarly to what has been achieved by Xin *et al.* (2006), Cui *et al.* (2015). The absorption peaks are due to the vibrational and rotational transitions of the water vapor cluster bond. The absorption lines indicate the presence of water inside the fibre and demonstrates the potential of the fibre reported herein to act as a waveguide-based gas sensor.

5.3 Discussion

In this manuscript, we report the design, fabrication, and characterization of simple hollow-core fibres showing low loss and near-zero dispersion in the terahertz range, which represents a promising path towards the accomplishment of efficient, low-loss, low-dispersion, and broadband terahertz transmission. A novel single-step fabrication method is adopted to provide efficient, simple, and low-cost fibres with different dimensions. The experimental analyses demonstrated fibres with total attenuation–transmission and coupling loss–of few dB in the studied frequency range, reaching values as low as 2 dB at 3.4 THz for sample #3 (20 mm long). Also, fibres with a near-zero dispersion of less than 0.6 ps/THz/cm are demonstrated. The results reported herein reveal the potential of such a remarkably simple fabrication technique for obtaining microstructured terahertz hollow-core optical fibres.

While attaining low dispersion values is essential for adequately transmitting signals stemming from pulsed terahertz sources, having low-loss hollow terahertz waveguides provide a promising path for the realisation of ultrasensitive gas sensing. We anticipate that the analyses presented in this chapter will impact the development of low-loss ultrafast short-distance terahertz transmission devices and future gas sensing experiments. Finally, since the guidance in IC fibres is favoured when the spatial overlap between the core mode and the modes in the cladding is minimized, designing fibres with hypocycloid-shaped core contours (i.e., negative curvature) (Wang *et al.* 2011, Debord *et al.* 2013) appears as an efficient approach for reducing the overlap between the core and cladding modes and, hence, for attaining fibres with lower loss levels. Thus, future developments will consider the fabrication of hypocycloid-shaped core fibres.

In the following chapter, the effect of surface plasmon resonance in biochemical sensing is discussed. The discussion is followed by various optimized optical fibre design in the visible to mid-infrared regime. The performance analysis of all the fibres are carried out and fabricated a simplified fibre that can be used for further biochemical sensing analysis.

Surface plasmon resonance biosensor

AS technology continues to advance, the development of novel sensing systems opens up new possibilities for low cost, practical biosensing applications. In this chapter, we demonstrate optical fibre based surface plasmon resonance (SPR) and localized surface plasmon resonance (LSPR) sensors for biochemical sensing. Beside the fibre design, the sensitivity, loss, length of usable fibre, limit of detection, and figure of merit of the sensors are also discussed. Various structured and coated fibre designs are discussed and one of the optimized fibre is fabricated that is ready to be used as a sensor.

6.1 Localized surface plasmon resonance biosensor

In this section, we demonstrate a localized surface plasmon resonance (LSPR) system that combines both wave-guiding and plasmonic resonance sensing with a single microstructured polymeric structure. Characterizing the sensor using Finite Element Method (FEM) simulation results show a record wavelength sensitivity (WS) of 111000 nm/RIU, high amplitude sensitivity (AS) of 2050 RIU⁻¹, high sensor resolution and limit of detection (LOD) of 9×10^{-7} RIU and 8.12×10^{-12} RIU²/nm respectively. Furthermore, these sensors have the capability to detect an analyte within the refractive index (RI) range of 1.33 to 1.43 in the visible to mid-IR therefore being potentially suitable for applications in biomolecular and chemical analyte detection.

6.1.1 Introduction

LSPR is an optical phenomenon that is a result of surface plasmon excitation in nanoparticles or nanogratings of size smaller than the wavelength of light. The high optical confinement and local field enhancement capability of LSPR are widely implemented for surface-enhanced Raman scattering (SERS) analysis where enhanced electromagnetic fields near metal nanostructure promote significant Raman response of deposited proteins/molecules that are in contact with the metal (Maier *et al.* 2003, Kalachyova *et al.* 2015). The use of photonic crystal fibre (PCF) has advantages in terms of tunability, size, and immunity to electromagnetic interference in combination with LSPR makes the sensor suitable for a range of sensing applications. For bioanalyte detection and SERS response intensification several studies with different techniques including surface plasmon resonance (SPR) and LSPR have been carried out (Wang *et al.* 2018, Cao *et al.* 2018, Rifat *et al.* 2018, Lu *et al.* 2018). Using tungsten disulfide to support SPR, sensitivity of 2459.3 nm/RIU for RI ranging from 1.33 to 1.36 has been reported (Wang *et al.* 2018). Using a D-shaped fibre structure researchers obtained a maximum WS of 44567 nm/RIU (Cao *et al.* 2018).

Note that, recent studies (Wang *et al.* 2018, Cao *et al.* 2018, Rifat *et al.* 2018, Lu *et al.* 2018) were carried out using SPR technology and used either internal sensing or external sensing using a D-shaped structure. In internal sensing, the filling and flushing of the analyte is challenging, whereas the D-shaped PCF requires external surface polishing

to give its shape. Here, internal sensing refers to filling various air holes of the fibre with the analyte solution—this can be carried out via a syringe (ie. withdrawal or pumping mode)—whereas external sensing refers to contacting the analyte to the fibre surface. Note that, our recent study on SPR showed a high WS (62000 nm/RIU) and AS (1415 RIU⁻¹) that comes with high confinement loss (CL) (300 dB/cm) (Islam *et al.* 2018i). However, it has been necessary to eliminate thick cladding layers from these fibres to allow fields to interact directly through evanescent waves arising from the core/cladding boundary region, resulting in a loss of mechanical strength. Therefore, LSPR based sensors are introduced as a solution to enhance the sensing performance as well as minimizing the size and cost (Lu *et al.* 2018, Paul and Biswas 2018). Using nanospheres, researchers were able to achieve a maximum WS of 27000 nm/RIU (Paul and Biswas 2018) whereas the use of a Au grating reports a maximum WS of 3340 nm/RIU with extremely low AS that also comes with high CL (Lu *et al.* 2018). Therefore, there is scope to develop an improved theoretical framework of PCF based biosensors that may eventually lead to different practical implementations in both the medical and chemical industries.

Here, we aim to design a sensor that can improve the absorption, resolution, and LOD with low CL. Therefore we propose a dual channel based LSPR sensor having a Au grating as a plasmonic metal with the analyte channel in contact with Au that facilitates external sensing. Considering the fabrication feasibility, we describe the optimized sensor by analysing different structures with variations in key geometrical parameters.

6.1.2 Design methodology, simulation, and optimization

The design, Fig. 6.1(a), and computational analysis of the sensor are carried out using COMSOL multiphysics 5.3 set to an extremely fine mesh size with a degree of freedom of 739945, number of elements of 105616, and minimum element quality of 0.324. On a silica (SiO₂) substrate the air holes are placed in such a way that so as to confine the electric field to the center of the fibre and interact strongly with the metal. A thinner TiO₂ layer is used in contact with the SiO₂ so that the Au can adhere strongly to SiO₂. The basic data for the model, such as the RI of SiO₂, TiO₂, and Au is obtained from Vial *et al.* (2005), Tatian (1984). The air hole diameters are defined as d_1 , d_2 , and d_3 , the outer surface radius and pitch from the center to d_2 are defined as r_1 and Λ_1 , and TiO₂, Au, analyte and the perfectly matched layer (PML) thicknesses are defined as t_t , t_g ,

6.1 Localized surface plasmon resonance biosensor

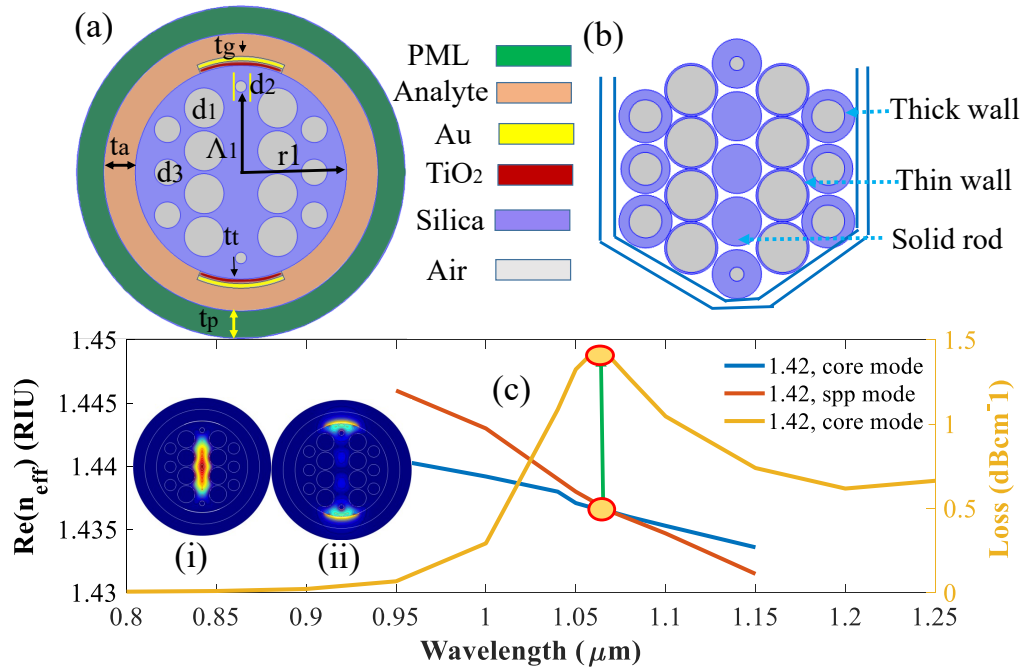


Figure 6.1. Schematic and mode field characteristics of the LSPR biosensor. (a) Schematic of the cross section; (b) stacked preform and (c) dispersion relation between core guided mode, plasmonic mode and loss spectra at the core mode having the inset of (c) shows the electromagnetic field distribution (i) core mode and (ii) SPP mode, (Islam *et al.* 2019d).

t_a , and t_p respectively. Note that the PML is a computational boundary that absorbs scattered waves from the PCF. The scaled down air holes of diameter d_2 and d_3 help to reduce the CL as it contributes to reduced scattering of light from the center of the fibre. The stacked capillary diagram of the sensor is shown in Fig. 6.1(b) showing that it can be fabricated using capillary stacking. In terms of fabrication the thicker wall capillary indicates smaller air holes and solid rods indicate no air holes. Fig. 6.1(c) indicates that when the phase matching of $\text{Re}(n_{\text{eff}})$ between the core guided mode and SPP mode occurs then the sensor is then at resonance and thus a maximum loss peak is obtained. Inset of Fig. 6.1(c) shows the electric field distribution in the core guided mode (i) and SPP mode (ii). We considered $d_c = 0.18\Lambda$, $d = 0.70\Lambda$, $d_1 = 0.09\Lambda$, $\Lambda = 3.75 \mu\text{m}$, $t_a = 1.5 \mu\text{m}$, $t_p = 1.80 \mu\text{m}$ and varied the Au and TiO_2 thickness respectively to get optimum t_g and t_t , and then at optimum t_g and t_t we characterise the sensor with SPR and LSPR.

6.1.3 Results and discussion

Starting with Au we vary the t_g to 20 nm, 30 nm and 40 nm and the obtained characteristics that are shown in Fig. 6.2(a–b). Comparing 20 nm and 30 nm we can see that the obtained CL for 20 nm is less than 30 nm. Though the AS is almost the same (2754 RIU⁻¹ for 20 nm and 2752 RIU⁻¹ for 30 nm), the WS for 30 nm is higher (15000 nm/RIU) than 20 nm (8000 nm/RIU). Therefore we choose 30 nm as optimum. Now, comparing 30 nm with 40 nm we see that the loss peak broaden at 40 nm thus the AS also reduces in a large scale as shown in Fig. 6.2(a–b). Thus considering the loss, WS and AS we consider 30 nm as the optimum Au thickness. Here the CL, WS, and AS are calculated using the equation $8.686 \frac{2\pi}{\lambda} \text{Im}(n_{\text{eff}}) \times 10^4$ (dB/cm); $\frac{\Delta\lambda_{\text{peak}}}{\Delta n_a}$ (nm/RIU) and $-\frac{1}{\alpha(\lambda, n_a)} \frac{\delta\alpha(\lambda, n_a)}{\delta n_a}$ (RIU⁻¹) (Islam *et al.* 2018i) respectively, where λ indicates the operating wavelength in microns, $\text{Im}(n_{\text{eff}})$ is the imaginary part of the complex RI of the core mode, $\Delta\lambda_{\text{peak}}$ denotes the wavelength difference between the loss peak shift and Δn_a indicates the change in analyte RI, $\alpha(\lambda, n_a)$ is the overall loss and the difference between two loss spectra due to a small change of analyte RI is denoted by $\delta\alpha(\lambda, n_a)$.

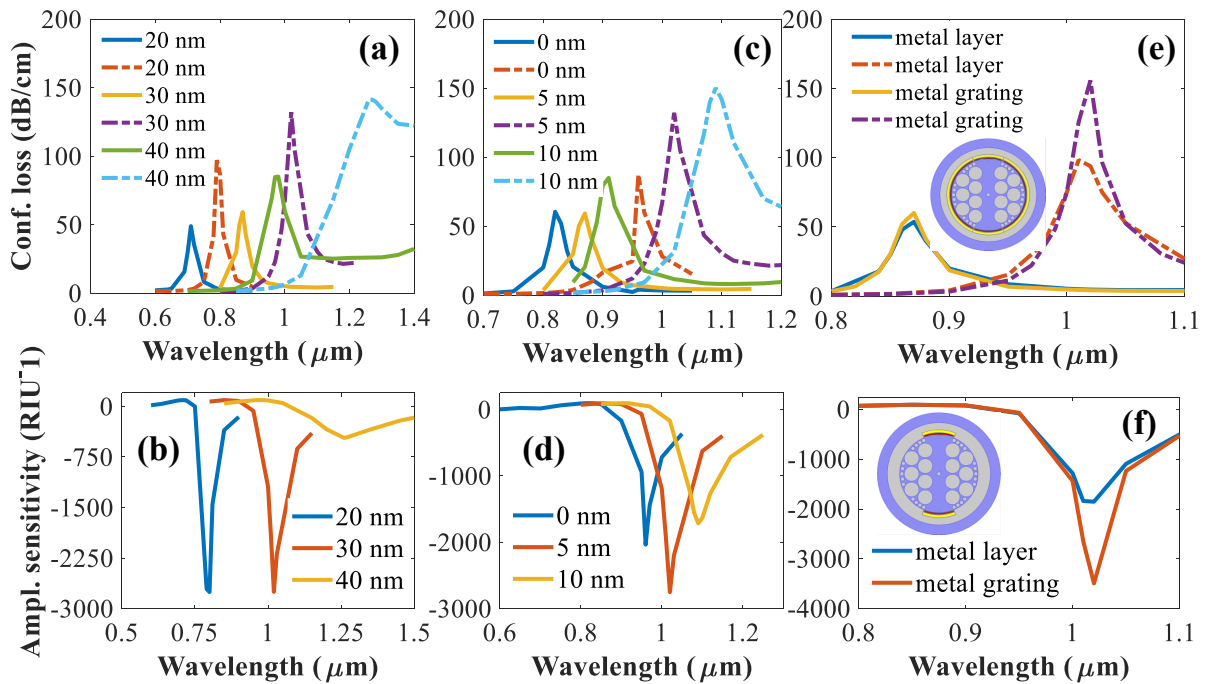


Figure 6.2. Loss and sensitivity for metallic thickness variation. (a–b) CL and AS with t_g variation; (c–d) CL and AS with t_t variation; and (e–f) CL and AS having SPR and LSPR, (Islam *et al.* 2019d).

6.1 Localized surface plasmon resonance biosensor

The optimization of TiO_2 is illustrated in Fig. 6.2(c–d). It indicates that without TiO_2 the CL is low, however that comes with low WS and AS because TiO_2 has a high RI and acts as a transition metal and when placed between SiO_2 and Au it generates large number of electrons at the surface. This creates a strong evanescent wave and attracts the fields from the core guided mode to interact strongly with the plasmonic mode and therefore increases CL, which also increases the sensitivity. Without the TiO_2 coating, the plasmonic Au exhibits poor adhesion to the SiO_2 , and easily flakes off with light pressure (Rifat *et al.* 2016). To provide proper adhesion, a thin layer of TiO_2 is included to provide the necessary adhesion. A 10 nm coating between the SiO_2 and the Au, increases the CL and broadens the loss peak. However, a slightly thinner layer (5 nm), is found to restore the sharp loss peak, required to achieve the high AS.

The reason for utilizing LSPR instead of SPR is shown in Fig. 6.2(e–f). We observe that with LSPR a sharper loss peak results in around 1.85 times larger AS than with SPR. In LSPR, excitation of surface electrons occurs over a small portion of surface that results in lowering the CL. This is because plasmons are only created in a localized area and not on the whole surface. Note that, this is also the reason for obtaining sharper loss peak as fields from the core can strongly interact with the specified portion of the surface. The corresponding WS and AS with LSPR and SPR are 14000 nm/RIU, 15000 nm/RIU and 3500 RIU^{-1} , 1900 RIU^{-1} respectively. Moreover, LSPR requires less Au and TiO_2 , which may result in improved cost effectiveness for real-world applications. Note that, in Figs. 6.2, 6.3, and 6.4 the solid and dashed lines indicates the performance for RI of 1.41 and 1.42 respectively.

Considering the LSPR at optimum Au and TiO_2 thickness we then optimize the analyte and PML. We start with the analyte layer and vary it to 1.2 μm , 1.5 μm , 1.8 μm and 2.1 μm . The characteristics shown in Fig. 6.3(a–b) illustrate that at low t_a , the sensor experiences low loss, however that comes with low AS (1350 RIU^{-1}). As t_a increases, the loss peaks begin sharpening and a sharper loss peak is obtained at $t_a = 1.8 \mu\text{m}$. Therefore, maximum AS (3500 RIU^{-1}) is obtained at that thickness. Increasing from 1.8 μm we can see that the AS starts to decrease. Therefore, considering the loss peak broadening and AS, we choose 1.8 μm as the optimum t_a . Then, keeping t_a fixed to 1.8 μm with other optimal design parameters we optimize the t_p . We can see that at $t_p = 1.50 \mu\text{m}$ the AS is low as compared to $t_p = 1.80 \mu\text{m}$ and 2.1 μm . However when

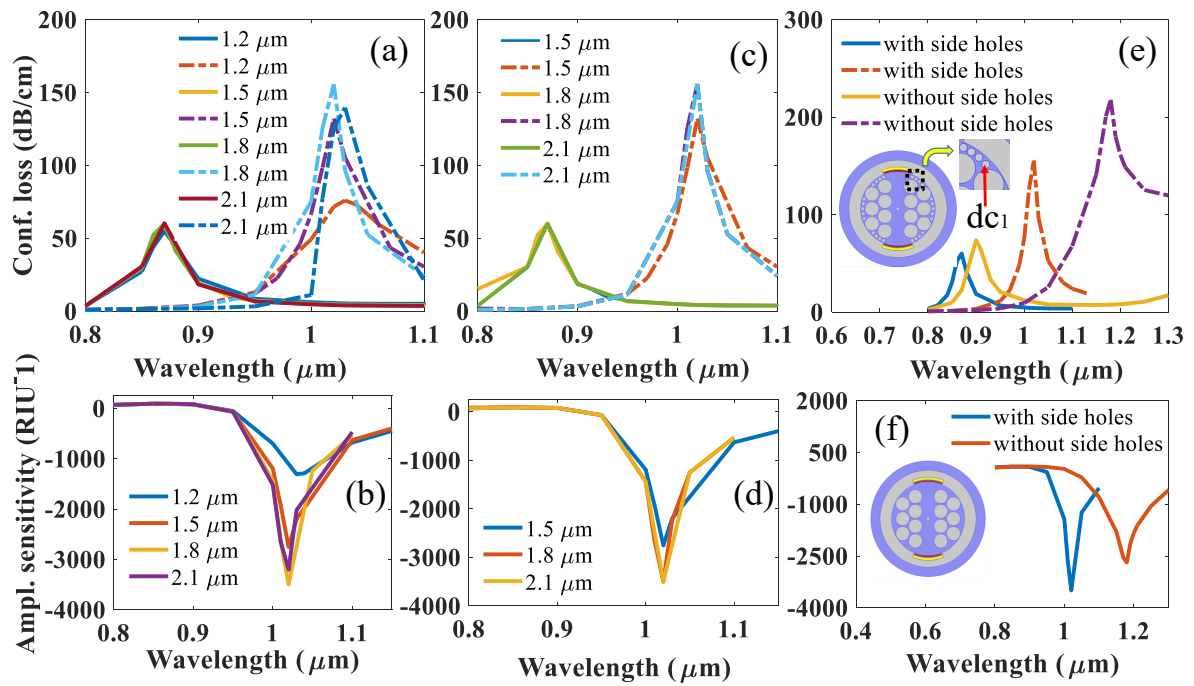


Figure 6.3. Loss and sensitivity for geometric optimization. (a–b) CL and AS having t_a variation; (c–d) CL and AS having t_p variation; and (e–f) CL and AS having side air holes near the surface, (Islam *et al.* 2019d).

we increase t_p to $1.80 \mu\text{m}$ the AS also increases and any further increase of PML does not change the characteristics of the fibre sensor. Therefore we choose $1.80 \mu\text{m}$ as the optimum PML thickness.

Until now we have optimized different geometrical parameters including selection between SPR and LSPR by considering few smaller shaped air holes of diameter $d_{c1} = d_c$ closest to the sensing surface as shown in Fig. 6.2(e–f) and Fig. 6.3(e). The reason for utilizing such small air holes is to help confine more light into the core and prevent light from being scattered out to the surface. We can see from Fig. 6.3(e–f) that with d_{c1} near the surface the sensor shows a remarkable AS with sharper loss peak. However, a number of holes close to the surface creates fabrication difficulties. The reason is, there is insufficient space near the surface to place the same sized capillary to produce the smaller air holes. One possible solution may be to use a smaller size capillary outer diameter. However, different sized holes during the fibre drawing process is problematic in terms of maintaining even pressure through all the holes. Considering this fact and in order to simplify the design, we remove d_{c1} and characterize the sensor. We find that, Fig. 6.3(e–f), removing d_{c1} reduces the sensing performance and increases the

6.1 Localized surface plasmon resonance biosensor

loss (AS reduces to 2850 RIU^{-1} from 3500 RIU^{-1}). However, considering feasibility of fabrication we choose the sensor without d_c as optimum, as shown inset of Fig. 6.3(f).

The analysis illustrated in Fig. 6.2 and Fig. 6.3 shows that the optimized sensor exhibits very high CL, which is a limitation in terms of practical implementations of the sensor because it also limits the sensor length. Note that, we place an air hole at the center of diameter $d_c = d_2 = 0.18\Lambda$ so that it can deflect the electromagnetic waves from the center towards the metal dielectric interface. The motivation is to enhance the light-matter interaction, however that comes with a high CL. We find that removal of d_c decreases the CL from 73 dB/cm to 16 dB/cm for an analyte RI 1.41 and from 218 dB/cm to 39 dB/cm for an analyte RI of 1.42. We find that the resulting change in WS and AS is almost negligible, as shown in Fig. 6.4(a–b). Therefore considering the CL we choose the sensor structure without d_c as optimum.

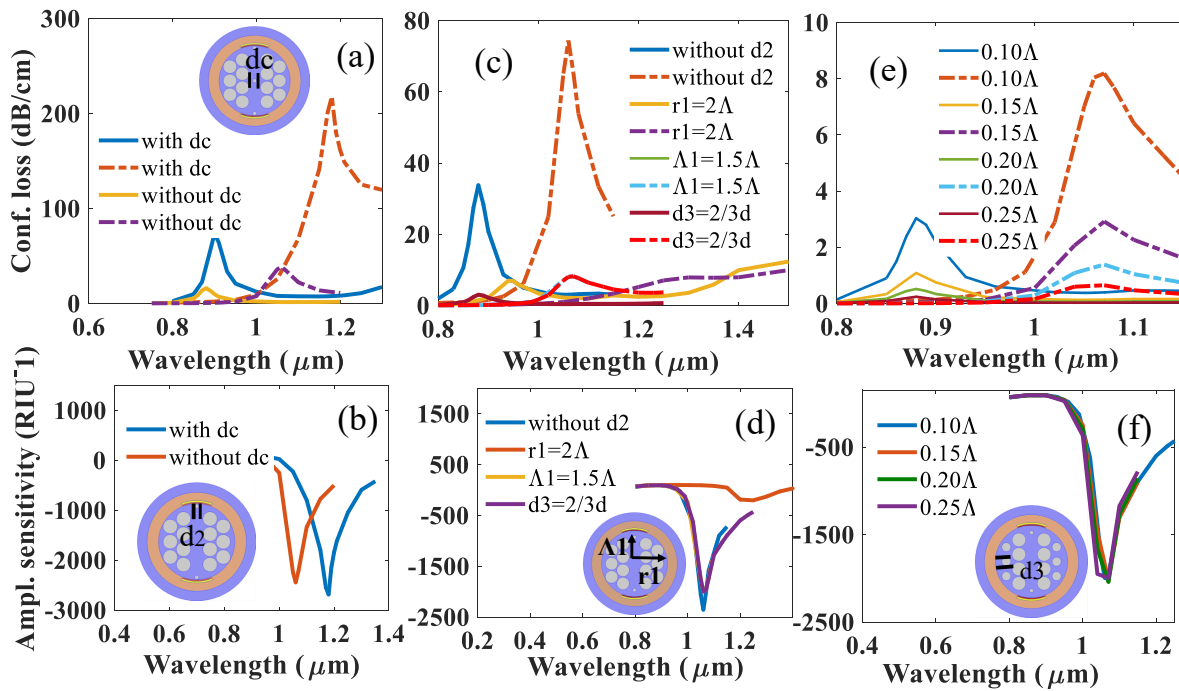


Figure 6.4. Loss and sensitivity for analyte variation. (a–b) CL and AS of the LSPR sensor with and without d_c ; (c–d) CL and AS having the effect of d_2 , the outer surface radius (r_1), the pitch Λ_1 and the air holes of diameter d_3 ; and (e–f) CL and AS having different size of d_2 , (Islam *et al.* 2019d).

The fabrication of the fibre shown in Fig. 6.4(b) is challenging because of the position of d_2 so close to the surface. It is impossible to place a capillary of size d_1 at the position

of d_2 and maintain the shape of the surface. Several solutions to these problems have been considered, including (i) removing d_2 , (ii) increasing the radius of outer surface r_1 and (iii) reducing the pitch distance Λ_1 of d_2 from center, or (iv) machining the surface of the silica preform after fabrication. We characterize the sensor considering all the possible solutions and the obtained characteristics are shown in Fig. 6.4(c–d). We started by removing d_2 and found that a high AS of 2360 RIU^{-1} can be obtained, but with a high CL of 34 dB/cm for 1.41 and 75 dB/cm for 1.42 than with d_2 . This is because without d_2 the electromagnetic waves from the center of the fibre interact directly with the plasmonic metal that assists in creating high sensitivity, however this comes at the price of large scattering that results in high CL. Therefore, it is important to limit the scattering of light and thus we decide to retain d_2 , but with optimized position so that loss can be reduced further maintaining sensitivity and fabrication feasibility.

Next, keeping d_2 in its previous position ($\Lambda_1 = 1.75\Lambda$) we then increased the radius of the outer surface (r_1) from where we find an extremely low AS of 122 RIU^{-1} with broadening of loss peak. Therefore without varying r_1 , we place d_2 in a position where capillaries of diameter d_1 can be used to create both hole sizes required for this design. As such we reduce the pitch, $\Lambda_1 = 1.5\Lambda$, of d_2 and maintain sufficient space from the surface to the air hole. Fabrication will use pressurization of the capillaries to achieve the desired size of d_2 . We can see the resulting characteristics, from Fig. 6.4(c–d), with extremely low CL, 3 dB/cm for 1.41 and 8 dB/cm for 1.42. The optimized sensor, shown in Fig. 6.4(d), also exhibits a high AS of 2050 RIU^{-1} and WS of 111000 nm/RIU .

However, in the present optimized structure there is another problem that is still challenging for fabrication. We can see that, as shown in the inset of Fig. 6.4(d), the air hole of diameter d_3 is still close to the surface that may also be a challenge for fabrication. Note that it is necessary to keep d_3 so that it can act as an obstacle for scattered light from the core and assist with tighter confinement at the center of the fibre. Considering the fabrication difficulties there are two possible solutions to facilitate fabrication. One is to increase (r_1) and the another is to reduce the diameter of d_3 and characterise the sensing performance. Previously we observed that increasing r_1 dramatically reduces the AS and therefore the only option now is to reduce d_3 . Reducing d_3 to $d_3 = 2/3d$ we can see that the CL, AS and WS has not change notably. The reason is the pitch

6.1 Localized surface plasmon resonance biosensor

distance between the air holes (d_1) in first ring of cladding. Note that, the reduced diameter for d_3 is still larger than the spacing between air holes of diameter d_1 . Therefore, d_3 are able to reflect back the scattered light inside the center of the fibre to maintain the performance with easier fabrication. Therefore, we choose $d_3 = 2/3d_1$ as optimum diameter in the second ring of the cladding.

Note that, the size of d_2 have also impact on CL and sensitivity therefore we also optimize it that is shown in Fig. 6.4(e–f). We found that, increasing size of d_2 decreases the CL however careful attention should also be given to choose optimum d_2 so that light wave get sufficient path to interact with the plasmonic metal at the surface. A larger diameter of d_2 act as an obstacle of interacting the light from the core with the portion of metal surface. Therefore, after a certain diameter of d_2 , with reduction of CL the WS and AS also start to reduce and loss peak starts to get broad again. Thus, considering both CL, WS and AS we choose $d_2 = 0.20\Lambda$ as optimum.

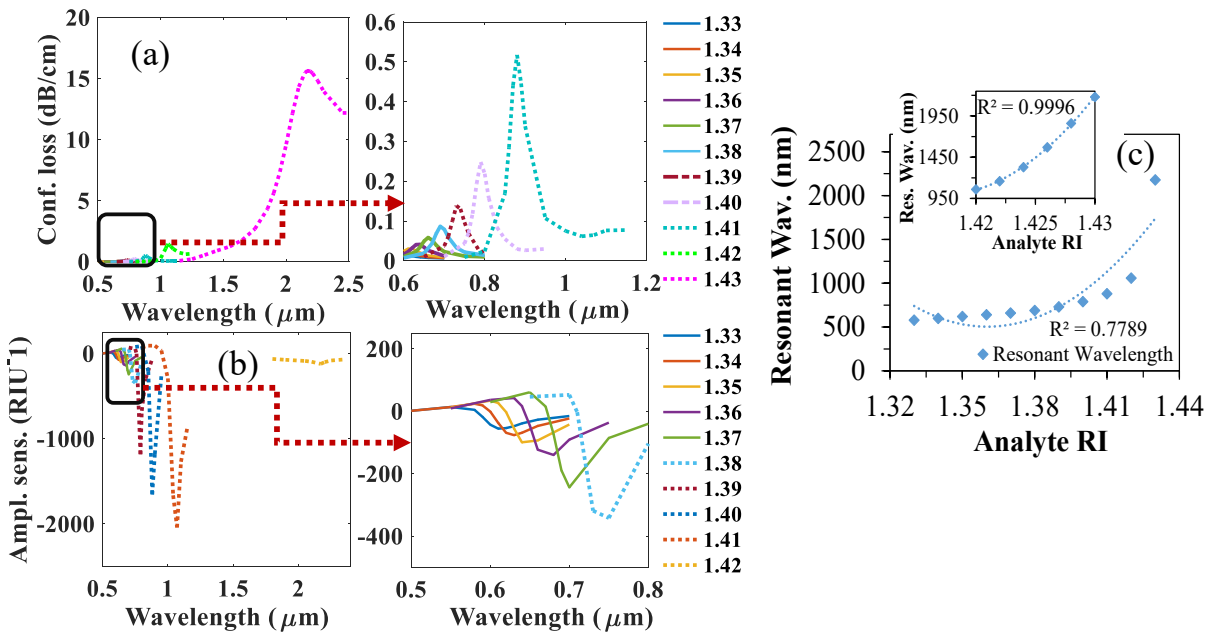


Figure 6.5. Sensing performance of the optimized LSPR bisensor. (a) CL, (b) AS and (c) fibre linearity having optimized geometrical parameters of the sensor (Islam *et al.* 2019d).

The CL and sensitivity experienced by the sensor with changing of RI is shown in Fig. 6.5(a–b). It can be seen from Fig. 6.5(a–b) that the sensor is highly sensitive with the change of environment RI that also comes with negligible CL. The losses at resonance peaks for analyte RI 1.33 to 1.43 are found to be 0.02, 0.024, 0.03, 0.041, 0.058,

0.087, 0.14, 0.25, 0.52, 1.43, and 15.63 dB/cm, see Fig. 6.5(a), which are extremely low with corresponding resonance peak wavelengths of 580, 600, 620, 640, 660, 690, 730, 790, 880, 1060, and 2180 nm. Note that, the increment of CL with RI is due to lower penetration of electromagnetic field towards the core and higher penetration towards the LSPR region. Therefore according to the resonance peak shift we obtain a record WS of 111000 nm/RIU moreover having sharp resonance peak the sensor also attains a record AS of 2050 RIU⁻¹. To the best of our knowledge the obtained WS and AS is maximum with minimum CL in the literature of biosensing. Also note that, we characterized the sensor for an analyte RI from 1.33 to 1.43, one of the reason is most of the biochemical and biomedical analytes varies within the RI range of 1.33 to 1.43 (Aray *et al.* 2016a, Yetisen *et al.* 2016). Moreover, we can see from Fig. 6.5(a) that the loss peak broadens for analyte RI of 1.43 that leads to low amplitude sensitivity of around 120 RIU⁻¹, Fig. 6.5(b). Therefore we characterise the sensor for an RI of upto 1.43 because further increase may lead to false detection of analytes due to such broadening of the loss peak.

The proposed sensor shows the full-width-half-maximum (FWHM) values are 130, 82, 71, 63, 55, 52, 47, 48, 59 and 138 for analyte RI of 1.33 to 1.42 respectively. With the increase of analyte RI, resonance peak becomes sharper however, after a certain RI loss spectra start broadening. Moreover, the linearity of the proposed sensor upto RI of 1.43 is $R^2 = 0.7789$ however a more linear characteristics $R^2 = 0.9662$ is obtained upto RI of 1.42, Fig. 6.5(c). In addition, the linearity between 1.42 and 1.43 also shown in inset Fig. 6.5(c) where the obtained R^2 is 0.9996.

The sensor length is an important consideration that varies in proportion to CL. Accordingly, for an analyte RI from 1.33 to 1.43 the proposed sensor shows a high sensor length of 217, 181, 145, 106, 75, 50, 31, 17, 8, 3, and 0.27 cm respectively. Note that high sensor length is suitable for practical sensing.

The sensor resolution and LOD are also two important factors in biosensing which control the extent to which the sensor can precisely detect small changes in sizes and nearby RI (Paul and Biswas 2018, White and Fan 2008). Considering $\lambda_{\min} = 0.1$ nm, according to WS the maximum resolution of the sensor goes upto 9×10^{-7} RIU. Therefore the sensor can detect a tiny change of environmental RI variation that is of the

6.1 Localized surface plasmon resonance biosensor

order of 10^{-7} . Moreover, based on the obtained maximum resolution the maximum LOD of the sensor is 8.12×10^{-12} RIU²/nm that are best in the literature of biosensing.

In summary, here we show a low loss, highly sensitive LSPR-PCF based sensor for SERS response intensification in the visible to mid-IR spectrum. We demonstrated the way how we obtained a sensor design with optimized geometrical parameters. Our study shows, the sensor can attain a record WS and AS of 111000 nm/RIU and 2050 RIU⁻¹ with maximum sensor resolution and LOD of 9×10^{-7} RIU and 8.12×10^{-12} RIU²/nm respectively. As shown in Fig. 6.1(b) the proposed sensor can be made using capillary stacking and open new possibilities for highly sensitive and precise detection of bioanalytes.

6.2 A hi-bi ultra-sensitive SPR fibre sensor

In this section, a simple, miniature, and highly sensitive photonic crystal fibre (PCF) based surface plasmon resonance (SPR) sensor is proposed. The target analyte and the plasmonic material are at the outer surface of the fibre making practical applications feasible. A 30 nm gold (Au) layer supports surface plasmons. A thin titanium dioxide (TiO₂) layer is used to assist adhesion of Au on the glass fibre. The fibre cross section is formed purely by circular-shaped holes simplifying the preform manufacturing process. A high birefringence (hi-bi) fibre is obtained by means of an array of air holes at the center of the fibre. A Finite Element Method (FEM) is employed to analyse the surface plasmon properties of the proposed PCF-SPR sensor. By optimizing the geometric parameters, a maximum wavelength sensitivity (WS) of 25,000 nm/RIU and an amplitude sensitivity (AS) of 1,411 RIU⁻¹ for a dielectric refractive index (RI) range of 1.33–1.38 is obtained. Moreover, an estimated maximum resolution of 4×10^{-6} and Figure of Merit (FOM) of 502 is obtained that ensures high detection accuracy of small RI changes. Owing to its sensitivity and simple architecture, the proposed sensor has potential application in a range of sensing application including biosensing.

6.2.1 Introduction

Surface plasmon resonance (SPR) is a phenomenon that occurs when the frequency of incoming photons match the frequency of surface electrons. A slight change in surrounding RI potentially changes the effective RI experienced by the surface plasmon polariton (SPP) mode causing a shift of resonance wavelength and the unknown dielectric can be detected by observing the resonance peak shift. Note that the exploitation of SPR is advantageous for optical sensing because of its effectiveness, real-time detection and convenient operation (Homola *et al.* 1999, Carrascosa *et al.* 2014). Notably, SPR technology is promising for applications in food safety, security, medical testing, biomolecular analyte detection, and medical diagnostics (Carrascosa *et al.* 2014, Lee *et al.* 2009).

In recent years, SPR modes supported by PCF have gained significant attention due to (i) the freedom to adjust optical parameters, by design, through the geometry of the structure, (ii) light weight, and (iii) controllable birefringence, making it ideal for a range of sensing applications (Islam *et al.* 2017a, Islam *et al.* 2018j, Dash and Jha 2016,

Dash and Das 2018, Dash *et al.* 2018, Dash and Jha 2015). Various optical fibre based RI sensing methods have been reported in the literature that include fibre Bragg grating (FBGs) (Iadicicco *et al.* 2005, Chryssis *et al.* 2005, Osório *et al.* 2017), long period fibre gratings (LPFGs) (Patrick *et al.* 1998), and modal interferometers (Zhou *et al.* 2015) etc. Chryssis *et al.* (2005) reported a RI sensor with an etched FBG, while in order to increase the sensitivity to environmental RI's the same etching process can also be applied to LPFGs (Patrick *et al.* 1998). Modal interferometers using tapered single mode fibre and based on core diameter mismatch provide new sensing opportunities (Zhou *et al.* 2015, Zibaii *et al.* 2010). However, most of the reported sensors provide low sensitivity (Tien *et al.* 2018).

With the development of nanotechnology, several ways of improving the sensing performance of conventional SPR sensing techniques have emerged. One of the key strategies is the use of gold or silver nano particles with a diameter in the range of several tens nanometers or smaller where free electrons are trapped on a nanoparticle surface (Zeng *et al.* 2017). Under proper optical excitation these free electrons can oscillate collectively, and this results in localized SPR (LSPR). Note that, like SPR, LSPR is also sensitive to the change in the localized dielectric medium (Lopez *et al.* 2017). However, in addition to metallic nanoparticles recent advancements have shown other choices for sensitivity enhancement. The choices are quantum dots (QDs), graphene, hydrogel, magnetic and silicon nanoparticles and in most of the cases the sensitivity enhancement can be carried out using analyte enrichment. Recent reports show that plasmonic nanostructured arrays can also be used as a technique to improve the sensing performance (Jiang *et al.* 2018, Chau *et al.* 2017).

Utilizing the properties of PCF and different plasmonic materials, research has been carried out for SPR sensing. Generally, there are two types of SPR sensing approaches; (i) internal sensing and (ii) external sensing. In the internal sensing approach, the metal coating and dielectric fluid are placed inside the fibre. For example, this can be achieved by selectively filling air holes with the dielectric liquid to be analyzed. Using this internal sensing approach Shuai *et al.* (2012) designed a sensor with multi-analyte coating fibre and achieved a maximum negative sensitivity of $-5,500$ nm/RIU. Later, Xue *et al.* (2013) proposed a Au coated fibre where the dielectric and metallic channel

were considered inside the surface. Moreover, Gao *et al.* (2014a) proposed a TiO₂ coating based fibre that also fails to improve the sensing performance. Recently, Rifat *et al.* (2018) improved the sensitivity using the internal sensing approach. However, fabrication of this PCF is difficult due to (i) the need for internal metal coating and (ii) the requirement for filling the small air holes with the target dielectric (Rifat *et al.* 2017). Moreover, refilling and emptying of selected air holes is quite difficult and time consuming and thus the internal sensing approach is not feasible for real-time sensing (Luan *et al.* 2015).

Note that a PCF with a D-shaped structure provides a possible solution to internal sensing as the metallic and dielectric channels can be placed on the flat surface of the fibre and in direct contact with the external medium. A numerical study of D-shaped structure shows that the flat surface achieves high sensitivity (Rifat *et al.* 2016, Haque *et al.* 2018, Haque *et al.* 2019). A numerical study on dual sided polished fibre is also reported (Liu *et al.* 2018b). An experimental study on a side-polished structure shows a high wavelength sensitivity of 21,700 nm/RIU with the RI range of 1.33 to 1.34. Although the cleaning of a D-shaped PCF is advantageous for refilling with the dielectric liquid, the standard surface polishing and etching of particular parts of a micro-structured PCF are challenging in practice (Dash and Jha 2015, Rifat *et al.* 2016).

Considering the limitations of the internal sensing mechanism and sensing with a side polished PCF, external sensing is attractive as an approach for practical applications. In an external sensing, the dielectric fluid is placed in contact with the outer metallic layer of the PCF, that facilitates the cleaning and re-use of the fibre sensor with subsequent dielectrics. Therefore, considering external sensing, Dash and Jha (2014) proposed a graphene-coated fibre and achieved a maximum WS and AS of 5,000 nm/RIU and 860 RIU⁻¹ respectively. For further improvement, we propose a rectangular core gold coated SPR sensor that can achieve improved sensing performance, however achieving a rectangular shaped core is inconvenient for fabrication (Islam *et al.* 2018i). A spiral-shaped PCF has also been proposed but failed to improve the sensing performance (Hasan *et al.* 2017). Liu *et al.* (2018c) proposed a gold-coated fibre that achieves a maximum WS of 15,180 nm/RIU, however, due to large loss peak broadening they obtained a low AS of 498 RIU⁻¹.

In this section, we show a highly birefringent PCF-SPR sensor where the detection of unknown dielectrics can be carried out externally. The aim is to achieve improved WS and AS with high sensor resolution, long sensor length and high FOM. The simplicity in design enables a fabrication feasible PCF that opens the opportunity to commercial utilization of the sensor.

6.2.2 Modelling and theoretical analysis of the sensor

The modelling and numerical analysis is carried out using commercially available software COMSOL 5.3a where the *Wave Optics* module with the *Electromagnetic Waves, Frequency Domain* (EWFD) solver is used to investigate the guided response. The *Physics Controlled Mesh* sequence with *Extremely Fine* element size were used to obtain the best accuracy in numerical simulations where the structure subdivides into 229,042 number of elements with minimum element quality of 0.7081, average element quality of 0.9618, element area ratio of 4.274×10^{-4} , and mesh area of $116 \mu\text{m}^2$. For meshing the Au layer we use the *resolve wave in lossy media* function of COMSOL where Au is meshed in free space with a maximum mesh element size and that ensures simulation accuracy. The mesh characteristics of the Au layer are as follows, the number of vertices = 16,332, number of elements = 27,220, maximum element size = $0.122 \mu\text{m}$, minimum element quality = 0.8537, Average element quality = 0.951, and mesh area = $0.6715 \mu\text{m}^2$. Note that, the proposed model converged with the defined mesh property.

We use silica (SiO_2) glass as the bulk material whose RI profile can be obtained from the Sellmeier equation (Malitson 1965),

$$n = \sqrt{1 + \frac{0.696\lambda^2}{\lambda^2 - 0.0047} + \frac{0.408\lambda^2}{\lambda^2 - 0.014} + \frac{0.897\lambda^2}{\lambda^2 - 97.934}} \quad (6.1)$$

where λ in micron stands for the wavelength of light. Note that, Eqn. 6.1 is valid for the wavelength region of 0.22 to $3.71 \mu\text{m}$ (Malitson 1965). At the center of the SiO_2 fibre an array of air holes of diameter d_c are used. The function of these air holes is to deflect the electromagnetic (EM) wave from the center towards the metal so that a strong plasmonic effect can be created. These also helps to create birefringence via an asymmetry required for maintaining the polarization modes. Although it is possible to create birefringence using a rectangular or an elliptical shaped air hole in the core, this is at the cost of increased fabrication complexity.

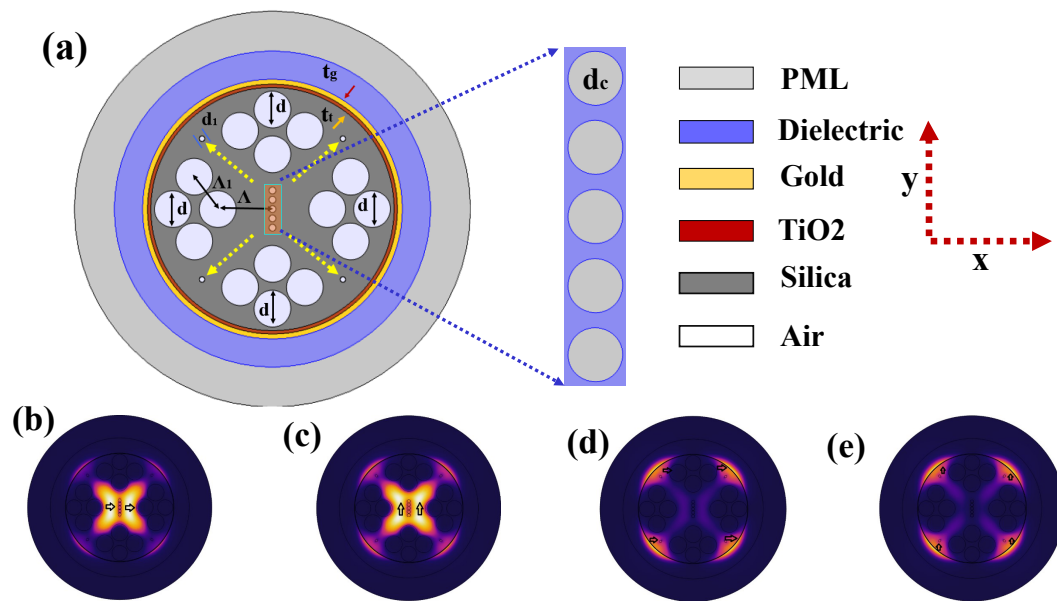


Figure 6.6. Schematic cross section and propagation modes of the Hi-Bi sensor. (a) Schematic cross section with an enlarged view of the core where the yellow arrows indicate the direction of coupling of the core mode with the plasmonic mode; the optical field distribution at fundamental core mode (b) x -pol., (c) y -pol., and SPP mode at (d) x -pol., (e) y -pol. at a dielectric RI of 1.36 with resonance wavelength of $0.77 \mu\text{m}$ for x -pol. and $0.79 \mu\text{m}$ for y -pol. (Islam *et al.* 2019b).

The cladding is based on circular shaped air holes of diameters d , and d_1 . Arrangement of air holes having diameter d is carried out in such a way so that these can force the EM field to interact strongly with the metal. This facilitates a strong plasmonic effect in the created interaction channels—the created channels with the help of air holes of diameter d are shown by dotted yellow arrows in Fig. 6.6(a). Here, four air holes of diameter d_1 are also placed on the way of the interaction channels that helps to reduce the confinement loss (CL) significantly. The E-field distribution of the proposed PCF-SPR for both x and y polarization is shown in Fig. 6.6(b–e). It can be observed that light is well confined in the core for both the polarization and interacts strongly with the plasmonic mode. The strong plasmonic property is an indication of achieving high WS and AS.

In contrast to previously reported PCFs (Dash and Jha 2014, Hasan *et al.* 2017, Liu *et al.* 2018c) highlighted in Tab. 6.2, the proposed sensor is novel in the sense that it creates birefringence by creating asymmetry at the center of the fibre, creates four distinct channels for light interaction with the plasmonic metal, uses an additional layer (TiO_2)

to support Au and improves the sensing performance over a large scale.

There are several materials such as gold (Au), silver (Ag), aluminium (Al), copper (Cu), indium tin oxide (ITO), and titanium nitride (TiN) that can be used to support surface plasmons in the optical frequency range. Among them, Au and Ag are widely used because of their relatively low loss in the visible to near-infrared (West *et al.* 2010). The Ag gives rise to a sharper resonance peak compared to Au, however, when placed in a humid environment it becomes oxidized and this reduces the analyte detection accuracy (Rifat *et al.* 2015). On the other hand, Au is chemically stable, bio-compatible, and gives rise to a larger shift in the resonance wavelength. However, for very thin Au layers it experiences island growth and may flake off from the glass fibre. The material dispersion of gold can be characterized by the Drude-Lorentz model (Vial *et al.* 2005),

$$\varepsilon_m = \varepsilon_\infty - \frac{\omega_D^2}{\omega(\omega + j\gamma_D)} + \frac{\Delta_\varepsilon \cdot \Omega_L^2}{(\omega^2 - \Omega_L^2) - j\Gamma_L \omega} \quad (6.2)$$

where $\varepsilon_\infty = 5.9673$, $\Delta_\varepsilon = 1.09$ denotes the permittivity and the weighting vector respectively, ω represents the angular frequency, ω_D is defined as the plasma frequency and γ_D represents the damping frequency, where $\omega_D/2\pi = 2113.6$ THz, and $\gamma_D/2\pi = 15.92$ THz. Moreover, Ω_L and Γ_L indicate the frequency and spectral width of the Lorentz oscillator where $\Omega_L/2\pi = 650.07$ THz and $\Gamma_L/2\pi = 104.86$ THz (Vial *et al.* 2005).

To solve the adhesion problem of Au, a thin TiO₂ layer that has high RI having the features of non-toxicity and environmental compatibility is frequently used in between Au and glass. The deposition of TiO₂ thin film also increases the surface plasmonic excitation that generate enhanced evanescent field. These create enhanced interaction of surface plasmons with its contacting dielectric, improves the sensitivity. This is because the TiO₂ has a high refractive index than the fibre itself. Therefore when a thin film of TiO₂ is placed on the glass surface it strongly attract the field from the core guided mode and strong coupling is created between the core guided and the plasmonic mode (Tien *et al.* 2018, Rifat *et al.* 2016). Note that, there are multiple anisotropic microcrystallite rutile and sphalerite phases of TiO₂, with very high refractive index, and an amorphous phase with varying degrees of density (Kischkat *et al.* 2012). Both the phases have different refractive index profiles that must be considered during an experiment. However, as this is a simulation study, we therefore use a generalized

form of isotropic TiO_2 whose refractive index profile can be obtained from the following equation (DeVore 1951),

$$n_t = \sqrt{5.913 + \frac{2.441 \times 10^7}{\lambda^2 - 0.803 \times 10^7}} \quad (6.3)$$

where, n_t denotes the RI of TiO_2 and λ is in Angstroms.

At the Au surface we consider a dielectric layer where an analyte of particular refractive index (n_a) can be placed. Note that we consider the dielectric layer in contact with the outer surface so that filling and cleaning of analytes can be carried out easily. As this is a simulation study therefore the Au surface is not functionalized hence the surrounding of the sensor is homogeneous and has the refractive index of n_a . Therefore, the thickness of dielectric layer does not have any impact on the sensing performance, however, for simulation purposes we consider a constant dielectric thickness of $2.0 \mu\text{m}$. As surface plasmons are extremely sensitive to the change of environmental RI, changes in local RI on the plasmonic metal surface can be determined by observing the changes of resonance wavelength, phase or intensity (Špačková *et al.* 2016). We vary the dielectric RI on the surface and observe the sensing performance. Note that this method of considering the analyte layer and method of calculating the sensitivity follows the standard approach in a number of references (Lee *et al.* 2009, Dash and Jha 2015, Iadicicco *et al.* 2005, Lopez *et al.* 2017, Rifat *et al.* 2018, Rifat *et al.* 2016, Liu *et al.* 2018b, Hasan *et al.* 2017, Aray *et al.* 2016b, Ding *et al.* 2017, Jiao *et al.* 2018, Luan *et al.* 2015, Chu *et al.* 2018, Liu *et al.* 2018b).

A mathematical boundary condition, ie. a perfectly matched layer (PML), which by definition absorbs any energy that might be radiated, is added at the outer surface of the computational region. Note that there is no physical existence of the PML in practice, however, convenient to use in order to make the computation region finite (Shin and Fan 2012). The optical properties of the PML are similar to the dielectric and therefore PML thickness also has no impact on the overall sensing performance. However, for simulation purposes we consider a PML thickness similar to the dielectric thickness.

The proposed sensor is feasible for fabrication as it contains only circular shaped air holes. The different size of air holes can be realized using the standard stack-and-draw

6.2 A hi-bi ultra-sensitive SPR fibre sensor

method (Amouzad Mahdiraji *et al.* 2014, Russell 2003). Drilling in the preform stage is also a possible route to create the holes and fabricate the fibre (Kostecki *et al.* 2012). The thin Au and TiO₂ layer can be achieved using chemical vapor deposition (CVD), high-pressure microfluidic chemical deposition and wheel polishing methods (Zhang *et al.* 2007).

The performance evaluation of the sensor is carried out using the resonance peak shift of the CL spectra that can be obtained from the following equation (Dash *et al.* 2018, Du *et al.* 2012),

$$\alpha_{\text{loss}} = 8.686 \times \frac{2\pi}{\lambda} \times \text{Im}(n_{\text{eff}}) \times 10^4, \text{ dB/cm} \quad (6.4)$$

where λ indicate the operating wavelength in microns, and $\text{Im}(n_{\text{eff}})$ represents the imaginary part of the complex RI of the core guided mode.

The sensitivity of a sensor can be determined using both the wavelength and amplitude interrogation technique. According to the wavelength interrogation method the WS of a sensor can be calculated by (Akowuah *et al.* 2012)

$$S_W(\lambda) = \frac{\Delta\lambda_{\text{peak}}}{\Delta n_a}, \quad (6.5)$$

where, $\Delta\lambda_{\text{peak}}$ denotes the wavelength difference between the loss peak shift and Δn_a indicates the change in dielectric RI.

The other sensing measurement method known as amplitude sensitivity that can be determined using the amplitude interrogation method (Gauvreau *et al.* 2007),

$$S_A(\lambda) = -\frac{1}{\alpha(\lambda, n_a)} \frac{\delta\alpha(\lambda, n_a)}{\delta n_a} \quad (6.6)$$

where $\alpha(\lambda, n_a)$ is the overall loss where the dielectric RI is equal to n_a , $\delta\alpha(\lambda, n_a)$ represents the difference between two consecutive loss spectra due to a change of dielectric RI, and δn_a indicates the change in dielectric RI.

Besides the high sensitivity of a sensor, the the length of the metal covered fibre is also an important property. Considering the input power launched into the fibre is P_0 , the detected power at the output can be obtained by the following expression (Dash and Jha 2016)

$$P(L, \lambda, n_a) = P_0 e^{-\alpha(\lambda, n_a)L} \quad (6.7)$$

where $\alpha(\lambda, n_a)$ is the attenuation constant and can be defined by Eqn. 6.7, L indicates the sensing length that can be defined by

$$L = \frac{1}{\alpha(\lambda, n_a)}. \quad (6.8)$$

The goal of this work is to propose a fibre design based solely on circular holes and whose metal layers are in the external interface of the waveguide. The fibre also needs to be highly birefringent in order to allow the transmitted signal to keep its linear polarization state along all fibre length. Denoting n_x and n_y the effective refractive indices of x and y polarization, the birefringence can be calculated as

$$B = n_x - n_y. \quad (6.9)$$

Sensor resolution that depends on the WS/AS determines the degree of dielectric RI detection. It can be determined by the following equation (Hautakorpi *et al.* 2008),

$$R = \frac{\Delta n_a \Delta \lambda_{\min}}{\Delta \lambda_{\text{peak}}} \quad (6.10)$$

where, Δn_a represents a change in dielectric RI, $\Delta \lambda_{\min}$ defines the estimated minimum wavelength resolution, and $\Delta \lambda_{\text{peak}}$ determines the difference in resonance peak shift.

6.2.3 Sensor performance analysis

The performance analysis of the proposed sensor is carried out by optimizing different geometrical parameters that include Au film thickness t_g , TiO₂ film thickness t_t , air hole diameters d and d_1 , and number of core air holes n_c .

Optimization of film thickness

Our simulations focused on the visible to near infra-red region and the sensor performance was evaluated from 0.5 to 1.2 μm . Initially we tuned the geometrical parameters of the PCF and obtained an improved sensing performance with $d_c = 0.125\Lambda$, $d = 0.67\Lambda$, $d_1 = 0.09\Lambda$, $\Lambda = 1.65 \mu\text{m}$, $\Lambda_1 = 1.16 \mu\text{m}$, $n_c = 5$, $t_g = 30 \text{ nm}$, and t_t

6.2 A hi-bi ultra-sensitive SPR fibre sensor

= 5 nm. However, to show the performance variation with different parameter we first vary the t_t thickness while keeping the other parameters constant. The effect is shown in Fig. 6.7(a–b), where it can be seen that without TiO_2 the CL is relatively low, however, the WS and AS are also low. As the t_t increases the CL also increases and resonance peak shifts towards longer wavelengths. For $t_t = 10$ nm the CL is higher than $t_t = 0$ nm and $t_t = 5$ nm, moreover the loss peak broadens that results a low AS than experienced with $t_t = 5$ nm. Therefore, considering the loss peak broadening, WS and AS we choose $t_t = 5$ nm as optimum.

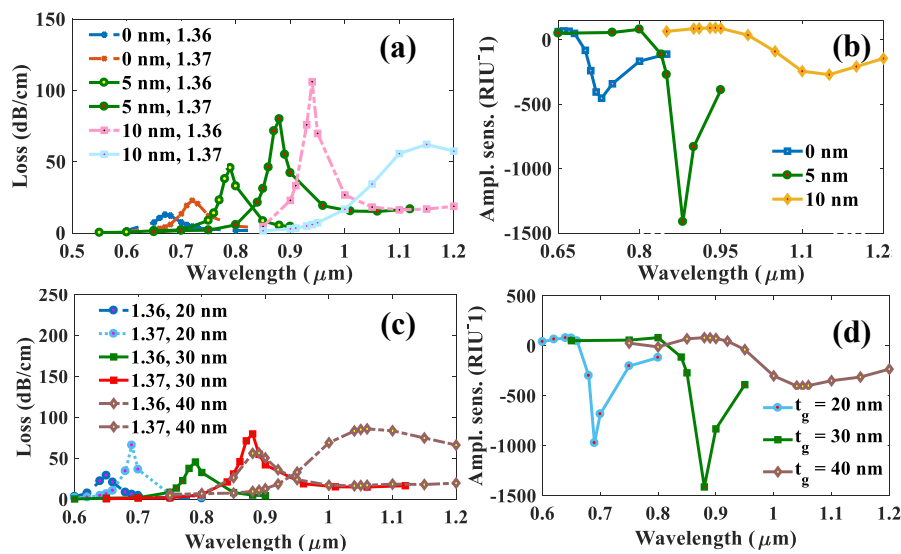


Figure 6.7. Optimizing the plasmonic materials of the sensor. CL, for RI of 1.36 and 1.37, and AS (for 1.36), for the variation of TiO_2 thickness where t_g kept fixed at 30 nm (a-b); and for the variation of Au thickness where t_t kept fixed at 5 nm (c-d), (Islam *et al.* 2019b).

It is well known that the Au film thickness t_g has a sharp impact on the CL, resonance peak shift and sensing performance of a fibre SPR sensor. Therefore, to investigate the effect of Au on the sensing performance we varied t_g and kept other parameters constant. The performance of the sensor with t_g variation is shown in Fig. 6.7(c–d) which indicate that increasing t_g increases the CL and shifts the resonance peak towards longer wavelengths by means of broadening the loss peak, Fig. 6.7(c). Using $t_g = 40$ nm drastically reduces the AS Fig. 6.7(d) and induces a high loss reducing the maximum length of the fibre that could be metal coated—this is not desirable for a practical implementation. For $t_g = 20$ nm, the CL is low, however, that comes with a lower AS (970 RIU^{-1}) than $t_g = 30$ nm ($1,412 \text{ RIU}^{-1}$). Moreover, the WS at $t_g = 30$ nm

is greater (9,000, nm/RIU) than $t_g = 20$ nm (4,000, nm/RIU). Therefore, we consider 30 nm as optimum Au thickness.

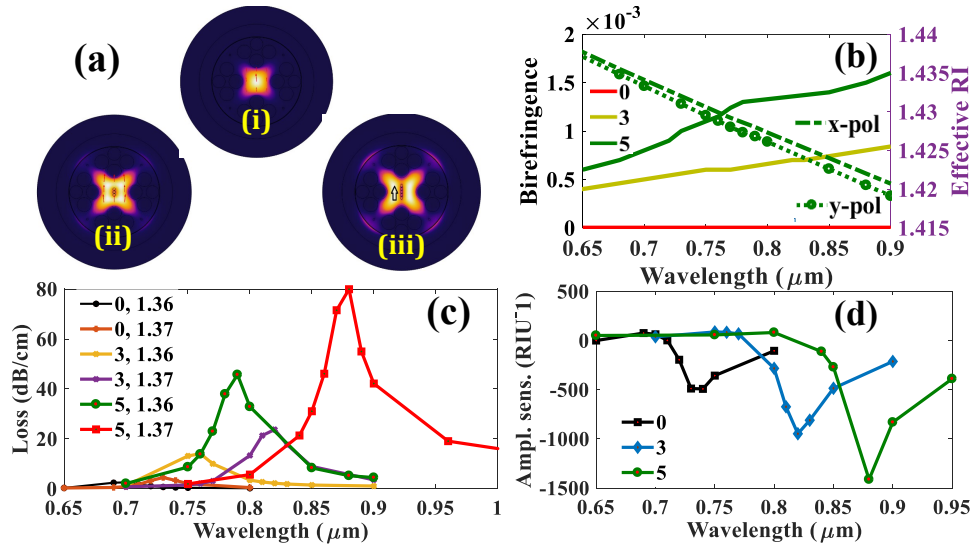


Figure 6.8. Optical field distribution at fundamental core mode. (i) solid core where $n_c = 0$, (ii) changing $n_c = 3$, and (iii) $n_c = 5$ (a); birefringence having $n_c = 0, 3, 5$, and effective RI of x and y -pol for an analyte RI of 1.36 (b), CL for an analyte RI of 1.36 and 1.37 (c), and AS for an analyte RI of 1.36 (d), having $n_c = 0, 3$, and 5, (Islam *et al.* 2019b).

Effect of core air holes on birefringence and sensing performance

The number of air holes in the core (n_c) has significant impact on the CL and overall sensitivity of the PCF-SPR sensor. Therefore, we observe the effect of solid core as well as core with different number of air holes. At optimized TiO_2 and Au thickness ($t_t = 5$ nm and $t_g = 30$ nm) with other constant values, the obtained electric field distribution having solid core, core with three air holes and core with five air holes is shown in Fig. 6.8(a). It is observable that the EM field within a solid core has low interaction with the surface whereas maximum interaction is obtained with a core possessing five air holes. It can be seen that, with solid core, the sensor experiences negligible CL, Fig. 6.8(c), however, that comes with low sensitivity, Fig. 6.8(d) and undesirable close to zero birefringence, Fig. 6.8(b). Note that birefringence is an important property of a fibre based plasmonic sensor as it will lead to a differential sensitivity between x - and y -polarized signals. More importantly, the input signal launched on the fibre axis will keep its polarization state along the fibre (Dash and Jha 2014, Liu *et al.* 2018c, Dash and Jha 2016).

6.2 A hi-bi ultra-sensitive SPR fibre sensor

Moreover, a birefringent fibre is required for signal detection. This is based on launching polarized broadband light in one of the fibre polarization axes while detecting the transmitted signal in a fibre spectrometer. By characterizing the wavelength and amplitude shift of the transmitted spectrum, and using previously measured data, the RI of the fluid that baths the fibre can be characterized.

With $n_c = 3$ we can see that the sensitivity increases over that of a solid core, however, maximum WS and AS with high birefringence is obtained having $n_c = 5$. Therefore, we consider $n_c = 5$ as optimum of our designed sensor. We can see the fibre birefringence increases with the wavelength. This behaviour is related with the fact that longer wavelengths spread more within the fibre cross section being more influenced by the asymmetric holes distribution. Note that, we also investigate the sensor performance at $n_c = 1$, however, we do not consider that as optimum because it creates zero birefringence with low sensitivity.

Note that the coupling between the fibre core mode and the plasmonic mode depends on the polarization of optical signal that reaches the coated region of the fibre. The device response can be analysed with the help of Fig. 6.10(a–d) where it can be noted the phase-matching wavelength and coupling strength (in practical terms, the induced loss) depend on the polarizing state of the guided mode (x or y direction). To obtain a sensing device with a reproducible and predictable response this phase matching should be as independent as possible of external spurious influences as fibre bending, temperature variations etc. The use of a single mode hi-bi fibre helps to address this issue. In our proposed design we reached such situation with a microstructured optical fibre whose cross section is formed just by circular holes, turning its fabrication feasible via the well-known stacking-and-draw technique (Russell 2003) or by directly drilling the holes on the fibre preform stage (Kostecki *et al.* 2012).

Our fibre is, in practical terms, single mode as the first higher order mode presents a CL that is 1.37 times bigger than the fundamental core mode. The fibre is also highly birefringence ($B \sim 10^{-3}$) when we add the central holes in the core area—see Fig. 6.8(b). This means that any linearly polarized light that is launched on the x or y axis of the fibre will keep this polarization stage along the fibre length, independently of external mechanical and thermal perturbations the fibre may suffer. By choosing between

launching the input signal in the y or x axes we can select between improving the fibre sensitivity (y -axis) or reducing the loss (x -axis) what can lead to longer metal coated sections.

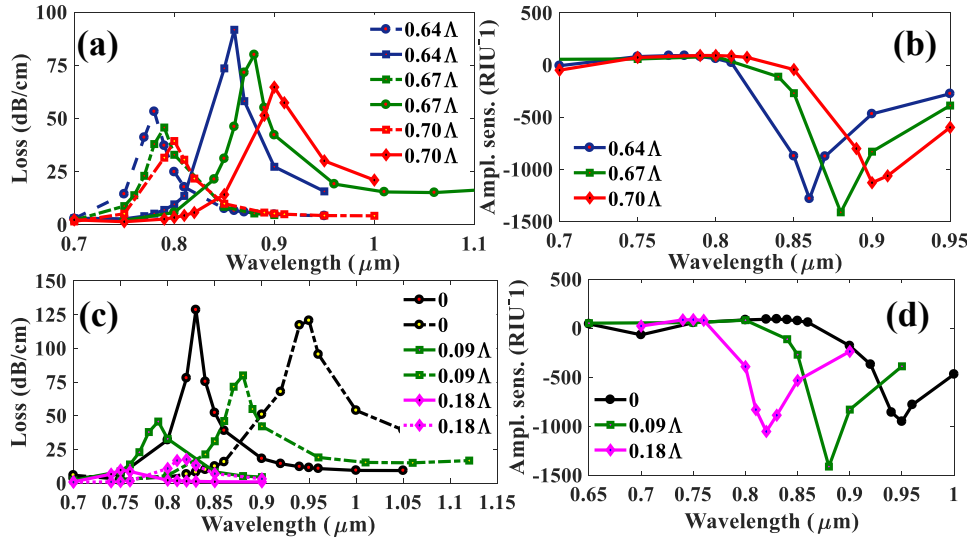


Figure 6.9. Confinement loss and amplitude sensitivity. CL having RI's of 1.36 (dashed line), 1.37 (solid line) and AS (1.36) on the variation of d , (a-b); and CL having RI's of 1.36 (solid line), 1.37 (dashed line) and AS (1.36) on the variation of d_1 , (c-d), (Islam *et al.* 2019b).

Effect of cladding air holes d and d_1

The effect of cladding air holes of diameter d is shown in Fig. 6.9(a) and Fig. 6.9(b). We can see that, higher CL is obtained at $d = 0.64\Lambda$ and lower AS is obtained at $d = 0.70\Lambda$. However, moderate CL and highest sensitivity are obtained at 0.67Λ therefore we choose 0.67Λ as optimum for d .

The air holes d_1 at four corners have also significant impact on CL and overall sensing performance of the sensor. Therefore we investigated the performance of the sensor with and without d_1 that is shown in Fig. 6.9(c-d). It can be seen that without d_1 the sensor experiences a high CL that also comes with a low wavelength and AS as compared to the fibre having d_1 . This is because, without d_1 the EM fields from the core scattered largely towards the metal therefore creates high CL with loss peak broadening, however, placing air holes at four corners limits scattering and therefore reduce the loss. Hence we decided to keep air holes at four corners, however, with optimized diameter. Note that, we cannot make $d_1 = d$ because that will prevent the EM fields

6.2 A hi-bi ultra-sensitive SPR fibre sensor

dielectric RI	Peak wavelength (nm)		Amplitude sensitivity (RIU ⁻¹)		Wavelength sensitivity (nm/RIU)		Figure of merit (FOM)	
	x-pol	y-pol	x-pol	y-pol	x-pol	y-pol	x-pol	y-pol
1.33	670	670	242	242	2,000	3,000	42	64
1.34	690	700	398	455	4,000	4,000	89	90
1.35	730	740	631	826	4,000	5,000	91	104
1.36	770	790	1311	1412	8,000	9,000	182	178
1.37	850	880	837	404	16,100	25,000	319	502
1.38	1011	1120	N/A	N/A	N/A	N/A	N/A	N/A

Table 6.1. Performance analysis of the proposed sensor. The wavelength sensitivity, the amplitude sensitivity, and the FOM is analysed over analyte RI variation.

from passing through and interacting with the metal to create an evanescent wave. Therefore we varied d_1 and found $d_1 = 0.18\Lambda$ shows low CL, however, $d_1 = 0.09\Lambda$ shows improved sensing performance. Therefore, we choose $d_1 = 0.09\Lambda$ as the optimum diameter of the corner air holes.

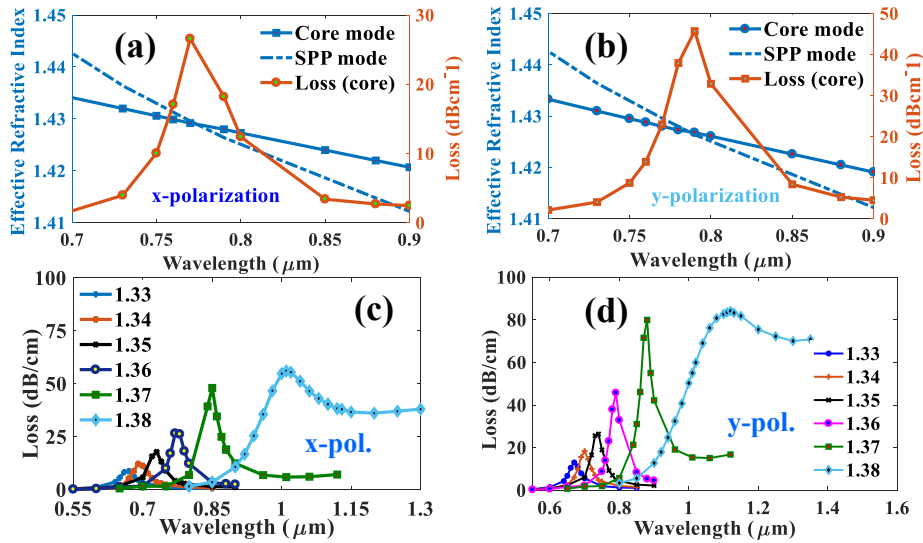


Figure 6.10. The wavelength dependent dispersion relation of the proposed sensor at fundamental core mode, SPP mode and loss spectra for an dielectric RI $n_a = 1.36$, at (a) x-pol, (b) y pol.; CL at optimized geometrical parameters including the metal thickness for (c) x-pol., and (d) y-pol, (Islam *et al.* 2019b).

Dispersion relation and optimized sensor performance

The dispersion relation of the proposed sensor for a dielectric RI of 1.36 is shown in Fig. 6.10(a–b). It can be seen that at the RI matching point of the core mode and SPP

Ref.	Sensing Approach	RI Range	B = B _x -B _y	Amp. Sens.(RIU ⁻¹)	Max. Wavel. Sens. (nm/RIU)	Sensor Resolution	FOM
(Haque <i>et al.</i> 2018)	External (side polished)	1.18–1.36	-	1,054	20,000	5×10^{-6}	-
(Haque <i>et al.</i> 2019)	External (side polished)	1.22–1.37	-	1,872	51,000	1.96×10^{-6}	566
(Dash and Jha 2014)	External	1.33–1.37	-	860	5,000	4×10^{-5}	-
(Hasan <i>et al.</i> 2017)	External	1.33–1.38	-	420.4	4,600	2.17×10^{-5}	-
(Liu <i>et al.</i> 2018c)	External	1.40–1.43	-	498	15,180	5.68×10^{-6}	-
This Thesis	External	1.33–1.38	1.6×10^{-3}	1,411	25,000	4×10^{-6}	502

Table 6.2. Comparison of performance of the proposed sensor with prior sensors. The sensing approach, birefringence, sensitivity, sensor resolution, and FOM are considered as performance measurement metrics.

mode the CL reaches to its maximum. The higher loss is obtained at y -polarization than the loss in x -polarization as high penetration of electric field from the core towards the dielectric occurs at y -polarization.

Fig. 6.10(c–d) show the peak shift of absorption loss for a range of dielectric RI. Here, all the performance evaluation of the sensor is based on change of effective refractive index of the core guided mode. From Fig. 6.10(c) we can see that the loss peaks are obtained at 670, 690, 730, 770, 850, and 1,011 nm where the wavelength differences are 20, 40, 40, 80, and 161 nm respectively for dielectric RI range of 1.33–1.38. Similarly for the y -polarization, according to Fig. 6.10(d) the wavelength differences are 30, 40, 50, 90, and 250 nm respectively.

In this study we focused on the refractive index range around water (1.33 to 1.37) due its possible application in real time analysis of samples with biological interest. The waveguide geometrical parameters and the metals thickness were optimized to this range as well. There are a number of biological agents and chemical solutions that have refractive index within the specified range (1.33-1.38) (for example, ethanol = 1.361, acetone = 1.36, 10% glucose solution in water = 1.3477, 20% glucose solution in water = 1.3635, liver (human) = 1.369, intestinal mucosa (human) = 1.329-1.338) etc that the proposed sensor can detect. Note that the reported RI range is very similar to

6.2 A hi-bi ultra-sensitive SPR fibre sensor

previously reported SPR sensors (Dash and Jha 2014, Liu *et al.* 2018c, Aray *et al.* 2016b, Luan *et al.* 2015). However, instead of using the name of dielectrics we used the relative refractive indices in order to generalize the discussion.

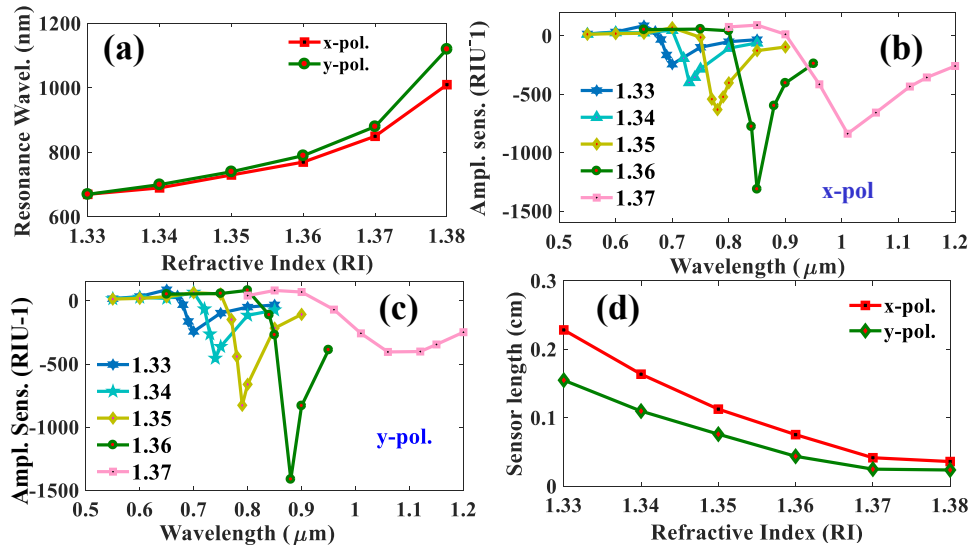


Figure 6.11. Relationship between the resonance wavelength with refractive indices. Resonance wavelength vs dielectric RI (a); AS for x -pol (b); AS for y -pol (c); and Sensing length (d), having $n_a = 1.33$ – 1.38 and for both x and y polarization mode, Islam *et al.* (2019b).

According to the wavelength interrogation method mentioned in Eqn. 6.5 the obtained WS's for the x polarization are 2,000, 4,000, 4,000, 8,000 and 16,000 nm/RIU while for the y -polarization the sensitivities are 3,000, 4,000, 5,000, 9,000 and 25,000 nm/RIU for RI range of 1.33–1.37 respectively. In Fig. 6.11(a), we further show the change of resonance wavelength by means of dielectric RI from where the wavelength sensitivity can easily be calculated for x - and y - polarized signals.

Apart from WS, the sensing performance is also carried out using the amplitude interrogation (AI) method as mentioned in Eqn. 6.6. Note that, obtaining an AS is less complex than WS as it does not require spectrum monitoring, whereas dielectric detection is carried out for a particular wavelength (Gauvreau *et al.* 2007). Fig. 6.11(b–c) show the AS of the proposed sensor for both x and y polarization. We can see that with the increase of dielectric RI the AS increases upto $n_a = 1.36$ and then starts to decrease. This is because, a sharp loss peak is obtained up to $n_a = 1.37$ that then starts broadening thus the AS also begins to decrease.

The sensing length with different dielectric RI variation is shown in Fig. 6.11(d) that is derived from Eqn. 6.11. It indicates that as the dielectric RI increases the sensing length decreases because the length of a sensor is totally dependent on the absorption loss. According to the observation of Fig. 6.11(d) we can conclude that sensing length of a few millimetres to a centimetre can be used to detect dielectrics over a useful range of refractive indices.

According to Eqn. 6.10, for a best-case estimate considering $\Delta\lambda_{\min} = 0.1 \text{ nm}$, the proposed sensor shows high wavelength sensing resolution of 6.21×10^{-6} in the x polarization and 4×10^{-6} in the y polarization. Therefore, the proposed sensor can in principle detect a tiny change in RI of the order of 10^{-6} .

Another important metric known as the FOM characterizes the overall performance of a sensor that can be defined as a ratio of sensitivity to full width at half maximum (FWHM) ($\text{FOM} = S_{\lambda} \text{ (nm/RIU) / FWHM (nm)}$) (Liu *et al.* 2018b, Srivastava *et al.* 2013). A high performance sensor can be realized when the sensitivity increase and FWHM decrease. The FOM for different dielectrics of the proposed sensor is shown in Tab. 6.1 from where we can see that a maximum FOM of 319 is obtained for x -polarization and 502 is obtained for y -polarization. Note that, a larger FOM means a better detection limit (Liu *et al.* 2018b).

The performance evaluation based on WS, AS and FOM with changing dielectric RI is shown in Tab. 6.1. It can be seen that, maximum AS of 1,311 and 1,412 RIU^{-1} , maximum WS of 16,100 and 25,000 nm/RIU , and maximum FOM of 319 and 502 are obtained for the x and y polarizations respectively. A detail performance analysis of the proposed sensor with the prior sensors that use external sensing approach is carried out and shown in Tab. 6.2. Comparing with the purely external (not side polished) sensing approach based sensors it can be seen that the proposed sensor shows improved performance in consideration to wavelength sensitivity, AS, birefringence, sensor resolution and FOM.

In this section, a simple Au-TiO₂ based PCF-SPR sensor is analysed. Based on optimized structural parameters, the polarization sensitive sensor shows a relatively high AS of 1,411 RIU^{-1} and WS of 25,000 nm/RIU with high degree of detection limit. The

6.2 A hi-bi ultra-sensitive SPR fibre sensor

fibre design is also highly birefringent what potentially improves the sensing performance. Moreover, the sensor attains a high FOM that indicates the high overall sensing performance. The practical utilization of the sensor is simple as it utilizes an external sensing approach with only circular shaped air holes. The long length of the sensor is another attractive feature that in addition with suitable surface functionalisation makes the proposed sensor promising for biosensing applications.

6.3 An exposed core localized SPR biosensor

Here we characterize an exposed core photonic crystal fibre (PCF) for biosensing applications. Surface plasmons are excited within gold (Au) strips and titanium dioxide (TiO₂) is employed to support adhesion of Au with glass. In consideration of ease of fabrication, only four air holes are used to simplify the sensor structure. Simulation results show an improved wavelength and amplitude sensitivity of 34,000 nm/RIU and 1,170 RIU⁻¹ respectively that comes with a low confinement loss (CL) of 0.79 dB/cm. Results also indicate a low full width at half maximum (FWHM) that contributes to high figure of merit (FOM) of 310.

6.3.1 Introduction

Sensors based on localized surface plasmon resonance (LSPR) are in increasing demand as they are cost effective, easy-to-use and portable point-of-care diagnostics platforms that require small sample volume and real time response. Surface plasmons were first introduced with prism coupling for gas detection and biosensing applications (Liedberg *et al.* 1983). Surface plasmons are surface charges generated when the electromagnetic (EM) field is confined and propagates along the interface between a metal and dielectric. This propagation of light along a metal-dielectric interface excites the metal surface electrons to initiate oscillation—creating a surface plasmon wave (SPW) (Zhao *et al.* 2014). Surface plasmons are extremely sensitive to the environment therefore a tiny change in environmental refractive index (RI) potentially shifts the resonance of the SPP mode and an unknown dielectric of different RI can be detected by observing the resonance peak shift in the response. Note that prism-coupled SPR sensors are widely used but are bulky in size thus limiting the range of application (Gupta and Verma 2009).

Among biosensing devices, PCF based optical sensors are considered advantageous because of their properties leading to light weight, single mode guidance of light, design flexibility, immunity to electromagnetic interference, and controllable birefringence (Lopez *et al.* 2017, Otupiri *et al.* 2015). Among the plasmonic sensors, LSPR sensors are regarded as a novel counterpart of the well established surface plasmon resonance (SPR) sensors, as the LSPR sensing area can be strongly confined to the size

6.3 An exposed core localized SPR biosensor

of the structure that supports it, which can potentially improve the sensing performance. In LSPR, the SP excitation takes place in metal particles or strips where their size is smaller than the wavelength of light. Devices based on LSPR are advantageous because of their effectiveness, strong optical confinement, local field enhancement and real-time detection (Gao *et al.* 2014b, Homola *et al.* 1999, Carrascosa *et al.* 2014, Dash and Jha 2014, Islam *et al.* 2019d).

Since the emergence of fibre SPR sensors (Jorgenson and Yee 1993), experimental studies based on standard fibres were carried out to demonstrate SPR phenomena in biological sensing applications. Different types of fibres including multimode (Zhang *et al.* 2017), single mode (Coelho *et al.* 2015), microstructured (Wu *et al.* 2017), twin core (Liu *et al.* 2015), tapered coreless fibre (Ding *et al.* 2017), and fibres with doped core (Jha and Badenes 2009) have been investigated. Note that, multimode fibres have relatively large core diameter providing efficient optical coupling as compared to that of single mode fibre. However, the large number of propagation modes in a multimode fibre requires phase matching. The twin core fibre, tapered coreless fibre and doped core fibre add additional complexity in fabrication. Therefore, it is necessary to consider fibres that can achieve improved sensing performance over the standard fibres with ease of fabrication (Jorgenson and Yee 1993, Zhang *et al.* 2017, Coelho *et al.* 2015, Wu *et al.* 2017, Liu *et al.* 2015, Ding *et al.* 2017, Jha and Badenes 2009). Holey fibres show the potential of improved sensing performance with low transmission loss however the design must consider fabrication feasibility (Islam *et al.* 2018e, Islam *et al.* 2018i, Islam *et al.* 2019d). For applications such as low loss transmission, interferometric based sensing, and different order of harmonic generation (Wu *et al.* 2017, Azman *et al.* 2019, Hu and Ho 2017, Warren-Smith *et al.* 2019, Li *et al.* 2018b), several experimental studies have already been carried out that have enhanced the possibility of utilizing the holey fibres for plasmonic sensing applications.

Considering the merits of optical fibre, recently we reported an optical sensor in the visible to mid-infrared range (Islam *et al.* 2018e, Islam *et al.* 2018i, Islam *et al.* 2019b). By using gold (Au) as the plasmonic metal we obtained a high sensitivity however that comes with high CL. Moreover, due to the use of a large number of different sized air holes the fabrication is challenging. Using a similar sensing approach different sensor structures were also proposed (Liu *et al.* 2018c) however they failed to improve the

sensing performance and presented additional complexity for fabrication. A different type of SPR sensor also known as a D-shaped PCF is also reported for sensing applications, however, there are practical difficulties in polishing the surface in order to obtain the D-shape (Liu *et al.* 2018b). An internal sensing mechanism has been reported for PCFs, however, filling them with the analyte and cleaning for re-use present practical difficulties (Rifat *et al.* 2018). Here, internal sensing refers to filling PCF air holes with the analyte solution—this can be carried out via a syringe (ie. withdrawal or pumping mode)—whereas external sensing refers to contacting the analyte to the fibre surface.

However, it has been necessary to eliminate thick cladding layers from these fibres (Islam *et al.* 2018e, Islam *et al.* 2018i, Islam *et al.* 2019b, Liu *et al.* 2018c, Liu *et al.* 2018b, Rifat *et al.* 2018) to allow fields to interact directly through evanescent waves arising from the core/cladding boundary region, resulting in a loss of mechanical strength. As a solution, LSPR based sensors were introduced to enhance the sensing performance as well as minimizing the size and cost (Paul and Biswas 2018, Chen *et al.* 2019). The use of metallic nano-spheres and nano-gratings shows an improvement in wavelength sensitivity (WS) however that comes with low amplitude sensitivity (AS) and high CL (Islam *et al.* 2019b, Paul and Biswas 2018, Chen *et al.* 2019). Recently, we show that the use of plasmonic metal strips at the surface of the fibre shows potential for sensing applications (Islam *et al.* 2019d). However, there is scope to develop an improved theoretical framework for PCF based biosensors that may eventually lead to ease of fabrication and practical implementations in both the medical and chemical industries.

In this section, we show a simple PCF–LSPR sensor that contains only four air holes to complete the structure. Plasmons are created using metal strips at the outer surface. The design goal is to achieve a simple, fabrication feasible sensor with high sensing performance and low loss.

6.3.2 Geometric structure and numerical modelling of the proposed PCF-LSPR sensor

The 3D view of the proposed sensor is shown in Fig. 6.12. The modelling and numerical analysis are carried out using finite element method based software COMSOL 5.4. *Electromagnetic Waves, Frequency Domain* (EWFD) solver with *extremely fine* element size

6.3 An exposed core localized SPR biosensor

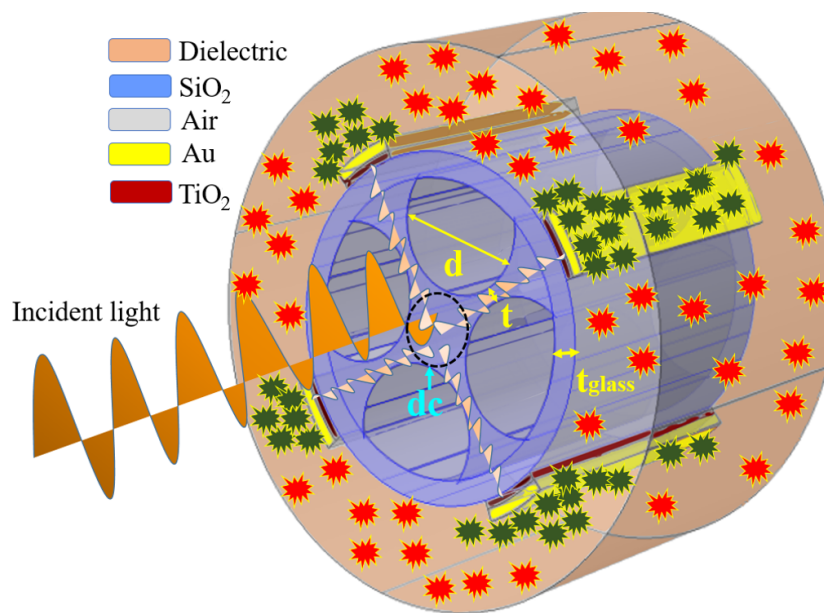


Figure 6.12. 3D view of the proposed sensor where light impinges at the center of the fibre. Here d_c is the core diameter; the magenta and yellow strips at the outer surface indicate TiO_2 and Au layers and the molecules indicated in green and red at the dielectric layer indicate bound and free molecules respectively; where the Au can be functionalized to bind to target molecules, (Islam *et al.* 2019c).

is used to obtain improved element quality. The average element quality achieved with *extremely fine* element type is 0.89 whereas for *extra fine*, *finer* and *normal* element types the element qualities are 0.85, 0.84 and 0.83 respectively. These provide the simulation accuracy of the analysis carried out for the proposed sensor. To form the cladding, four non-touching air holes (d) are used where the core d_c is exposed in all directions. This arrangement makes the electromagnetic (EM) field of the core to travel towards the plasmonic metal to form necessary plasmons for sensing. Here, instead of using a large number of air holes we used only four air holes arranged in a way so that they can reduce the CL and improve the sensing performance. Note that, the CL can be reduced by making the air holes close to each other however EM fields from the core need sufficient space to move towards the metal surface.

Note that, instead of using a continuous metallic layer at the glass surface we use metal gratings, which help localize the plasmons (Islam *et al.* 2019d). The metal strips are $2.7 \mu\text{m}$ in width while the gap between strips is $10 \mu\text{m}$. At the metal surface we use dielectrics with different RI. Greater specificity to a particular analyte can be achieved via metal surface functionalization. When an axial ray propagates down the fibre it

creates EM fields and at the same time excites the metal surface electrons. The functionalized metal then attracts the targeted molecules/proteins and the resonance peak shift can then be observed via an optical spectrum. In order to make the computational region finite an anisotropic perfectly matched layer (PML) boundary condition is used with similar optical characteristics to the contacting dielectric. Note that, as the PML is a boundary condition for the purpose of simulation, the thickness of this layer is not physically relevant. We choose the PML thickness similar to the dielectric layer thickness.

Fabrication of the metal coated exposed core fibre can be carried out in a few steps. First of all, the four air holes can be created by drilling a fused silica rods using an ultrasonic mill. The preform can then be stretched using a drawing tower to form the inner structure of the final preform before drawing the fibre (Schartner *et al.* 2017, Kostecki *et al.* 2012). The thin Au and TiO₂ layer can be achieved using chemical vapor deposition (CVD), high-pressure microfluidic chemical deposition and wheel polishing methods (Zhang *et al.* 2007).

The conceptual diagram, in Fig. 6.12, shows incident light impinging at the center of the fibre and exciting electrons at the Au surface, thereby creating plasmons. At the dielectric surface the magenta molecules represent those in solution whereas the molecules represented in green are bound to the Au surface.

6.3.3 Performance analysis of the proposed sensor

The dispersion relation of the core mode and SPP mode is shown in Fig. 6.13, where we see that at the phase matching point resonance occurs, which satisfies the theoretical conditions for surface plasmon resonance. Inset of Fig. 6.13 also shows the EM field distribution from where it can be seen that the light is well confined in the core region, which results in low loss. It can also be seen that strong plasmonic interactions occur at the metal dielectric interface, which enhances the detection strength of surrounding environmental changes. Here, note that the proposed sensor creates four distinct channels to guide EM field towards the gold plasmonic strips. The inset of Fig. 6.13 shows the strong field confinement at the metal strips. This indicates a strong plasmonic effect created at the interface between the gold and the dielectric. Note that, a similar

6.3 An exposed core localized SPR biosensor

approach in creating plasmons has been reported (Rifat *et al.* 2016, Haque *et al.* 2019, Tien *et al.* 2018).

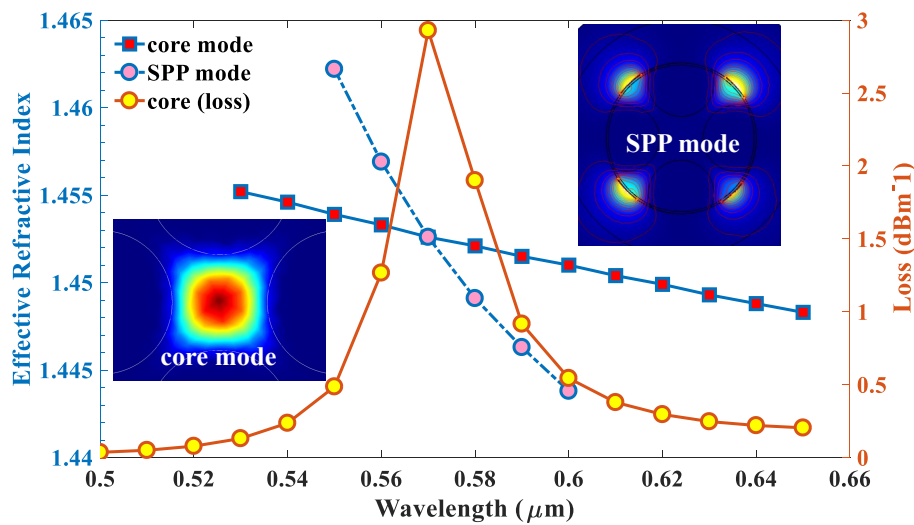


Figure 6.13. Dispersion relation of the core mode, SPP mode and loss spectra. Dispersion relation of the core mode, SPP mode and loss spectra of core mode for dielectric RI of 1.33, where insets shows EM field confinement at core and SPP region, (Islam *et al.* 2019c).

At the initial stage of parameter optimization we consider cladding air hole diameter $d = 3.30 \mu\text{m}$ that relates to core diameter (d_c) and the distance between cladding air holes (t), TiO_2 thickness $t_t = 5 \text{ nm}$, dielectric layer thickness of $2 \mu\text{m}$ and vary the Au thickness to 20, 30 and 40 nm for a dielectric RI of 1.33 and 1.34. We observe that a change in t_g changes the CL, WS, AS and the resonance peak shift.

In Fig. 6.14(a–b), it is determined that as the Au thickness increases the resonance peak shifts towards longer wavelengths. The wavelength sensitivities obtained for $n_a = 1.33$ having t_g at 20, 30 and 40 nm are 1,000, 2,000 and 2,000 nm/RIU respectively however the amplitude sensitivities are 172, 210 and 175 RIU^{-1} , also shown in Tab. 6.3. For an Au thickness of 40 nm we find that the loss peak broadens, thus increasing the FWHM whilst reducing the FOM. This leads to false detection of analytes (Islam *et al.* 2018i). Therefore, considering the WS, AS and loss peak broadening we select 30 nm as optimum Au thickness.

Using TiO_2 thickness of 0, 5 and 10 nm we find that the CL, AS and WS is improved for $t_t = 0 \text{ nm}$ as shown in Fig. 6.14(c–d), Tab. 6.3. However, as mentioned previously

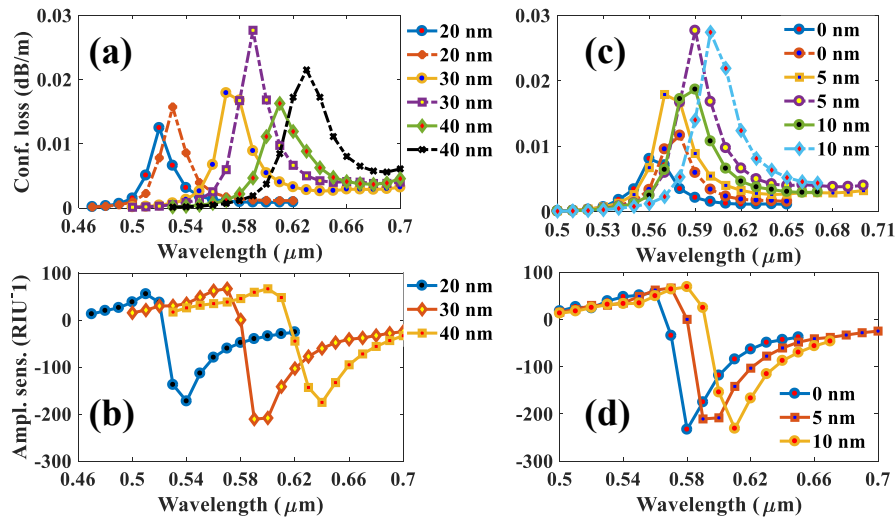


Figure 6.14. Optimization of geometric parameters. Optimization of Au thickness t_g (a–b); TiO₂ thickness t_t (c–d), considering the dielectric RI of 1.33 (solid line) and 1.34 (dashed line), (Islam *et al.* 2019c).

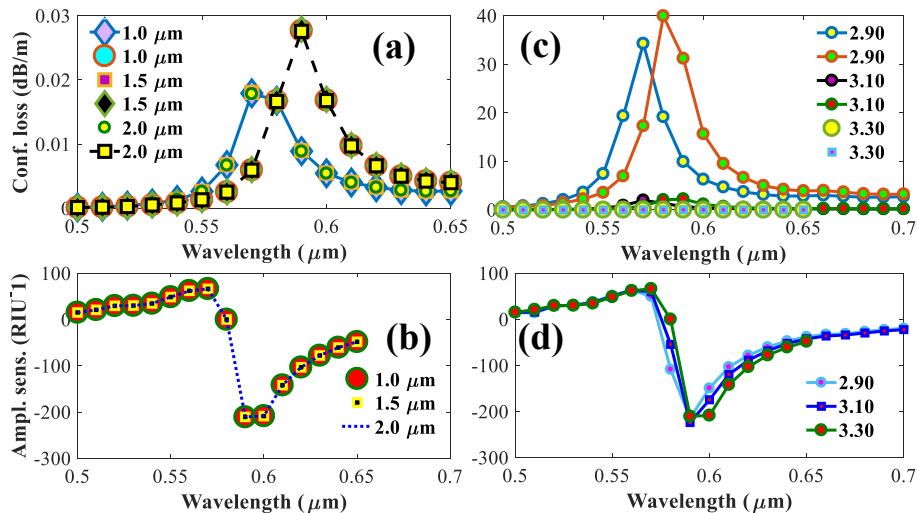


Figure 6.15. Loss and sensitivity regarding outer dielectric. (a–b) Confinement loss and amplitude sensitivity by varying the dielectric layer thickness and, and (c–d) confinement loss and amplitude sensitivity by varying the cladding air hole diameter d considering dielectric RI $n_a = 1.33$ and 1.34, (Islam *et al.* 2019c).

6.3 An exposed core localized SPR biosensor

without TiO₂ the plasmonic metal Au may flake off from the glass fibre and therefore it is important to consider a thin layer of TiO₂. For $t_t = 10$ nm we find that the CL is higher and broader. This is because of the high RI of TiO₂ with increased thickness. Therefore considering the loss and peak broadening we select a thin TiO₂ layer of 5 nm between the Au and glass.

The dielectric layer thickness is also varied to 1.0, 1.5 and 2.0 μm to determine any change in sensing performance; Fig. 6.15(a–b), Tab. 6.3. We find that there is no change in loss and sensing performance therefore the dielectric thickness has no impact on the overall sensing performance. The targeted dielectric optical properties are the same for any dielectric thickness and therefore change of dielectric thickness does not impact on overall sensing performance. However, for purposes of the simulation we assume 2.0 μm as the dielectric thickness.

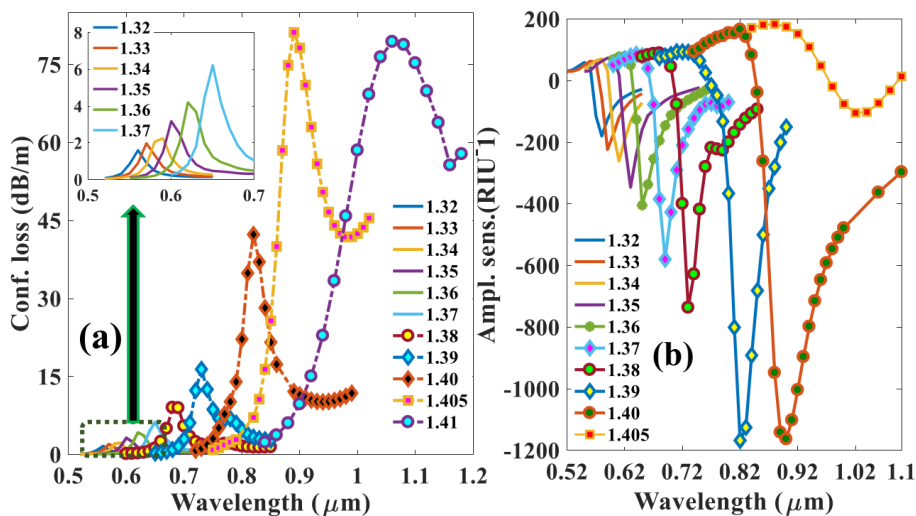


Figure 6.16. Loss and sensing performance of the optimized fibre sensor. CL (a); and AS (b) of the proposed sensor with optimized geometric parameters for a dielectric RI of 1.32–1.41, (Islam *et al.* 2019c).

The cladding air hole diameter d has significant impact on CL and overall sensing performance as illustrated in Fig. 6.15(c–d), Tab. 6.3. An increase in d reduces the core diameter and distance between two air holes, defined as t in Fig. 6.12. As t reduces the EM field in the core is confined strongly and cannot reach the plasmonic metal and therefore this reduces the CL. However, it is important to have sufficient space so that the EM field from the core mode can interact with the plasmonic metal to produce an

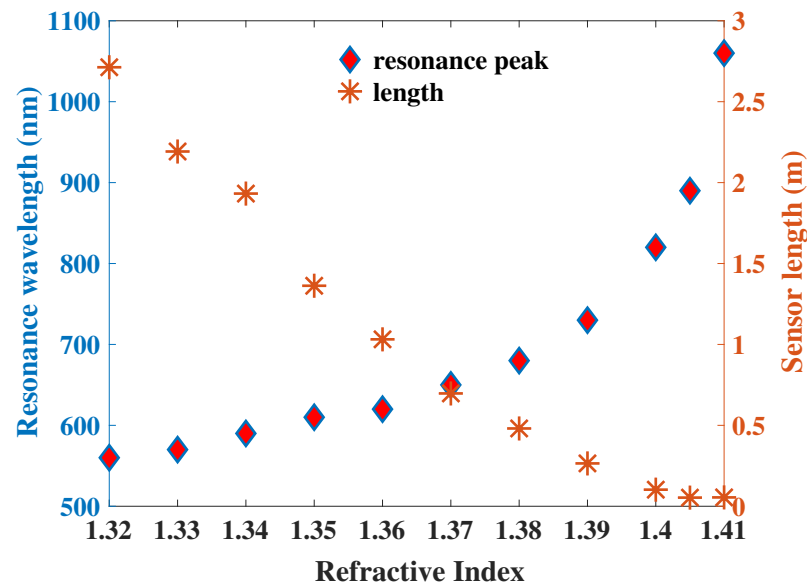


Figure 6.17. Resonance wavelength and sensor length with the variation of RI. The analysis is carried out for RI variation, (Islam *et al.* 2019c).

evanescent wave. Considering these competing issues, we selected d as 2.90, 3.10, and 3.30 μm where WS are 1, 000, 2, 000 and 2, 000 nm/RIU respectively. We neglect to consider 2.90 μm as optimum as it increases the CL with low sensitivity. For $d = 3.30 \mu\text{m}$ the air holes become too closer and act as an obstacle for the core mode to interact with the metal. Therefore considering the light interaction with metal, CL and sensing performance we choose $d = 3.10 \mu\text{m}$ as optimum.

Using optimized geometric parameters the CL and AS of the proposed sensor is shown in Fig. 6.16(a–b) that illustrates extremely low CL and high sensitivity. The physical reason of attaining such performance is the choice of plasmonic material and the arrangement of cladding air holes for trapping light inside the core. We see that the CL increases with the increase of dielectric RI. This is because the EM fields from the core interact more strongly with the plasmonic metal. The detection range of the sensor is determined within the RI range of 1.32–1.41. Based on the fibre geometry, the background material and plasmonic effects, a sharper loss peak is obtained upto a RI of 1.405 and starts broadening from 1.41. The resonance wavelengths for dielectric RI 1.32–1.41 are 560, 570, 590, 610, 620, 650, 680, 730, 820, 890 and 1,060 nm respectively with a maximum wavelength and amplitude sensitivity of 34,000 nm/RIU and

6.3 An exposed core localized SPR biosensor

1,170 RIU⁻¹ respectively.

References	Loss (dB/cm)	Air holes	WS, nm/RIU	AS, RIU ⁻¹	FOM	Resolution, RIU
(Zhang <i>et al.</i> 2017)	-	standard	3,038	-	-	-
(Coelho <i>et al.</i> 2015)	-	standard	5,100	-	-	1.56×10^{-3}
(Wu <i>et al.</i> 2017)	35	82	21,700	-	-	-
(Islam <i>et al.</i> 2018i)	300	20	62,000	1,415	958	1.61×10^{-6}
(Islam <i>et al.</i> 2019d)	15	14	1,11,000	2,050	-	9×10^{-7}
(Liu <i>et al.</i> 2018c)	110	8	15,180	498	-	5.68×10^{-6}
(Liu <i>et al.</i> 2018b)	17	34	14,660	1,222	255	6.82×10^{-6}
(Rifat <i>et al.</i> 2018)	475	100+	11,000	1,420	407	9.1×10^{-6}
(Paul and Biswas 2018)	1	17	18,000	-	-	5.56×10^{-6}
Proposed	0.79	4	34,000	1,170	310	2.94×10^{-6}

Table 6.3. Comparison of the proposed exposed core sensor with prior SPR sensors. The comparison is carried out by considering the peak loss, number of air holes used, wavelength sensitivity, amplitude sensitivity, FOM, and resolution.

The resonance wavelength and sensor length as a function of RI is shown in Fig. 6.17. This indicates that resonance wavelength varies linearly with RI therefore the sensor shows a highly linear ($R^2 = 0.9336$ using linear fitting) sensing characteristics. Besides, due to negligible CL the sensor also attains a high sensor length of 0.4–2.9 m for RI range of 1.32 to 1.41. Note that, the sensor length is inverse of its CL and defined by the equation (Islam *et al.* 2018i),

$$L = \frac{1}{\alpha_{\text{loss}}(\lambda, n_a)} \quad (6.11)$$

where α_{loss} represents the CL. We see that as the RI increases the sensor length decreases, this is because of the increasing trend of CL with RI.

Sensor resolution is also an important factor that determines the fraction change of RI the sensor can detect. It can be found by,

$$R = \frac{\Delta n_a \Delta \lambda_{\text{min}}}{\Delta \lambda_{\text{peak}}} \quad (6.12)$$

where, Δn_a represents a change in dielectric RI, $\Delta \lambda_{\text{min}}$ defines the minimum wavelength resolution, and $\Delta \lambda_{\text{peak}}$ determines the difference in resonance peak shift. For a

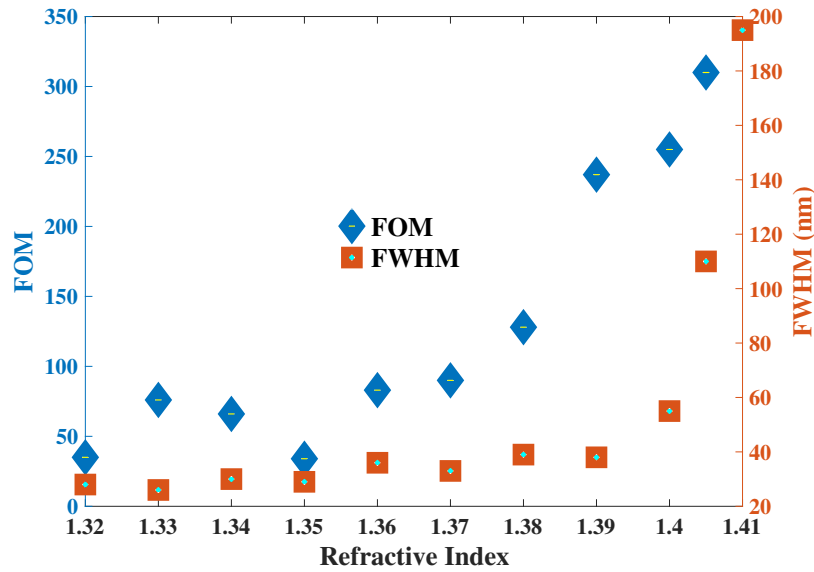


Figure 6.18. FOM and FWHM with RI variation. The analysis is carried out for RI variation (Islam *et al.* 2019c).

best case estimate considering, $\Delta\lambda_{\min} = 0.1 \text{ nm}$ (Islam *et al.* 2018i, Islam *et al.* 2019d, Liu *et al.* 2018c, Liu *et al.* 2018b, Rifat *et al.* 2018, Paul and Biswas 2018), with that the sensor achieves a high sensing resolution of 2.94×10^{-6} . Therefore, the proposed sensor can in principle detect a tiny change in RI of the order of 10^{-6} (Hautakorpi *et al.* 2008).

The figure of merit (FOM) is an important metric that determines the overall performance of a sensor. The FOM can be determined by (Islam *et al.* 2018i),

$$\text{FOM} = \frac{S_{\lambda} \text{ (nm/RIU)}}{\text{FWHM (nm)}} \quad (6.13)$$

where, S_{λ} (nm/RIU) is the WS and FWHM is the full width at half maximum. In order to achieve high FOM the FWHM should be low and sensitivity should be high. Accordingly we obtain a maximum FOM of 310 for the dielectric RI of 1.405.

The obtained characteristics of the proposed sensor is compared with recently reported plasmonic sensors that is shown Tab. 6.3. Considering the design simplicity, low loss and overall sensing performance it is evident that the proposed holey fibre sensor has improved performance over the others reported previously (Zhang *et al.* 2017, Coelho *et al.* 2015, Wu *et al.* 2017, Dash and Jha 2014, Islam *et al.* 2018i, Liu *et al.* 2018c, Liu *et al.* 2018b, Rifat *et al.* 2018, Paul and Biswas 2018, Chu *et al.* 2018) that also satisfies

6.4 Fabrication and coating

our design goal to develop a practical LSPR biosensor.

In this section, a simple exposed-core four-hole based PCF-LSPR sensor is discussed for RI sensing. Numerical studies show that the sensor can achieve a maximum WS of 34,000 nm/RIU, AS of 1,170 RIU⁻¹, FOM of 310, estimated maximum resolution of 2.94×10^{-6} , and a low maximum CL of 0.79 dB/cm. More importantly, the sensor achieves improved sensing performance at the expense of only four circular shaped air holes that reduces the fabrication complexity in a large scale as compared to previous reports. Due to the simplicity of the sensor we believe that it will be feasible for fabrication and owing to the high sensing performance it will potentially serve as a sensing device for high RI biochemicals.

6.4 Fabrication and coating

After playing with several fibre designs we decide to fabricate a three hole exposed fibre instead of four hole as discussed in (Islam *et al.* 2019c). Moreover instead of using the plasmonic nano-particles we used continuous metallic sheet. The fabricated and coated fibre is shown in Fig. 6.19, where the fabrication is followed by the similar procedure as followed in KostECKI *et al.* (2012), Warren-Smith *et al.* (2009).

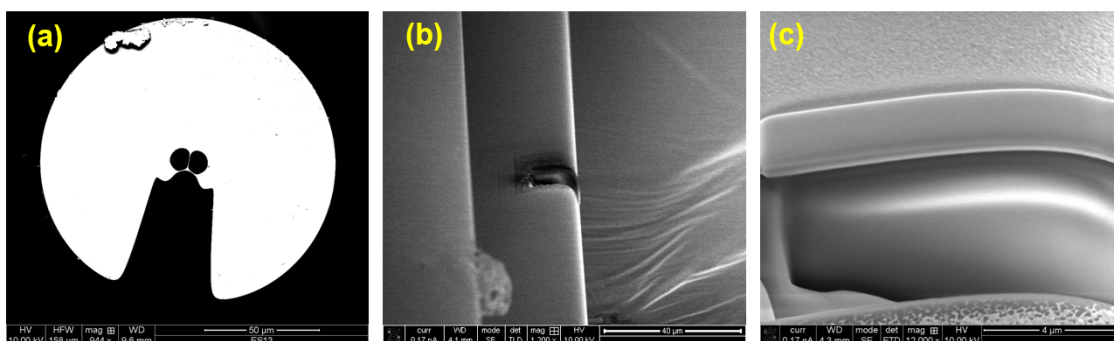


Figure 6.19. Fabrication and coating of the exposed core fibre. (a) SEM of the three-hole exposed core fibre, (b) SEM of the exposed side of the fibre after 5 nm titanium and 30 nm gold coating, (c) SEM of the cut portion of the exposed that was carried out to accurately measure the coating thickness.

The gold coating is followed by fibre splicing by a single mode fibre. The reason is the usable fibre length. With plasmonic metal coating the loss of the fibre increase significantly, these reduce the usable fibre length, where the usable fibre length for

sensing is inversely proportional to the loss of the fibre. After splicing with a single mode fibre the usable fibre length increase and that is used for further coating with TiO_2 and Au. Both the TiO_2 and Au was coated on the fibre surface following the sputtering technique.

6.5 Conclusion

In this chapter, surface plasmon and localized surface plasmon resonance sensors are studied. Various simplified sensor designs and their analyses are shown. Simulation results indicate that the fibres can achieve remarkably high amplitude and wavelength sensitivity with low loss and high figure of merit. One of the optimized fibres is fabricated and coated for future biochemical sensing experiments.

The following chapter shows a tunable graphene plasmonic metasurface for multi-band super-absorption and terahertz sensing. The tunability of the metasurface is achieved by changing graphene chemical potential. The sensing performance for different dielectric refractive index variation is also analysed and presented.

Electrically tunable graphene metasurface

WE study a plasmon induced tunable metasurface for multiband superabsorption and terahertz sensing. It consists of a graphene sheet that facilitates perfect absorption where the graphene pattern at the top layer creates an enhanced evanescent wave that facilitates the metasurface to work as a sensor. The modelling and numerical analysis are carried out using Finite Element Method (FEM) based software, CST microwave studio where a genetic algorithm (GA) is used to optimize the geometric parameters, and metasurface tunability is achieved via an external gate voltage on the graphene. By exploiting graphene's tunable properties we demonstrate a multiband super-absorption spectra having a maximum absorption of 99.7% in a frequency range of 0.1–2.0 THz that also maintain unique optical performance over a wide incidence angle. Further results show how the super-absorber can be used as a sensor, where the resonance frequency shifts with the refractive index of the surrounding environment.

7.1 Tunable graphene metasurface

7.1.1 Introduction

Plasmonic superabsorption (also known as perfect absorption) and wave trapping by means of plasmonic metasurfaces have attracted considerable attention due to promising new techniques for light manipulation, with potential applications in the field of energy harvesting, filtering, thermal imaging, electromagnetically induced transparency, and high performance sensing (Grant *et al.* 2016, Yang *et al.* 2017, Kim *et al.* 2016, Liao *et al.* 2016, Keshavarz and Vafapour 2019). A promising pathway to take advantage of the above applications is to employ metasurfaces, offering a wide degree of freedom for tailoring the material's electromagnetic (EM) properties. Manipulation of an incident wave in a metasurface is followed by transmission or reflection propagation modes. For the transmission mode, several challenges, including transmission efficiency, obstruct its large scale deployment. The theoretical upper limit of the transmission efficiency of an ultra thin metasurface is about 25% (Monticone *et al.* 2013). Transmission efficiency can be increased by making the metasurface thin (Qin *et al.* 2016). Compared to the transmission type metasurface, the metasurface designed to operate in reflection mode, can achieve an efficiency of close to 100%. This is because a metasurface can be made highly reflective, while also modulating the reflected wave by suitably tailoring the phase (Yu *et al.* 2011).

The excitation of plasmons within sub-wavelength structures on the metasurface leads to localization of electric and magnetic fields (Zheng *et al.* 2019, Wang *et al.* 2017b, Beruete and Jáuregui-López 2020), creating strong light-matter interaction suitable for sensing (Keshavarz and Vafapour 2019, Beruete and Jáuregui-López 2020, Zeng *et al.* 2015). Plasmons at the surface facilitate strong interaction with the surrounding environment (Zeng *et al.* 2015), enabling the application of the superabsorber for sensing of dielectrics that have spectral signatures at terahertz frequencies (Luo *et al.* 2019, Zeng *et al.* 2015).

While there have been a number of previous studies that have demonstrated absorption with terahertz metamaterials (Liu *et al.* 2016, Astorino *et al.* 2018, Wu *et al.* 2018, Liu *et al.* 2018a, Nguyen and Lim 2017, Yang *et al.* 2018a), these suffer low light-matter interaction with a low figure of merit. Moreover, proposed metamaterial devices not

only exhibit extensive losses but also present numerous challenges to nano-fabrication, requiring a large number of layers. Previously, it has been shown that significant field trapping and enhancement can be obtained by exploiting the multilayer structure of metamaterials or metasurfaces forming a Fabry-Pérot (F-P) cavity where absorption enhancement occurs due to increased light-matter interaction with multiple reflections inside the cavity (Chen 2012). Therefore, multilayered metamaterials have been proposed however those were able to achieve single (He 2015) and triple (Chen *et al.* 2018c) absorption band in the terahertz frequency range. Beside terahertz metamaterials and metasurfaces, various fiber optic (Islam *et al.* 2019b, Islam *et al.* 2019d) and planar (Abdelsalam *et al.* 2019, Gao *et al.* 2019, Yang *et al.* 2018b) plasmonic sensors are also studied and investigated in the visible to infrared region, however, those sensors are suitable to detect bio-analytes that have a spectral fingerprint in the frequency of interests. In comparison with terahertz sensors (Liu *et al.* 2016, Astorino *et al.* 2018, Wu *et al.* 2018, Liu *et al.* 2018a, Nguyen and Lim 2017, Yang *et al.* 2018a, Debus and Bolivar 2007), the microwave biosensor requires large area whereas the plasmonic sensors in the visible to infrared range (Abdelsalam *et al.* 2019, Gao *et al.* 2019, Yang *et al.* 2018b, Kabashin *et al.* 2009) requires complicated fabrication process (Chen *et al.* 2012). Moreover, many complex molecules have collective vibrational and rotational fingerprints in terahertz region, resulting in unique characteristic spectra (Chen *et al.* 2018c, Zheng *et al.* 2012). Suitable terahertz sensors are of importance for capturing the terahertz fingerprint of materials and complex molecules.

The metasurface perfect absorber based on the excitation of surface plasmon polaritons (SPPs) has the common problem of a single-band, which greatly limits its application especially for infra-red detection, imaging, and sensing devices. The multi-band absorbers have greater tuneability than the single band absorbers. All multiband perfect absorbers are based on the combination of fundamental plasmon resonances of different sized periodic metallic/dielectric resonators. The strong interaction between the different resonators greatly limits the number of perfect absorption bands. Excitation of higher-order plasmon resonances is a promising way to design multi-band absorbers with over four absorbance bands.

7.1 Tunable graphene metasurface

Recently, graphene-based devices with multiple resonance excitations have been proposed that can be applied to enhance the light-matter interaction, increasing the possibility for multiband sensing. Multiple channels and multiplexing operations are highly required in systems including optical communication, absorbers, spectroscopy and sensors, and filters (Yao *et al.* 2017). Recent studies show that multiband absorbers are essential for frequency selective detection that reduces environmental disturbance and enhances detection accuracy. Moreover, for the applications in terahertz thermal imaging, multiple-band absorbers, especially those that have more than four resonance peaks are in critical need of development (Chen 2012, Wang *et al.* 2017a).

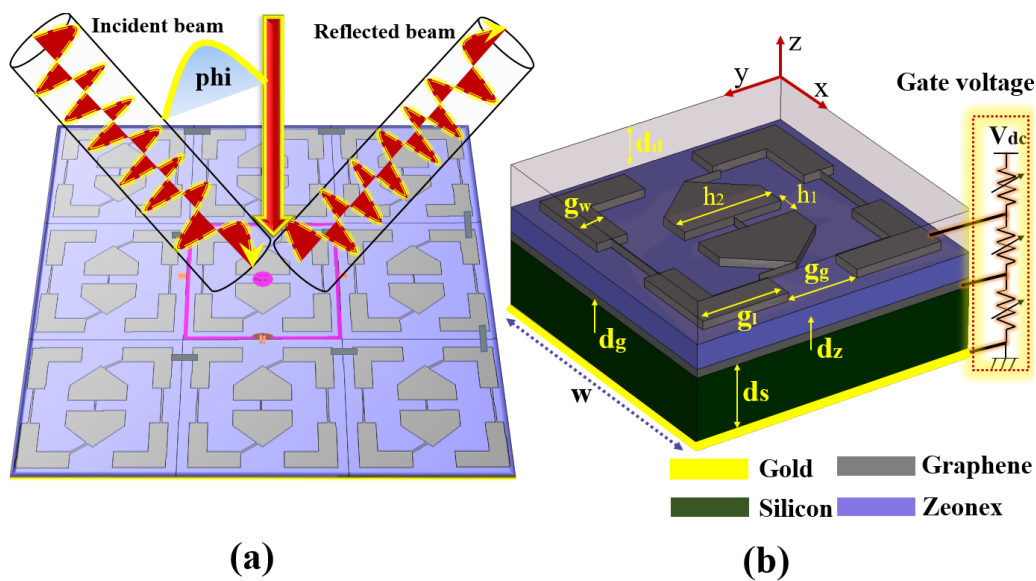


Figure 7.1. Schematic of the electrically tunable graphene metasurface. (a) The proposed metasurface showing the incident and reflected terahertz beam, (b) the unit cell showing dimensions of different geometrical parameters including the electrical connection among the layers, the chronology of materials from the bottom layer is gold-silicon-graphene sheet-Zeonex-graphene pattern (Islam *et al.* 2020d).

Therefore, considering the efficiency of metasurface operational modes and application of multiple band absorbers, we study on a multilayer graphene metasurface that is able to trap the light strongly and enhance the surface plasmon effect. A gold mirror is used to reflect the incident terahertz waves, with tunable absorption in reflection mode and negligible transmission. We use high-resistive silicon between the gold and graphene sheet that also support the device. A dielectric Zeonex layer is used between graphene sheet and graphene pattern because of its suitable blend of properties in the terahertz band. Graphene sheet is used to increase the absorption whereas graphene pattern

creates strong plasmons for enhanced sensing. To accelerate the design procedure we applied a genetic algorithm (GA) interface to CST to obtain the final design parameters.

7.1.2 Design, simulation and fabrication methodology

The unit cell of the proposed graphene metasurface is illustrated in Fig. 7.1(a) where *Frequency domain solver* with *Floquet-port* boundary conditions are used to achieve the properties of the metasurface. The *Floquet-port*, where the unit cells are defined in the x and y directions and open space in z -direction, is used exclusively with planar-periodic structures. In the z -axis, perfectly matched layer (PML) is used to guarantee no scattering, leading to the accuracy of the results. Common examples are phased arrays and frequency selective surfaces which can be idealized as infinitely large. The analysis of the infinite structure is then accomplished by analyzing a unit cell. Linked boundaries most often form the sidewalls of a unit cell, but in addition, a boundary condition is required to account for the infinite space above. The *Floquet-port* is designed for this purpose. Boundaries that are adjacent to a *Floquet-port* must be linked boundaries.

We select the *tetrahedral* mesh type having adaptive mesh refinement, the mesh subdivides the structure into a large number of tetrahedrons, which is required to achieve the desired simulation accuracy. To ensure zero transmission, the gold dispersive medium with a thickness larger than the penetration depth of terahertz is used (Biabanifard and Abrishamian 2018). The graphene sheet is used to enhance the absorption and the graphene pattern enhances plasmonic fields, which are beneficial for sensing applications.

The relative permittivity of gold is described by the Drude model (Zhu *et al.* 2012),

$$\varepsilon(\omega) = \varepsilon_{\infty} - \frac{\omega_p^2}{\omega^2 + i\omega\gamma} \quad (7.1)$$

where, ε_{∞} , ω_p , and γ are the permittivity at infinite frequency, plasma frequency and collision frequency representing loss. These values for gold are 1.0, $1.38 \times 10^{16} \text{ rad}\cdot\text{s}^{-1}$ and $1.23 \times 10^{13} \text{ s}^{-1}$ respectively, and for silicon are 11.68, $4.94 \times 10^{13} \text{ rad}\cdot\text{s}^{-1}$, and $1.117 \times 10^{13} \text{ s}^{-1}$ respectively (Zhu *et al.* 2012). Another Drude-type semiconductor, silicon, is a dissipative element that supports the metasurface. Silicon can be regarded

7.1 Tunable graphene metasurface

as a highly lossy material in the terahertz regime and can be easily processed using standard lithography technologies. The relative permittivity of silicon can be obtained following Eqn. 7.1, where $\varepsilon_\infty = 11.7$. From the Hall effect analysis, the carrier concentration and electron mobility of the silicon wafer are measured to be $8.8 \times 10^{16} \text{ cm}^{-3}$ and $814.3 \text{ cm}^2\text{V}^{-1}\text{s}^{-1}$ respectively. They correspond to $\omega_p = 4.94 \times 10^{13} \text{ rad}\cdot\text{s}^{-1}$ and $\gamma = 1.117 \times 10^{13} \text{ s}^{-1}$ which are used in the design (Pu *et al.* 2012, Cheng *et al.* 2015).

In order to achieve optimal results in the terahertz band, we also select cyclo-olefin polymer (COP), Zeonex as another dielectric. The relative permittivity of Zeonex is 2.34 (Yang *et al.* 2018a, Tuniz and Kuhlmeier 2015, Islam *et al.* 2019e). Zeonex is chosen due to its unique optical properties such as low absorption loss, high glass transition temperature, negligible material dispersion, insensitivity to humidity, can be readily injection molded, or extruded into film and sheet (Shim *et al.* 2019, Islam *et al.* 2019e, Cunningham *et al.* 2011). It has very low absorption loss in the terahertz region that makes it suitable for terahertz applications. Moreover, Zeonex is resistive to most acids and solvents. Therefore, it is a suitable candidate for the substrate of an absorber in the terahertz region (Shim *et al.* 2019, Islam *et al.* 2019e).

Note that, graphene is considered as one of the key materials for the proposed device, upon which the absorption and other applications related to perfect absorption is totally dependent. The graphene is a single layer of sp^2 carbon atoms arranged in a honeycomb lattice and has recently triggered research activities worldwide due to its remarkable optical, mechanical, and chemical properties (Novoselov *et al.* 2004, Bonaccorso *et al.* 2010). The graphene permittivity $\varepsilon_{G,t}$ can be expressed as (Zhu *et al.* 2013, Liu and Jian 2014, Yang *et al.* 2014a, Cheng *et al.* 2019, Hanson 2008, Cao *et al.* 2017),

$$\varepsilon_{G,t} = 1 + j \frac{\sigma(\omega)}{\varepsilon_0 \omega d_g} \quad (7.2)$$

here ω is the angular frequency, d_g is the graphene thickness, and ε_0 is the permittivity in vacuum.

The surface conductivity (σ) of graphene including both intraband (σ_{intra}) and interband (σ_{inter}) transitions are governed by the Kubo formula (Zhu *et al.* 2013, Liu and Jian 2014, Yang *et al.* 2014a, Cheng *et al.* 2019, Hanson 2008),

$$\sigma(\omega, \tau, \mu_c, T) = \sigma_{\text{intra}} + \sigma_{\text{inter}} \quad (7.3)$$

$$\sigma_{\text{intra}}(\omega, \tau, \mu_c, T) = -j \frac{e^2 k_B T}{\pi \hbar^2 (\omega - j2\tau)} \left(\frac{\mu_c}{k_B T} + 2 \ln(e^{-\mu_c/k_B T} + 1) \right) \quad (7.4)$$

$$\sigma_{\text{inter}}(\omega, \tau, \mu_c, T) = -j \frac{e^2}{4\pi \hbar} \ln \left(\frac{2\mu_c + (\omega - j2\tau)\hbar}{2\mu_c - (\omega - j2\tau)\hbar} \right) \quad (7.5)$$

where e is the electron charge, μ_c is the graphene chemical potential, τ is the scattering rate that is considered 0.1 ps and where the reason for choosing this value is described in Appendix C, T is the temperature in Kelvin that is considered 300 K for this proposed device, k_B is the Boltzmann's constant, and $\hbar = \frac{h}{2\pi}$ is the reduced Planck's constant. In order to use graphene in the simulation, the permittivity is calculated using Eqn. 7.2 and imported using the user defined dispersion list of CST. The same importing process is repeated in case of any graphene parameter changes. Note that, to support the electrical gating process, the graphene patterns are electrically connected via thin 0.1 μm graphene-stripes (Fardoost *et al.* 2016).

In order to manufacture the proposed device, the following steps can be followed. Firstly, high-resistivity 98.28 μm thick silicon with gold coating on one side and graphene sheet on the other, can be deposited by chemical vapor deposition (CVD). The CVD grown graphene can also be transferred to the silicon substrate (Kang *et al.* 2012). The thin 5.79 μm Zeonex layer can then be deposited by spin coating and cured at vacuum oven. The top graphene pattern can then be achieved using a standard lithography process (Astorino *et al.* 2018).

7.1.3 Parameter optimization-genetic algorithm

The optimization of the proposed device parameters including the thickness of silicon and Zeonex, as well as the dimensions of the top graphene patterns, are carried out using the iterative genetic algorithm (GA) method with built-in optimization tools available in CST Microwave studio. Using GA, it is possible to find the optimized design parameters to achieve a certain goal. It generates points into parameter space and then refines them through multiple generations, with random parameter mutation. The set goal for our optimization was to achieve maximum reflection (S_{11}) within the frequency range 0.1–2.0 THz. In the GA, the population size was set to 4×8 , maximum 30 iterations, a mutation rate of 60% with an anchor value of 10%. The optimized values obtained using GA are $d_s = 98.28 \mu\text{m}$, $d_z = 5.79 \mu\text{m}$, $w = 67.58 \mu\text{m}$, $g_w = 7.44 \mu\text{m}$,

7.1 Tunable graphene metasurface

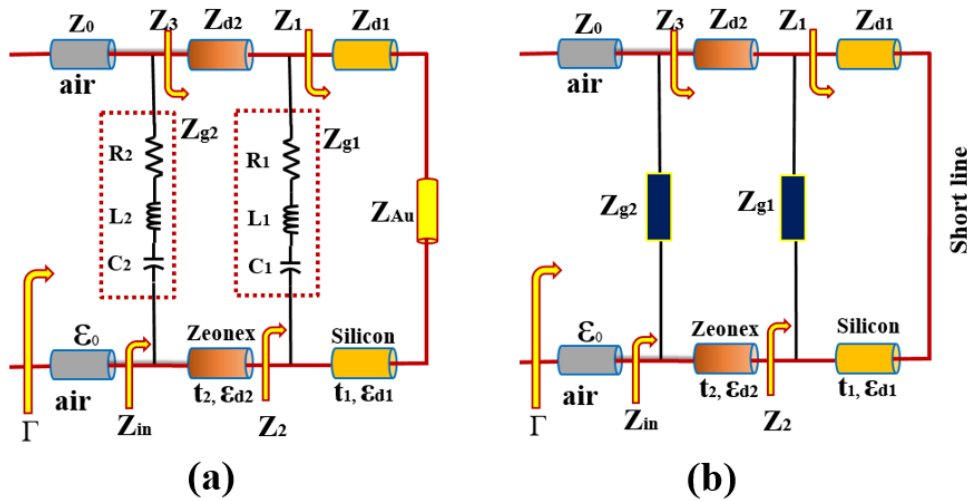


Figure 7.2. Equivalent circuit model of the metasurface. (a) Equivalent circuit model for the graphene based tunable superabsorber; (b) simplified model, (Islam *et al.* 2020d).

$g_g = 17.06 \mu\text{m}$, $g_1 = 21 \mu\text{m}$, $h_1 = 5 \mu\text{m}$, $h_2 = 15.62 \mu\text{m}$, all the parameters are defined in Fig. 7.1(b). We also place a dielectric layer in contact with the patterned graphene, with a thickness defined as d_d .

7.1.4 Transmission line theory and equivalent circuit modelling of the proposed device

When the incident wave is perpendicular to the surface, the absorption A is obtained from the S -parameters by the formula

$$A = 1 - |S_{21}(\omega)|^2 - |S_{11}(\omega)|^2 \quad (7.6)$$

where S_{11} and S_{21} are considered as reflection and transmission coefficients respectively. Note that the silicon has a high refractive index, with gold thickness larger than the terahertz skin depth, there is negligible transmission through the structure with the transmission coefficient is equal to zero, $|S_{21}(\omega)| = 0$. Therefore, the simplified form to calculate the absorption for the proposed device is

$$A = 1 - |S_{11}(\omega)|^2. \quad (7.7)$$

We apply transmission line theory with the equivalent circuit model (ECM) for the proposed superabsorber, as shown in Fig. 7.2(a). In the ECM, the bottom gold layer can be considered as a short transmission line, with the impedance of silicon, Zeonex and air

defined by Z_{d1} , Z_{d2} and Z_0 . The impedance of metallic gold is denoted by Z_{Au} which is a short circuit in the simplified model of the ECM, as illustrated in Fig. 7.2(b). The graphene sheet and graphene pattern is modeled by an RLC circuit network denoted by Z_{g1} and Z_{g2} in the ECM. The resistance R and the inductance L are a property of graphene, whereas the capacitance C is created by the gap between the graphene pattern and the graphene gate. In the ECM, the transmission channel corresponding to free space is denoted as Z_0 , with the input surface impedance of the ECM shown as follows,

$$Z_1 = jZ_{d_s} \cdot \tan(\beta_d d_s) \quad (7.8)$$

$$Z_2 = \frac{Z_1 \cdot Z_{g1}}{Z_1 + Z_{g1}} \quad (7.9)$$

$$Z_3 = Z_{d_z} \frac{Z_2 + jZ_{d_z} \cdot \tan(\beta_d d_z)}{Z_{d_z} + jZ_2 \cdot \tan(\beta_d d_z)} \quad (7.10)$$

$$Z_{in} = \frac{Z_3 \cdot Z_{g2}}{Z_3 + Z_{g2}} \quad (7.11)$$

where $Z_{d_s} = \frac{Z_0(120 \cdot \pi)}{\epsilon_{d_s}}$ is the impedance of silicon; $Z_{d_z} = \frac{Z_0}{\epsilon_{d_z}}$ is the impedance of the Zeonex and β_d is the propagation constant of the propagating terahertz waves in the dielectric substances. Based on the effective medium theory the imaginary part of impedance must be equal to zero at the resonant point (Smith *et al.* 2005). Therefore the corresponding reflection efficiency τ can be expressed as

$$\tau = S_{11} = \frac{\text{Re}(Z_{in}) - Z_0}{\text{Re}(Z_{in}) + Z_0}. \quad (7.12)$$

Note that, the dielectric permittivities of silicon, Zeonex and air are defined as ϵ_{d_s} , ϵ_{d_z} and ϵ_0 where d_s and d_z represent the silicon and Zeonex thickness.

7.1.5 Results and discussion

At normal incidence angle, the characteristics of reflection (R), transmission (T), and absorption (A) of the proposed metasurface is illustrated in Fig. 7.3 which shows a negligible transmission, highly efficient reflection and five bands of perfect absorption peaking at 99.7%, within a frequency range of 0.1–2.0 THz. The optimum parameters obtained using genetic algorithm (GA) are used, together with a graphene at a chemical potential of $\mu_c = 0.2$ eV. A graphene thickness of 1 nm, equivalent to a tri-layer, was selected such that the appropriate mesh size resulted in a reasonably short simulation time (Liu and Aydin 2016). Note that the metasurface is polarization insensitive

7.1 Tunable graphene metasurface

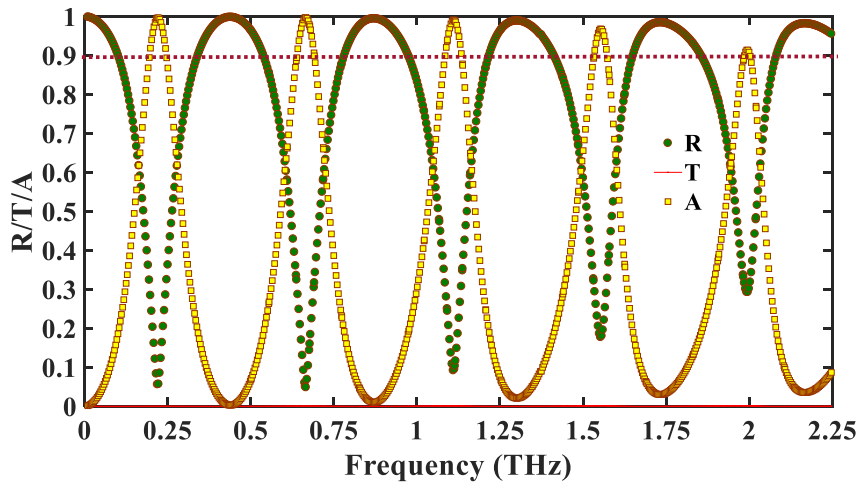


Figure 7.3. Performance of the metasurface in terms of reflection, transmission, and absorption. The reflection (R), transmission (T), and absorption (A) characteristics of the proposed metasurface at optimized design parameters having $\mu_c = 0.2$ eV and at a normal incidence angle, (Islam *et al.* 2020d).

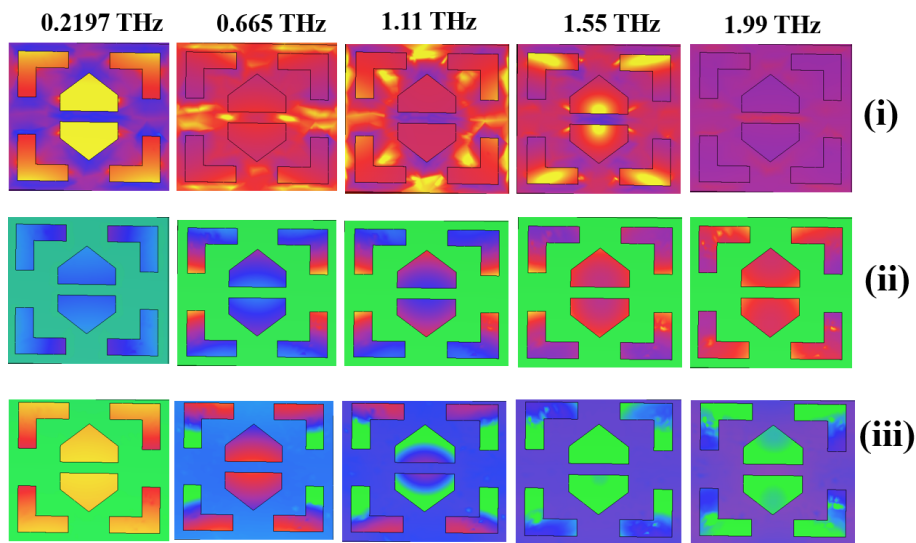


Figure 7.4. Electric field pattern of the metasurface. (i) E-field, (ii) electrical energy density, and (iii) power flow density.

as it shows similar optical characteristics at both transverse electric (TE) and transverse magnetic (TM) mode. Therefore for further simulation and characterization, we consider the TE polarization mode.

In later subsections of this chapter, we discuss the physics of multiband absorption, the effect of graphene chemical potential, the effect of changing the incidence angle and performance of the metasurface at fabrication tolerances.

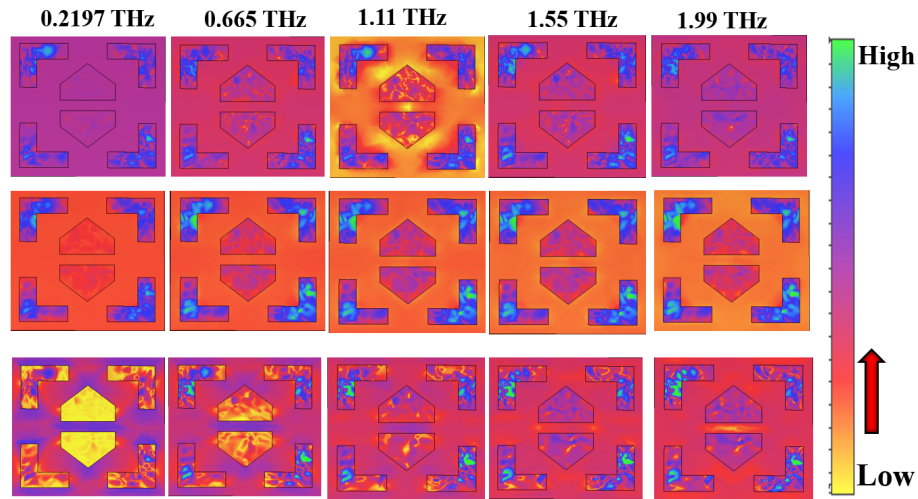


Figure 7.5. H-field pattern of the proposed metasurface (i) H-field, (ii) magnetic energy density, and (iii) power flow of the proposed device at optimized design parameters at resonance frequencies of 0.2197, 0.665, 1.11, 1.55 and 1.99 THz, (Islam *et al.* 2020d).

7.1.6 Mechanism of plasmon enhancement and multiband superabsorption

To explore the science behind multiband superabsorption, we show different mode fields including E-field, H-field, electric energy density, magnetic energy density, power flow and power flow density in Fig. 7.4 and Fig. 7.5. It is found that different edges of graphene pattern excites at different frequencies, causing multiband resonance peaks. The excitation of the first plasmonic mode occurs when the frequency of the incoming photons matches with the first localized mode of the graphene pattern. Thus some photons are absorbed, and the others are reflected or transmitted through the graphene pattern. Transmitted photons are reflected back by the second graphene layer or eventually from the Au reflector, and some of them come out of the structure with a phase difference of $2\beta sd = \pi$, where d is the total distance travelled by the wave. This process is repeated multiple times, and these partial reflections destructively interfere with each other, leading to zero overall reflection. On the other hand, the transmission channel is closed by the Au reflector; thus, the incoming wave is completely trapped, and is finally absorbed in the structure.

The number of absorption bands of the proposed metasurface is dependent on the top graphene pattern and geometrical dimensions of Zeonex and silicon. These phenomena can be verified from Fig. 7.6 where a performance study with and without

7.1 Tunable graphene metasurface

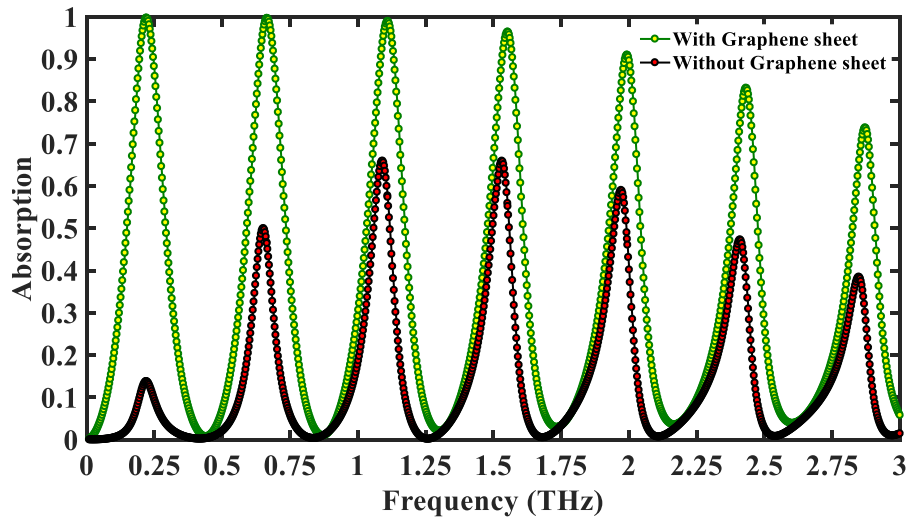


Figure 7.6. Effect of graphene on the metasurface performance. Effect of graphene sheet in between silicon and Zeonex on the overall performance of the metasurface (Islam *et al.* 2020d).

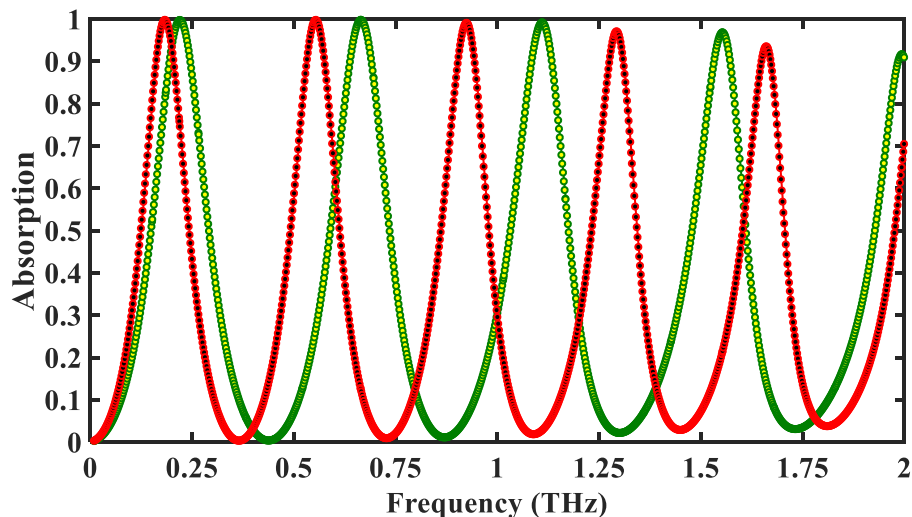


Figure 7.7. Effect of graphene on resonance frequency. Dependence of resonance peaks on the overall dimension of the metasurface, the green line indicates the performance of the metasurface at an optimized dimension while the red line indicates the performance at 20% increased from its optimum dimension (Islam *et al.* 2020d).

graphene sheet is shown. It can be seen that the resonance frequencies remain the same without the graphene sheet, therefore the graphene sheet does not have any effect on the number of absorption bands but have a strong affect in enhancing plasmons at the top graphene pattern. One way to have multi-band absorption is to design a unit cell that have Fabry-perot components with multiple resonating elements. The edges are then place where the plasmons can be excited with enhanced intensity. The intensity of

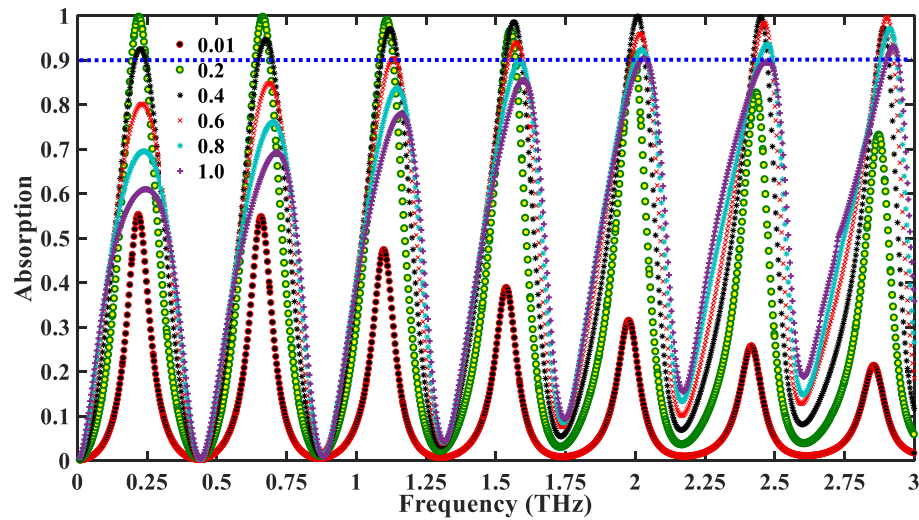


Figure 7.8. Frequency tunability of the metasurface. The tunability of the metasurface by changing the graphene chemical potential at a normal incidence angle (Islam *et al.* 2020d).

fields at different resonance frequencies is shown in Fig. 7.4 and Fig. 7.5 where it can be seen that the surface plasmons are excited in different patterns at different frequencies and thus the metasurface acts as a multiband absorber. Note that, a possible way of converting the proposed multiband absorber to a broadband absorber would require to pattern both the graphene layer and tune the other geometrical properties.

The frequencies where high absorption is observed depends on the polymer dimensions. In order to exploit this effect, we increased the overall dimension by 20% while the top graphene pattern dimensions were kept the same. The obtained result is shown in Fig. 7.7, where we see that as the dimension of the metasurface increases the resonance frequencies shift towards lower frequencies. Therefore, the operating frequency is totally dependent on the metasurface dimension, which can be chosen by design. Note that the separation between absorption peaks is regular, this is due to the structural symmetry and interference in the vertical cavity.

7.1.7 Dynamically tunable property enabled by graphene

The optical properties of graphene are highly dependent on its Fermi energy, which is considered as the origin of dynamic tunability of the proposed device. To realize tunability, we add an external bias voltage, as shown in Fig. 7.1, to modulate the chemical

7.1 Tunable graphene metasurface

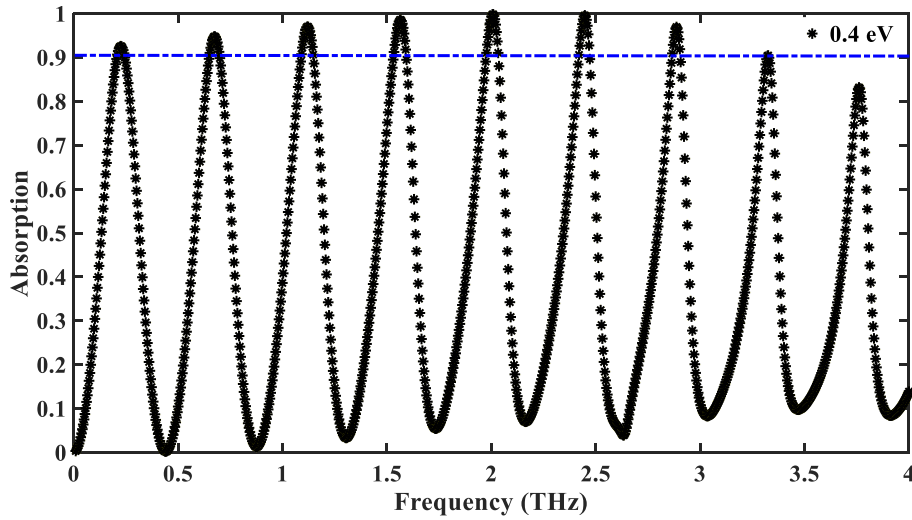


Figure 7.9. Effect of graphene chemical potential. Absorption at $\mu_c = 0.4$ eV to illustrate the effect of chemical potential on the overall performance of the absorber (Islam *et al.* 2020d).

potential of graphene as described by the following equation (Liu *et al.* 2017),

$$\mu_c = \hbar v_f \sqrt{\frac{\pi \epsilon_0 \epsilon_r d_z \sqrt{V_g}}{e d_z}} \quad (7.13)$$

where μ_c is the chemical potential of graphene, \hbar is the Planck's constant, $v_f = 10^6$ m/s is the Fermi velocity, ϵ_0 and ϵ_r are the relative permittivity of vacuum and dielectric spacer respectively, e is the electron charge, $\sqrt{V_g}$ is the external bias voltage, and d_z is the thickness of dielectric spacer between graphene sheet and graphene pattern.

In order to exploit the dynamic tunability property of the superabsorber, the chemical potential of graphene is varied from 0.01 to 1 eV. The characteristics is shown in Fig. 7.8 where it is observed that at $\mu_c = 0.01$ eV the metasurface does not act as a superabsorber because the absorption peaks do not reach high values (above 60%). However, as μ_c increases the amplitude of signal reflection decreases, therefore according to Eqn. 7.7 the absorption also increases. It is found that for $\mu_c = 0.2$ eV, five-band superabsorption can be obtained having a maximum absorption of 99.7% within the frequency range of 0.1–2 THz. It is important to note we are defining superabsorption when its value exceeds 90% as indicated by the horizontal dashed line in Fig. 7.3 and Fig. 7.8. The multiple bands are due to the plasmon excitation of different graphene patterns at different frequencies. An eight-band superabsorber can be obtained for a 0.4 eV, shown in Fig. 7.9, causing a resonance shift to higher frequencies. Therefore, increasing μ_c increases the absorption bands and shifts the resonance to higher

frequencies. One can choose a suitable μ_c considering the desired application and operating frequency range. In our case, we choose 0.2 eV for further characterization of the proposed device.

7.1.8 Wide angle of incidence

We further characterize the angle dependent response of the proposed plasmonic superabsorber that is illustrated in Fig. 7.10. As clearly shown that the absorber can achieve similar absorption performance up to around an oblique incidence angle of 70° however there is a shifting trends of absorption peaks towards the higher frequencies. For a particular angle, 0° for example, it is noticeable that the absorption intensity decreases with the increase of frequency and therefore we obtain superabsorption upto around 2.0 THz and then the absorption decreases.

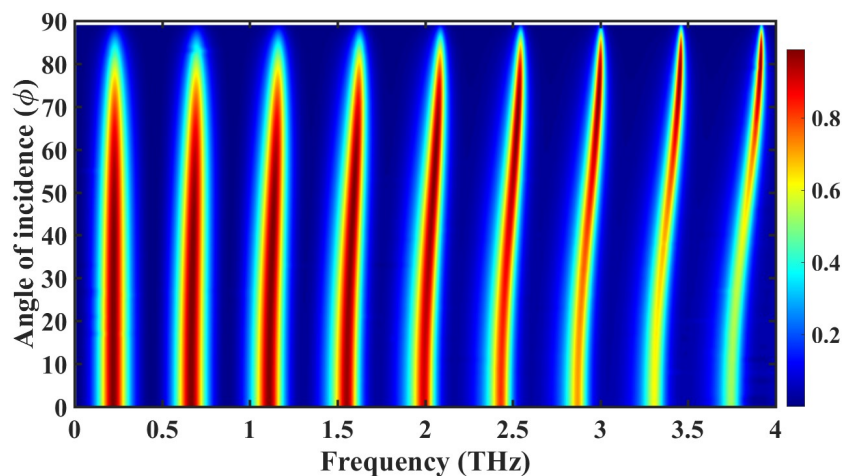


Figure 7.10. Angle dependence of the graphene metasurface. Dependence of incident angle of the terahertz signal at optimized design conditions. The colourbar at the right side indicate the intensity of absorption, showing high intensity of absorption of around 2.0 THz with angle of incidence of around 70° which means the proposed absorber shows similar optical characteristics of upto around 70° and 2.0 THz (Islam *et al.* 2020d).

These particular characteristics of the absorber are totally dependent on the geometrical parameters such as thickness of silicon, as well as the optical properties of Zeonex and graphene. Note that at normal incidence angle the parameters of the proposed superabsorber are optimized to operate in the low terahertz range (upto around 2.0 THz).

7.1 Tunable graphene metasurface

However, these parameters can be tuned as required by application, performance, as well as the desired frequency range.

7.1.9 Characterization of the proposed device considering fabrication tolerances

Fabrication tolerances and their effect on device performance were estimated by varying the dimensions of the metasurface. The results are shown in Fig. 7.11, illustrating the reflection and absorption performance for a $\pm 10\%$ variation of dimensions.

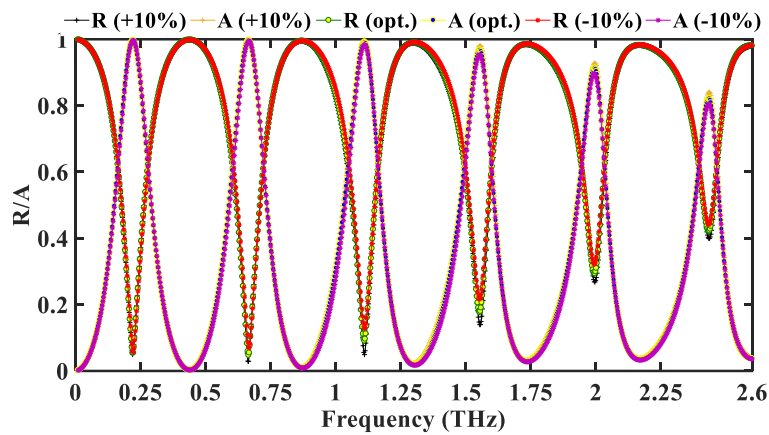


Figure 7.11. Performance variation considering fabrication tolerance. Performance variation of the proposed superabsorber by varying the dimension of the metasurface to $\pm 10\%$, under normal incidence angle and fixed graphene chemical potential of 0.2 eV.

We find slight changes in the reflection and absorption curves, but no significant effect on the device performance.

7.1.10 Application to refractive index sensing

To simulate a sensing application, we applied a dielectric layer over the patterned graphene, and the characteristics of the sensor with different dielectric thickness, d_d , is illustrated in Fig. 7.12. We see that applying a dielectric in contact with the graphene pattern changes the reflection and resonance frequency, which is the desirable property enabling the application of the proposed device as a sensor. However, the d_d also has impact on the overall sensing performance, as observed in previous literature

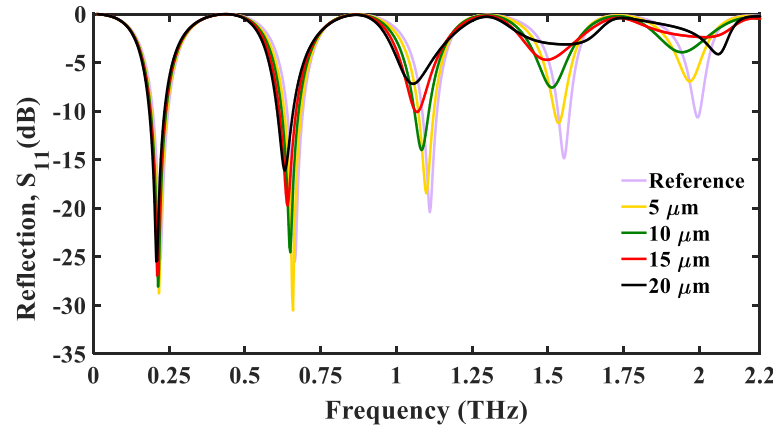


Figure 7.12. Performance of the metasurface as a sensor. Performance of the proposed device as a sensor at optimum design parameters, $\mu_c = 0.2$ eV and changing the dielectric layer thickness, d_d adjacent to the graphene pattern, Islam *et al.* (2020d).

(Chen and Fan 2017). To verify this, we changed d_d and observed the performances. We found that increasing d_d increases the resonance shifts which also broadens the reflection peak. These result illustrates a broadened first full width at half maximum (FWHM), that in turn reduces the figure of merit (FOM), which is a function of FWHM (FOM = Sensitivity/FWHM) (Offermans *et al.* 2011, Muhammad *et al.* 2019).

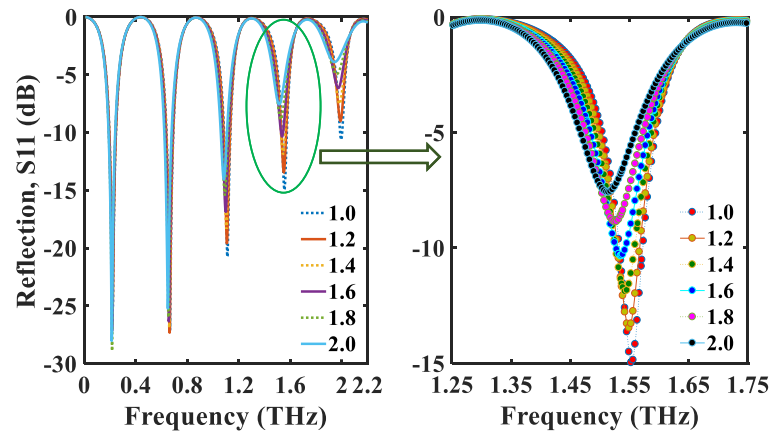


Figure 7.13. Performance of the metasurface by changing dielectric properties. Variation of resonance peak by changing the dielectric refractive indices adjacent to graphene pattern, by using optimum design parameters, $d_d = 10$ μm , and $\mu_c = 0.2$ eV.

As the FWHM increases the FOM decreases, indicating overall performance reduction of the sensor. Comparing $d_d = 5$ and 10 μm , we see that 5 μm shows sharper resonance peaks however 10 μm shows improved sensing performance, albeit with a slight degradation of resonance quality factor. Further increase of d_d shows a larger FWHM.

7.1 Tunable graphene metasurface

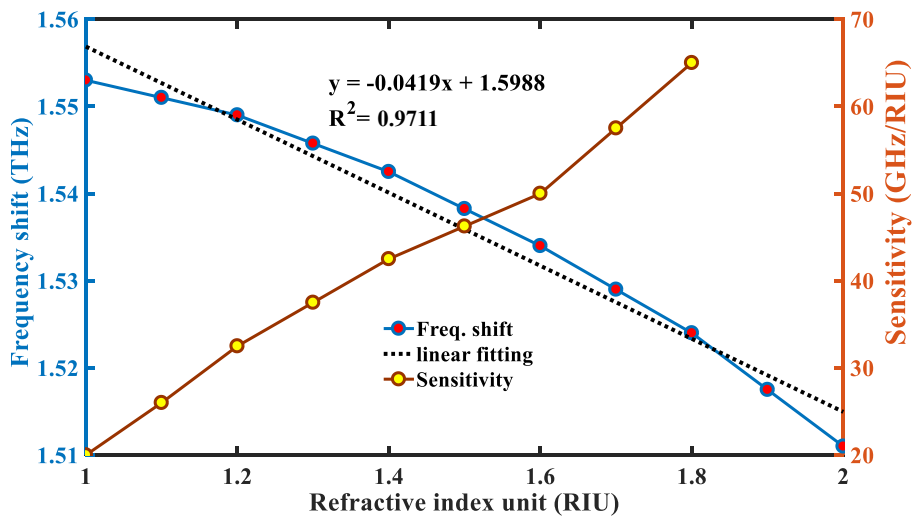


Figure 7.14. Linearity of the sensor. Frequency shift and sensitivity as a function of refractive index, The dotted line indicates an approximate linear fit. For the linear fit of the frequency shift curve we have $R^2=0.9711$ (Islam *et al.* 2020d).

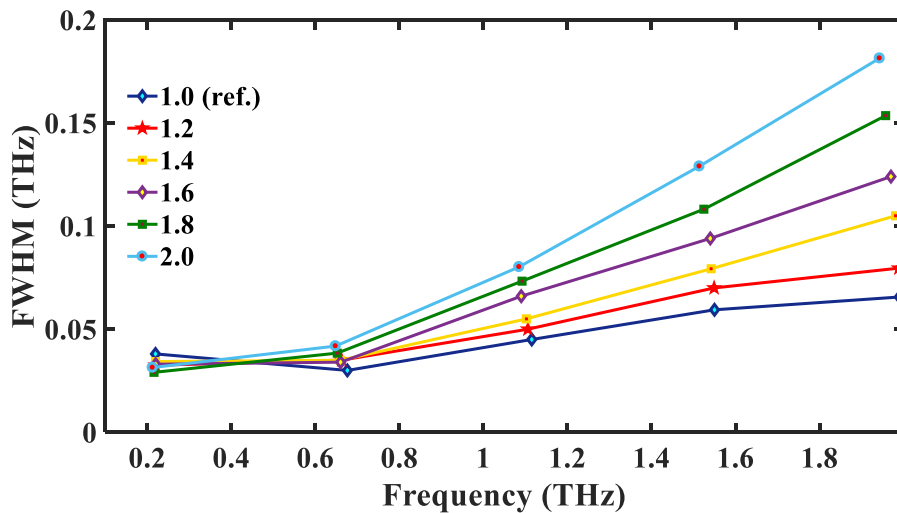


Figure 7.15. FWHM of the metasurface. The achieved FWHM as a function of frequency of the metasurface (Islam *et al.* 2020d).

Therefore we found optimum sensitivity near $d_d = 10 \mu\text{m}$, and intend to carry out further characterization of the sensing properties of the device. Thus, considering d_d fixed at $10 \mu\text{m}$ we changed the refractive indices of the dielectric adjacent to graphene pattern, Fig. 7.13. We see that as the refractive index changes the resonance peak shifts, providing useable sensitivity.

The resonance frequency shift and sensing performance having different dielectric refractive index variation is shown in Fig. 7.14 where the FWHM is shown in Fig. 7.15.

Literature Refs.	Operating band	Coupling mode	Number of bands	Sensitivity
(He <i>et al.</i> 2017)	0.1–2 THz	plasmon	two	0.242 THz/RIU
(Cong <i>et al.</i> 2015)	0.5–0.9 THz	plasmon	one	23.5% RIU ⁻¹
(Meng <i>et al.</i> 2012)	1.2–2.0 GHz	EIT-like	two	77.25 mm/RIU
(Chen <i>et al.</i> 2009)	0.1–100 THz	EIT-like	two	1200 nm/RIU
(Yahiaoui <i>et al.</i> 2015)	0.15–0.85 THz	plasmon	two	54.18 GHz/RIU
This thesis	0.1–2.25 THz	localized plasmon	five	76 GHz/RIU

Table 7.1. Comparison of the proposed multi-band device with prior reported devices. The comparison is carried out considering the number of bands achieved by the proposed metasurface and the sensitivity.

These illustration indicate that as the dielectric refractive index increases the sensitivity also increases, due to the increasing concentration of dielectrics over the graphene surface. A linear approximation of the frequency shift is estimated using linear fitting that gives $R^2 = 0.9711$. The obtained value of R^2 indicate that the sensor have sufficient precision.

In terms of sensitivity, the limit of detection (LOD) is defined as the minimum level that can be detected with 99% fidelity. The LOD can be calculated by, $LOD = 3\varepsilon/\text{sensitivity}$, where ε denotes the output uncertainty or standard deviation. Considering a 1% standard deviation, the sensor achieves a maximum LOD of 4×10^{-4} (Guider *et al.* 2015, Homola 2008).

7.2 Conclusion

The characteristics of FWHM as shown in Fig. 7.15 indicate that as the dielectric refractive index and frequency increases the FWHM also increases, as the dielectric concentration and frequency increases, the resonance peak broadens.

A comparative analysis of the proposed device over the previously reported devices is carried out which is shown in Tab. 7.1. The comparison indicates that the proposed metasurface uses the localized plasmon mode that means the plasmons will be concentrated along some of the edges of the graphene pattern, which results in pentaband terahertz absorption, together with enhanced sensitivity.

7.2 Conclusion

We numerically demonstrate that a graphene based tunable metasurface can be used for multiband absorption and sensing. The field distributions in graphene pattern show the excited plasmons at different resonance frequencies that indicates the benefits of achieving multiband absorption. Varying the graphene chemical potential, the number of absorption bands can be varied. We show that at a chemical potential of 0.2 eV, the metasurface can achieve five absorption bands, which is promising for sensing applications. The metasurface has a maximum sensitivity of 76 GHz/RIU, with a linearity of $R^2 = 0.9711$ and a considerable LOD. The metasurface can also illustrate similar optical performance over a wide acceptance angle of the incident terahertz beam that is also robust against fabrication tolerances. Owing to the above mentioned properties, the proposed metasurface is considered promising for multi-spectral applications of terahertz technology.

In the following chapter we study on the design, fabrication, and experiment on a ultrahigh-Q all dielectric terahertz metasurface. The design procedure including the optimization of a structure is discussed and a similar structure is fabricated and characterized.



Bound states in the continuum for guided terahertz plasmons

IN this chapter we demonstrate the simulation, fabrication, and experiment on all dielectric high- Q terahertz metasurfaces. Firstly, a metasurface having rectangular patterned germanium (Ge) resonator metasurface is studied including the sensing property. Secondly, a slightly different structure containing elliptical silicon (Si) resonator is optimized and analyzed. The second metasurface is fabricated and experimented using the THz-TDS. The experimental outcome is compared with the simulated outcome. Both of the metasurfaces are optimized using genetic algorithm (GA).

8.1 High-Q guided terahertz plasmons

Owing to strong light confinement ability, the optical resonators are of great interest to the scientific community. However, the confinement ability of resonators has only a limited lifetime because of unavoidable scattering. Their optical performances are often limited by this out-of-plane scattering caused by fabrication defects. The interference of light waves that are guided by a physical mechanism known as the Bound States in the Continuum (BIC), can suppress the scattering that could lead to improved optical devices. Utilizing the BIC effect, we propose a standard metasurface having two asymmetrical bricks of germanium (Ge) creating out-of-plane asymmetry. The device parameters are optimized by Genetic Algorithm (GA) where the goal set to achieve maximum reflection. The results show that the device can achieve an ultra-high Q factor of 7245, and high figure of merit (FOM) of 280. To our knowledge, the achieved Q -factor and FOM are the maximum achieved by any terahertz metasurface so far. Owing to strong light confinement ability, the metasurface is highly sensitive to its surrounding environment, therefore can also be used as a refractive index sensor.

8.1.1 Introduction

Light manipulation by plasmonic metasurfaces is of great interest nowadays because of their unique ability to arbitrarily modulate the amplitude, phase, and polarization of the electromagnetic waves (Zhang *et al.* 2016, Genevet *et al.* 2017, Chen *et al.* 2018a). The wavefront modulation at a metasurface relies on the geometric shapes, sizes, the orientation angles of different patterns on the metasurface, and on the materials (Wei *et al.* 2020). In comparison with conventional optical components and bulk metamaterials, the metasurfaces benefit from reduced absorption loss, improved light-matter interaction, relatively easy fabrication, and compact size (Wei *et al.* 2020, Islam *et al.* 2020d). The compact size is particularly advantageous for on-chip integration with other nanophotonic devices. Metasurfaces have a plethora of potential applications including holography (Huang *et al.* 2018, Wan *et al.* 2017, Ahmed *et al.* 2017b), data storage (Pégard and Fleischer 2011), electromagnetically induced transparency (Diao *et al.* 2019), filtering (Sima *et al.* 2017), vortex beam generation (Yang *et al.* 2014b), metalens (Chen *et al.* 2018b), transmission (Ma *et al.* 2018b), nonlinear optics (Li *et al.* 2017a, Xiao *et al.* 2018b), and sensing (Islam *et al.* 2020d, La Spada 2019).

However, the fabrication imperfections of metasurface devices produces scattering loss that limits the device efficiency and sensitivity. The physical mechanism, BIC, can significantly reduce the scattering loss and confine light inside the continuum by interference mechanism (Koshelev and Kivshar 2019). The interference of waves is a physical mechanism that occurs when two waves coincide with one another and produce a combined wave. Two types of interference mechanisms can occur, constructive and destructive. When the crests of two waves coincide with one another, their combined amplitude will be the sum of individual amplitudes of each wave. This phenomena is known as constructive interference. However, if the crest of one wave meets with the trough of another wave, the combined amplitude will be the difference of each wave amplitude. This mechanism is known as destructive interference (Koshelev and Kivshar 2019, Hsu *et al.* 2016).

Through optical resonance of light waves, these interference phenomena provide a means of achieving strong light confinement and light-matter interaction, to increase the signal amplitude. The BIC is formed by the destructive interference of several light waves that have similar wave-vectors, where the wave-vector describes the wave velocity and direction of propagation (Rybin and Kivshar 2017). Note that BIC has the property that it can remain localized even though it coexists with a radiating wave that can carry the energy away (Koshelev and Kivshar 2019, Hsu *et al.* 2016). Originally, the term BIC appeared in quantum mechanics, however it has subsequently been realized in numerous fields, including and later explained by the destruction of light interference. In BIC, the coupling constants of all radiating waves vanish via continuous parameter tuning. If the coupling constant vanishes due to asymmetry then the BIC is known as symmetry protected. In general, the BIC increases the light confinement and creates a very sharp resonance, greatly increasing the Q -factor of the metasurface device.

Recently, metasurfaces made from high index resonant dielectrics have emerged as an essential building block because of their low intrinsic losses and unique light control capability. The use of high index dielectrics increase the light localization on the surface that is extremely sensitive to external environments (Hsu *et al.* 2016, Kuznetsov *et al.* 2016). To achieve high Q -factor in the optical regime, several different approaches have been reported in the literature by different research groups (Campione *et al.* 2016,

8.1 High-Q guided terahertz plasmons

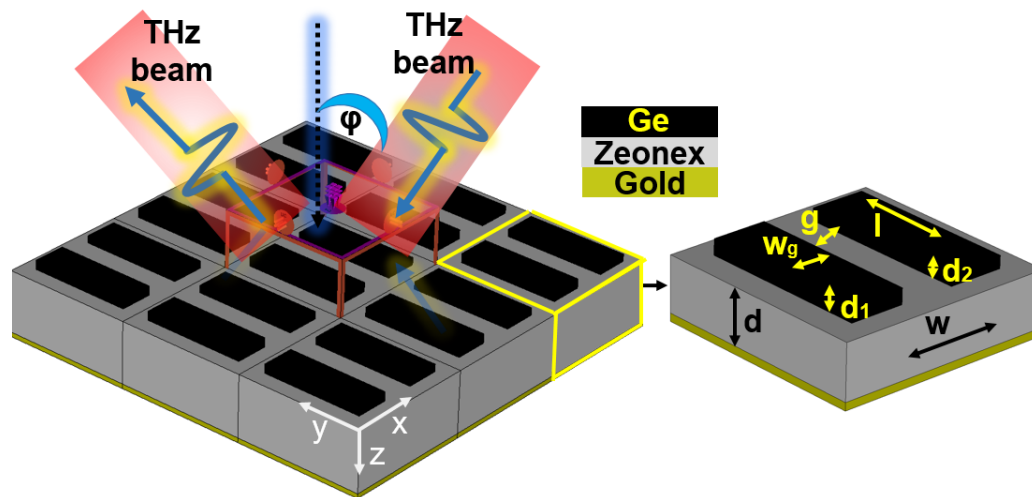


Figure 8.1. Schematic of the all dielectric metasurface reflector. Structure of the proposed high- Q terahertz metasurface enabled by BIC, and the unit cell with various geometric dimensions.

Leitis *et al.* 2019, Sui *et al.* 2018, Koshelev *et al.* 2018, Algorri *et al.* 2019), however achieving high Q -factors in terahertz regime remains an active and difficult research problem. Jansen *et al.* (2011) reported an experimental study of asymmetric split ring resonators achieving a Q -factor of 30 within a 0.2–0.4 THz range. An ultra-sensitive refractive index metasurface sensor was proposed by Singh *et al.* (2014), showing that the Fano resonance of the metasurface can also attain high Q -factors. Using Fano resonance on a metallic metasurface, Srivastava *et al.* (2016) obtained an improvement in Q -factor.

These studies demonstrate that at terahertz frequencies, the Q -factor of a metasurface is extremely sensitive to metallic conductive properties and geometries. Investigating the BIC mechanism, Han *et al.* (2019) theoretically and experimentally demonstrated that the proposed all dielectric metasurface can achieve a Q -factor of around 250 within a terahertz frequency of 0.3–0.6 THz. The terahertz devices discussed above (Jansen *et al.* 2011, Singh *et al.* 2014, Srivastava *et al.* 2016, Han *et al.* 2019) all show promising characteristics, yet there remains scope to propose new metasurface devices that can achieve high Q -factors.

In this chapter, we study an all-dielectric metasurface to obtain a high Q -factor in the terahertz frequency range. We utilize the BIC mechanism to reduce scattering and confine signal to the high index silicon surface, using a genetic search algorithm to find a maximum Q . Our simulation results show that the metasurface can achieve a

high Q -factor of around 7245 along with a high FOM of 280 in reflection, which was found to provide better efficiency than transmission (Islam *et al.* 2020d). The reported metasurface exhibits strong plasmons on the Ge interface, which results in a high sensitivity to the external environment. Our results show that the metasurface can achieve a maximum refractive index (RI) sensitivity of 56 GHz/RIU in the terahertz frequency range.

8.1.2 Design, simulation, optimization, and fabrication methodology

The design and simulation of the proposed metasurface is carried out via CST studio suite. A *frequency-domain* solver, and *tetrahedral* mesh type is considered in simulation. In a *Floquet port* boundary condition the unit cell is defined in the x - y direction and the open add space in the z -direction. Details of boundary conditions and mesh type is extensively discussed in our previous publication (Islam *et al.* 2020d). To make the metasurface work as a reflector, metallic gold were considered as a PEC type material. The properties of gold can be derived from the below formula,

$$\varepsilon(\omega) = \varepsilon_{\infty} - \frac{\omega_p^2}{\omega^2 + i\omega\gamma} \quad (8.1)$$

where, ε_{∞} is the permittivity at infinite frequency, ω_p is defined as plasma frequency, and γ represents the collision frequency. These values for ε_{∞} , ω_p , and γ are 1.0, $1.38 \times 10^{16} \text{ rad}\cdot\text{s}^{-1}$ and $1.23 \times 10^{13} \text{ s}^{-1}$ respectively (Zhu *et al.* 2012).

The gold base holds a substrate composed of a pure Zeonex polymer with a high terahertz transparency, low loss tangent, negligible water absorption, and low absorption coefficient which makes it well suited for terahertz applications. The material properties of Zeonex were obtained by experimental measurement as previously published (Islam *et al.* 2020b, Islam *et al.* 2019e). Germanium (Ge) was selected because of its high dielectric permittivity compared to Zeonex. The dielectric constant of Ge was taken to be 16.08 from (Randall and Rawcliffe 1967). The proposed metasurface design illustrating both the array and an enlarged inset showing the unit cell is shown in Fig. 8.1, where the direction of terahertz propagation and geometric design parameters are also indicated.

8.1 High-Q guided terahertz plasmons

The optimization of various parameters of the metasurface is carried out using the built in optimization tool of CST studio-*genetic algorithm*. The desired goal was set to maximise the scattering coefficient S_{11} , so that maximum absorption can be obtained in the desired frequency. The optimized values of the parameters defined at Fig. 8.1 are $d = 67.0 \mu\text{m}$, $w = 143.46 \mu\text{m}$, $d_1 = 10 \mu\text{m}$, $d_2 = 8 \mu\text{m}$, $g = w_g = 36.05 \mu\text{m}$, and $l = 108 \mu\text{m}$ respectively. We also place a dielectric layer adjacent to Zeonex and top germanium layer that is not shown in Fig. 8.1 but defined as d_d throughout the thesis.

8.1.3 Step by step fabrication procedure

The step by step procedure for fabricating the desired metasurface is outlined through Fig. 8.2.

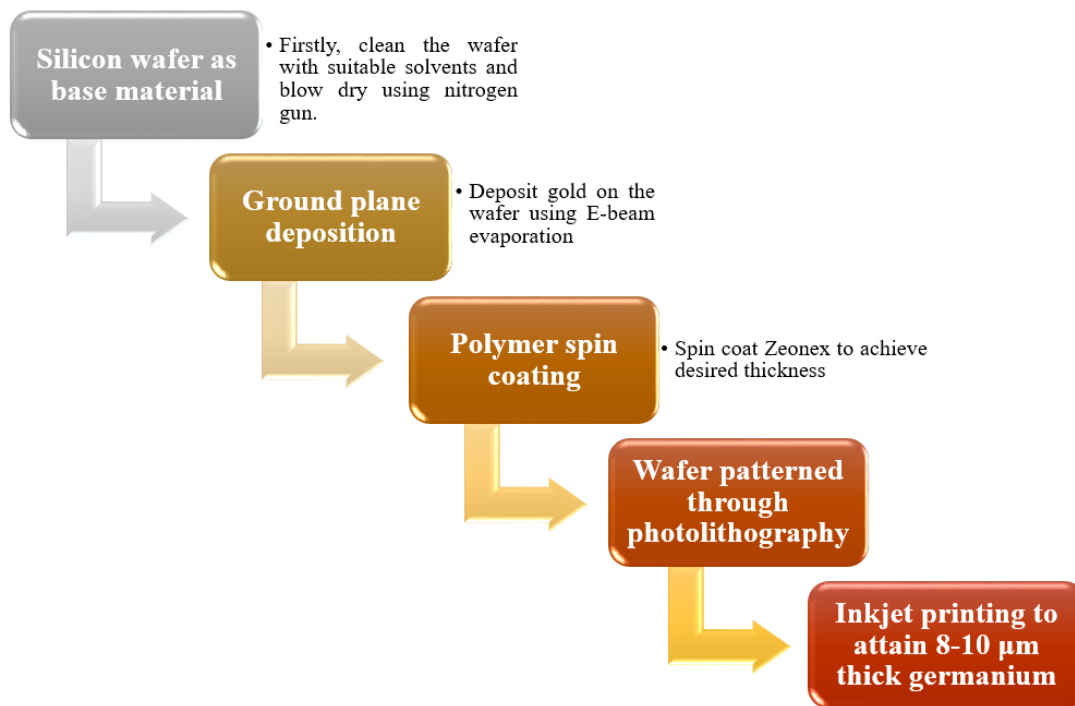


Figure 8.2. Step by step fabrication procedure of the high Q metasurface. Considering silicon wafer as a base material, and Inkjet printing for achieving Ge thickness.

Firstly, a 3-inch silicon oriented wafer is to be cleaned with acetone and isopropanol alcohol. Thereafter, it will be dried with high purity compressed nitrogen. Next, the wafer will be coated with the metallic ground plane. This ground plane would comprise of gold, which will be deposited at room temperature by electron beam evaporation. Zeonex will then be spin-coated on the metallic ground plane. The thickness

for Zeonex can be calibrated with a stylus profilometer (Dektak XT - Bruker) to be the desired thickness. The wafer will then be patterned on the metal-backed Zeonex layer using the standard photo-lithography technique (Ako *et al.* 2019). Depositing thick germanium is a challenging step—for this, we can possibly adopt ink-jet printing to achieve the desired thickness of germanium (McLeod and Tabor 2020). This printing process can possibly ensure the high accuracy of the deposited layers. An alternate method could be spray coating of germanium, however, there will be a possibility of minor thickness variation in this approach. Moreover, low temperature vapour phase epitaxy of Ge followed by photolithography may also create the pattern.

8.1.4 Equivalent circuit modelling and mathematical expressions

The absorption (A) for a perpendicular incidence wave to the surface can be calculated by

$$A = 1 - |S_{21}(\omega)|^2 - |S_{11}(\omega)|^2 \quad (8.2)$$

where S_{21} and S_{11} are the transmission and reflection coefficients respectively. Note that, the background material Zeonex has high terahertz transparency, however due to the gold metallic plane the transmission is zero, therefore the absorption is only dependent on the reflection of the signal. Thus, the simplified form of absorption can be written as

$$A = 1 - |S_{11}(\omega)|^2. \quad (8.3)$$

According to the equivalent circuit model as shown in Fig. 8.3, the transmission is zero, and the reflection can be found by transmission line theory. From Fig. 8.3 we get

$$Z_1 = jZ_{d_z} \cdot \tan(\beta_d d_z) \quad (8.4)$$

and

$$Z_{in} = \frac{Z_1 \cdot Z_g}{Z_1 + Z_g} \quad (8.5)$$

where $Z_{d_z} = \frac{Z_0(120 \cdot \pi)}{\epsilon_{d_z}}$ is the Zeonex impedance; and β_d is the propagation constant of the propagating terahertz waves.

Based on the effective medium theory the imaginary part of impedance must be equal to zero at the resonant point (Smith *et al.* 2005). Therefore the corresponding reflection

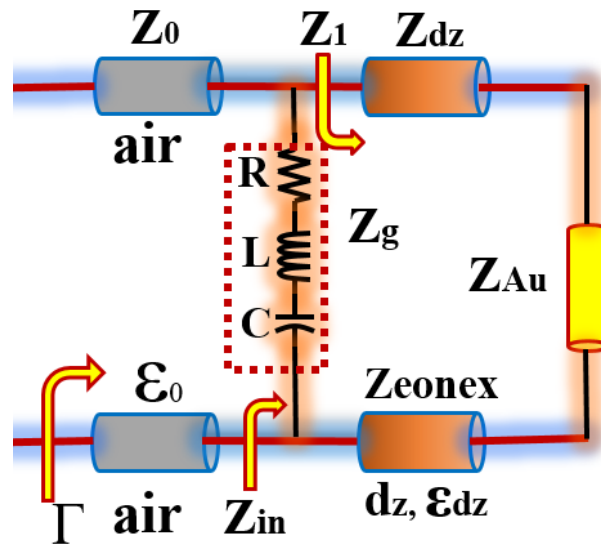


Figure 8.3. Equivalent circuit modelling of the high-q metasurface. Showing the R, L, and C for generated from the resonator.

efficiency τ can be expressed as

$$\tau = S_{11} = \frac{\text{Re}(Z_{in}) - Z_0}{\text{Re}(Z_{in}) + Z_0} \quad (8.6)$$

Note that, the dielectric permittivities of Zeonex and air are defined as ϵ_{dz} , and ϵ_0 where d_z represent the Zeonex thickness.

From the reflection coefficient, the Q-factor can be found from the full width at half maximum (FWHM) and the resonance frequency (f_c) using the following formula

$$\text{Q-factor} = \frac{f_c}{\text{FWHM}} \quad (8.7)$$

Note that the FWHM is the width of a line shape at half of its maximum amplitude. Therefore according to Eqn. 8.7, the Q-factor will be higher when there will be a sharp resonance peak as such the FWHM will be lower and vice versa.

For sensitivity analysis the following formula was used

$$\text{Sensitivity} = \frac{\delta f}{\delta \text{RI}} \quad (8.8)$$

where δf is the differences in frequencies between the consecutive resonance points and δRI is the refractive index difference.

Besides the sensitivity, the figure of merit (FOM) of a plasmonic device is also important as it indicates the detection limit of the device. The FOM is strongly limited by the sensitivity and the resonance linewidth FWHM (Homola *et al.* 1999), that can be defined by the following formula (Offermans *et al.* 2011, Muhammad *et al.* 2019)

$$\text{FOM} = \frac{S}{\text{FWHM}}. \quad (8.9)$$

The FOM of a device can be increased by increasing the sensitivity and/or decreasing the FWHM.

The limit of detection (LOD) is an important parameter of a sensor that can be defined as the minimum input quantity that can be distinguished with more than 99% fidelity, this can be calculated as

$$\text{LOD} = \frac{3\varepsilon}{\text{sensitivity}}, \quad (8.10)$$

where ε is defined as the output uncertainty. Accordingly, the high sensitivity enhances the LOD.

8.2 Results and discussion

Tuning and optimizing the geometrical parameters by genetic algorithm, the resultant reflection, transmission, and absorption of the proposed device is shown in Fig. 8.4. It is found that a sharp reflection peak is obtained at a frequency 1.4491 THz, define as the resonance frequency (f_c) where maximum reflection occurs. The choice of substrate material, high index dielectric, pattern and geometry of the dielectrics, and optimization of their dimensions, is responsible for the sharp resonance and the resultant high Q -factor.

Measurement shows that an extremely narrow full width at half maxima (FWHM) of 0.0002 at a resonance frequency (f_c) = 1.4491 THz, results a high Q -factor of 7245. To our knowledge this is highest Q -factor obtained in the terahertz frequency so far. Note that the transmission is negligible because of the gold reflector, likewise the absorption is nearly unity because of the strong reflection.

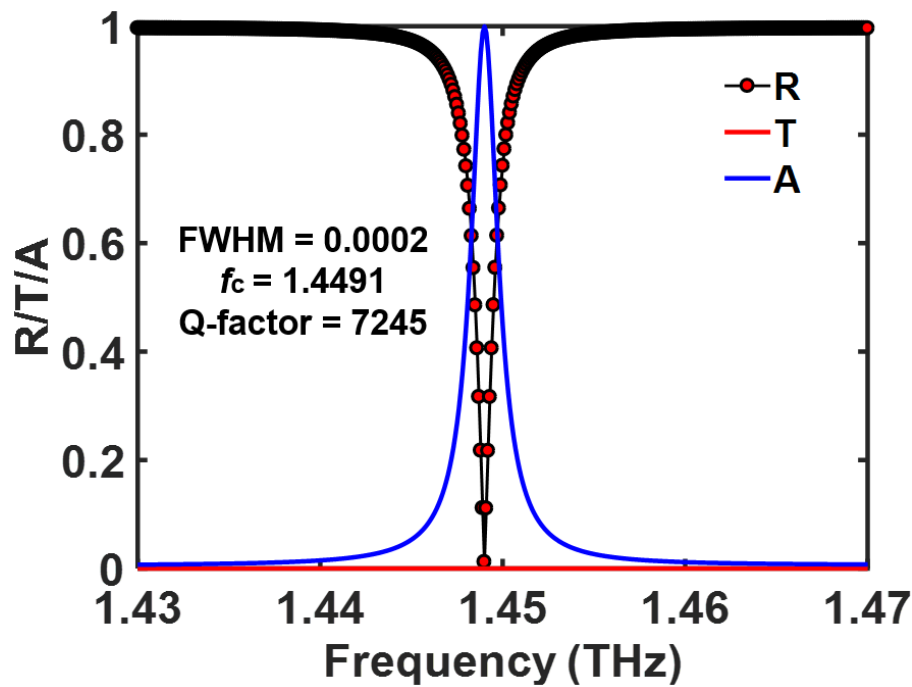


Figure 8.4. Performance in consideration to reflection, transmission, and absorption of the all dielectric metasurface. Reflection (R), Transmission (T), and Absorption (A) spectra of the proposed device having the optimized parameter dimensions and without top dielectric layer.

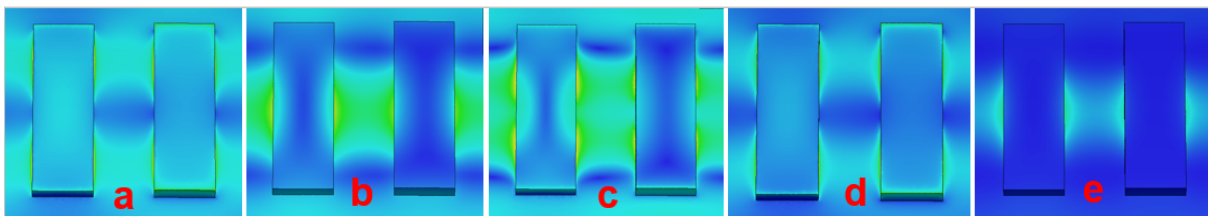


Figure 8.5. Mode field patterns of the high-q metasurface. Mode field patterns of the proposed metasurface, (a) E-field, (b) H-field, (c) Power flow, (d) E-energy density, and (e) H-energy density.

8.2.1 Mechanism behind plasmon enhancement and sharp resonance

The proposed metasurface shown in Fig. 8.1 consists of a high index dielectric (Ge) pattern on one side, a polymer substrate in between, and a metal ground plane on the other side. To explore the science behind the strong surface plasmons we show different mode fields including E-field, H-field, Power flow, E-energy density, and H-energy density, shown in Fig. 8.5 (a-e). We see that the mode fields are strongly confined in the Ge bars, the one reason is the high refractive index of Ge and the other reason is

the optimized asymmetry of the Ge bars. The excitation of the plasmonic mode happens when the photons from the incident electromagnetic wave interact with the Ge bars of almost sub-wavelength dimensions. At resonance frequency of the Ge bars, the incoming electromagnetic energy is strongly coupled and dissipated in the high index Ge and the polymer substrate due to the dielectric loss. This results in the absorption of energy at the resonance frequency. For the cases of multiband absorbers, some of the photons usually reflect from the substrate or eventually from the metal reflector, creating the second plasmons. Leading by destructive interference of the reflected photons, the process repeats multiple times until zero reflection occurs (Islam *et al.* 2020d). Due to the metallic back-plane, the transmitted energy through the sample is zero. At frequencies other than the resonant frequency the incident electromagnetic wave is reflected and no energy is absorbed.

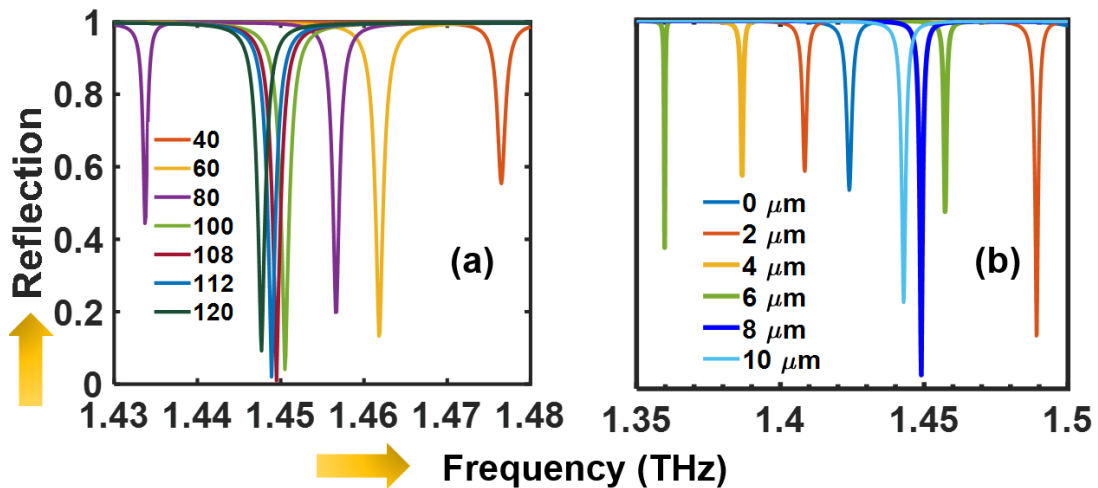


Figure 8.6. Performance by varying the Ge resonator. At other optimum design conditions, the performance of the metasurface by varying the (a) Ge length, (b) Ge thickness d_2 variation by keeping d_1 fixed.

8.2.2 Performance considering the germanium length and thickness variation

We explore the sensitivity of the genetic algorithm (GA) optimised parameters by showing performance degradation due to variations in the Ge length and thickness. The performance of the device by varying the Ge length and keeping all other parameters optimum is shown in Fig. 8.6(a). It shows similar performance at $l = 100, 108, 112,$ and $120 \mu\text{m}$, however the best performance is achieved at $l = 108 \mu\text{m}$, as optimized by

genetic algorithm.

Similarly, we carried out performance analysis by varying d_2 and keeping all other parameters optimum, Fig. 8.6(b). We find that for the symmetry case, $d_1 = d_2 = 10 \mu\text{m}$, with $d_2 = 0 \mu\text{m}$, and other asymmetry cases except $d_2 = 8 \mu\text{m}$ the device shows reduced performances. It is important to note that the performance of the device not only depends on the Ge but also to every geometric dimension of each material. The results shown in Fig. 8.6(a) and Fig. 8.6(b) are only for Ge variation, and do not include the proportionate variation of every dimensions. Therefore for a particular variation of parameters the results changes significantly. For example at $l = 40 \mu\text{m}$ we can see that the resonance frequency shifts forward with a reduction of reflection coefficient, while a slight variation does not affect the performance significantly. In case of fabrication, there might be slight variation from the optimized dimensions. A further analysis having proportional variation of material dimensions is discussed later that will give a clear insight of how the device will work with a proportional variation of the material's geometry.

8.2.3 Performance considering the fabrication imperfections

Device robustness is an important factor that must be considered with any purported new design. This indicates how the proposed device will perform in case of fabrication imperfections when the dimensions vary by a factor of say, $\pm 2\%$ as shown in Fig. 8.7. It was found that the device's Q -factor for such a variation remains almost the same, while the resonant frequency shifts significantly. For a $+2\%$ variation, the resonance frequency shifts forward to around 1.48 THz, while -2% variation results the resonance frequency shifts backward to 1.42 THz. At optimum parameters the resulting Q -factor is 7245, while for -2% and $+2\%$ parametric variation, the Q -factors are 7250 and 7190 respectively. These results indicate that the device can be easily tuned to operate in the desired frequency range.

8.2.4 Angle dependence of the metasurface

The angle dependencies of the metasurface over frequency is characterized and illustrated in Fig. 8.8. It shows that the metasurface works up to an oblique incidence angle of around 50° , however as the angle increases the performance of the metasurface starts

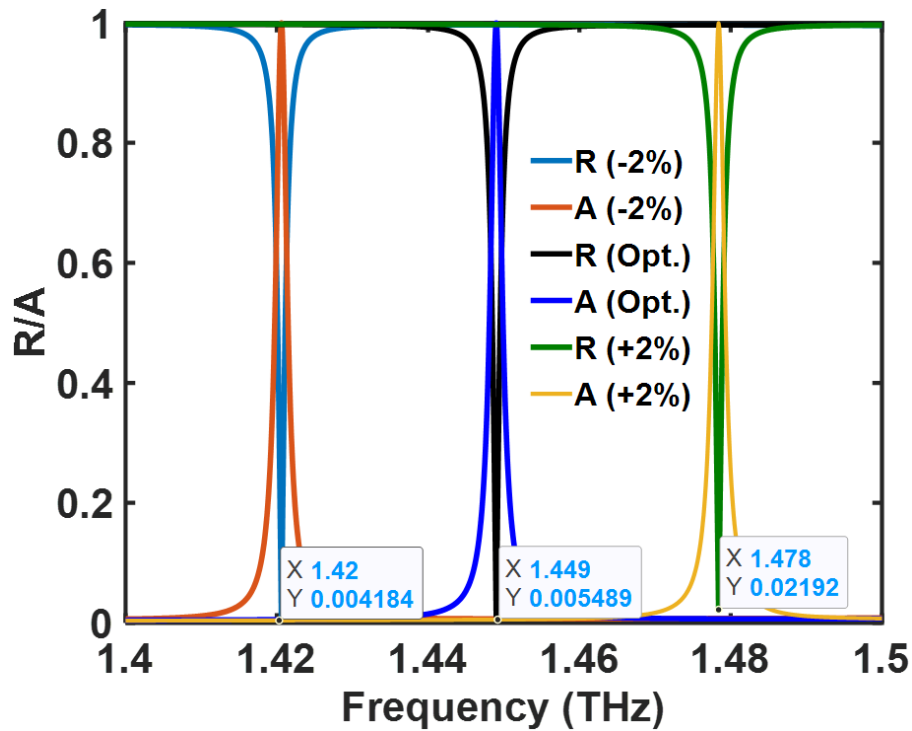


Figure 8.7. Performance variation by considering the fabrication tolerance. Reflection, and Absorption of the device for $\pm 2\%$ parametric variation, indicating the performance and resonance frequency shifts.

to decrease gradually. Note that this performance variation over angle is dependent on the metasurface structure, the materials used, the patterning and the dimensions of the materials. Also note that the metasurface is optimized at the normal incidence angle, and therefore this design works best at a normal angle of incidence.

8.2.5 Application in sensing

The proposed high- Q metasurface offers high sensitivity in sensing applications. In order to produce a sensor from this device, we first place a dielectric layer at the top surface, and observe the performance variation as the dielectric thickness is varied. The results are shown in Fig. 8.9. Initially we consider the refractive index of water (1.33) as a reference and changed the dielectric thickness, Fig. 8.9(a), we see that increasing the dielectric thickness shifts the resonance frequency further, which also reduces the absorption at the same time. For example, if we consider $25 \mu\text{m}$ as the dielectric thickness then we can see that the shift of resonance frequency from $0 \mu\text{m}$ to $25 \mu\text{m}$ is larger, however the reflection at $25 \mu\text{m}$ is lower than for other thickness. Therefore

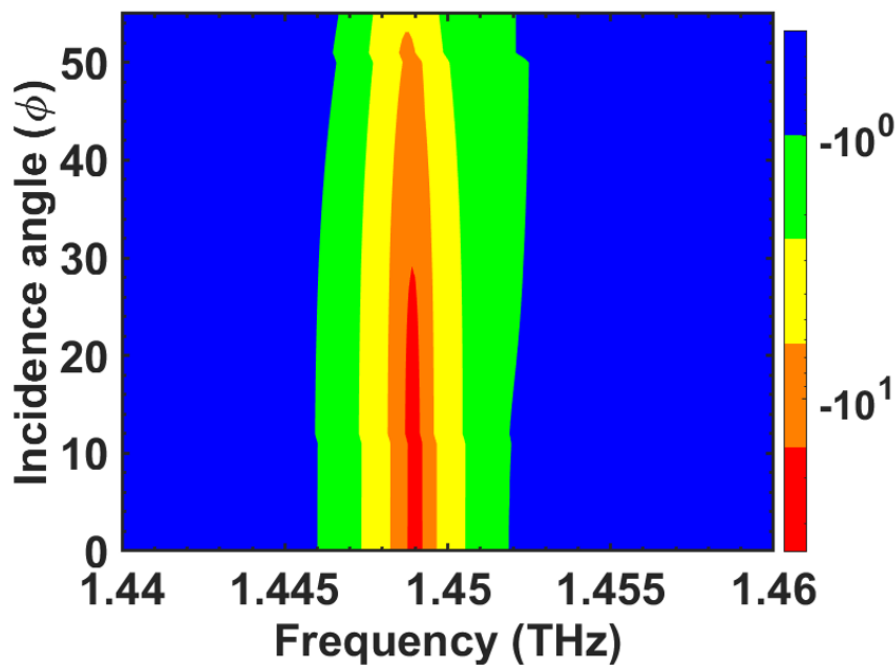


Figure 8.8. Angle dependencies of the all dielectric metasurface. Angle dependence of the proposed metasurface showing a sharp reflection up to around 50° of incidence terahertz beam. We show logarithmic scaling of the color bar as it helps better presentation of the plotting since a linear scaling obscures the true sharpness of the resonance peak.

considering both the frequency shift and absorption we investigate the $20 \mu\text{m}$ dielectric thickness for further analysis. We further change the dielectric refractive index and find that the resonance frequency shifts as the refractive index changes. The high field confinement at the Ge bar enables the device to detect the surrounding environmental changes.

An analysis of the frequency shift over refractive index is also carried out, with results shown in Fig. 8.10. This illustrates how the sensor can attain an average refractive index sensitivity of 55 GHz/RIU , with a high linearity of 0.9997, a negligible root mean square error (RMSE), and importantly with an excellent quality factor. The Q -factor variation over refractive index is also analyzed and shown in Fig. 8.10(b). We find that the highest Q -factor is achieved while the analyte dielectric constant is low and the Q -factor start to decrease with the increase refractive index. While the analyte refractive index is low, majority of the field confinement occurs at the high index germanium bar that creates sharp resonance. The sharp resonances are the key for achieving low FWHM and in turn the high Q -factor. When the analyte refractive index increase, less

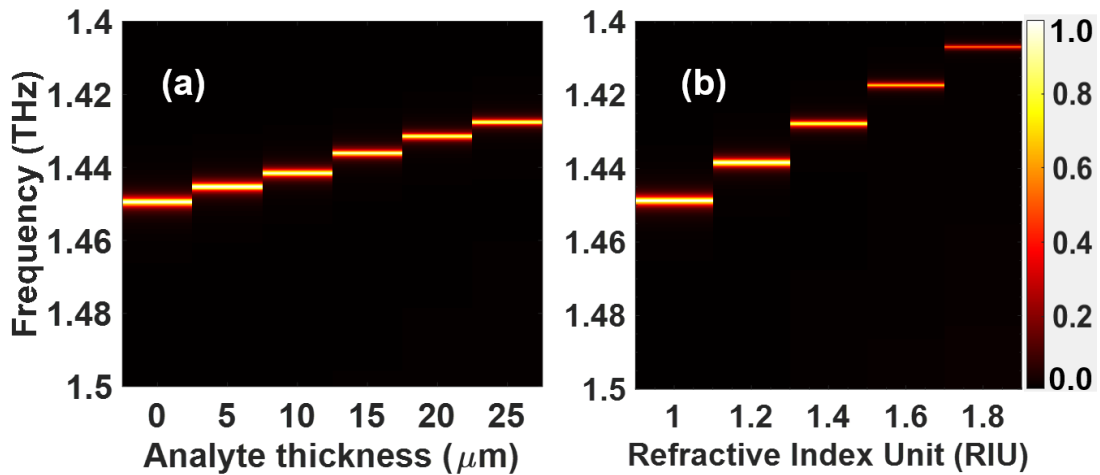


Figure 8.9. Performance as a sensor of the all dielectric metasurface. (a) Absorption spectrum by dielectric thickness variation by keeping the dielectric refractive index of water. (b) Absorption spectrum by dielectric refractive index variation by keeping the dielectric by keeping the dielectric thickness $20 \mu\text{m}$.

field confines at the high index bar while the mode fields also start to split into the imposed dielectrics. These broaden the resonance peak as shown in Fig. 8.9 and thus the FWHM increases. These in turn decrease the Q -factor.

The FOM is an important property that is directly related to sensitivity and the FWHM, as indicated in Eqn. 8.9. Owing to sharp resonance of the proposed metasurface, the FWHM is extremely narrow and therefore high FOM is obtained. Results indicate that the device can achieve a maximum FOM of 280. Apart from FOM, the LOD of the device is also analyzed. Considering 1% output uncertainty the proposed device shows a maximum LOD of 5.35×10^{-4} .

The proposed device properties at optimum design conditions is tabulated and shown in Tab. 8.1. Changing the refractive index of topmost dielectric layer, the resonance frequency, FWHM, Q -factor, sensitivity, FOM, and LOD are analyzed. It shows that the performance at refractive index of 1.0 is higher than other RI values, this is because the resonance peak is sharpened without any analyte.

The overall performance of the device is also compared with other related works found in the literature. The comparison in Tab. 8.2 indicate that the proposed metasurface shows improved performances in consideration to Q -factor and FOM in the terahertz

8.2 Results and discussion

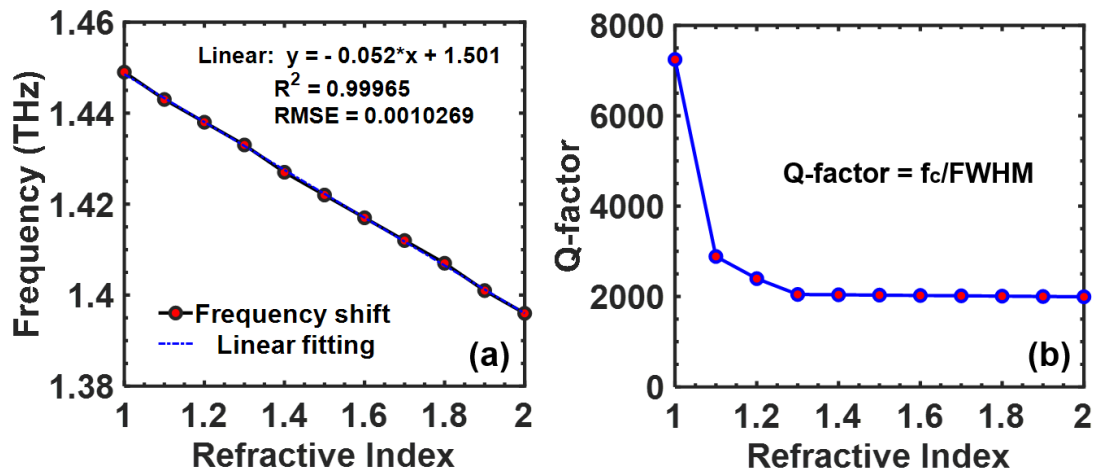


Figure 8.10. Linearity and Q-factor. (a) Frequency shift over refractive index, a linear fitting is also shown. (b) Achieved Q-factor over refractive index variation.

Refractive Index (RI)	f_c (THz)	FWHM (THz)	Q-factor	Sensitivity (GHz/RIU)	FOM (RIU ⁻¹)	LOD (RIU/GHz).
1.0	1.4491	0.0002	7245	56	280	5.35×10^{-4}
1.1	1.4435	0.0005	2887	51	102	5.88×10^{-4}
1.2	1.4384	0.0006	2397	53	88	5.66×10^{-4}
1.3	1.4331	0.0007	2047	53	88	5.66×10^{-4}
1.4	1.4278	0.0007	2039	52	74	5.76×10^{-4}
1.5	1.4226	0.0007	2032	52	74	5.76×10^{-4}
1.6	1.4174	0.0007	2024	52	74	5.76×10^{-4}
1.7	1.4122	0.0007	2017	52	74	5.76×10^{-4}
1.8	1.407	0.0007	2010	52	74	5.76×10^{-4}
1.9	1.4018	0.0007	2002	52	74	5.76×10^{-4}
2.0	1.3967	0.0007	1995	51	72	5.88×10^{-4}

Table 8.1. Properties of the proposed high-Q device at optimum design parameters obtained by genetic algorithm. This indicating that the FWHM is narrow and therefore the Q-factor is reasonably high.

frequency range. To the best of our knowledge the achieved Q-factor and FOM are the maximum in the terahertz frequency range.

References	Operating frequency	Q-factor	Sensitivity	FOM (RIU ⁻¹)	LOD (RIU/GHz)
(Cong <i>et al.</i> 2015)	terahertz	11.6	23.7% RIU ⁻¹	2.30	–
(Meng <i>et al.</i> 2012)	terahertz	180	77.25 mm/RIU	8.14	–
(Chen <i>et al.</i> 2009)	terahertz	13.6	1200 nm/RIU	2.86	–
(Jansen <i>et al.</i> 2011)	terahertz	31	–	–	–
(Xie <i>et al.</i> 2018)	terahertz	58	–	–	–
(Al-Naib <i>et al.</i> 2009)	gigahertz	300	–	–	–
(Srivastava <i>et al.</i> 2016)	terahertz	328	–	169	–
(Tian <i>et al.</i> 2020)	near-infrared	640	–	–	–
(Chen and Fan 2020)	terahertz	212.19	–	–	–
This thesis	terahertz	7245	56 GHz/RIU	280	5.35×10^{-4}

Table 8.2. Performance analysis of the proposed high Q metasurface with prior reported metasurfaces. The Q-factor and the FOM are the key performance parameters of the proposed germanium metasurface.

In summary, we have demonstrated a BIC enabled metasurface that shows highest (to our knowledge) Q-factor and FOM in the terahertz frequency range. The metasurface is governed by the out-of-plane asymmetry of the Ge pattern that is created by different Ge thickness. To prove the sensitivity to external environments we place a dielectric on the top surface. Changing the refractive indices of the top dielectric we found a maximum refractive index sensitivity of 56 GHz/RIU, interestingly the sensitivities comes with a highly linearity of 0.999. Beside obtaining high Q-factor, narrow FWHM, high FOM, and high linearity we also found an estimate of sensor LOD which is in the order of 10^{-4} .

8.3 Fabrication of the all-dielectric metasurface

We fabricate a slightly different metasurface structure, where the top rectangular pattern is replaced by elliptical pattern. Therefore, by using ellipse as a resonator we optimized the structure using genetic algorithm. We also replace the resonator material as silicon, instead of using germanium. The new optimized dimension of the metasurface is shown in Fig. 8.11.

8.3 Fabrication of the all-dielectric metasurface

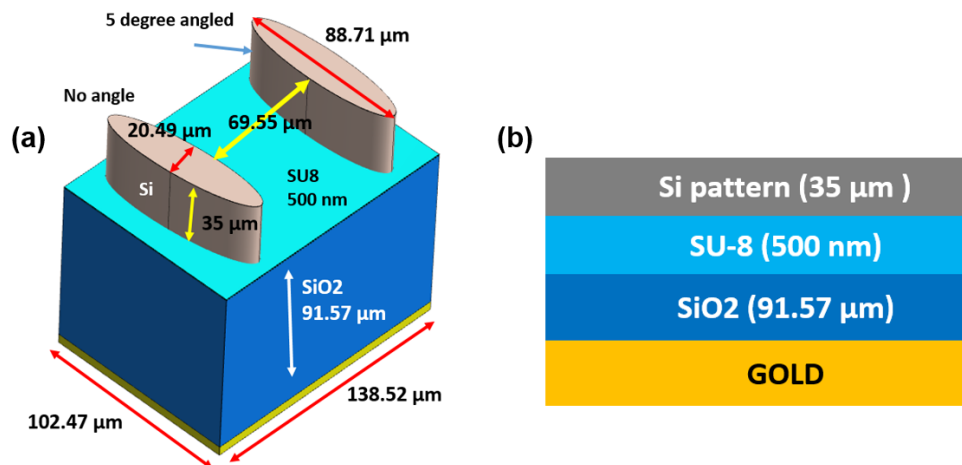


Figure 8.11. Schematic of the structure contains elliptical resonator. (a) Schematic of the metasurface structure, (b) showing the materials used and their dimensions.

To realize the metasurface absorber, an unconventional fabrication procedure is car-

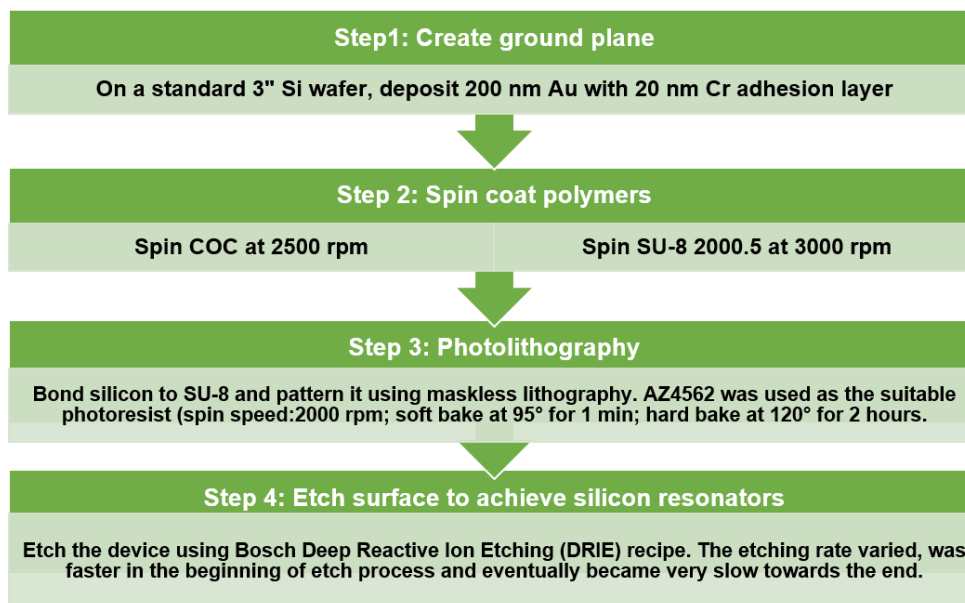


Figure 8.12. Step-by-step fabrication method of the all dielectric silicon metasurface.

ried out. Typically, the fabrication processes involves a standard photo-lithography patterning and plasma etching process to establish the resonators on polymers. Firstly, gold was deposited as the ground plane on a silicon wafer. Cyclic Olefin Copolymer (COC) and SU-8 films of desired thicknesses are spun on gold. This process was immediately followed by bonding of high resistive silicon wafer to the 500 nm thick SU-8. This silicon was patterned through mask less lithography and developed using a suitable developer. Thereafter, the silicon was dry etched using Bosch recipe. This deep

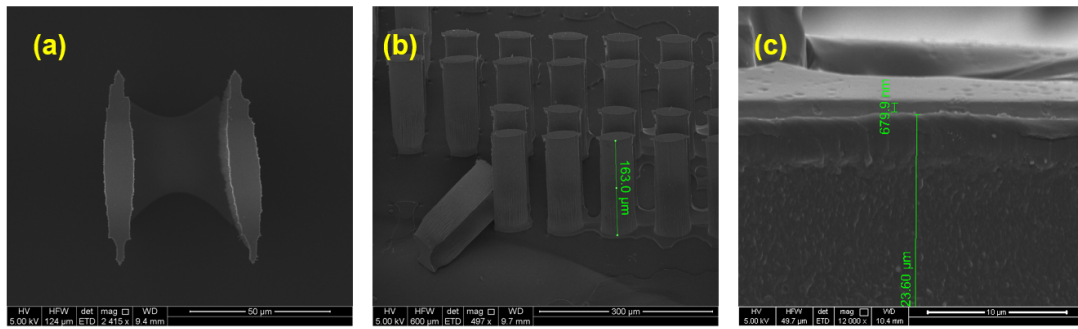


Figure 8.13. SEM images of the fabricated samples. (a) SEM image of the unit cell, (b) SEM image of the sample showing the thickness of the silicon resonator, (c) SEM image of the fabricated sample showing the thickness of COC and SU-8.

silicon etch recipe uses a two-step plasma process which alternates between deposition (C_4F_8) and etching (SF_6). Fig. 8.12 is a schematic highlighting the fabrication sequence. After following the procedure indicated at Fig. 8.12 we did our first trial of fabrication.

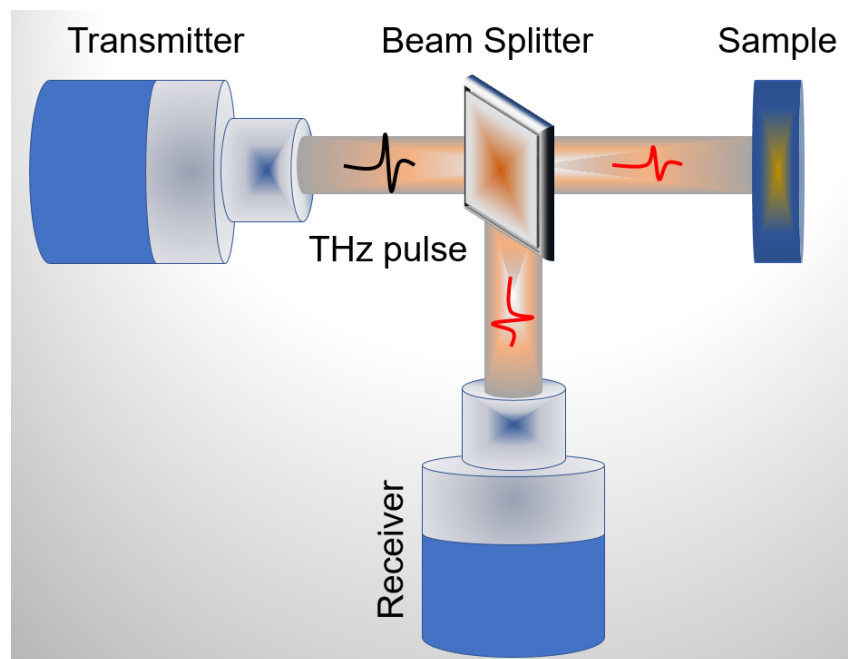


Figure 8.14. Experimental setup for reflection measurement, indicating the positioning of transmitter, beam splitter, sample, and receiver.

We got the dimensions of background COC, and SU-8 as optimized but a significant variation of our top resonator. In the second trial we optimized the background dielectric thickness a little, and processing for the fabrication is going on.

8.4 Experiment on the metasurface

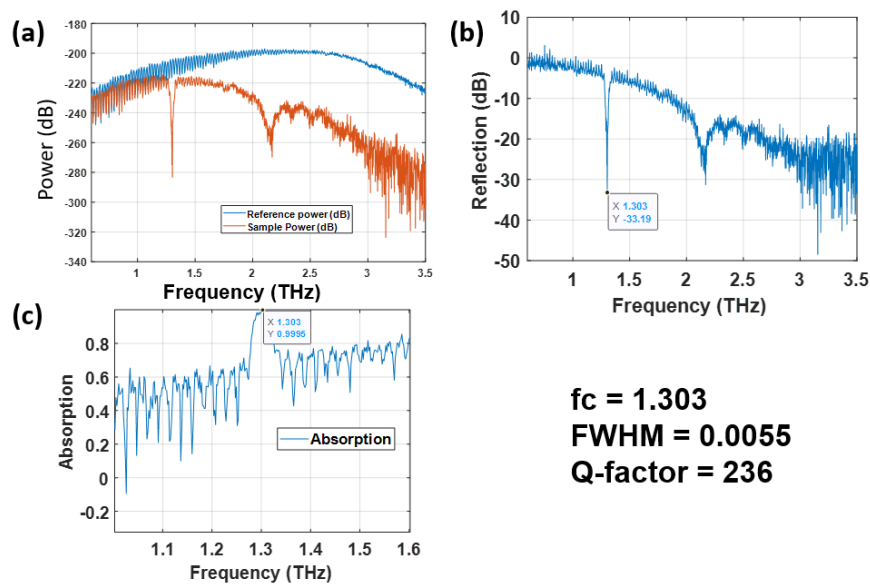


Figure 8.15. Experimental outcome of the fabricated metasurface. (a) Indicating the measured power of the referenced and sampled signal, (b) showing the measured reflection spectra where a clear resonance peak is observed, (c) the absorption spectra showing almost unit absorption.

The SEM images of the fabricated samples is shown in Fig. 8.13. From where the unit cell, and dimension of parameters can be seen. As compared to the optimized structure, shown in Fig. 8.11, we can see a clear difference of material thickness's on the fabricated samples showing in Fig. 8.13. With the obtained thickness's in fabrication we carry out the simulation further and found a Q -factor of around 800 that is significantly lower than the optimized dimensions where we got a Q -factor of around 4000.

8.4 Experiment on the metasurface

An experimental analysis of the sample that we got in the first fabrication trial is carried out. The schematic of the experimental setup is shown in Fig. 8.14. As the optimized sample is a reflector and works in oblique incidence angle therefore we need to use the beam splitter. The beam splitter has a splitting ratio of 50%, meaning half of the incoming beam from the transmitter transmits towards and sample and reflects back towards the beam splitter. The reflected signal from the sample is then directs towards the receiver.

The experimental outcome of the fabricated metasurface is shown in Fig. 8.15. The reflection spectra showing in Fig. 8.15(b) indicating a sharp clear peak around 1.3 THz that exactly matches with the simulation. The Q -factor we get is around 250 that is less than expected, the is because of the change of material properties during fabrication. Moreover, we can see a clear fabrication imperfection where the SU-8 is not uniformly distributed over the COC surface, this may also affecting the result. However, in general there is a good match of the experiment and simulation outcome in regards to position of the resonance frequency.

8.5 Conclusion

In summary, we have demonstrated the simulation of a BIC enabled high q all dielectric metasurface, and further fabrication and experiment on a slightly different metasurface. We can see both the simulated and experimented metasurface showing remarkable property at terahertz, which can be suitable for developing advanced terahertz devices. Owing to the performance shown by the studied metasurfaces, it may pave the way for realizing ultra-fast meta-devices and affords new possibilities for exploring next-generation optoelectronic devices.

In the following Chapter, we summarizes our discussion and concludes the thesis. We present the aim, methodology, results, and future directions for each work we carried out.

Conclusion and future remarks

THIS chapter concludes the work presented in this thesis. Chapter 1, 2 and 3 contains the relevant background information, the properties of the materials used, and a brief review of terahertz optical fibres. This covers the motivation behind the studies, the frequency of interests, the materials used to design the photonic devices, and the waveguiding, simulation, fabrication, and experimental methodologies of terahertz optical fibre. Chapter 4 to 5 describe the original contributions to the design and realization of terahertz waveguides and gas sensor. Chapter 5 also presents a table-top fabrication method to fabricate any kind of terahertz optical fibre. Chapter 6 presents the contribution related to fibre based plasmonic sensors in the visible to mid-IR range. Chapter 7 and 8 presents the contribution related to plasmonic metasurface. Specially, Chapter 7 shows a graphene based tunable plasmonic metasurface and Chapter 8 shows an all dielectric high- Q metasurface in the terahertz regime. Lastly, an outlook for future research on terahertz metasurfaces is presented.

9.1 Thesis overview

The overview of the thesis including the motivation each study, their methodology, the obtained results, and the future directions are discussed in this chapter.

9.2 Chapter 2: Experimental analysis of glasses and polymers: materials for terahertz

9.2.1 Aim

Use of correct optical and dielectric properties of materials are important for designing and analysing any photonic devices. Keeping this in mind, the main aim of this work is to obtain the correct optical, thermal, and chemical properties of selected materials that are frequently used for terahertz applications.

9.2.2 Methodology

Samples of Topas (5013 L-10) and Zeonex (480R) grades are prepared from raw pellets. Initially, filaments of those materials are made using a Filabot EX2 filament Extruder and used for 3D printing of the samples. We put the pellets inside a metal holder placed into a furnace at 200°C for 48 hours. The samples are then cooled down and removed from the holder, and then cut and polished to make both the surfaces flat, smooth and parallel.

The polishing is graded using progressively finer silicon carbide (SiC) sandpaper, of grit sizes 120, 240, 320, 400, 800, 1200 and 2500 μm respectively. The samples are then given a final polish and smoothed using water based diamond suspension of 3 μm particle size. The sample of UV-resin is made using Stereolithography (SLA) 3D printing technology and polished before the experiment. Note that all other samples are cut and polished using the same procedure and all the measured samples have similar thickness of around 3 mm.

Finally, transmission setup of the THz-TDS is used to characterize the samples in a closed environment purged with nitrogen.

The chemical stability test is carried out in highly acidic (low pH) H_2SO_4 (10 M) solution, saline NaCl (3.5 M) solution, and basic (high pH) NaOH (10 M) solution (here, M indicates molar concentration). These solutions were agitated by a mechanical shaker at 200 rpm for 24 hrs to observe any effect of a chemical attack on the materials.

For thermal stability testing, the thermogravimetric (TG) and derivative thermogravimetric (DTG) analysis were carried out using non-isothermal thermogravimetric analysis setup, TA Instruments (Q-500, Tokyo, Japan). The thermal analyzer is temperature calibrated between experiments using the Curie point of nickel as a reference. The experiment is performed under a nitrogen environment at a purge rate of 60 ml/min.

9.2.3 Results

At terahertz frequencies, the dielectric and optical properties including the refractive index, dielectric constant, bandwidth, absorption coefficient, dielectric loss, and transmittance of the samples are measured and signal processed. This is in good agreement with the literature and from here we confirm the properties of materials that we further use for designing and fabricating fibre and metasurface based samples.

From the chemical stability test, no significant mass change ($\pm 1.5\%$) is found for any of the tested materials and this demonstrates the extreme chemical stability of these materials against acidic and saline environments.

From the thermal stability testing we find that Teflon has highest thermal stability among the experimented samples and starts losing its weight due to evaporation from around 525°C and ends up at around 620°C . While the other three materials HDPE, Topas, and Zeonex have shown similar thermal characteristics and start losing weight from 440°C and ending up at around 480 to 500°C .

9.2.4 Future direction

There are significant directions to research on materials. One future work may be to make plasmonic polymer materials. This can be carried out by either mixing low loss polymer solvent with either graphene or metals, gold, silver, and then using that material as a plasmonic material. This way the chemical and thermal stability will also be increased with a sacrifice in loss. This hybrid material can then be used to make a

sensor that will not required external plasmonic material coating.

The content of Chapter 2 is published in *IRMMW-THz-2019*, and *IEEE Access* (Islam *et al.* 2019e, Islam *et al.* 2020b).

9.3 Chapter 3: Terahertz optical fibre

9.3.1 Aim

Terahertz optical fibres are essential for developing the full potential of complex terahertz systems. In Chapter 3, we aim to combine the recent development of terahertz optical fibres with different geometries and guiding mechanisms, the background materials, the fabrication and measurement techniques, and potential applications.

9.3.2 Methodology

We examine various optical fibre types including tube fibres, solid core fibre, hollow-core photonic bandgap, antiresonant fibres, porous-core fibres, metamaterial-based fibres, and their guiding mechanisms. The past and present trends of fabrication methods, including drilling, stacking, extrusion and 3D printing, are elaborated. Fibre characterization methods including different optics for terahertz time-domain spectroscopy (THz-TDS) setups are reviewed and application areas including short-distance data transmission, imaging, sensing, and spectroscopy are discussed.

9.3.3 Results

The work on terahertz optical fibre discussed throughout Chapter 3 combines, the analysis of suitable materials that can be used to make a low loss terahertz optical fibre; a comprehensive review of various geometry including the microstructured photonic crystal fibre, the hollow-core fibre, the antiresonant fibre and the metamaterial-based fibres; the guiding mechanism of each type of fibres; an analysis of different methodology of fibre fabrication and characterization.

From the discussion, it can be noted that every fibre has some advantages and disadvantages and there is a trade-off between low loss, bandwidth and fabrication feasibility. For example, hollow-core fibre can provide low loss terahertz guidance and comparatively simple fabrication at the expense of low bandwidth of operation. On the other hand, porous fibre can provide larger bandwidth but with higher loss and increased fabrication complexity as compared to hollow-core fibres. Metamaterial-based waveguides are still in their infancy by comparison.

The various fabrication methodologies discussed indicate the possibilities of fabricating various geometries of terahertz optical fibres. For example, the drilling method is suitable for fabricating circular hole patterns only, whereas the extrusion and 3D printing techniques can fabricate any type of complex and asymmetric fibre geometries. The most common method for terahertz fibre characterization is the use of THz-TDS where different optics setups can be used to focus signal onto the fibre core. Among the various terahertz applications short-range high throughput transmission, gas, and chemical sensing and imaging show significant promise.

9.3.4 Future direction

Free-space terahertz wave propagation is still widely used, but terahertz waveguides and, in particular, optical fibres are gaining increasing attention. Their importance is related to the concept of developing complex terahertz configurations that potentially combine sources and detectors with a reliable and simple way of terahertz transmission. Antiresonant fibres stand out among other hollow-core fibres, due to their robustness to fabrication tolerances, geometrical simplicity, and hence fabrication feasibility. Combining simplicity and low attenuation with high bandwidth, single-mode guidance, and low dispersion is, for most applications, the main target. Fibres possessing composite cladding, with metamaterial inclusions, better confine the terahertz signal (Li *et al.* 2016a), and fibres that are helically twisted to guide modes with orbital angular momentum are two of the most exciting directions for actual and near future investigations.

Different manufacturing techniques are being used to produce such fibres, but 3D printing technology represents a clear advantage in terms of cost, time, easiness, and

potential for manufacture of speciality fibres (Cruz *et al.* 2018) already integrated with other components required for a particular application. The whole fibre cross-section can be produced simultaneously (Atakaramians *et al.* 2009a)—this is different from 3D printing or stacking-and-draw, for example. Simple and complex waveguides can be obtained by carefully designing the extrusion die, ram speed and furnace temperature profile. Extrusion of fibre projects with intrinsic low confinement loss due mostly air guidance, and while using low terahertz loss materials, is an interesting route to be wider explored.

Due to their large overall dimensions, with external diameters as big as 10 mm in some situations (Yang *et al.* 2016, Lai *et al.* 2009), some terahertz fibres are not mechanically flexible and this reduces the practical interest in applications requiring long waveguide lengths. Investigating ways of producing flexible fibres via selection of the required mechanical properties the fibre material and the fibre geometry, such as fibres with high air filling fraction and thin external jackets, as well as studying waveguide curvature loss will help develop this field further. Combining special coatings such as graphene (Mittendorff *et al.* 2017) could extend the functionalities of terahertz fibres and will likely be a hot topic in this vibrant research area.

Terahertz waves have been demonstrated as promising technology to non intrusive analysis in biological, medical, chemical, and industrial applications. However, compact, portable, cost effective and robust devices need to be developed. In this scenario, the terahertz optical fibres, usually fabricated in short lengths, represent a challenge and a great opportunity to make such devices a reality.

The content of Chapter 3 is published in *Optics Express* (Islam *et al.* 2020a).

9.4 Chapter 4: Terahertz waveguides: modelling and analysis

9.4.1 Aim

After a brief review of terahertz optical fibre, the aim of Chapter 4 is to design, simulate, and analyse various terahertz optical fibre to get an optimal fibre for terahertz

guidance and sensing. The goal is not only to achieve low loss but also high birefringence, and low and flat dispersion. For creating birefringence it is important to have asymmetry among the polarization modes, therefore we use either elliptical, rectangular, or circular air holes structured in a way so that it can create birefringence. There is a trade-off between the loss and the birefringence when one increases another decrease or vice versa.

9.4.2 Methodology

The design and simulation of all the contributed waveguides are carried out using the full vector Finite Element Method (FEM) method based on commercially available software COMSOL multiphysics. The *Electromagnetic Waves, emw* solver with a *Physics-controlled mesh* sequence having an *Extremely fine* mesh element size is used to get high accuracy output from the simulation software. A perfectly matched layer (PML) boundary condition is considered at the outer surface to make the computational region finite. In all of the waveguide design we choose either Topas (COC) or Zeonex (COP) because of their remarkable properties at terahertz.

9.4.3 Results

To achieve the goal, we design and investigate both symmetric and asymmetric terahertz waveguide in consideration to loss, birefringence, dispersion, and sensing. We achieve low loss by both symmetrical and asymmetrical fibre structure (Islam *et al.* 2016a, Islam *et al.* 2017a, Islam *et al.* 2018g, Islam *et al.* 2018d, Islam *et al.* 2018h, Islam *et al.* 2017c, Islam *et al.* 2017d, Islam *et al.* 2017b), however to achieve high birefringence, required for polarization preserving applications, we need to design asymmetrical fibre structure (Islam *et al.* 2018c, Sultana *et al.* 2019b, Islam *et al.* 2018f). The high sensitivity is achieved in hollow core asymmetrical fibre where birefringence is also required (Islam *et al.* 2017a, Islam *et al.* 2018j, Ahmed *et al.* 2019, Islam *et al.* 2019a).

9.4.4 Future direction

Fibre design with low loss, high birefringence, near zero dispersion, and high sensitivity all are achieved by various designs and presented in this chapter. But there is scope

for work on designing simpler terahertz waveguides that can be realized by straightforward fabrication and can be further experimented on for transmission and sensing.

The content of Chapter 4 is published in *IEEE Sensors Journal*, *IET Communications*, *Optics Communications*, *Applied Optics*, *Optical Materials*, *Optical fibre Technology*, *Electronics Letters*, *Optik*, *Photonic Network Communications*, and *Sensing and Biosensing Research* (Islam *et al.* 2017a, Islam *et al.* 2018j, Islam *et al.* 2018f, Islam *et al.* 2018d, Islam *et al.* 2018h, Islam *et al.* 2019a, Ahmed *et al.* 2019, Sultana *et al.* 2019b, Islam *et al.* 2018c, Islam *et al.* 2018g, Islam *et al.* 2017c, Islam *et al.* 2017d, Islam *et al.* 2017b, Islam *et al.* 2016a).

9.5 Chapter 5: Tabletop fabrication for terahertz specialty optical fibre sensor

9.5.1 Aim

The aim of this chapter is to develop a novel antiresonant hollow core terahertz optical fibre that exhibits low loss, near-zero dispersion, wide operating bandwidth, and is suitable as an ultra-sensitive gas sensor. The another aim is to fabricate the fibre by exploiting an efficient low-cost single-step extrusion method.

9.5.2 Methodology

Similar to Chapter 4, the design and simulation of the hollow core fibre is carried out using the full vector Finite Element Method (FEM) method based software COMSOL multiphysics. Analytical analysis is also carried out to validate the simulation result. An efficient, simple, and cost-effective method of fabricating asymmetric complex polymer fibres are used to fabricate the fibre. The experimental analysis of the fibre is also carried out using the TAS7400TS Advantest terahertz system.

9.5.3 Results

The experimental analyses demonstrate that fibres with total attenuation and coupling loss—of a few dB in the studied frequency range, reach values as low as 2 dB

at 3.4 THz. Also, fibres with a near-zero dispersion of less than 0.6 ps/THz/cm are achieved. The results reported herein reveal the potential of such a remarkably simple fabrication technique for obtaining microstructured terahertz hollow-core optical fibres. The results also demonstrate the gas sensing ability of terahertz optical fibre.

9.5.4 Future direction

As a possible next step of this research would be to fabricate the fibre using a hybrid material. Here, by hybrid we mean the combination of two or more material, Zeonex and graphene for example. This material is then be able to create plasmons and that will be suitable for biological sensing. This will reduce the hardle of coating a polymer fibre by another plasmonic material.

The another direction can be to coat the fibre cladding with graphene and this may reduce the loss by reducing the scattering loss and make the fibre more suitable for gas sensing.

The content of Chapter 5 is submitted for publication at *Advanced Photonics Research* (Islam *et al.* 2021).

9.6 Chapter 6: Surface plasmon resonance biosensor

9.6.1 Aim

The aim of Chapter 6 is to design and analyse optical fibre-based plasmonic sensors that operate in the visible to mid-infrared regime instead of the terahertz regime. The aim is also to fabricate one of the optimized fibres for further use for sensing experiments.

9.6.2 Methodology

The simulation of the plasmonic sensors are carried out using COMSOL multiphysics simulation software. A simplified form of one of the optimized sensors is fabricated by extrusion technique, the fabricated fibre is then spliced using a single mode fibre

9.7 Chapter 7: Electrically tuneable graphene metasurface

because the usable length of the designed fibre is short. The fibre surface is then gold-coated using sputtering technique to be used for further experimental analysis.

9.6.3 Results

The simulation results indicate that the fibres presented in Chapter 6 showing significant performance improvement in consideration to loss, sensitivity, and design simplicity over the previously reported plasmonic sensors. In our analysis, a maximum wavelength sensitivity of 111000 nm/RIU, amplitude sensitivity of 2050 RIU⁻¹, resolution of 9×10^{-7} RIU, and limit of detection (LOD) of 8.12×10^{-12} RIU²/nm is achieved. Importantly this is achieved in a fibre having only three air holes with a significant low loss of 0.79 dB/cm. To our knowledge, this is a remarkable achievement in plasmonic sensing.

9.6.4 Future direction

The fabricated and coated fibre can be used to further analysis of biological sensing. Surface fictionalization can be carried out to detect specific proteins/molecules including viruses such as COVID-19. On the gold coated surfaces nanoparticles of graphene can also be deposited as it may enhance the sensing performance.

The content of chapter 6 is published in *IRMMW-THz-2018*, *Optics Express*, *IEEE Access*, *Optics Letters*, *Journal of Optical Society of America B*, and in *IEEE Sensors Journal* (Islam *et al.* 2018e, Islam *et al.* 2018i, Islam *et al.* 2019b, Islam *et al.* 2019d, Islam *et al.* 2019c, Mollah and Islam 2020).

9.7 Chapter 7: Electrically tuneable graphene metasurface

9.7.1 Aim

Plasmonic superabsorption (also known as perfect absorption) and wave trapping by means of plasmonic metasurfaces have attracted considerable attention due to promising new techniques for light manipulation, with potential applications in the field

of energy harvesting, filtering, thermal imaging, electromagnetically induced transparency, and high performance sensing (Grant *et al.* 2016, Yang *et al.* 2017, Kim *et al.* 2016, Liao *et al.* 2016, Keshavarz and Vafapour 2019). The aim of Chapter 7 is to study on a multilayer graphene metasurface that is able to trap the light strongly and enhance the surface plasmon effect. A further aim is to make the metasurface suitable for biochemical sensing.

9.7.2 Methodology

The design and simulation of the graphene metasurface is carried out using Finite Element Method (FEM) based software, CST microwave studio where a genetic algorithm (GA) is used to optimize the geometric parameters, and metasurface tunability is achieved via an external gate voltage on the graphene.

9.7.3 Results

From the simulation result of the optimized metasurface we find strong field confinement in graphene pattern. Varying the graphene chemical potential, the number of absorption bands can be varied. We show that at a chemical potential of 0.2 eV, the metasurface can achieve five absorption bands, which is promising for sensing applications. The metasurface has a maximum sensitivity of 76 GHz/RIU, with a linearity of $R^2 = 0.9711$ and a considerable LOD. The metasurface can also illustrate similar optical performance over a wide acceptance angle of the incident terahertz beam that is also robust against fabrication tolerances.

9.7.4 Future direction

More work can be carried out using continuous graphene sheets or graphene nanoparticles in the top surface to demonstrate sensor performance. The further work can be the realization of the graphene metasurface for biosensing applications.

The content of chapter 7 is published in *IRMMW-THz-2019*, and *Carbon* (Islam *et al.* 2019f, Islam *et al.* 2020d).

9.8 Chapter 8: Bound states in the continuum for guided terahertz plasmons

9.8.1 Aim

The aim of this work is to design and analyse a high- Q metasurface at terahertz. The further aim is to realize the metasurface to plasmonic sensing application.

9.8.2 Methodology

Similar to the previous Chapter, the design and simulation of the high- Q metasurface is carried out using Finite Element Method (FEM) based software, CST microwave studio where a genetic algorithm (GA) is used to optimize the geometric parameters.

To realize the metasurface absorber, an unconventional fabrication procedure is carried out. Typically, the fabrication processes involve a standard photolithography patterning and plasma etching process to establish the resonators on polymers. Note that THz-TDS having reflection spectroscopy is used to experiment on the fabricated metasurface.

9.8.3 Results

In simulation we find that the optimized metasurface can achieve a high- Q factor of around 4000 which is highest at terahertz to our knowledge. We find strong field confinement at the top silicon resonator which is highly sensitive to the external environment. Changing the top dielectric refractive indices we found a maximum refractive index sensitivity of 56 GHz/RIU, interestingly the sensitivities come with a highly linearity of 0.999. Beside obtaining high Q factor, narrow FWHM, high FOM, and high linearity we also found an estimate of sensor LOD which is in the order of 10^{-4} .

9.8.4 Future direction

Further experiment on the metasurface can be carried out to examine the sensing performance. A liquid flow channel with an inlet and outlet adjacent to the top surface of

the metasurface can be made. This will allow the top surface to be filled with biochemical analytes.

The content of this chapter is published in *IRMMW-THz-2020* (Islam *et al.* 2020c), and an extended version is to be submitted in a journal.

Terahertz experiment setups

This research has implemented extensive experimental studies on materials, fibres, and metasurfaces in Chapter 2, Chapter 5, and Chapter 8. The setups are outlined in this appendix.

A.1 Terahertz setup for material characterization

The terahertz setup for material characterization as discussed in Chapter 2 is shown in the following figure, Fig. A.1. This uses a dual-channel ultrashort pulse laser (Advantest TAS7400TS) with a pulse width of ≤ 50 fs (using 1.5 m fibre), employing a simple configuration for fiber-coupled, free space terahertz generation and detection. The phase modulation measurement method relies on the difference in phase (arrival time) due to changes in wave path. The reference and sample phases are then required to obtain the optical properties of the sample. The terahertz receiver Advantest model TAS1230 is fabricated with a photo-conductive antenna coupled to a hyper-hemispherical silicon lens in a fiber pigtailed compact housing.

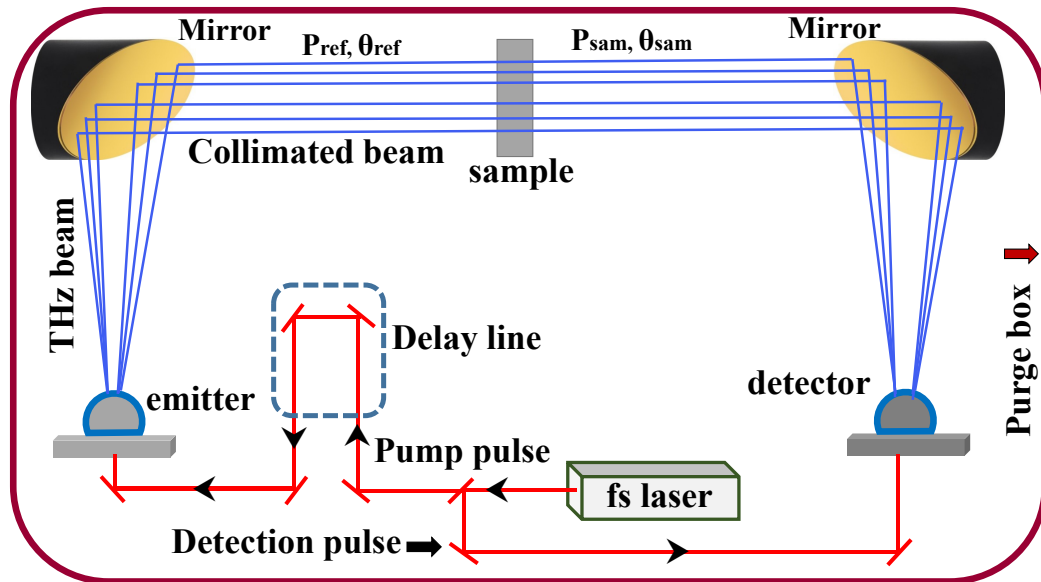


Figure A.1. Schematic of experimental set-up of the enclosed THz-TDS system with a purge box filled with nitrogen. Two parabolic mirrors creating a parallel beam where a sample holder is used to hold the sample, the reference signal (P_{ref} and θ_{ref}) is obtained by removing the samples whereas the sampled signal (P_{sam} and θ_{sam}) is obtained when a sample is in place as shown in the photograph, (b) the actual set-up, Islam *et al.* (2020b).

The Advantest model TAS1130 transmitter with a lithium niobate crystal waveguide has a bandwidth of 0.5 to 7 THz (Advantest 2021). Two off-axis gold-coated parabolic mirrors (Edmund optics) with an effective focal length of 150 mm are used to create a parallel collimated beam for spectroscopy. To ensure the beam passing through the sample, we insert an iris of diameter less than the sample diameter. The reason

for this standard setup is to obtain more averaged data from the measurements. In consideration to sample dimension, different types of sample holders were utilized to constrain the measurement to the sample and ensure consistent results. The system was enclosed with a custom made purge box to ensure negligible water vapors in the experiment system.

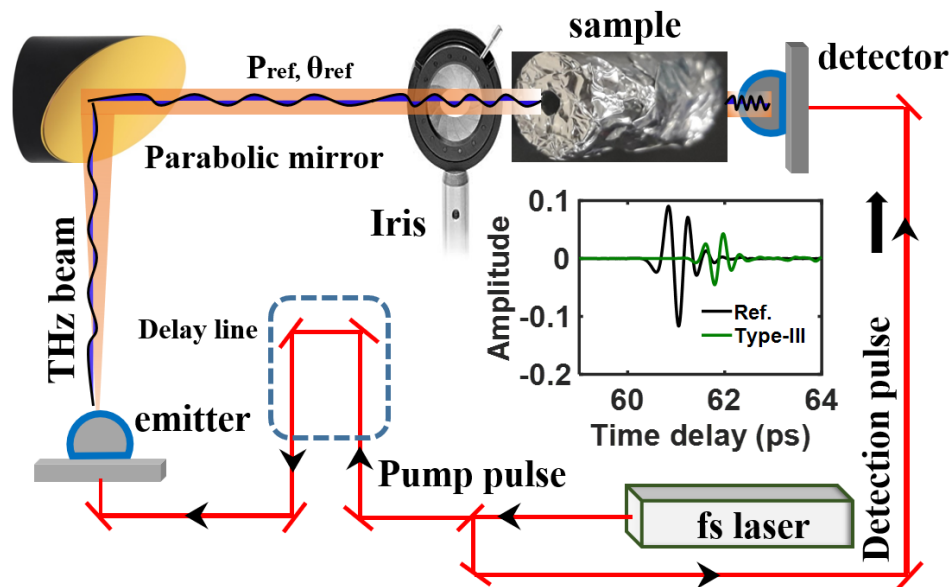


Figure A.2. The experimental setup for fibres transmission measurement. The setup encompasses a femtosecond (fs) laser, a terahertz emitter, a detector, a parabolic mirror, an iris, and the sample itself. The whole system is enclosed in a purge box containing dry air. The inset shows typical reference and sampled signals, Islam *et al.* (2021).

A.2 Experiment setup for terahertz fibre characterization

The experiment setup for terahertz fibre characterization as discussed in Chapter 5 is shown in the following figure, Fig. A.2. In the experiment, a gold-coated parabolic mirror with a focal length of 100 mm is used to focus the beam towards the waveguide core, and an iris is used to block undesired signals coupling to the core. The fibre waveguide is then placed on a translation stage, and a specially designed 3D-printed fibre holder is used to provide mechanical support. To ensure that the terahertz beam is coupled to the fibre core only, we wrap the waveguide with aluminum foil, while keeping the core region unblocked. The system is enclosed in a custom-made purge box filled with dry air, in order to minimize the presence of water vapor and avoid water-induced absorption. Additionally, care is taken to ensure minimal humidity

A.3 Experiment setup for terahertz metasurface characterization

levels inside the purge box, which was monitored with a hygrometer. Typical reference and sample signals are presented in the inset in Fig. A.2.

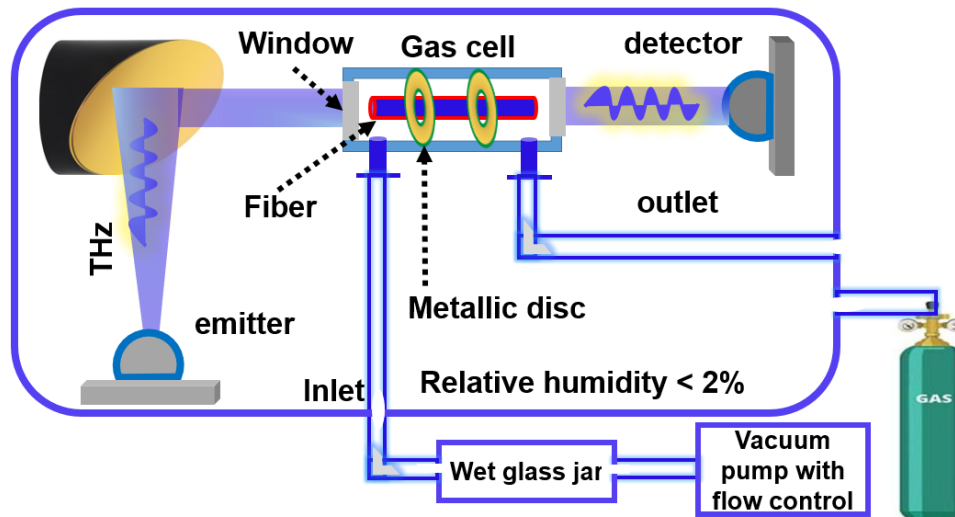


Figure A.3. The experimental setup for fibres humid air sensing. In this setup a vacuum pump is used for continuous flow of humid air. During the measurements, the flow rate through the cell is kept significantly low. The cell contains a tissue wetted by milli-Q water. Two metallic discs are used to hold the fibre straight and block the stray of the terahertz signal coming from outside of the fibre, Islam *et al.* (2021).

The fibre sensing is carried out in a slightly different experiment setup, as shown in Fig. A.3. In addition to the fibre transmission experiment, an additional gas cell, wet glass jar, and vacuum pump to control the vapour flow is used.

A.3 Experiment setup for terahertz metasurface characterization

The experiment setup for characterizing terahertz metasurface is presented, broadly discussed in Chapter 8. The schematic of the experimental setup is shown in Fig. A.4. As the optimized sample is a reflector and works in oblique incidence angle therefore the beam splitter has been used. The beam splitter has a splitting ratio of 50%, meaning half of the incoming beam from the transmitter transmits towards and sample and reflects back towards the beam splitter. The reflected signal from the sample is then directs towards the receiver. The experiment was carried out using a purge box filled

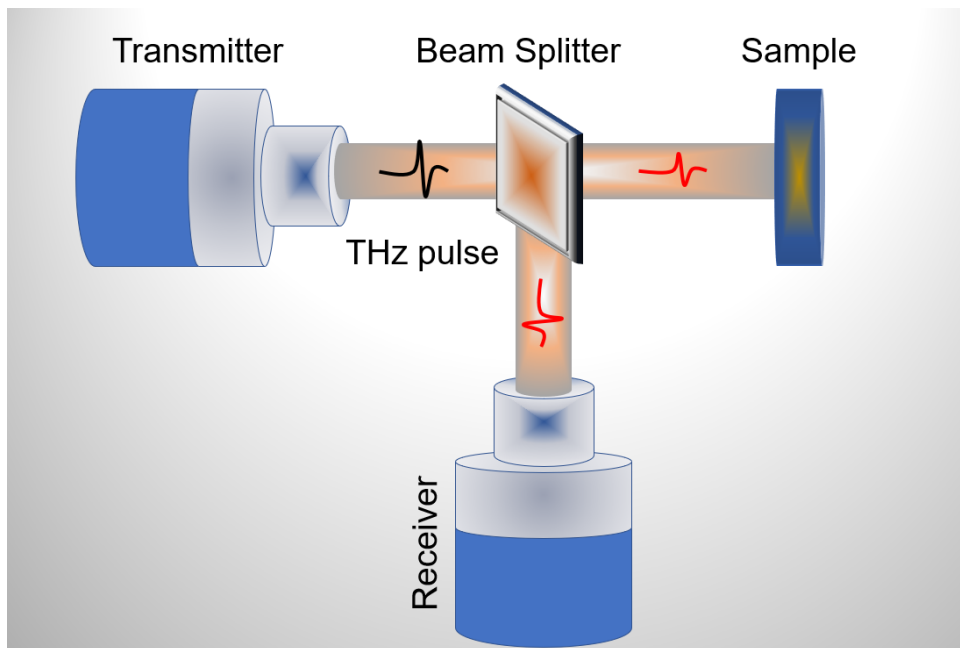


Figure A.4. The experimental setup for metasurface reflection measurement. In this setup a beam splitter is used to help measure the reflection. During measurement the system was enclosed in a purge box containing nitrogen.

with nitrogen, these makes sure there were no water vapour present inside the chamber. The reference signal was taken by placing a flat gold mirror instead of the sample which is then compared with the sampled signal to ensure the resonance peak.

Simulation procedure in COMSOL Multiphysics

B.1 Simulation tools

Maxwell's equations need to be solved to investigate the electromagnetic properties of the simulated wave propagation in the fiber. Using pure mathematical approach, it is difficult to find optimized fiber designs that can predict the characteristics of practical fiber. Because, the complex physics simulation in fiber model have the information about the simulation domains, material properties, 2D or 3D geometries, etc. On the other hand, only a very few simple canonical problems have been solved by Maxwell's equations.

Three popular computational electromagnetic methods are used to simulate the wave propagation and to numerically configure the geometries and boundary conditions for practical problems: finite-difference method (FDM), finite-volume method (FVM), and finite-element methods (FEM). Each method has its own advantages and disadvantages depending on the specific problems. Based on these methods, many commercial software packages are available, such as FDTD solutions, HFSS, COMSOL, IE3D and FEKO.

B.2 Finite element method

In this thesis we used FEM to simulate the fibre propagation modes and dispersion characteristics. The study of FEM is possible by electromagnetic simulation software, this include COMSOL Multiphysics, CST, HFSS, etc. The FEM is a full-wave numerical technique to obtain the approximate solutions for electromagnetic boundary value

B.3 COMSOL multiphysics

problems of the mathematical physics. The basic principle is to discretise the whole computing domain into finite number of triangles or tetrahedral sub-domains (mesh) so that the arbitrary geometries can be modelled accurately. As a result, the remarkable advantage of FEM is the flexibility in modelling of complicated geometries and distribution of media and the good handling capabilities of the inhomogeneous medium (Each element can have different material property). The perfectly matched layers (PML) need to be used in the FEM to truncate the mesh for the unbounded problems. The FEM can solve the linear, non-linear and 2D/3D problems. Furthermore, The FEM is a frequency domain method which makes it efficient in dealing with narrow-band problems.

B.3 COMSOL multiphysics

COMSOL Multiphysics software is a simulation platform that design devices and process the calculations according to the modelling workflow—from defining geometries, material properties and the physics that describe the specific phenomena for producing the accurate and trustworthy results based on the FEM method. The advantages of COMSOL Multiphysics is custom made simulation tools that contain all the benefits of a model built with the Model builder, without the extraneous information. The COMSOL Multiphysics software can run and test from the COMSOL Desktop, using Windows, macOS, and Linux operating system. In addition, COMSOL interfaces with a lot of useful third-party software, such as MATLAB and computer aided design (CAD) programmes. The step by step design procedure of a terahertz optical fibre is presented below.

B.3.1 Step A: Model wizard.mph

Launch COMSOL Multiphysics and select the Model Wizard. The Model Wizard is a good starting point, as it allows us to set up some initial project configurations. We can set the dimensionality for our model, choose the physics interface we would like to use and add the studies to define how the model should be analysed. Inside Model Wizard there is an option for Select Space Dimension for 3D, 2D axisymmetric, 2D, 1D Axisymmetric, 1D and 0D.

Model description

To simulate the fibre model as accurately as possible, we have to build a 3D model and run COMSOL simulation on the 3D fibre structure. However, due to large memory allocation and slow computation in 3D model, we applied the 2D model to simulate the fibre propagation modes and dispersion properties.

Select physics

The select physics interface tree can process the results for any engineering field such as AC/DC, Acoustics, Chemical Species Transport, Fluid Flow, Heat Transfer, Optics, Structural Mechanics and Mathematics.

Optics tree

The Optics tree in Select Physics are capable to analyse the Wave optics for Electromagnetic Waves, Beam Envelopes (ewbe), Electromagnetic Waves, Frequency Domain (ewfd), Electromagnetic Waves, Time Explicit (teew), Electromagnetic Waves, Transient (ewt).

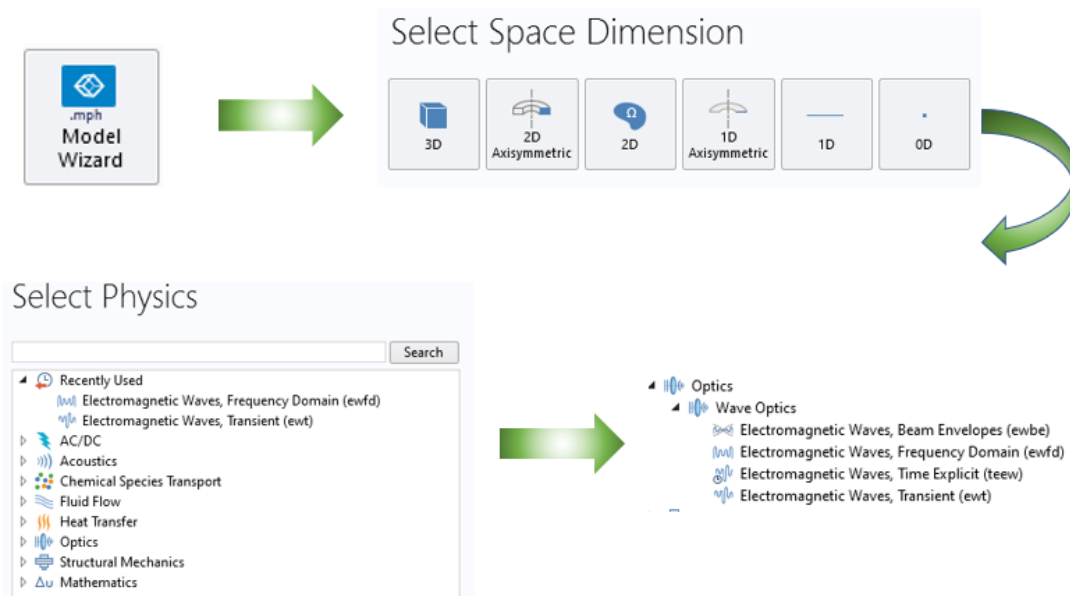


Figure B.1. Step by step COMSOL Simulation procedure. This include upto opening the *Wave Optics* module to use the *Electromagnetic Waves, Frequency Domain (ewfd)*.

The wave optics module

The wave optics module is an add on to the COMSOL Multiphysics software, is an efficient choice for optical modelling. There are features available for modelling optical systems, such as the material library includes dispersion relations for the refractive indices of more than 1400 materials. The wave optics module includes tools for modelling the following:

- Device, crystals
- Terahertz device
- Optical fiber
- Gratings
- Nonlinear optics
- Lasers
- Metamaterials
- Graphene
- Optical sensors.

Select the **Electromagnetic Waves, Frequency Domain (EWFD)** and click the **Add** button. The physical interface adds the Electromagnetic Waves, Frequency Domain (EWFD). The dependent variable is Electric field (E) and electric field components are E_x , E_y , E_z . The Wave Optics, Electromagnetic Waves, Frequency Domain interface is used to solve for time-harmonic electromagnetic field distributions.

To continue press the **Study**. The physics interface supports the study types. General studies support the Frequency Domain, Eigenfrequency and preset studies for selected physics interfaces supports the adaptive frequency sweep, Frequency Domain, Modal, Mode Analysis, Wavelength Domain, and Boundary Mode Analysis.

- The Frequency Domain study type is used for source driven simulations for a single frequency or a sequence of frequencies.

- The Eigenfrequency study type is used to find resonance frequencies and their associated eigenmodes in resonant cavities.
- This physics interface solves the time-harmonic wave equation for the electric field.

The next step is to add the **Frequency Domain** in study for electromagnetic wave propagation, it is used to compute the transmission and reflection versus frequency.

The final step before designing the geometry is to push the **Done** after adding the selected study and selected Physics Interface and finish the initial setup.

Precise Initial setup: 1. 2D as the space dimension

2–4. Optics ⇒ Wave optics ⇒ Electromagnetic Waves, Frequency Domain (ewfd) as the physics interface ⇒ Add

5–6. General Studies ⇒ Frequency Domain as for study

7. press Done to finish the initial setup.

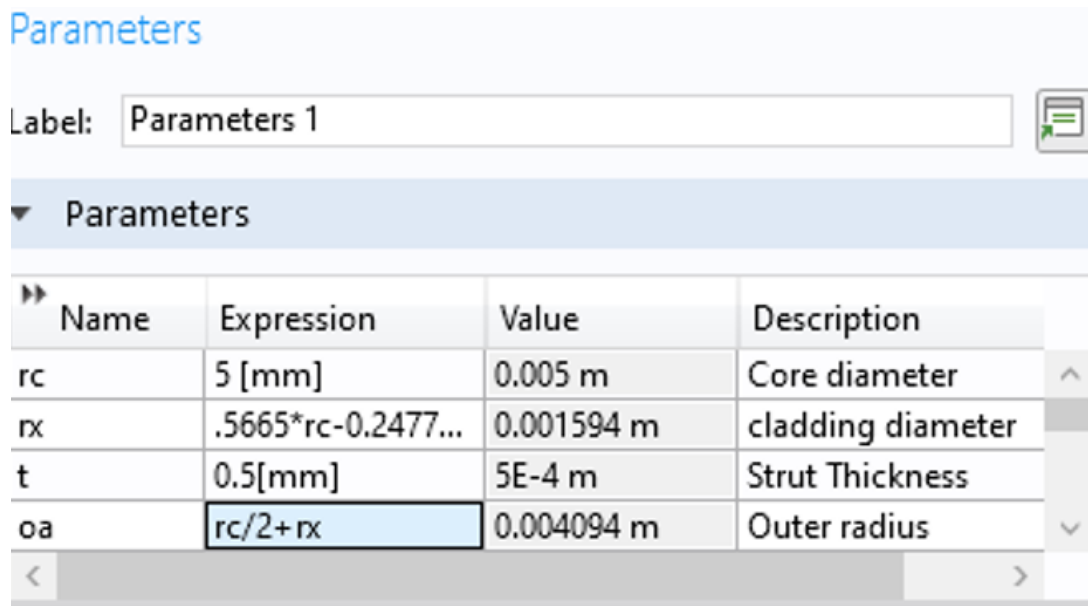
B.3.2 Step B: Model builder

Model tree has four nodes such as **Global Definitions, Component 1, Study, Results**.

1. Global Definitions ⇒ Parameters 1 in the model builder.

Inside the **Parameters 1**, there is a blank table with four headers as **Name, expression, values, and description** for constructing our own model. **Name** assign variables for the required parameters so that with the modification in **Expression** value it may change the geometry model directly. Also, parametric sweep or optimization process, **Name** keeps simulation simple. **Expression** assign the corresponding parameter value to model. The **description** gives a clear concept of the parameters, what it is. The **description** part is possible to skip. The **Parameters** window of COMSOL with basic parameters setup is shown in Fig. B.2.

2. **Component 1** tree occupies five nodes such as **Definitions, geometry 1, materials, Electromagnetic Waves, Frequency Domain (ewfd), and Mash 1**.



The screenshot shows the 'Parameters' window in COMSOL. At the top, there is a 'Label' field containing 'Parameters 1'. Below this is a table with four columns: 'Name', 'Expression', 'Value', and 'Description'. The table contains four rows of parameters: 'rc' with expression '5 [mm]' and value '0.005 m'; 'rx' with expression '.5665*rc-0.2477...' and value '0.001594 m'; 't' with expression '0.5[mm]' and value '5E-4 m'; and 'oa' with expression 'rc/2+rx' and value '0.004094 m'. The 'oa' row is highlighted in blue. There are also expand/collapse icons on the right side of the table.

Name	Expression	Value	Description
rc	5 [mm]	0.005 m	Core diameter
rx	.5665*rc-0.2477...	0.001594 m	cladding diameter
t	0.5[mm]	5E-4 m	Strut Thickness
oa	rc/2+rx	0.004094 m	Outer radius

Figure B.2. Parameters setup in COMSOL simulation. This include Name, expression, values, and description.

Geometry

1. Right click on the **geometry 1** in the **Model Builder**, provides various pattern including **circular, ellipse, rectangular, square, point, polygon, Bezier polygon, Boolean and partitions**, etc for the geometrical shapes. Selects the required pattern.
2. The **Setting window** appears at the middle between the **Model Builder** and **Graphics window** to settle the geometry size and shape, position, rotation angle, layers.
3. Also, by clicking the **geometry 1** selects the length unit like km, m, μm , nm, etc for the setting parameter unit setting.
4. Select the **Build Selected** or **Build All Objects** to allow the selected pattern or whole geometry, respectively in the **Graphics** window.
5. Repeat the steps 1-3 to complete the whole geometry.

Materials

Now, it is the time for assigning the required materials for the completed geometry pattern.

1. Right click on the **Materials** located inside the **Component 1** at the **Mode Builder** window. Materials offers **Add Material from the library** which shows the built-in materials list in the fourth window, or **Browse Materials** in the new tab, or **Blank Material** in the Setting window etc.
2. Select the **Blank Material** and right click to rename the **Material 1 (mat 1)** to specific name for example Zeonex.
3. **Repeat** the steps 1-2 to deal with more than one material in the geometry and label the materials name like Zeonex, air.
4. Click the geometry domains from the **Graphics** window for assigning the material. This will also add or subtract the domain in the selection box of the **Setting** window. To ensure the correct domain for the correct material, select the **Zoom in/Zoom Box/Zoom to selections/Zoom extents** from the Graphics window. In the **Setting** window the **Geometric Entity Selection** can be for **All domains or Manual** to select the domain entity.
5. When the material is selected, the **Material Contents** allows only the real part and imaginary part of the Refractive index. We have to fill the **Values** columns to determine as green marked properties from the **Material Properties** ⇒ **Electromagnetic Models** ⇒ **refractive Index**. A basic diagram, Fig. B.3, showing the COMSOL window after defining a material.

Electromagnetic Waves, Frequency Domain (EWFD)

The physics interface will again call the **Electromagnetic Waves, Frequency Domain (ewfd)** in the **Model Builder** window.

1. Select the **Electromagnetic Waves, Frequency Domain (ewfd)** in the **Model Builder** window.
2. The corresponding **Perfect Electric Conductor 1** will be automatically selected.

Mesh 1

Meshing is **discretization** part of computing **finite element methods** to simulate and analyse the structure numerically. Meshing is one of the most memory-intensive steps

B.3 COMSOL multiphysics

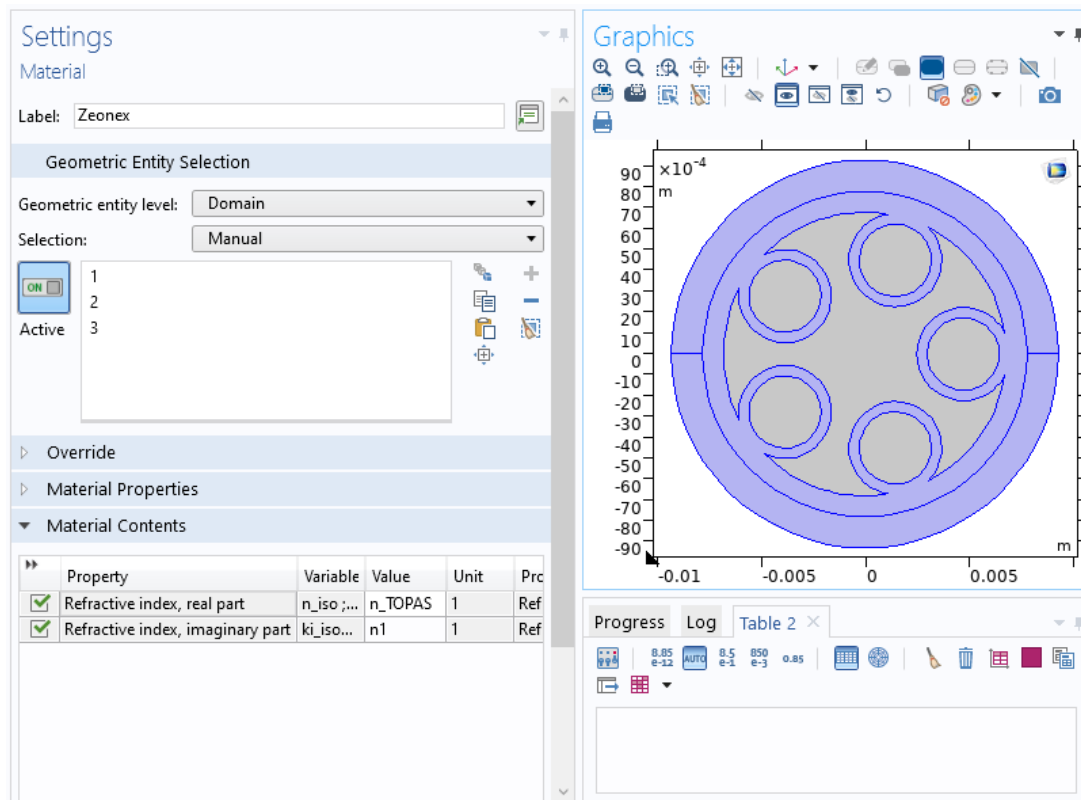


Figure B.3. Material definition in COMSOL. Showing the COMSOL window after defining a material.

when it comes to setting up and solving a finite element problem. The error in the numerical simulation is depend on the mesh size. Therefore, before simulation, we have to choose an accurate and efficient mesh size to reduce the error.

1. Right click on the **Mesh 1, Component 1** at the **Mode Builder** window to have the Size.
2. Select the **Size** under the **Mesh 1**. Calibrate for the General physics and pre-defined the mesh size as extremely fine to reduce the computation error. Also, extremely fine mesh size needs more memory space to compute the simulation.

As with all numerical approximations, the final simulation results are prone to errors. For the COMSOL multi-physics and mainly for the FEM the errors are likely due to the mesh size. Large number of mesh elements are highly recommended as they divide the whole device by a large number of smaller elements (Davidson 2010, Dickinson *et al.* 2014). Unfortunately, the large number of mesh size requires long computational time with large memory size and processing power of the machine.

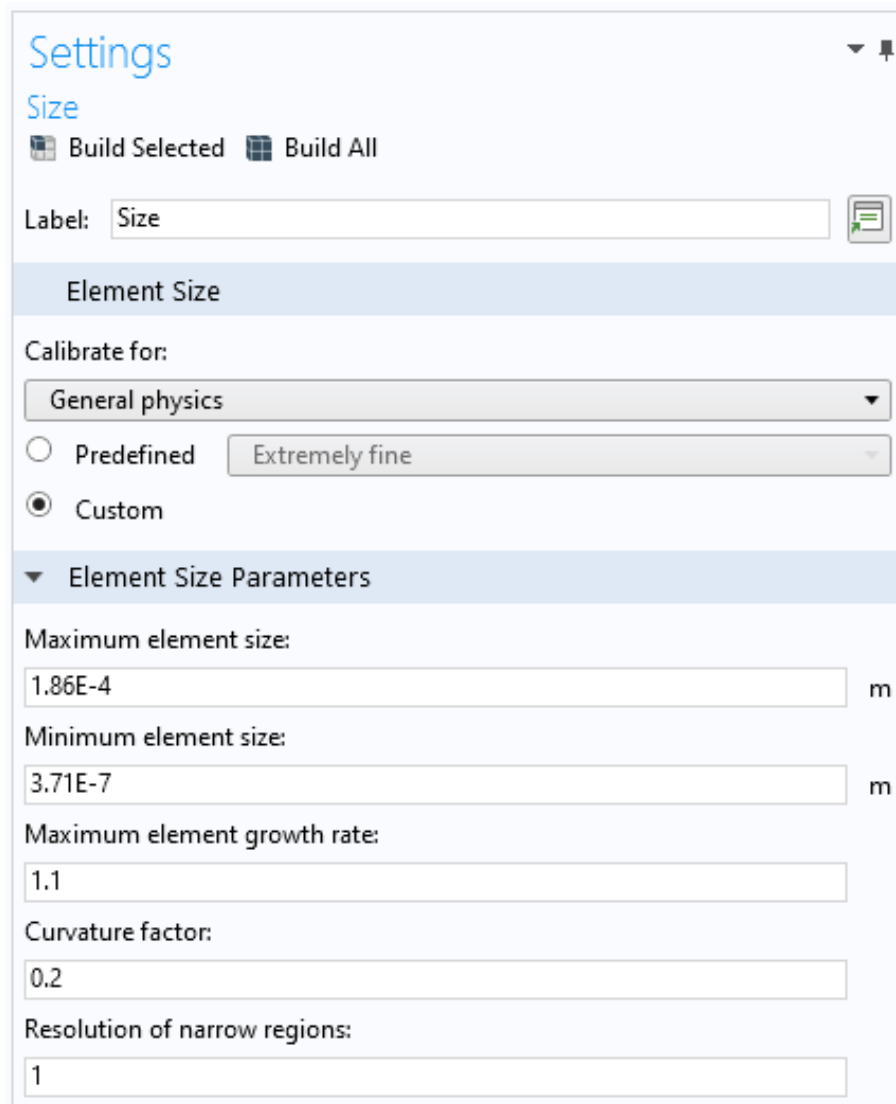


Figure B.4. Mesh definition in COMSOL. Showing the COMSOL window after defining a custom mesh.

Results and simulation in COMSOL

After designing the waveguide structure, it is now the final step to simulate the structure and analyze the mode fields.

There are several steps to follow to get the simulation done. The steps are presented below-

1. Click on **Study 1** ⇒ **Step 1:Mode Analysis**.
2. Under **Step 1: Mode Analysis** need to fill out all the required information in the **Study Settings**. This includes **Mode analysis frequency**, **Desired number of modes**, and **Search for modes around**.

3. Click on **Compute** under **Study**, and this will simulate the structure.
4. After the simulation right click on **Derived Values** and then click **Global Evaluation**.
5. To see the mode field pattern click on **Electric Field (EWFD)** under **Results**.

In summary, in this Appendix we present the step by step procedure of COMSOL Multiphysics simulation. In the next Appendix we will present the required MATLAB coding to obtain the optical properties of 2D materials, graphene and black phosphorous. The MATLAB coding for obtaining the the property of an optical fibre from the experimental data will also be presented.

MATLAB Code

This appendix presents MATLAB code for obtaining the plasma and collision frequency of graphene and Black Phosphorous (BP) that are used in Chapter 7, the code for obtaining optical properties from terahertz experimental data is also presents, these are used for signal processing in Chapter 2, and Chapter 6.

C.1 Matlab Code for obtaining optical properties of Graphene, BP, and optical fibre

%%% 1. MATLAB code for obtaining Black phosphorous (BP) plasma frequency and cut-off frequency

```
% Md. Saiful Islam  
% The University of Adelaide  
%%-----
```

```
e=1.6e-19;      % the electron charge  
Epsilon0=8.854e-14; % dielectric permittivity of classical vacuum
```

```
%effective masses  
m0=9.1e-35;    % electron mass  
mx=0.17*m0;  
my=1.12*m0;  
kB=1.38e-23;   % the Boltzmann's constant  
T=300;         % temperature in kelvin  
hbar=1.05e-34; % reduced Planck's constant  
chem=0.3;      % chemical potential
```

C.1 Matlab Code for obtaining optical properties of Graphene, BP, and optical fibre

```
%relationship between chemical potential with n
n=((sqrt(mx*my)*kB*T)/(pi*hbar^2))*log(1+exp(chem/0.02585));

%plasma frequency components.
wpx=sqrt((n*e^2)/(Epsilon0*mx*1e-6));
wpy=sqrt((n*e^2)/(Epsilon0*my*1e-6));

%plasma frequency along the x and y directions.
PF=wpx+wpy;

%The model must have a thickness t, so N3d=N2d/t, we set t to 1e-6 cm. When the thickness is thin
enough, it is similar to the 2D case.

u=1000;      %mobility value

%collision frequency components
wcx=e/(u*mx);wcy=e/(u*my);

%collision frequency
CF=wcx+wcy;

%% 2. MATLAB code for obtaining graphene plasma frequency and cut-off frequency
%%-----

%Values of different graphene parameters

%Vacuum permittivity
epsilon=1;

%frequency in THz
f2=10;

%linespacing
f=linspace(0.01,f2,1000)*1e12;

%radian frequency
w = 2*pi*f; T=300;

%temperature in kelvin
% Ta=6.750;
% ta=Ta*1E-12;

%the scattering rate that is considered 0.1 ps
ta=1.0e-13

% the Boltzmann's constant
kb=1.38064852e-23;

% reduced Planck's constant
hb=(6.62606957e-34)/2/pi;
```

```

j=sqrt(-1);
% the electron charge
e= 1.602176565E-19;

% the graphene chemical potential
Uc=0.2;

% chemical potential [ev]
Ef=Uc*e;

% Graphene thickness(1 Layer)
dg=1E-9;
E0=8.854223E-12;

%Graphene plasma frequency
Wp=sqrt((2*(e^2)*kb*T)/(E0*dg*pi*(hb^2)))*log(2*cosh(Ef/(2*kb*T)))

%Graphene collision frequency
Cfreq=1/ta

%%%%%%%%%%%%%%%%%%%%%%%%%%%%%%%%%%%%%%%%%%%%%%%%%%%%%%%%%%%%%%%%%%%%%%%%
%%%%%%%%%%%%%%%%%%%%%%%%%%%%%%%%%%%%%%%%%%%%%%%%%%%%%%%%%%%%%%%%%%%%%%%%

```

%% 3. MATLAB code for characterizing the loss of a terahertz optical fibre.

```

%%-----%%

```

```

clc;
    close all;
    %%%%%%%%%time domain experimental data%%%%%%%%
    time = 'time.xlsx';
        T1 = xlsread(time);
            s=5;

    %%%%%%%%%reference of the measured signal%%%%%%%%
    reference = 'r_45.xlsx';
        R = xlsread(reference);

    %%%%%%%%%reference_3%%%%%%%%
    reference1 = 'r_40.xlsx';
        R19 = xlsread(reference1);

    %%%%%%%%%reference_3%%%%%%%%
    reference2 = 'r_rest.xlsx';
        Rrest = xlsread(reference2);

    %%%%%%%%%Sample_1%%%%%%%%
    sample1 = 's_45.xlsx';
        S = xlsread(sample1);

    %%%%%%%%%Sample_2%%%%%%%%
    sample2 = 's_40.xlsx';
        S2 = xlsread(sample2);

```

C.1 Matlab Code for obtaining optical properties of Graphene, BP, and optical fibre

```
%%%%%%%%%%Sample_3%%%%%%%%%
sample3 = 's_23.xlsx';
S3 = xlsread(sample3);

%%%%%%%%%%Sample_4%%%%%%%%%
sample4 = 's_19.xlsx';
S4 = xlsread(sample4);

%%%%%%%%%%Sample_5%%%%%%%%%
sample5 = 's_17.xlsx';
S5= xlsread(sample5);

%%%%%%%%%%Simulation_frequency%%%%%%%%%
simulation_frequency = 'f45_simulation.xlsx';
fsimu = xlsread(simulation_frequency);

%%%%%%%%%%Simulation_loss%%%%%%%%%
simulation_loss = 'l45_simulation.xlsx';
losssimu = xlsread(simulation_loss);

%%%%%%%%%%FFT of reference%%%%%%%%%
% https://au.mathworks.com/help/matlab/ref/fft.html

T=T1(25)-T1(24); % finding interval
Fs=1./T; % finding frequency
Y = fft(R); % taking fft
L= length(R); % number of samples
f1=fft(T1);

%%%%%%%%%% amplitude of fft%%%%%%%%%
P2 = abs(Y./L);
P1 = P2(1:L./2+1);
P1(2:end-1) = 2*P1(2:end-1);

% %%%%%%%%%%%FFT of reference19%%%%%%%%%

% https://au.mathworks.com/help/matlab/ref/fft.html
% finding interval
Y19 = fft(R19); % taking fft
L19= length(R19); % number of samples

%%%%%%%%%% amplitude of fft%%%%%%%%%
P219 = abs(Y19./L19);
P119 = P219(1:L19./2+1);
P119(2:end-1) = 2*P119(2:end-1);

% https://au.mathworks.com/help/matlab/ref/fft.html
% finding interval

Yrest = fft(Rrest); % taking fft
Lrest= length(Rrest); % number of samples
```



```

%%%%%%%%%%%%%%FFT of sample_45mm%%%%%%%%%%%%%%

% https://au.mathworks.com/help/matlab/ref/fft.html
Ys = fft(S); % taking fft
Ls= length(S);

%%%%%%%%%%%%%% amplitude of sample_1 fft%%%%%%%%%%%%%%
P2s = abs(Ys./Ls);
P1s = P2s(1:Ls./2+1);
P1s(2:end-1) = 2*P1s(2:end-1);

% %%%%%%%%%%%%%%%FFT of sample_2_40mm%%%%%%%%%%%%%%

% https://au.mathworks.com/help/matlab/ref/fft.html
Ys2 = fft(S2); % taking fft
Ls2= length(S2);

%%%%%%%%%%%%%% amplitude of sample_2 fft%%%%%%%%%%%%%%
P2s2 = abs(Ys2./Ls2);
P1s2 = P2s2(1:Ls2./2+1);
P1s2(2:end-1) = 2*P1s2(2:end-1);

%%%%%%%%%%%%%%FFT of sample_3-23mm%%%%%%%%%%%%%%

Ys3 = fft(S3); % taking fft
Ls3= length(S3);

%%%%%%%%%%%%%% amplitude of sample_3 fft%%%%%%%%%%%%%%
P2s3 = abs(Ys3./Ls3);
P1s3 = P2s3(1:Ls3./2+1);
P1s3(2:end-1) = 2*P1s3(2:end-1);

%%%%%%%%%%%%%%FFT of sample_4_19mm%%%%%%%%%%%%%%
Ys4 = fft(S4); % taking fft
Ls4= length(S4);

%%%%%%%%%%%%%% amplitude of sample_4 fft%%%%%%%%%%%%%%
P2s4 = abs(Ys4./Ls4);
P1s4 = P2s4(1:Ls4./2+1);
P1s4(2:end-1) = 2*P1s4(2:end-1);

%%%%%%%%%%%%%%FFT of sample_5_17mm%%%%%%%%%%%%%%

Ys5 = fft(S5); % taking fft
Ls5= length(S5);

%%%%%%%%%%%%%% amplitude of sample_5 fft%%%%%%%%%%%%%%
P2s5 = abs(Ys5./Ls5);
P1s5 = P2s5(1:Ls5./2+1);
P1s5(2:end-1) = 2*P1s5(2:end-1);

%%%%%%%%%%%%%% FREQUENCY%%%%%%%%%%%%%%
f = Fs.*(0:(L./2))./L;

```

C.1 Matlab Code for obtaining optical properties of Graphene, BP, and optical fibre

```
%%%%%%%%%% POWER of reference%%%%%%%%%%
Pe = P1.^2;
P = smooth(Pe,s,'moving');

%%%%%%%%power(dB)
Pdbe = 10.*log(P);
Pdb = smooth(Pdbe,s,'moving');

%%%%%%%%%% POWER of reference_19%%%%%%%%%%
Pe19 = P119.^2;
P19 = smooth(Pe19,s,'moving');

%%%%%%%%power(dB)
Pdbe19 = 10.*log(P19);
Pdb19 = smooth(Pdbe19,100,'moving');

%%%%%%%%%% POWER of reference_rest%%%%%%%%%%
Perest = P1rest.^2;
Prest = smooth(Perest,s,'moving');

%%%%%%%%power(dB)
Pdberest = 10.*log(Prest);
Pdbrest = smooth(Pdberest,100,'moving');

%%%%%%%%%% POWER of Sample_1%%%%%%%%%%
Pse=P1s.^2;
Ps = smooth(Pse,s,'moving');
%%%%%%%%power(dB)
Pdbse = 10.*log(Ps);
Pdbse = smooth(Pdbse,100,'moving');

%%%%%%%%%% POWER of Sample_2%%%%%%%%%%
Pse2=P1s2.^2;
Ps2 = smooth(Pse2,s,'moving');
%%%%%%%%power(dB)
Pdbse2 = 10.*log(Ps2);
Pdbse2 = smooth(Pdbse2,100,'moving');

%%%%%%%%%% POWER of Sample_3%%%%%%%%%%
Pse3=P1s3.^2;
Ps3 = smooth(Pse3,s,'moving');
%%%%%%%%power(dB)
Pdbse3= 10.*log(Ps3);
Pdbse3 = smooth(Pdbse3,100,'moving');

%%%%%%%%%% POWER of Sample_4%%%%%%%%%%
Pse4=P1s4.^2;
Ps4 = smooth(Pse4,s,'moving');

%%%%%%%%power(dB)
Pdbse4= 10.*log(Ps4);
Pdbse4 = smooth(Pdbse4,100,'moving');
```

```

%%%%%%%%%%%% POWER of Sample_5%%%%%%%%%%%%
Pse5=P1s5.^2;
    Ps5 = smooth(Pse5,s,'moving');
%%power(dB)
Pdbse5= 10.*log(Ps5);
    Pdb5 = smooth(Pdbse5,100,'moving');

% % % % % % % % amplitude of reference PLOT % % % % % % % % % % % %
figure
    plot(f,P1,f,P1s);
        legend('FFT Reference','FFT Sample');
            xlabel('Frequency (THz)')
                ylabel('reference amplitude')
                    xlim([0.0 8.0])
                        grid on

% % % % % % % % Reference POWER PLOT % % % % % % % % % % % %
figure
    plot(f,P,f,Ps);
        legend('Reference power','Sample Power');
            xlabel('Frequency (THz)')
                ylabel('reference power')
                    xlim([0.0 8.0])
                        grid on

% % % % % % % % Reference POWER DB % % % % % % % % % % % %
figure
    plot(f,Pdb,f,Pdb5);
        xlabel('Frequency (THz)')
            legend('Reference power (dB)','Sample Power (dB)');
                ylabel('reference power dB')
                    xlim([0.0 5.0])
                        grid on

% % % % % % % % % % % % Transmission % % % % % % % % % % % % % % % %
Trans100 = Ps./P;
    Trans40 = Ps2./P19;
    Trans19 = Ps4./Prest;

% % % % % % % % % % % % Transmission_sample40 % % % % % % % % % % % % % % % %
figure;
    plot(f,Trans100,f,Trans40_1,f,Trans23,f,Trans19,f,Trans17,'LineWidth',3);
        set(gca,'linewidth',2,'FontSize',25,'FontName','Times New Roman')
            legend('experiment 45mm','experiment 40 mm', 'experiment 23 mm',
                'experiment 19 mm', 'experiment 17 mm');
                xlabel('Frequency (THz)')
                    ylabel('Transmission')
                        xlim([0.7 4.0])
                            hold on

```

C.1 Matlab Code for obtaining optical properties of Graphene, BP, and optical fibre

```
%%%%%%%%%% Transmission Loss in dB %%%%%%%%%%%
Loss100 = -10*log10(Trans100);
Loss40 = -10*log10(Trans40);
Loss19 = -10*log10(Trans19);

%%%%%%%%%% Transmission Loss in dB %%%%%%%%%%%
figure;
plot(f, Loss100, f, Loss40_1, f, Loss23, f, Loss19, f, Loss17, 'LineWidth', 3);
legend('experiment 45mm', 'experiment 40 mm', 'experiment 23 mm',
'experiment 19 mm', 'experiment 17 mm');
xlabel('Frequency (THz)')
ylabel('Transmission Loss (dB)')
xlim([0.5 4.0])
hold on

figure;
yyaxis left
plot(f, Loss100, 'LineWidth', 3);
legend('experiment type-I');
ylabel('Loss (dB)')

yyaxis right
plot(fsimu, losssimu, 'LineWidth', 3);
legend('Measurements, type-I', 'Simulation, type-I');
xlabel('Frequency (THz)')
ylabel('Loss (dB/mm)')
xlim([0.5 5.0])
hold on

% %%%%%%%%%%% Transmission Loss in dB/mm %%%%%%%%%%%
Loss1 = Loss100./45;
Loss2 = Loss40_1./40;
Loss4 = Loss23./23;
Loss5 = Loss19./19;
Loss6 = Loss17./17;

%%%%%%%%%% Transmission Loss in dB/mm %%%%%%%%%%%
figure;
plot(f, Loss1, f, Loss2, f, Loss4, f, Loss5, f, Loss6, 'LineWidth', 3);
legend('experiment 45mm', 'experiment 40 mm', 'experiment 23 mm', 'experiment
19 mm', 'experiment 17 mm');
set(gca, 'linewidth', 2, 'FontSize', 25, 'FontName', 'Times New Roman')
xlabel('Frequency (THz)')
ylabel('Transmission Loss (dB/mm)')
xlim([0.5 4.0])

%%%%%%%%%% Absorption coefficient %%%%%%%%%%%
Lossab1 = Loss1./4.343;
Lossab2 = Loss2./4.343;
Lossab5 = Loss5./4.343;

%%%%%%%%%% Absorption coefficient %%%%%%%%%%%
figure;
plot(f, Lossab1, f, Lossab2, f, Lossab4, f, Lossab5, f, Lossab6, 'LineWidth', 3);
set(gca, 'linewidth', 2, 'FontSize', 25, 'FontName', 'Times New Roman')
legend('experiment 45mm', 'experiment 40 mm', 'experiment 23 mm',
'experiment 19 mm', 'experiment 17 mm');
xlabel('Frequency (THz)')
ylabel('Absorption coefficient (mm^-1)')
xlim([0.5 4.0])
```

%% 4. MATLAB code for dispersion characterization of a terahertz optical fibre.

```

% Md. Saiful Islam
% The University of Adelaide
%%-----

data = 'all ri.xlsx'; %importing the refractive index data
n= xlsread(data); %read the data

a= n(:,2); %selecting column for refractive index
f=n(:,1); % selecting the frequency row
neff1=real(a); %real value of the effective refractive index
w=2*pi*f; %angular frequency
c=3*10^8; %speed of light

disp1=diff(neff1)./diff(w); % differentiating the refractive index values
w1=w(1:length(w)-1);

disp2=diff(disp1)./diff(w1); % second order differentiation
w2=w(1:length(w)-2);

disp= 10^10*(2/c)*disp1(1:length(disp1)-1)+(w2./c).*disp2;%equation of dispersion
s=f(1:length(f)-2);
dispersion1 = smooth(disp,10,'moving');

%Plotting the dispersion
yyaxis left
plot(s,dispersion1,'linewidth',2.5);
set(gca,'FontName','Times New Roman','FontSize',30);
xlabel('Frequency (THz)','FontName','Times New
Roman','fontweight','b','FontSize',30);
ylabel('\beta_2 (ps/THz/cm)','FontName','Times New
Roman','fontweight','b','FontSize',30);
xlim ([0.5 4.0]);

```


Bibliography

- ABBOTT-D., AND ZHANG-X.-C. (2007). Special issue on T-ray imaging, sensing, and detection, *Proceedings of the IEEE*, **95**(8), pp. 1509–1513.
- ABDELSALAM-M., MAHMOUD-A. M., AND SWILLAM-M. A. (2019). Polarization independent dielectric metasurface for infrared beam steering applications, *Scientific Reports*, **9**, Art. No. 10824.
- ADEMGIL-H. (2014). Highly sensitive octagonal photonic crystal fiber based sensor, *Optik*, **125**(20), pp. 6274–6278.
- ADEMGIL-H., AND HAXHA-S. (2015). PCF based sensor with high sensitivity, high birefringence and low confinement losses for liquid analyte sensing applications, *Sensors*, **15**(12), pp. 31833–31842.
- ADVANTEST-C. (2021). Terahertz wave spectroscopy and analysis platform, www.advantest.com/products/terahertzspectroscopic-imaging-systems, Advantest, accessed 15th May 2021.
- AGRAWAL-G. P. (2012). *Fiber-optic Communication Systems*, Vol. 222, John Wiley & Sons.
- AHMED-K., AHMED-F., ROY-S., PAUL-B. K., AKTAR-M. N., VIGNESWARAN-D., AND ISLAM-M. S. (2019). Refractive index-based blood components sensing in terahertz spectrum, *IEEE Sensors Journal*, **19**(9), pp. 3368–3375.
- AHMED-K., CHOWDHURY-S., PAUL-B. K., ISLAM-M. S., SEN-S., ISLAM-M. I., AND ASADUZZAMAN-S. (2017a). Ultrahigh birefringence, ultralow material loss porous core single-mode fiber for terahertz wave guidance, *Applied Optics*, **56**(12), pp. 3477–3483.
- AHMED-R., YETISEN-A. K., YUN-S. H., AND BUTT-H. (2017b). Color selective holographic retroreflector array for sensing applications, *Light: Science and Applications*, **6**(2), Art. No. e16214.
- AKO-R. T., LEE-W. S., BHASKARAN-M., SRIRAM-S., AND WITHAYACHUMNANKUL-W. (2019). Broadband and wide-angle reflective linear polarization converter for terahertz waves, *APL Photonics*, **4**(9), Art. No. 096104.
- AKO-R. T., UPADHYAY-A., WITHAYACHUMNANKUL-W., BHASKARAN-M., AND SRIRAM-S. (2020). Dielectrics for terahertz metasurfaces: Material selection and fabrication techniques, *Advanced Optical Materials*, **8**(3), Art. No. 1900750.
- AKOWUAH-E. K., GORMAN-T., ADEMGIL-H., HAXHA-S., ROBINSON-G. K., AND OLIVER-J. V. (2012). Numerical analysis of a photonic crystal fiber for biosensing applications, *IEEE Journal of Quantum Electronics*, **48**(11), pp. 1403–1410.
- ALGORRI-J., ZOGRAFOPOULOS-D., FERRARO-A., GARCÍA-CÁMARA-B., BECCHERELLI-R., AND SÁNCHEZ-PENA-J. (2019). Ultrahigh-quality factor resonant dielectric metasurfaces based on hollow nanocuboids, *Optics Express*, **27**(5), pp. 6320–6330.

Bibliography

- AL-NAIB-I. A., JANSEN-C., AND KOCH-M. (2009). High Q-factor metasurfaces based on miniaturized asymmetric single split resonators, *Applied Physics Letters*, **94**(15), Art. No. 153505.
- AMING-A., UTHMAN-M., CHITAREE-R., MOHAMMED-W., AND RAHMAN-B. A. (2016). Design and characterization of porous core polarization maintaining photonic crystal fiber for THz guidance, *IEEE Journal of Lightwave Technology*, **34**(23), pp. 5583–5590.
- AMOUZAD MAHDIRAJI-G., CHOW-D. M., SANDOGHCHI-S., AMIRKHAN-F., DERMOSESIAN-E., YEO-K. S., KAKAEI-Z., GHOMEISHI-M., POH-S. Y., AND YU GANG-S. (2014). Challenges and solutions in fabrication of silica-based photonic crystal fibers: an experimental study, *Fiber and Integrated Optics*, **33**(2), pp. 85–104.
- AMRANI-F., OSÓRIO-J. H., DELAHAYE-F., GIOVANARDI-F., VINCETTI-L., DEBORD-B., GÉRÔME-F., AND BENABID-F. (2021). Low-loss single-mode hybrid-lattice hollow-core photonic-crystal fibre, *Light: Science & Applications*, **10**, Art. No. 10.
- ANTHONY-J., LEONHARDT-R., AND ARGYROS-A. (2013). Hybrid hollow core fibers with embedded wires as THz waveguides, *Optics Express*, **21**(3), pp. 2903–2912.
- ANTHONY-J., LEONHARDT-R., ARGYROS-A., AND LARGE-M. C. (2011a). Characterization of a microstructured Zeonex terahertz fiber, *JOSA B*, **28**(5), pp. 1013–1018.
- ANTHONY-J., LEONHARDT-R., LEON-SAVAL, SERGIO-G., AND ARGYROS-A. (2011b). THz propagation in kagome hollow-core microstructured fibers, *Optics Express*, **19**(19), pp. 18470–18478.
- ARAY-A., CHIAVAIOLI-F., ARJMAND-M., TRONO-C., TOMBELLI-S., GIANNETTI-A., CENNAMO-N., SOLTANOLKOTABI-M., ZENI-L., AND BALDINI-F. (2016a). SPR-based plastic optical fibre biosensor for the detection of c-reactive protein in serum, *Journal of Biophotonics*, **9**(10), pp. 1077–1084.
- ARAY-A., SAGHAFIFAR-H., AND SOLTANOLKOTABI-M. (2016b). Calculation of dispersion relation and single mode operation in surface plasmon resonance based fiber optic refractive index sensors, *Journal of Lightwave Technology*, **34**(11), pp. 2782–2788.
- ARGYROS-A. (2013). Microstructures in polymer fibres for optical fibres, THz waveguides, and fibre-based metamaterials, *International Scholarly Research Notices*, **2013**, Art. No. 785162.
- ARGYROS-A., AND PLA-J. (2007). Hollow-core polymer fibres with a kagome lattice: potential for transmission in the infrared, *Optics Express*, **15**(12), pp. 7713–7719.
- ARIF-M. F. H., AHMED-K., ASADUZZAMAN-S., AND AZAD-M. A. K. (2016). Design and optimization of photonic crystal fiber for liquid sensing applications, *Photonic Sensors*, **6**(3), pp. 279–288.
- ARIF-M. F. H., AND BIDDUT-M. J. H. (2017). A new structure of photonic crystal fiber with high sensitivity, high nonlinearity, high birefringence and low confinement loss for liquid analyte sensing applications, *Sensing and Biosensing Research*, **12**, pp. 8–14.
- ARIK-E., KORAL-C., ALTAN-H., AND ESENTÜRK-O. (2013). A new method for alcohol content determination of fuel oils by terahertz spectroscopy, *38th Int. Conf. on Infra. Milli. and Tera. Waves (IRMMW-THz)*, IEEE. DOI: 10.1109/IRMMW-THz.2013.6665885.

- ARROSPIDE-E., DURANA-G., AZKUNE-M., ALDABALDETREKU-G., BIKANDI-I., RUIZ-RUBIO-L., AND ZUBIA-J. (2018). Polymers beyond standard optical fibres—fabrication of microstructured polymer optical fibres, *Polymer International*, **67**(9), pp. 1155–1163.
- ASADUZZAMAN-S., AND AHMED-K. (2017). Microarray-core based circular photonic crystal fiber for high chemical sensing capacity with low confinement loss, *Optica Applicata*, **47**, pp. 41–49.
- ASTORINO-M. D., FASTAMPA-R., FREZZA-F., MAIOLO-L., MARRANI-M., MISSORI-M., MUZI-M., TEDESCHI-N., AND VEROLI-A. (2018). Polarization-maintaining reflection-mode THz time-domain spectroscopy of a polyimide based ultra-thin narrow-band metamaterial absorber, *Scientific Reports*, **8**, Art. No. 35253.
- ATAKARAMIANS-S., AFSHAR-S., EBENDORFF-HEIDPRIEM-H., NAGEL-M., FISCHER-B. M., ABBOTT-D., AND MONRO-T. M. (2009a). THz porous fibers: design, fabrication and experimental characterization, *Optics Express*, **17**(16), pp. 14053–14062.
- ATAKARAMIANS-S., AFSHAR-S., FISCHER-B. M., ABBOTT-D., AND MONRO-T. M. (2008). Porous fibers: a novel approach to low loss THz waveguides, *Optics Express*, **16**(12), pp. 8845–8854.
- ATAKARAMIANS-S., AFSHAR-S., FISCHER-B. M., ABBOTT-D., AND MONRO-T. M. (2009b). Low loss, low dispersion and highly birefringent terahertz porous fibers, *Optics Communications*, **282**(1), pp. 36–38.
- ATAKARAMIANS-S., AFSHAR-S., MONRO-T. M., AND ABBOTT-D. (2013). Terahertz dielectric waveguides, *Advances in Optics and Photonics*, **5**(2), pp. 169–215.
- ATAKARAMIANS-S., AFSHAR-S., NAGEL-M., EBENDORFF-HEIDPRIEM-H., FISCHER-B. M., MONRO-T. M., AND ABBOTT-D. (2009c). Experimental investigation of dispersion properties of THz porous fibers, *34th Int. Conf. on Infra. Milli. and Tera. Waves (IRMMW-THz)*, IEEE. DOI: 10.1109/ICIMW.2009.5324967.
- AUSTON-D. H., CHEUNG-K., VALDMANIS-J., AND KLEINMAN-D. (1984). Cherenkov radiation from femtosecond optical pulses in electro-optic media, *Physical Review Letters*, **53**(16), Art. No. 1555.
- AZMAN-M. F., MAHDIRAJI-G. A., WONG-W. R., AONI-R. A., AND ADIKAN-F. R. M. (2019). Design and fabrication of copper-filled photonic crystal fiber based polarization filters, *Applied Optics*, **58**(8), pp. 2068–2075.
- BABITA., AND RASTOGI-V. (2013). Dispersion flattened single mode optical fiber with large effective area, *AIP Conference Proceedings*, **1536**(1), pp. 729–730.
- BAGCHI-S., ACHLA-R., AND MONDAL-S. K. (2017). Electrospun polypyrrole-polyethylene oxide coated optical fiber sensor probe for detection of volatile compounds, *Sensors and Actuators B: Chemical*, **250**, pp. 52–60.
- BALAKRISHNAN-J., FISCHER-B. M., AND ABBOTT-D. (2009). Fixed dual-thickness terahertz liquid spectroscopy using a spinning sample technique, *IEEE Photonics Journal*, **1**(2), pp. 88–98.
- BAO-H., NIELSEN-K., BANG-O., AND JEPSEN-P. U. (2015). Dielectric tube waveguides with absorptive cladding for broadband, low-dispersion and low loss THz guiding, *Scientific Reports*, **5**, Art. No. 7620.

Bibliography

- BAO-H., NIELSEN-K., RASMUSSEN-H. K., JEPSEN-P. U., AND BANG-O. (2012). Fabrication and characterization of porous-core honeycomb bandgap THz fibers, *Optics Express*, **20**(28), pp. 29507–29517.
- BARH-A., PAL-B. P., AGRAWAL-G. P., VARSHNEY-R. K., AND RAHMAN-B. A. (2015). Specialty fibers for terahertz generation and transmission: a review, *IEEE Journal of Selected Topics in Quantum Electronics*, **22**(2), pp. 365–379.
- BARTON-G., VAN EIJKELNBORG-M. A., HENRY-G., LARGE-M. C., AND ZAGARI-J. (2004). Fabrication of microstructured polymer optical fibres, *Optical Fiber Technology*, **10**(4), pp. 325–335.
- BEARD-M. C., TURNER-G. M., AND SCHMUTTENMAER-C. A. (2001). Subpicosecond carrier dynamics in low-temperature grown GaAs as measured by time-resolved terahertz spectroscopy, *Journal of Applied Physics*, **90**(12), pp. 5915–5923.
- BEARD-M. C., TURNER-G. M., AND SCHMUTTENMAER-C. A. (2002). Measuring intramolecular charge transfer via coherent generation of THz radiation, *The Journal of Physical Chemistry A*, **106**(6), pp. 878–883.
- BERAVAT-R., WONG-G. K., FROSZ-M. H., XI-X. M., AND RUSSELL-P. S. J. (2016). Twist-induced guidance in coreless photonic crystal fiber: A helical channel for light, *Science Advances*, **2**(11), Art. No. e1601421.
- BERUETE-M., AND JÁUREGUI-LÓPEZ-I. (2020). Terahertz sensing based on metasurfaces, *Advanced Optical Materials*, **8**(3), Art. No. 1900721.
- BIABANIFARD-M., AND ABRISHAMIAN-M. S. (2018). Ultra-wideband terahertz graphene absorber using circuit model, *Applied Physics A*, **124**(12), Art. No. 826.
- BIRKS-T., ROBERTS-P., RUSSELL-P. S. J., ATKIN-D., AND SHEPHERD-T. (1995). Full 2-D photonic bandgaps in silica/air structures, *Electronics Letters*, **31**(22), pp. 1941–1943.
- BOLIVAR-P. H., BRUCHERSEIFER-M., RIVAS-J. G., GONZALO-R., EDERRA-I., REYNOLDS-A. L., HOLKER-M., AND DE MAAGT-P. (2003). Measurement of the dielectric constant and loss tangent of high dielectric-constant materials at terahertz frequencies, *IEEE Transactions on Microwave Theory and Techniques*, **51**(4), pp. 1062–1066.
- BONACCORSO-F., SUN-Z., HASAN-T., AND FERRARI-A. (2010). Graphene photonics and optoelectronics, *Nature Photonics*, **4**(9), Art. No. 611.
- BOWDEN-B., HARRINGTON-J. A., AND MITROFANOV-O. (2007). Silver/polystyrene-coated hollow glass waveguides for the transmission of terahertz radiation, *Optics Letters*, **32**(20), pp. 2945–2947.
- BOWDEN-B., HARRINGTON-J. A., AND MITROFANOV-O. (2008a). Fabrication of terahertz hollow-glass metallic waveguides with inner dielectric coatings, *Journal of Applied Physics*, **104**(9), Art. No. 093110.
- BOWDEN-B., HARRINGTON-J. A., AND MITROFANOV-O. (2008b). Low-loss modes in hollow metallic terahertz waveguides with dielectric coatings, *Applied Physics Letters*, **93**(18), Art. No. 181104.
- CAMPIONE-S., LIU-S., BASILIO-L. I., WARNE-L. K., LANGSTON-W. L., LUK-T. S., WENDT-J. R., RENO-J. L., KEELER-G. A., AND BRENER-I. (2016). Broken symmetry dielectric resonators for high quality factor Fano metasurfaces, *ACS Photonics*, **3**(12), pp. 2362–2367.

- CAO-E., GUO-X., ZHANG-L., SHI-Y., LIN-W., LIU-X., FANG-Y., ZHOU-L., SUN-Y., AND SONG-Y. (2017). Electrooptical synergy on plasmon–exciton-codriven surface reduction reactions, *Advanced Materials Interfaces*, **4**(24), Art. No. 1700869.
- CAO-S., SHAO-Y., WANG-Y., WU-T., ZHANG-L., HUANG-Y., ZHANG-F., LIAO-C., HE-J., AND WANG-Y. (2018). Highly sensitive surface plasmon resonance biosensor based on a low-index polymer optical fiber, *Optics Express*, **26**(4), pp. 3988–3994.
- CAO-Y., NALLAPPAN-K., GUERBOUKHA-H., GERVAIS-T., AND SKOROBOGATIY-M. (2019). Additive manufacturing of resonant fluidic sensors based on photonic bandgap waveguides for terahertz applications, *Optics Express*, **27**(20), pp. 27663–27681.
- CARRASCOSA-L. G., SINA-A. A. I., PALANISAMY-R., SEPULVEDA-B., OTTE-M. A., RAUF-S., SHIDDIKY-M. J., AND TRAU-M. (2014). Molecular inversion probe-based SPR biosensing for specific, label-free and real-time detection of regional dna methylation, *Chemical Communications*, **50**(27), pp. 3585–3588.
- CERQUEIRA JR-S. A. (2010). Recent progress and novel applications of photonic crystal fibers, *Reports on Progress in Physics*, **73**(2), Art. No. 024401.
- CHAFER-M., OSÓRIO-J. H., AMRANI-F., DELAHAYE-F., MAUREL-M., DEBORD-B., GÉRÔME-F., AND BENABID-F. (2019). 1-km hollow-core fiber with loss at the silica rayleigh limit in the green spectral region, *IEEE Photonics Technology Letters*, **31**(9), pp. 685–688.
- CHANG-T., ZHANG-X., ZHANG-X., AND CUI-H.-L. (2017). Accurate determination of dielectric permittivity of polymers from 75 GHz to 1.6 THz using both s-parameters and transmission spectroscopy, *Applied Optics*, **56**(12), pp. 3287–3292.
- CHAN-W. L., DEIBEL-J., AND MITTLEMAN-D. M. (2007). Imaging with terahertz radiation, *Reports on Progress in Physics*, **70**(8), Art. No. 1325.
- CHAU-Y.-F. C., WANG-C.-K., SHEN-L., LIM-C. M., CHIANG-H.-P., CHAO-C.-T. C., HUANG-H. J., LIN-C.-T., KUMARA-N., AND VOO-N. Y. (2017). Simultaneous realization of high sensing sensitivity and tunability in plasmonic nanostructures arrays, *Scientific Reports*, **7**, Art. No. 16817.
- CHEN-C.-Y., UN-I.-W., TAI-N.-H., AND YEN-T.-J. (2009). Asymmetric coupling between subradiant and superradiant plasmonic resonances and its enhanced sensing performance, *Optics Express*, **17**(17), pp. 15372–15380.
- CHEN-D., AND CHEN-H. (2010). A novel low-loss terahertz waveguide: Polymer tube, *Optics Express*, **18**(4), pp. 3762–3767.
- CHENG-J., FAN-F., AND CHANG-S. (2019). Recent progress on graphene-functionalized metasurfaces for tunable phase and polarization control, *Nanomaterials*, **9**(3), Art. No. 398.
- CHENG-Y. Z., WITHAYACHUMNANKUL-W., UPADHYAY-A., HEADLAND-D., NIE-Y., GONG-R. Z., BHASKARAN-M., SRIRAM-S., AND ABBOTT-D. (2015). Ultrabroadband plasmonic absorber for terahertz waves, *Advanced Optical Materials*, **3**(3), pp. 376–380.

Bibliography

- CHEN-H., CHEN-T.-H., TSENG-T.-F., LU-J.-T., KUO-C.-C., FU-S.-C., LEE-W.-J., TSAI-Y.-F., HUANG-Y.-Y., AND CHUANG-E. Y. (2011a). High-sensitivity in vivo THz transmission imaging of early human breast cancer in a subcutaneous xenograft mouse model, *Optics Express*, **19**(22), pp. 21552–21562.
- CHEN-H., LEE-W.-J., HUANG-H.-Y., CHIU-C.-M., TSAI-Y.-F., TSENG-T.-F., LU-J.-T., LAI-W.-L., AND SUN-C.-K. (2011b). Performance of THz fiber-scanning near-field microscopy to diagnose breast tumors, *Optics Express*, **19**(20), pp. 19523–19531.
- CHEN-H.-T. (2012). Interference theory of metamaterial perfect absorbers, *Optics Express*, **20**(7), pp. 7165–7172.
- CHEN-L.-J., CHEN-H.-W., KAO-T.-F., LU-J.-Y., AND SUN-C.-K. (2006). Low-loss subwavelength plasmonic fiber for terahertz waveguiding, *Optics Letters*, **31**(3), pp. 308–310.
- CHEN-N., CHANG-M., LU-X., ZHOU-J., AND ZHANG-X. (2019). Photonic crystal fiber plasmonic sensor based on dual optofluidic channel, *Sensors*, **19**(23), Art. No. 5150.
- CHEN-N.-N., LIANG-J., AND REN-L.-Y. (2013). High-birefringence, low-loss porous fiber for single-mode terahertz-wave guidance, *Applied Optics*, **52**(21), pp. 5297–5302.
- CHEN-S., LI-Z., ZHANG-Y., CHENG-H., AND TIAN-J. (2018a). Phase manipulation of electromagnetic waves with metasurfaces and its applications in nanophotonics, *Advanced Optical Materials*, **6**(13), Art. No. 1800104.
- CHEN-T., LI-S., AND SUN-H. (2012). Metamaterials application in sensing, *Sensors*, **12**(3), pp. 2742–2765.
- CHEN-W. T., ZHU-A. Y., SANJEEV-V., KHORASANINEJAD-M., SHI-Z., LEE-E., AND CAPASSO-F. (2018b). A broadband achromatic metalens for focusing and imaging in the visible, *Nature Nanotechnology*, **13**(3), pp. 220–226.
- CHEN-X., AND FAN-W. (2017). Ultrasensitive terahertz metamaterial sensor based on spoof surface plasmon, *Scientific Reports*, **7**, Art. No. 2092.
- CHEN-X., AND FAN-W. (2020). Tunable bound states in the continuum in all-dielectric terahertz metasurfaces, *Nanomaterials*, **10**(4), Art. No. 623.
- CHEN-X., FAN-W., AND SONG-C. (2018c). Multiple plasmonic resonance excitations on graphene metamaterials for ultrasensitive terahertz sensing, *Carbon*, **133**, pp. 416–422.
- CHEN-Z., YUAN-L., HEFFERMAN-G., AND WEI-T. (2015). Terahertz fiber bragg grating for distributed sensing, *IEEE Photonics Technology Letters*, **27**(10), pp. 1084–1087.
- CHEVILLE-R. A., AND GRISCHKOWSKY-D. (1998). Observation of pure rotational absorption spectra in the ν_2 band of hot H_2O in flames, *Optics Letters*, **23**(7), pp. 531–533.
- CHO-M., KIM-J., PARK-H., HAN-Y., MOON-K., JUNG-E., AND HAN-H. (2008). Highly birefringent terahertz polarization maintaining plastic photonic crystal fibers, *Optics Express*, **16**(1), pp. 7–12.
- CHOWDHURY-S., SEN-S., AHMED-K., AND ASADUZZAMAN-S. (2017). Design of highly sensible porous shaped photonic crystal fiber with strong confinement field for optical sensing, *Optik*, **142**, pp. 541–549.

- CHRYSSIS-A. N., LEE-S. M., LEE-S. B., SAINI-S. S., AND DAGENAIS-M. (2005). High sensitivity evanescent field fiber bragg grating sensor, *IEEE Photonics Technology Letters*, **17**(6), pp. 1253–1255.
- CHU-S., NAKKEERAN-K., ABOBAKER-A. M., APHALE-S. S., BABU-P. R., AND SENTHILNATHAN-K. (2018). Design and analysis of surface-plasmon-resonance-based photonic quasi-crystal fiber biosensor for high-refractive-index liquid analytes, *IEEE Journal of Selected Topics in Quantum Electronics*, **25**(2), Art. No. 6900309.
- COELHO-L., DE ALMEIDA-J., SANTOS-J., FERREIRA-R., ANDRÉ-P., AND VIEGAS-D. (2015). Sensing structure based on surface plasmon resonance in chemically etched single mode optical fibres, *Plasmonics*, **10**(2), pp. 319–327.
- COLE-B., WILLIAMS-J., KING-B., SHERWIN-M., AND STANLEY-C. (2001). Coherent manipulation of semiconductor quantum bits with terahertz radiation, *Nature*, **410**(6824), pp. 60–63.
- CONG-L., TAN-S., YAHIAOUI-R., YAN-F., ZHANG-W., AND SINGH-R. (2015). Experimental demonstration of ultrasensitive sensing with terahertz metamaterial absorbers: A comparison with the metasurfaces, *Applied Physics Letters*, **106**(3), Art. No. 031107.
- COOKE-D., MACDONALD-A., HRYCIW-A., WANG-J., LI-Q., MELDRUM-A., AND HEGMANN-F. (2006). Transient terahertz conductivity in photoexcited silicon nanocrystal films, *Physical Review B*, **73**(19), Art. No. 193311.
- CORDEIRO-C. M., FRANCO-M. A., CHESINI-G., BARRETTO-E. C., LWIN-R., CRUZ-C. B., AND LARGE-M. C. (2006). Microstructured-core optical fibre for evanescent sensing applications, *Optics Express*, **14**(26), pp. 13056–13066.
- CORDEIRO-C. M., NG-A. K., AND EBENDORFF-HEIDEPRIEM-H. (2020). Ultra-simplified single-step fabrication of microstructured optical fiber, *Scientific Reports*, **10**, Art. No. 9678.
- COUNY-F., AND BENABID-F. (2006). Large-pitch kagome-structured hollow-core photonic crystal fiber, *Optics Letters*, **31**(24), pp. 3574–3576.
- COUNY-F., BENABID-F., ROBERTS-P., LIGHT-P., AND RAYMER-M. (2007). Generation and photonic guidance of multi-octave optical-frequency combs, *Science*, **318**(5853), pp. 1118–1121.
- CRUZ-A. L., CORDEIRO-C., AND FRANCO-M. A. (2018). 3D printed hollow-core terahertz fibers, *Fibers*, **6**(3), Art. No. 43.
- CRUZ-A. L., FRANCO-M. A., CORDEIRO-C. M., RODRIGUES-G. S., OSÓRIO-J. H., AND DA SILVA-L. E. (2017). Exploring THz hollow-core fiber designs manufactured by 3D printing, *2017 SBMO/IEEE MTT-S Intl. Microwave and Optoelectronics Conference (IMOC)*, IEEE. DOI: 10.1109/IMOC.2017.8121109.
- CRUZ-A. L., MIGLIANO-A. C., AND FRANCO-M. A. (2013a). Polymer optical fibers for terahertz: Low loss propagation and high evanescent field, *2013 SBMO/IEEE MTT-S International Microwave & Optoelectronics Conference (IMOC)*, IEEE. DOI: 10.1109/IMOC.2013.6646442.
- CRUZ-A. L., MIGLIANO-A. C., AND FRANCO-M. A. (2013b). Refractive index sensor based on terahertz multimode interference fiber device, *Proc. SPIE Fifth European Workshop on Optical Fibre sensors*, **8794**, Art. No. 87940L.

Bibliography

- CRUZ-A. L., SERRÃO-V. A., BARBOSA-C. L., FRANCO-M. A., CORDEIRO-C. M., ARGYROS-A., AND TANG-X. (2015). 3D printed hollow core fiber with negative curvature for terahertz applications, *Journal of Micr. Opto. and Electro. Applications*, **14**, pp. 45–53.
- CRUZ-A., MIGLIANO-A., HAYASHI-J., CORDEIRO-C. M., AND FRANCO-M. (2013c). Highly birefringent polymer terahertz fiber with microstructure of slots in the core, *Proceedings of the 22nd Intl. Conf. on Plastic Optical Fibers (POF)*, Rio de Janeiro, Brazil, pp. 290–294.
- CUBILLAS-A. M., UNTERKOFLEDER-S., EUSER-T. G., ETZOLD-B. J., JONES-A. C., SADLER-P. J., WASSERSCHIED-P., AND RUSSELL-P. S. J. (2013). Photonic crystal fibres for chemical sensing and photochemistry, *Chemical Society Reviews*, **42**(22), pp. 8629–8648.
- CUI-H., ZHANG-X., SU-J., YANG-Y., FANG-Q., AND WEI-X. (2015). Vibration–rotation absorption spectrum of water vapor molecular in frequency selector at 0.5–2.5 THz range, *Optik*, **126**(23), pp. 3533–3537.
- CUNNINGHAM-P. D., VALDES-N. N., VALLEJO-F. A., HAYDEN-L. M., POLISHAK-B., ZHOU-X.-H., LUO-J., JEN-A. K.-Y., WILLIAMS-J. C., AND TWIEG-R. J. (2011). Broadband terahertz characterization of the refractive index and absorption of some important polymeric and organic electro-optic materials, *Journal of Applied Physics*, **109**(4), pp. 043505–043505.
- DAI-J., ZHANG-J., ZHANG-W., AND GRISCHKOWSKY-D. (2004). Terahertz time-domain spectroscopy characterization of the far-infrared absorption and index of refraction of high-resistivity, float-zone silicon, *JOSA B*, **21**(7), pp. 1379–1386.
- D'ANGELO-F., MICS-Z., BONN-M., AND TURCHINOVICH-D. (2014). Ultra-broadband THz time-domain spectroscopy of common polymers using THz air photonics, *Optics Express*, **22**(10), pp. 12475–12485.
- DASH-J. N., AND DAS-R. (2018). SPR based magnetic-field sensing in microchannelled PCF: a numerical approach, *Journal of Optics*, **20**(11), Art. No. 115001.
- DASH-J. N., AND JHA-R. (2014). Graphene-based birefringent photonic crystal fiber sensor using surface plasmon resonance, *IEEE Photonics Technology Letters*, **26**(11), pp. 1092–1095.
- DASH-J. N., AND JHA-R. (2015). On the performance of graphene-based D-shaped photonic crystal fibre biosensor using surface plasmon resonance, *Plasmonics*, **10**(5), pp. 1123–1131.
- DASH-J. N., AND JHA-R. (2016). Highly sensitive side-polished birefringent PCF-based SPR sensor in near IR, *Plasmonics*, **11**(6), pp. 1505–1509.
- DASH-J. N., DAS-R., AND JHA-R. (2018). AZO coated microchannel incorporated PCF-based SPR sensor: a numerical analysis, *IEEE Photonics Technology Letters*, **30**(11), pp. 1032–1035.
- DAVIDSON-D. B. (2010). *Computational Electromagnetics for RF and Microwave Engineering*, Cambridge University Press.
- DEBORD-B., ALHARBI-M., BRADLEY-T., FOURCADE-DUTIN-C., WANG-Y., VINCETTI-L., GÉRÔME-F., AND BENABID-F. (2013). Hypocycloid-shaped hollow-core photonic crystal fiber part I: Arc curvature effect on confinement loss, *Optics Express*, **21**(23), pp. 28597–28608.

- DEBORD-B., AMRANI-F., VINCETTI-L., GÉRÔME-F., AND BENABID-F. (2019). Hollow-core fiber technology: The rising of “gas photonics”, *Fibers*, **7**(2), Art. No. 16.
- DEBORD-B., AMSANPALLY-A., CHAFER-M., BAZ-A., MAUREL-M., BLONDY-J.-M., HUGONNOT-E., SCOL-F., VINCETTI-L., AND GÉRÔME-F. (2017). Ultralow transmission loss in inhibited-coupling guiding hollow fibers, *Optica*, **4**(2), pp. 209–217.
- DEBUS-C., AND BOLIVAR-P. H. (2007). Frequency selective surfaces for high sensitivity terahertz sensing, *Applied Physics Letters*, **91**(18), Art. No. 184102.
- DE NATALE-P., LORINI-L., INGUSCIO-M., NOLT-I. G., PARK-J. H., DI LONARDO-G., FUSINA-L., ADEP. A., AND MURRAY-A. G. (1997). Accurate frequency measurements for H₂O and 16O₃ in the 119 cm⁻¹ OH atmospheric window, *Applied Optics*, **36**(33), pp. 8526–8532.
- DENG-X., LI-L., ENOMOTO-M., AND KAWANO-Y. (2019). Continuously frequency-tuneable plasmonic structures for terahertz bio-sensing and spectroscopy, *Scientific Reports*, **9**, Art. No. 3498.
- DEVORE-J. R. (1951). Refractive indices of rutile and sphalerite, *JOSA*, **41**(6), pp. 416–419.
- DIAO-J., HAN-B., YIN-J., LI-X., LANG-T., AND HONG-Z. (2019). Analogue of electromagnetically induced transparency in an S-shaped all-dielectric metasurface, *IEEE Photonics Journal*, **11**(3), Art. No. 4601110.
- DICKINSON-E. J., EKSTRÖM-H., AND FONTES-E. (2014). Comsol multiphysics®: Finite element software for electrochemical analysis. a mini-review, *Electrochemistry communications*, **40**, pp. 71–74.
- DICTIONARY-M. (1982). The macquarie dictionary, *Macquarie Library Pty Ltd: Sydney*.
- DING-Z.-W., LANG-T.-T., WANG-Y., AND ZHAO-C.-L. (2017). Surface plasmon resonance refractive index sensor based on tapered coreless optical fiber structure, *Journal of Lightwave Technology*, **35**(21), pp. 4734–4739.
- DRUKTEINIS-J. S., MOONEY-B. P., FLOWERS-C. I., AND GATENBY-R. A. (2013). Beyond mammography: new frontiers in breast cancer screening, *The American Journal of medicine*, **126**(6), pp. 472–479.
- DUPUIS-A., ALLARD-J.-F., MORRIS-D., STOEFFLER-K., DUBOIS-C., AND SKOROBOGATIY-M. (2009). Fabrication and THz loss measurements of porous subwavelength fibers using a directional coupler method, *Optics Express*, **17**(10), pp. 8012–8028.
- DUPUIS-A., MAZHOROVA-A., DÉSEVÉDAVY-F., ROZÉ-M., AND SKOROBOGATIY-M. (2010). Spectral characterization of porous dielectric subwavelength THz fibers fabricated using a microstructured molding technique, *Optics Express*, **18**(13), pp. 13813–13828.
- DUPUIS-A., STOEFFLER-K., UNG-B., DUBOIS-C., AND SKOROBOGATIY-M. (2011). Transmission measurements of hollow-core THz bragg fibers, *JOSA B*, **28**(4), pp. 896–907.
- DU-Y., LI-S.-G., AND LIU-S. (2012). Wavelength-selective characteristics of high birefringence photonic crystal fiber with au nanowires selectively filled in the cladding air holes, *Chinese Physics B*, **21**(9), Art. No. 094219.

Bibliography

- EBENDORFF-HEIDPRIEM-H., AND MONRO-T. M. (2007). Extrusion of complex preforms for microstructured optical fibers, *Optics Express*, **15**(23), pp. 15086–15092.
- EBENDORFF-HEIDPRIEM-H., SCHUPPICH-J., DOWLER-A., LIMA-MARQUES-L., AND MONRO-T. M. (2014). 3D-printed extrusion dies: a versatile approach to optical material processing, *Optical Materials Express*, **4**(8), pp. 1494–1504.
- EMILIYANOV-G., HØIBY-P. E., PEDERSEN-L. H., AND BANG-O. (2013). Selective serial multi-antibody biosensing with Topas microstructured polymer optical fibers, *Sensors*, **13**(3), pp. 3242–3251.
- FAISAL-M., AND ISLAM-M. S. (2018). Extremely high birefringent terahertz fiber using a suspended elliptic core with slotted airholes, *Applied Optics*, **57**(13), pp. 3340–3347.
- FARDOOST-A., VANANI-F. G., AMIRHOSSEINI-A., AND SAFIAN-R. (2016). Design of a multilayer graphene-based ultrawideband terahertz absorber, *IEEE Transactions on Nanotechnology*, **16**(1), pp. 68–74.
- FEDERICI-J. F., SCHULKIN-B., HUANG-F., GARY-D., BARAT-R., OLIVEIRA-F., AND ZIMDARS-D. (2005). THz imaging and sensing for security applications—explosives, weapons and drugs, *Semiconductor Science and Technology*, **20**(7), Art. No. S266.
- FEDULOVA-E., NAZAROV-M. M., ANGELUTS-A., KITAI-M., SOKOLOV-V., AND SHKURINOV-A. (2012). Studying of dielectric properties of polymers in the terahertz frequency range, *Saratov Fall Meeting 2011: Optical Technol. in Biophy. and Medicine XIII*, **8337**, Art. No. 833701.
- FERGUSON-B., AND ZHANG-X.-C. (2002). Materials for terahertz science and technology, *Nature materials*, **1**, pp. 26–33.
- FISCHER-B., HOFFMANN-M., HELM-H., MODJESCH-G., AND JEPSEN-P. U. (2005a). Chemical recognition in terahertz time-domain spectroscopy and imaging, *Semiconductor Science and Technology*, **20**(7), Art. No. S246.
- FISCHER-B. M., HOFFMANN-M., HELM-H., WILK-R., RUTZ-F., KLEINE-OSTMANN-T., KOCH-M., AND JEPSEN-P. U. (2005b). Terahertz time-domain spectroscopy and imaging of artificial RNA, *Optics Express*, **13**(14), pp. 5205–5215.
- GALLOT-G., JAMISON-S., MCGOWAN-R., AND GRISCHKOWSKY-D. (2000). Terahertz waveguides, *JOSA B*, **17**(5), pp. 851–863.
- GAO-D., GUAN-C., WEN-Y., ZHONG-X., AND YUAN-L. (2014a). Multi-hole fiber based surface plasmon resonance sensor operated at near-infrared wavelengths, *Optics Communications*, **313**, pp. 94–98.
- GAO-S.-F., WANG-Y.-Y., DING-W., JIANG-D.-L., GU-S., ZHANG-X., AND WANG-P. (2018). Hollow-core conjoined-tube negative-curvature fibre with ultralow loss, *Nature Communications*, **9**, Art. No. 2828.
- GAO-S., PARK-C.-S., LEE-S.-S., AND CHOI-D.-Y. (2019). All-dielectric metasurfaces for simultaneously realizing polarization rotation and wavefront shaping of visible light, *Nanoscale*, **11**(9), pp. 4083–4090.

- GAO-Y., GAN-Q., AND BARTOLI-F. J. (2014b). Breakthroughs in photonics 2013: research highlights on biosensors based on plasmonic nanostructures, *IEEE Photonics Journal*, **6**(2), Art. No. 0700805.
- GAUVREAU-B., HASSANI-A., FEHRI-M. F., KABASHIN-A., AND SKOROBOGATIY-M. (2007). Photonic bandgap fiber-based surface plasmon resonance sensors, *Optics Express*, **15**(18), pp. 11413–11426.
- GENEVET-P., CAPASSO-F., AIETA-F., KHORASANINEJAD-M., AND DEVLIN-R. (2017). Recent advances in planar optics: from plasmonic to dielectric metasurfaces, *Optica*, **4**(1), pp. 139–152.
- GERECHT-E., DOUGLASS-K. O., AND PLUSQUELLIC-D. F. (2011). Chirped-pulse terahertz spectroscopy for broadband trace gas sensing, *Optics Express*, **19**(9), pp. 8973–8984.
- GÉRÔME-F., JAMIER-R., AUGUSTE-J.-L., HUMBERT-G., AND BLONDY-J.-M. (2010). Simplified hollow-core photonic crystal fiber, *Optics Letters*, **35**(8), pp. 1157–1159.
- GOTO-M., QUEMA-A., TAKAHASHI-H., ONO-S., AND SARUKURA-N. (2004). Teflon photonic crystal fiber as terahertz waveguide, *Japanese Journal of Applied Physics*, **43**(2B), Art. No. L317.
- GRANT-J., MCCRINDLE-I. J., AND CUMMING-D. R. (2016). Multi-spectral materials: hybridisation of optical plasmonic filters, a mid infrared metamaterial absorber and a terahertz metamaterial absorber, *Optics Express*, **24**(4), pp. 3451–3463.
- GRISCHKOWSKY-D., KEIDING-S., VAN EXTER-M., AND FATTINGER-C. (1990). Far-infrared time-domain spectroscopy with terahertz beams of dielectrics and semiconductors, *JOSA B*, **7**(10), pp. 2006–2015.
- GUIDER-R., GANDOLFI-D., CHALYAN-T., PASQUARDINI-L., SAMUSENKO-A., PEDERZOLLI-C., PUCKER-G., AND PAVESI-L. (2015). Sensitivity and limit of detection of bio sensors based on ring resonators, *Sensing and Biosensing Research*, **6**, pp. 99–102.
- GUO-R., STUEBLING-E.-M., BELTRAN-MEJIA-F., ULM-D., KLEINE-OSTMANN-T., EHRIG-F., AND KOCH-M. (2019). 3D printed terahertz rectangular waveguides of polystyrene and Topas: a comparison, *Journal of Infrared, Millimeter, and Terahertz Waves*, **40**, pp. 1–4.
- GUPTA-B. D., AND VERMA-R. K. (2009). Surface plasmon resonance-based fiber optic sensors: principle, probe designs, and some applications, *Journal of sensors*, **2009**, Art. No. 979761.
- HABIB-M. A., AND ANOWER-M. S. (2019). Design and numerical analysis of highly birefringent single mode fiber in THz regime, *Optical Fiber Technology*, **47**, pp. 197–203.
- HABIB-M. A., ANOWER-M. S., AND HASAN-M. R. (2018). Highly birefringent and low effective material loss microstructure fiber for THz wave guidance, *Optics Communications*, **423**, pp. 140–144.
- HAN-H., PARK-H., CHO-M., AND KIM-J. (2002). Terahertz pulse propagation in a plastic photonic crystal fiber, *Applied Physics Letters*, **80**(15), pp. 2634–2636.
- HAN-P., CHO-G., AND ZHANG-X.-C. (2000). Time-domain transillumination of biological tissues with terahertz pulses, *Optics Letters*, **25**(4), pp. 242–244.
- HAN-S., CONG-L., SRIVASTAVA-Y. K., QIANG-B., RYBIN-M. V., KUMAR-A., JAIN-R., LIM-W. X., ACHANTA-V. G., AND PRABHU-S. S. (2019). All-dielectric active terahertz photonics, driven by bound states in the continuum, *Advanced Materials*, **31**(37), Art. No. 1901921.

- HANSON-G. W. (2008). Dyadic green's functions and guided surface waves for a surface conductivity model of graphene, *Journal of Applied Physics*, **103**(6), Art. No. 064302.
- HAQUE-E., HOSSAIN-M. A., AHMED-F., AND NAMIHIRA-Y. (2018). Surface plasmon resonance sensor based on modified D-shaped photonic crystal fiber for wider range of refractive index detection, *IEEE Sensors Journal*, **18**(20), pp. 8287–8293.
- HAQUE-E., HOSSAIN-M. A., NAMIHIRA-Y., AND AHMED-F. (2019). Microchannel-based plasmonic refractive index sensor for low refractive index detection, *Applied Optics*, **58**(6), pp. 1547–1554.
- HARRINGTON-J. A., GEORGE-R., PEDERSEN-P., AND MUELLER-E. (2004). Hollow polycarbonate waveguides with inner Cu coatings for delivery of terahertz radiation, *Optics Express*, **12**(21), pp. 5263–5268.
- HARTUNG-A., KOBELKE-J., SCHWUCHOW-A., BIERLICH-J., POPP-J., SCHMIDT-M. A., AND FROSCH-T. (2015). Low-loss single-mode guidance in large-core antiresonant hollow-core fibers, *Optics Letters*, **40**(14), pp. 3432–3435.
- HASAN-M. R., AKTER-S., RIFAT-A. A., RANA-S., AHMED-K., AHMED-R., SUBBARAMAN-H., AND ABBOTT-D. (2017). Spiral photonic crystal fiber-based dual-polarized surface plasmon resonance biosensor, *IEEE Sensors Journal*, **18**(1), pp. 133–140.
- HASAN-M. R., ANOWER-M. S., ISLAM-M. A., AND RAZZAK-S. (2016). Polarization-maintaining low-loss porous-core spiral photonic crystal fiber for terahertz wave guidance, *Applied Optics*, **55**(15), pp. 4145–4152.
- HASANUZZAMAN-G., HABIB-M. S., RAZZAK-S. A., HOSSAIN-M. A., AND NAMIHIRA-Y. (2015). Low loss single-mode porous-core kagome photonic crystal fiber for THz wave guidance, *IEEE Journal of Lightwave Technology*, **33**(19), pp. 4027–4031.
- HASANUZZAMAN-G., IEZEKIEL-S., MARKOS-C., AND HABIB-M. S. (2018). Hollow-core fiber with nested anti-resonant tubes for low-loss THz guidance, *Optics Communications*, **426**, pp. 477–482.
- HASANUZZAMAN-G., RANA-S., AND HABIB-M. S. (2016). A novel low loss, highly birefringent photonic crystal fiber in THz regime, *IEEE Photonics Technology Letters*, **28**(8), pp. 899–902.
- HASSANI-A., AND SKOROBOGATIY-M. (2008). Surface plasmon resonance-like integrated sensor at terahertz frequencies for gaseous analytes., *Optics Express*, **16**(25), pp. 20206–20214.
- HASSANI-A., DUPUIS-A., AND SKOROBOGATIY-M. (2008). Porous polymer fibers for low-loss terahertz guiding, *Optics Express*, **16**(9), pp. 6340–6351.
- HAUTAKORPI-M., MATTINEN-M., AND LUDVIGSEN-H. (2008). Surface-plasmon-resonance sensor based on three-hole microstructured optical fiber, *Optics Express*, **16**(12), pp. 8427–8432.
- HAYES-J. R., POLETTI-F., ABOKHAMIS-M. S., WHEELER-N. V., BADDELA-N. K., AND RICHARDSON-D. J. (2015). Anti-resonant hexagram hollow core fibers, *Optics Express*, **23**(2), pp. 1289–1299.
- HEFFERMAN-G., CHEN-Z., YUAN-L., AND WEI-T. (2015). Phase-shifted terahertz fiber bragg grating for strain sensing with large dynamic range, *IEEE Photonics Technology Letters*, **27**(15), pp. 1649–1652.

- HE-J., YE-J., WANG-X., KAN-Q., AND ZHANG-Y. (2016). A broadband terahertz ultrathin multi-focus lens, *Scientific Reports*, **6**, Art. No. 28800.
- HE-X. (2015). Tunable terahertz graphene metamaterials, *Carbon*, **82**, pp. 229–237.
- HE-X., LI-S., YANG-X., SHI-S., WU-F., AND JIANG-J. (2017). High-sensitive dual-band sensor based on microsize circular ring complementary terahertz metamaterial, *Journal of Electromagnetic Waves and Applications*, **31**(1), pp. 91–100.
- HIDAKA-T., MINAMIDE-H., ITO-H., NISHIZAWA-J.-I., TAMURA-K., AND ICHIKAWA-S. (2005). Ferroelectric PVDF cladding terahertz waveguide, *IEE Journal of Lightwave Technology*, **23**(8), pp. 2469–2473.
- HIRATA-A., KOSUGI-T., TAKAHASHI-H., YAMAGUCHI-R., NAKAJIMA-F., FURUTA-T., ITO-H., SUGAHARA-H., SATO-Y., AND NAGATSUMA-T. (2006). 120-GHz-band millimeter-wave photonic wireless link for 10-Gbps data transmission, *IEEE Transactions on Microwave Theory and Techniques*, **54**(5), pp. 1937–1944.
- HIRATA-A., YAMAGUCHI-R., KOSUGI-T., TAKAHASHI-H., MURATA-K., NAGATSUMA-T., KUKUTSUN., KADO-Y., IAI-N., AND OKABE-S. (2009). 10-Gbps wireless link using InP HEMT MMICs for generating 120-GHz-band millimeter-wave signal, *IEEE Transactions on Microwave Theory and Techniques*, **57**(5), pp. 1102–1109.
- HOMOLA-J. (2008). Surface plasmon resonance sensors for detection of chemical and biological species, *Chemical Reviews*, **108**(2), pp. 462–493.
- HOMOLA-J., YEE-S. S., AND GAUGLITZ-G. (1999). Surface plasmon resonance sensors, *Sensors and Actuators B: Chemical*, **54**(2), pp. 3–15.
- HOSSAIN-M. A., AND NAMIHIRA-Y. (2014). Light source design using kagome-lattice hollow core photonic crystal fibers, *Optical Review*, **21**(5), pp. 490–495.
- HSU-C. W., ZHEN-B., STONE-A. D., JOANNOPOULOS-J. D., AND SOLJAČIĆ-M. (2016). Bound states in the continuum, *Nature Reviews Materials*, **1**(9), Art. No. 3190.
- HUA-C., SHI-HUA-M., WEN-XING-Y., XIU-MEI-W., AND XIAO-ZHOU-W. (2013). The diagnosis of human liver cancer by using THz fiber-scanning near-field imaging, *Chinese Physics Letters*, **30**(3), Art. No. 030702.
- HUANG-L., ZHANG-S., AND ZENTGRAF-T. (2018). Metasurface holography: from fundamentals to applications, *Nanophotonics*, **7**(6), pp. 1169–1190.
- HUBER-R., TAUSER-F., BRODSCHELM-A., BICHLER-M., ABSTREITER-G., AND LEITENSTORFER-A. (2001). How many-particle interactions develop after ultrafast excitation of an electron-hole plasma, *Nature*, **414**(6861), pp. 286–289.
- HU-D. J. J., AND HO-H. P. (2017). Recent advances in plasmonic photonic crystal fibers: design, fabrication and applications, *Advances in Optics and Photonics*, **9**(2), pp. 257–314.
- IADICICCO-A., CUSANO-A., CAMPOPIANO-S., CUTOLO-A., AND GIORDANO-M. (2005). Thinned fiber bragg gratings as refractive index sensors, *IEEE Sensors Journal*, **5**(6), pp. 1288–1295.

Bibliography

- ISLAM-M. R., HOSSAIN-M. A., ALI-S. I., SULTANA-J., AND ISLAM-M. S. (2018a). Design and characterization of an ultra low loss, dispersion-flattened slotted photonic crystal fiber for terahertz application, *Journal of Optical Communications*. DOI: <https://doi.org/10.1515/joc-2018-0152>.
- ISLAM-M. R., KABIR-M. F., TALHA-K. M. A., AND ISLAM-M. S. (2019a). A novel hollow core terahertz refractometric sensor, *Sensing and Biosensing Research*, **25**, Art. No. 100295.
- ISLAM-M. S., CORDEIRO-C. M., FRANCO-M. A., SULTANA-J., CRUZ-A. L., AND ABBOTT-D. (2020a). Terahertz optical fibers, *Optics Express*, **28**(11), pp. 16089–16117.
- ISLAM-M. S., CORDEIRO-C. M., NINE-M. J., SULTANA-J., CRUZ-A. L., DINOVISER-A., NG-B. W.-H., EBENDORFF-HEIDPRIEM-H., LOSIC-D., AND ABBOTT-D. (2020b). Experimental study on glass and polymers: Determining the optimal material for potential use in terahertz technology, *IEEE Access*, **8**, pp. 97204–97214.
- ISLAM-M. S., CORDEIRO-C. M., SULTANA-J., AONI-R. A., FENG-S., AHMED-R., DORRAKI-M., DINOVISER-A., NG-B. W.-H., AND ABBOTT-D. (2019b). A hi-bi ultra-sensitive surface plasmon resonance fiber sensor, *IEEE Access*, **7**, pp. 79085–79094.
- ISLAM-M. S., H-NG-B. W., AND ABBOTT-D. (2020c). Terahertz ultrahigh-Q metasurface enabled by out-of-plane asymmetry, *45th Int. Conf. on Infra. Milli. and Tera. Waves (IRMMW-THz)*, IEEE. DOI: 10.1109/IRMMW-THz46771.2020.9370414.
- ISLAM-M. S., ISLAM-M. R., SULTANA-J., DINOVISER-A., NG-B. W.-H., AND ABBOTT-D. (2019c). Exposed-core localized surface plasmon resonance biosensor, *JOSA B*, **36**(8), pp. 2306–2311.
- ISLAM-M. S., NG-B. W. H., AND ABBOTT-D. (2018b). Porous-core photonic crystal fibers guide polarization-preserving terahertz waves, *Laser Focus World*, **54**(5).
- ISLAM-M. S., RANA-S., ISLAM-M. R., FAISAL-M., RAHMAN-H., AND SULTANA-J. (2016a). Porous core photonic crystal fibre for ultra-low material loss in THz regime, *IET Communications*, **10**(16), pp. 2179–2183.
- ISLAM-M. S., SULTANA-J., AHMED-K., ISLAM-M. R., DINOVISER-A., NG-B. W.-H., AND ABBOTT-D. (2017a). A novel approach for spectroscopic chemical identification using photonic crystal fiber in the terahertz regime, *IEEE Sensors Journal*, **18**(2), pp. 575–582.
- ISLAM-M. S., SULTANA-J., AONI-R. A., HABIB-M. S., DINOVISER-A., NG-B. W.-H., AND ABBOTT-D. (2019d). Localized surface plasmon resonance biosensor: an improved technique for SERS response intensification, *Optics Letters*, **44**(5), pp. 1134–1137.
- ISLAM-M. S., SULTANA-J., ATAI-J., ABBOTT-D., RANA-S., AND ISLAM-M. R. (2017b). Ultra low-loss hybrid core porous fiber for broadband applications, *Applied Optics*, **56**(4), pp. 1232–1237.
- ISLAM-M. S., SULTANA-J., ATAI-J., ISLAM-M. R., AND ABBOTT-D. (2017c). Design and characterization of a low-loss, dispersion-flattened photonic crystal fiber for terahertz wave propagation, *Optik*, **145**, pp. 398–406.
- ISLAM-M. S., SULTANA-J., DINOVISER-A., AHMED-K., NG-B. W.-H., AND ABBOTT-D. (2018c). Sensing of toxic chemicals using polarized photonic crystal fiber in the terahertz regime, *Optics Communications*, **426**, pp. 341–347.

- ISLAM-M. S., SULTANA-J., DINOVIKSER-A., FAISAL-M., ISLAM-M. R., NG-B. W.-H., AND ABBOTT-D. (2018d). Zeonex-based asymmetrical terahertz photonic crystal fiber for multichannel communication and polarization maintaining applications, *Applied Optics*, **57**(4), pp. 666–672.
- ISLAM-M. S., SULTANA-J., DINOVIKSER-A., NG-B. W., BENABID-F., CORDEIRO-C. M., HEIDPRIEM-H. E., AND ABBOTT-D. (2021). Single-step fabrication and measurements of a hollow core anti-resonant terahertz optical fibre, *Advanced Photonics Research (Under Review June 2021)*.
- ISLAM-M. S., SULTANA-J., DINOVIKSER-A., NG-B. W.-H., AND ABBOTT-D. (2018e). A gold coated plasmonic sensor for biomedical and biochemical analyte detection, *43rd Int. Conf. on Infra. Milli. and Tera. Waves (IRMMW-THz)*, IEEE. DOI: 10.1109/IRMMW-THz.2018.8510018.
- ISLAM-M. S., SULTANA-J., DINOVIKSER-A., NG-B. W.-H., AND ABBOTT-D. (2018f). A novel Zeonex based oligoporous-core photonic crystal fiber for polarization preserving terahertz applications, *Optics Communications*, **413**, pp. 242–248.
- ISLAM-M. S., SULTANA-J., DORRAKI-M., ATAI-J., ISLAM-M. R., DINOVIKSER-A., NG-B. W.-H., AND ABBOTT-D. (2018g). Low loss and low dispersion hybrid core photonic crystal fiber for terahertz propagation, *Photonic Network Communications*, **35**(3), pp. 364–373.
- ISLAM-M. S., SULTANA-J., FAISAL-M., ISLAM-M. R., DINOVIKSER-A., NG-B. W., AND ABBOTT-D. (2018h). A modified hexagonal photonic crystal fiber for terahertz applications, *Optical Materials*, **79**, pp. 336–339.
- ISLAM-M. S., SULTANA-J., RANA-S., ISLAM-M. R., FAISAL-M., KAIJAGE-S. F., AND ABBOTT-D. (2017d). Extremely low material loss and dispersion flattened Topas based circular porous fiber for long distance terahertz wave transmission, *Optical Fiber Technology*, **34**, pp. 6–11.
- ISLAM-M. S., SULTANA-J., RIFAT-A. A., AHMED-R., DINOVIKSER-A., NG-B. W.-H., EBENDORFF-HEIDPRIEM-H., AND ABBOTT-D. (2018i). Dual-polarized highly sensitive plasmonic sensor in the visible to near-IR spectrum, *Optics Express*, **26**(23), pp. 30347–30361.
- ISLAM-M. S., SULTANA-J., RIFAT-A. A., DINOVIKSER-A., NG-B. W.-H., AND ABBOTT-D. (2018j). Terahertz sensing in a hollow core photonic crystal fiber, *IEEE Sensors Journal*, **18**(10), pp. 4073–4080.
- ISLAM-M., SULTANA-J., BIABANIFARD-M., VAFAPOUR-Z., NINE-M., DINOVIKSER-A., CORDEIRO-C., NG-B.-H., AND ABBOTT-D. (2020d). Tunable localized surface plasmon graphene metasurface for multiband superabsorption and terahertz sensing, *Carbon*, **158**, pp. 559–567.
- ISLAM-M., SULTANA-J., CORDEIRO-C. M., CRUZ-A. L., DINOVIKSER-A., NG-B.-H., AND ABBOTT-D. (2019e). Broadband characterization of glass and polymer materials using THz-TDS, *44th Intl. Conf. on Infra. Milli. and Tera. Waves (IRMMW-THz)*, IEEE. DOI: 10.1109/IRMMW-THz.2019.8874013.
- ISLAM-M., SULTANA-J., DINOVIKSER-A., NG-B.-H., AND ABBOTT-D. (2019f). Electrically tunable graphene metasurface for multiband superabsorption and terahertz sensing, *2019 44th Int. Conf. on Infra. Milli. and Tera. Waves (IRMMW-THz)*, IEEE. DOI: 10.1109/IRMMW-THz.2019.8873851.

Bibliography

- ISLAM-R., HABIB-M. S., HASANUZZAMAN-G., AHMAD-R., RANA-S., AND KAIJAGE-S. F. (2015). Extremely high-birefringent asymmetric slotted-core photonic crystal fiber in THz regime, *IEEE Photonics Technology Letters*, **27**(21), pp. 2222–2225.
- ISLAM-R., HABIB-M. S., HASANUZZAMAN-G., RANA-S., SADATH-M. A., AND MARKOS-C. (2016b). A novel low-loss diamond-core porous fiber for polarization maintaining terahertz transmission, *IEEE Photonics Technology Letters*, **28**(14), pp. 1537–1540.
- ISLAM-S., ISLAM-M. R., FAISAL-M., AREFIN-A. S., RAHMAN-H., SULTANA-J., AND RANA-S. (2016c). Extremely low-loss, dispersion flattened porous-core photonic crystal fiber for terahertz regime, *Optical Engineering*, **55**(7), Art. No. 076117.
- ISSA-N. A., VAN EIJKELNBORG-M. A., FELLEW-M., COX-F., HENRY-G., AND LARGE-M. C. (2004). Fabrication and study of microstructured optical fibers with elliptical holes, *Optics Letters*, **29**(12), pp. 1336–1338.
- JANSEN-C., AL-NAIB-I. A., BORN-N., AND KOCH-M. (2011). Terahertz metasurfaces with high Q-factors, *Applied Physics Letters*, **98**(5), Art. No. 051109.
- JASION-G. T., BRADLEY-T. D., HARRINGTON-K., SAKR-H., CHEN-Y., FOKOUA-E. N., DAVIDSON-I. A., TARANTA-A., HAYES-J. R., AND RICHARDSON-D. J. (2020). Hollow core NANF with 0.28 dB/km attenuation in the C and L bands, *Optical Fiber Communication Conference*, Optical Society of America, OSA. DOI: <https://doi.org/10.1364/OFC.2020.Th4B.4>.
- JEON-T.-I., ZHANG-J., AND GRISCHKOWSKY-D. (2005). THz Sommerfeld wave propagation on a single metal wire, *Applied Physics Letters*, **86**(16), Art. No. 161904.
- JEPSEN-P. U. (2019). Phase retrieval in terahertz time-domain measurements: a “how to” tutorial, *Journal of Infrared, Millimeter, and Terahertz Waves*, **40**(4), pp. 395–411.
- JEPSEN-P. U., JENSEN-J. K., AND MØLLER-U. (2008). Characterization of aqueous alcohol solutions in bottles with THz reflection spectroscopy, *Optics Express*, **16**(13), pp. 9318–9331.
- JEPSEN-P. U., MØLLER-U., AND MERBOLD-H. (2007). Investigation of aqueous alcohol and sugar solutions with reflection terahertz time-domain spectroscopy, *Optics Express*, **15**(22), pp. 14717–14737.
- JHA-R., AND BADENES-G. (2009). Effect of fiber core dopant concentration on the performance of surface plasmon resonance-based fiber optic sensor, *Sensors and Actuators A: Physical*, **150**(2), pp. 212–217.
- JIANG-J., WANG-X., LI-S., DING-F., LI-N., MENG-S., LI-R., QI-J., LIU-Q., AND LIU-G. L. (2018). Plasmonic nano-arrays for ultrasensitive bio-sensing, *Nanophotonics*, **7**(9), pp. 1517–1531.
- JIANG-X., CHEN-D., AND HU-G. (2013). Suspended hollow core fiber for terahertz wave guiding, *Applied Optics*, **52**(4), pp. 770–774.
- JIAO-S., GU-S., YANG-H., FANG-H., AND XU-S. (2018). Highly sensitive dual-core photonic crystal fiber based on a surface plasmon resonance sensor with a silver nano-continuous grating, *Applied Optics*, **57**(28), pp. 8350–8358.
- JIAQIANG-X., YUPING-C., DAOYONG-C., AND JIANIAN-S. (2006). Hydrothermal synthesis and gas sensing characters of ZnO nanorods, *Sensors and Actuators B: Chemical*, **113**(1), pp. 526–531.

- JORGENSEN-R. C., AND YEE-S. S. (1993). A fiber-optic chemical sensor based on surface plasmon resonance, *Sensors and Actuators B: Chemical*, **12**(3), pp. 213–220.
- KABASHIN-A. V., EVANS-P., PASTKOVSKY-S., HENDREN-W., WURTZ-G. A., ATKINSON-R., POLLARD-R., PODOLSKIY-V., AND ZAYATS-A. V. (2009). Plasmonic nanorod metamaterials for biosensing, *Nature Materials*, **8**(11), pp. 867–871.
- KAIJAGE-S. F., OUYANG-Z., AND JIN-X. (2013). Porous-core photonic crystal fiber for low loss terahertz wave guiding, *IEEE Photonics Technology Letters*, **25**(15), pp. 1454–1457.
- KALACHYOVA-Y., LYUTAKOV-O., KOSTEJN-M., CLUPEK-M., AND SVORCIK-V. (2015). Silver nanostructures: From individual dots to coupled strips for the tailoring of SERS excitation wavelength from near-UV to near-IR, *Electronic Materials Letters*, **11**(2), pp. 288–294.
- KANG-J., SHIN-D., BAE-S., AND HONG-B. H. (2012). Graphene transfer: key for applications, *Nanoscale*, **4**(18), pp. 5527–5537.
- KATAGIRI-T., SUZUKI-T., AND MATSUURA-Y. (2018). Time-domain terahertz gas spectroscopy using hollow-optical-fiber gas cell, *Optical Engineering*, **57**(5), Art. No. 054104.
- KATYBA-G., CHERNOMYRDIN-N., DOLGANOVA-I., PRONIN-A., MININ-I., MININ-O., ZAYTSEV-K., AND KURLOV-V. (2019). Step-index sapphire fiber and its application in a terahertz near-field microscopy, *Millimetre Wave and Terahertz and Technology XII*, **11164**, Art. No. 111640G.
- KATYBA-G. M., ZAYTSEV-K. I., CHERNOMYRDIN-N. V., SHIKUNOVA-I. A., KOMANDIN-G. A., ANZIN-V. B., LEBEDEV-S. P., SPEKTOR-I. E., KARASIK-V. E., AND YURCHENKO-S. O. (2018). Sapphire photonic crystal waveguides for terahertz sensing in aggressive environments, *Advanced Optical Materials*, **6**(22), Art. No. 1800573.
- KEMP-M. C. (2011). Explosives detection by terahertz spectroscopy—a bridge too far?, *IEEE Transactions on Terahertz Science and Technology*, **1**(1), pp. 282–292.
- KESHAVARZ-A., AND VAFAPOUR-Z. (2019). Sensing avian influenza viruses using terahertz metamaterial reflector, *IEEE Sensors Journal*, **19**(13), pp. 5161–5166.
- KIM-H. K., LEE-D., AND LIM-S. (2016). A fluidically tunable metasurface absorber for flexible large-scale wireless ethanol sensor applications, *Sensors*, **16**(8), Art. No. 1246.
- KISCHKAT-J., PETERS-S., GRUSKA-B., SEMTSIV-M., CHASHNIKOVA-M., KLINKMÜLLER-M., FEDOSENKO-O., MACHULIK-S., ALEKSANDROVA-A., AND MONASTYRSKIY-G. (2012). Mid-infrared optical properties of thin films of aluminum oxide, titanium dioxide, silicon dioxide, aluminum nitride, and silicon nitride, *Applied Optics*, **51**(28), pp. 6789–6798.
- KITAI-M., NAZAROV-M., NEDOREZOVA-P., AND SHKURINOV-A. (2017). Determination of the boundary transition temperatures in polypropylene on the basis of measurements in the terahertz band, *Radiophysics and Quantum Electronics*, **60**(5), pp. 409–416.
- KNIGHT-J. C. (2003). Photonic crystal fibres, *Nature*, **424**(6950), pp. 847–851.
- KNIGHT-J. C., BROENG-J., BIRKS-T. A., AND RUSSELL-P. S. J. (1998). Photonic band gap guidance in optical fibers, *Science*, **282**(5393), pp. 1476–1478.

- KOENIG-S., LOPEZ-DIAZ-D., ANTES-J., BOES-F., HENNEBERGER-R., LEUTHER-A., TESSMANN-A., SCHMOGROW-R., HILLERKUSS-D., AND PALMER-R. (2013). Wireless sub-THz communication system with high data rate, *Nature Photonics*, **7**(12), pp. 977–981.
- KOHLHAAS-R. B., REHN-A., NELLEN-S., KOCH-M., SCHELL-M., DIETZ-R. J., AND BALZER-J. C. (2017). Terahertz quasi time-domain spectroscopy based on telecom technology for 1550 nm, *Optics Express*, **25**(11), pp. 12851–12859.
- KOSHELEV-K., AND KIVSHAR-Y. (2019). Light trapping gets a boost, *Nature*, **574**, pp. 491–492.
- KOSHELEV-K., LEPESHOV-S., LIU-M., BOGDANOV-A., AND KIVSHAR-Y. (2018). Asymmetric metasurfaces with high-Q resonances governed by bound states in the continuum, *Physical Review Letters*, **121**(19), Art. No. 193903.
- KOSTECKI-R., EBENDORFF-HEIDPRIEM-H., DAVIS-C., MCADAM-G., WARREN-SMITH-S. C., AND MONRO-T. M. (2012). Silica exposed-core microstructured optical fibers, *Optical Materials Express*, **2**(11), pp. 1538–1547.
- KUZNETSOV-A. I., MIROSHNICHENKO-A. E., BRONGERSMA-M. L., KIVSHAR-Y. S., AND LUK'YANCHUK-B. (2016). Optically resonant dielectric nanostructures, *Science*, **354**(6314), Art. No. aag2472.
- LAI-C.-H., HSUEH-Y.-C., CHEN-H.-W., HUANG-Y.-J., CHANG-H.-C., AND SUN-C.-K. (2009). Low-index terahertz pipe waveguides, *Optics Letters*, **34**(21), pp. 3457–3459.
- LAI-C.-H., YOU-B., LU-J.-Y., LIU-T.-A., PENG-J.-L., SUN-C.-K., AND CHANG-H.-C. (2010). Modal characteristics of antiresonant reflecting pipe waveguides for terahertz waveguiding, *Optics Express*, **18**(1), pp. 309–322.
- LA SPADA-L. (2019). Metasurfaces for advanced sensing and diagnostics, *Sensors*, **19**(2), Art. No. 355.
- LEAHY-HOPPA-M., FITCH-M., ZHENG-X., HAYDEN-L., AND OSIANDER-R. (2007). Wideband terahertz spectroscopy of explosives, *Chemical Physics Letters*, **434**(4), pp. 227–230.
- LEEA-Y. S., KIMB-S., MAENGB-I., KANGB-C., AND OH-K. (2019). Low-loss terahertz pulse transmission through commercially available porous tubes with PTFE, *Sixth Intl. Workshop on Specialty Optical Fibers and Their Applications*, **11206**, Art. No. 112061S–1.
- LEE-B., ROH-S., AND PARK-J. (2009). Current status of micro-and nano-structured optical fiber sensors, *Optical Fiber Technology*, **15**(3), pp. 209–221.
- LEITIS-A., TITTL-A., LIU-M., LEE-B. H., GU-M. B., KIVSHAR-Y. S., AND ALTUG-H. (2019). Angle-multiplexed all-dielectric metasurfaces for broadband molecular fingerprint retrieval, *Science Advances*, **5**(5), Art. No. eaaw2871.
- LIAO-Z., LIU-S., MA-H. F., LI-C., JIN-B., AND CUI-T. J. (2016). Electromagnetically induced transparency metamaterial based on spoof localized surface plasmons at terahertz frequencies, *Scientific Reports*, **6**, Art. No. 27596.
- LIEDBERG-B., NYLANDER-C., AND LUNSTRÖM-I. (1983). Surface plasmon resonance for gas detection and biosensing, *Sensors and Actuators*, **4**, pp. 299–304.

- LI-G., ZHANG-S., AND ZENTGRAF-T. (2017a). Nonlinear photonic metasurfaces, *Nature Reviews Materials*, **2**(5), Art. No. 17010.
- LI-H., ATAKARAMIANS-S., LWIN-R., TANG-X., YU-Z., ARGYROS-A., AND KUHLMEY-B. T. (2016a). Flexible single-mode hollow-core terahertz fiber with metamaterial cladding, *Optica*, **3**(9), pp. 941–947.
- LI-H., ATAKARAMIANS-S., YUAN-J., XIAO-H., WANG-W., LI-Y., WU-B., AND HAN-Z. (2018a). Terahertz polarization-maintaining subwavelength filters, *Optics Express*, **26**(20), pp. 25617–25629.
- LI-H., REN-G., ATAKARAMIANS-S., KUHLMEY-B. T., AND JIAN-S. (2016b). Linearly polarized single tm mode terahertz waveguide, *Optics Letters*, **41**(17), pp. 4004–4007.
- LI-J., NALLAPPAN-K., GUERBOUKHA-H., AND SKOROBOGATIY-M. (2017b). 3D printed hollow core terahertz bragg waveguides with defect layers for surface sensing applications, *Optics Express*, **25**(4), pp. 4126–4144.
- LIN-H., WITHAYACHUMNANKUL-W., FISCHER-B. M., MICKAN-S., AND ABBOTT-D. (2008). Gas recognition with terahertz time-domain spectroscopy and spectral catalog: a preliminary study, *Terahertz Photonics*, **6840**, Art. No. 68400X.
- LIU-B., TANG-C., CHEN-J., ZHU-M., PEI-M., AND ZHU-X. (2017). Electrically tunable fano resonance from the coupling between interband transition in monolayer graphene and magnetic dipole in metamaterials, *Scientific Reports*, **7**, Art. No. 17117.
- LIU-C., QI-L., AND ZHANG-X. (2018a). Broadband graphene-based metamaterial absorbers, *AIP Advances*, **8**, Art. No. 015301.
- LIU-C., SU-W., LIU-Q., LU-X., WANG-F., SUN-T., AND CHU-P. K. (2018b). Symmetrical dual D-shape photonic crystal fibers for surface plasmon resonance sensing, *Optics Express*, **26**(7), pp. 9039–9049.
- LIU-C., YU-J., SUN-X., ZHANG-J., AND HE-J. (2003). Thermal degradation studies of cyclic olefin copolymers, *Polymer Degradation and Stability*, **81**(2), pp. 197–205.
- LIU-F., GAO-H. Y., XU-Q., AND ZHANG-Y. N. (2011). Fabrication and characteristics of elliptical-holes and near elliptical core hexangular lattice photonic crystal fibers based on polymer, *Advanced Materials Research*, Vol. 279, pp. 151–156.
- LIU-M., YANG-X., SHUM-P., AND YUAN-H. (2018c). High-sensitivity birefringent and single-layer coating photonic crystal fiber biosensor based on surface plasmon resonance, *Applied Optics*, **57**(8), pp. 1883–1886.
- LIU-X., LAN-C., LI-B., ZHAO-Q., AND ZHOU-J. (2016). Dual band metamaterial perfect absorber based on artificial dielectric “molecules”, *Scientific Reports*, **6**, Art. No. 28906.
- LIU-Y., AND JIAN-S. (2014). Tunable trapping and releasing light in graded graphene-silica metamaterial waveguide, *Optics Express*, **22**(20), pp. 24312–24321.
- LIU-Z., AND AYDIN-K. (2016). Localized surface plasmons in nanostructured monolayer black phosphorus, *Nano Letters*, **16**(6), pp. 3457–3462.

Bibliography

- LIU-Z., AND TAM-H.-Y. (2017). Fabrication and sensing applications of special microstructured optical fibers, *Selected Topics on Optical Fiber Technologies and Applications*, DOI: 10.5772/intechopen.70755.
- LIU-Z., WEI-Y., ZHANG-Y., ZHANG-Y., ZHAO-E., YANG-J., AND YUAN-L. (2015). Twin-core fiber SPR sensor, *Optics Letters*, **40**(12), pp. 2826–2829.
- LI-X., NGUYEN-L. V., ZHAO-Y., EBENDORFF-HEIDPRIEM-H., AND WARREN-SMITH-S. C. (2018b). High-sensitivity sagnac-interferometer biosensor based on exposed core microstructured optical fiber, *Sensors and Actuators B: Chemical*, **269**, pp. 103–109.
- LÖFFLER-T., BAUER-T., SIEBERT-K., ROSKOS-H. G., FITZGERALD-A., AND CZASCH-S. (2001). Terahertz dark-field imaging of biomedical tissue, *Optics Express*, **9**(12), pp. 616–621.
- LOPEZ-G. A., ESTEVEZ-M.-C., SOLER-M., AND LECHUGA-L. M. (2017). Recent advances in nanoplasmonic biosensors: applications and lab-on-a-chip integration, *Nanophotonics*, **6**(1), pp. 123–136.
- LUAN-N., WANG-R., LV-W., AND YAO-J. (2015). Surface plasmon resonance sensor based on D-shaped microstructured optical fiber with hollow core, *Optics Express*, **23**(7), pp. 8576–8582.
- LU-J., LI-Y., HAN-Y., LIU-Y., AND GAO-J. (2018). D-shaped photonic crystal fiber plasmonic refractive index sensor based on gold grating, *Applied Optics*, **57**(19), pp. 5268–5272.
- LU-J.-Y., YU-C.-P., CHANG-H.-C., CHEN-H.-W., LI-Y.-T., PAN-C.-L., AND SUN-C.-K. (2008). Terahertz air-core microstructure fiber, *Applied Physics Letters*, **92**(6), Art. No. 064105.
- LUO-J., TIAN-F., QU-H., LI-L., ZHANG-J., YANG-X., AND YUAN-L. (2017). Design and numerical analysis of a THz square porous-core photonic crystal fiber for low flattened dispersion, ultrahigh birefringence, *Applied Optics*, **56**(24), pp. 6993–7001.
- LUO-X., TSAI-D., GU-M., AND HONG-M. (2019). Extraordinary optical fields in nanostructures: from sub-diffraction-limited optics to sensing and energy conversion, *Chemical Society Reviews*, **48**(8), pp. 2458–2494.
- MAIER-S. A., KIK-P. G., ATWATER-H. A., MELTZER-S., HAREL-E., KOEL-B. E., AND REQUICHA-A. A. (2003). Local detection of electromagnetic energy transport below the diffraction limit in metal nanoparticle plasmon waveguides, *Nature Materials*, **2**(4), pp. 229–232.
- MA-J., SHRESTHA-R., ADELBERG-J., YEH-C.-Y., HOSSAIN-Z., KNIGHTLY-E., JORNET-J. M., AND MITTLEMAN-D. M. (2018a). Security and eavesdropping in terahertz wireless links, *Nature*, **563**(7729), pp. 89–93.
- MALITSON-I. H. (1965). Interspecimen comparison of the refractive index of fused silica, *JOSA*, **55**(10), pp. 1205–1209.
- MARKELZ-A. G., KNAB-J. R., CHEN-J. Y., AND HE-Y. (2007). Protein dynamical transition in terahertz dielectric response, *Chemical Physics Letters*, **442**(4), pp. 413–417.
- MARKELZ-A., ROITBERG-A., AND HEILWEIL-E. J. (2000). Pulsed terahertz spectroscopy of dna, bovine serum albumin and collagen between 0.1 and 2.0 THz, *Chemical Physics Letters*, **320**(2), pp. 42–48.

- MARKOV-A., AND SKOROBOGATIY-M. (2013). Two-wire terahertz fibers with porous dielectric support, *Optics Express*, **21**(10), pp. 12728–12743.
- MARKOV-A., GORGUTSA-S., QU-H., AND SKOROBOGATIY-M. (2012). Practical metal-wire THz waveguides, *arXiv preprint arXiv:1206.2984*.
- MARKOV-A., GUERBOUKHA-H., AND SKOROBOGATIY-M. (2014). Hybrid metal wire–dielectric terahertz waveguides: challenges and opportunities, *JOSA B*, **31**(11), pp. 2587–2600.
- MA-T., NALLAPAN-K., GUERBOUKHA-H., AND SKOROBOGATIY-M. (2017). Analog signal processing in the terahertz communication links using waveguide bragg gratings: example of dispersion compensation, *Optics Express*, **25**(10), pp. 11009–11026.
- MATSUURA-Y., AND TAKEDA-E. (2008). Hollow optical fibers loaded with an inner dielectric film for terahertz broadband spectroscopy, *JOSA B*, **25**(12), pp. 1949–1954.
- MAUREL-M., CHAFER-M., AMSANPALLY-A., ADNAN-M., AMRANI-F., DEBORD-B., VINCETTI-L., GÉRÔME-F., AND BENABID-F. (2018). Optimized inhibited-coupling kagome fibers at Yb-Nd: Yag (8.5 db/km) and Ti: Sa (30 db/km) ranges, *Optics Letters*, **43**(7), pp. 1598–1601.
- MA-Z., LI-Y., LI-Y., GONG-Y., MAIER-S. A., AND HONG-M. (2018b). All-dielectric planar chiral metasurface with gradient geometric phase, *Optics Express*, **26**(5), pp. 6067–6078.
- MBONYE-M., MENDIS-R., AND MITTLEMAN-D. M. (2009). A terahertz two-wire waveguide with low bending loss, *Applied Physics Letters*, **95**(23), Art. No. 233506.
- MCGOWAN-R., GALLOT-G., AND GRISCHKOWSKY-D. (1999). Propagation of ultrawideband short pulses of terahertz radiation through submillimeter-diameter circular waveguides, *Optics Letters*, **24**(20), pp. 1431–1433.
- MCLEOD-M., AND TABOR-C. (2020). Printable germanium inks for flexible optoelectronics, *Journal of Materials Chemistry C*, **8**(20), pp. 6771–6779.
- MEI-S., KONG-D., WANG-L., MA-T., ZHU-Y., ZHANG-X., HE-Z., HUANG-X., AND ZHANG-Y. (2019). Suspended graded-index porous core POF for ultra-flat near-zero dispersion terahertz transmission, *Optical Fiber Technology*, **52**, Art. No. 101946.
- MELINGER-J. S., YANG-Y., MANDEHGAR-M., AND GRISCHKOWSKY-D. (2012). THz detection of small molecule vapors in the atmospheric transmission windows, *Optics Express*, **20**(6), pp. 6788–6807.
- MENDIS-R., AND GRISCHKOWSKY-D. (2001). Undistorted guided-wave propagation of subpicosecond terahertz pulses, *Optics Letters*, **26**(11), pp. 846–848.
- MENG-F.-Y., WU-Q., ERNI-D., WU-K., AND LEE-J.-C. (2012). Polarization-independent metamaterial analog of electromagnetically induced transparency for a refractive-index-based sensor, *IEEE Transactions on Microwave Theory and Techniques*, **60**(10), pp. 3013–3022.
- MITTENDORFF-M., LI-S., AND MURPHY-T. E. (2017). Graphene-based waveguide-integrated terahertz modulator, *ACS Photonics*, **4**(2), pp. 316–321.
- MITTLEMAN-D., GUPTA-M., NEELAMANI-R., BARANIUK-R., RUDD-J., AND KOCH-M. (1999). Recent advances in terahertz imaging, *Applied Physics B*, **68**(6), pp. 1085–1094.

Bibliography

- MITTLEMAN-D. M. (2018). Twenty years of terahertz imaging, *Optics Express*, **26**(8), pp. 9417–9431.
- MITTLEMAN-D. M., HUNSCHE-S., BOIVIN-L., AND NUSS-M. C. (1997). T-ray tomography, *Optics Letters*, **22**(12), pp. 904–906.
- MITTLEMAN-D. M., JACOBSEN-R. H., NEELAMANI-R., BARANIUK-R. G., AND NUSS-M. C. (1998). Gas sensing using terahertz time-domain spectroscopy, *Applied Physics B*, **67**(3), pp. 379–390.
- MOHR-P. J., TAYLOR-B. N., AND NEWELL-D. B. (2008). CODATA recommended values of the fundamental physical constants: 2006, *Journal of Physical and Chemical Reference Data*, **80**(3), pp. 633–1284.
- MOLLAH-M. A., AND ISLAM-M. S. (2020). Novel single hole exposed-suspended core localized surface plasmon resonance sensor, *IEEE Sensors Journal*, **21**(3), pp. 2813–2820.
- MONRO-T. M., BELARDI-W., FURUSAWA-K., BAGGETT-J. C., BRODERICK-N., AND RICHARDSON-D. (2001). Sensing with microstructured optical fibres, *Measurement Science and Technology*, **12**(7), Art. No. 854.
- MONTICONE-F., ESTAKHRI-N. M., AND ALU-A. (2013). Full control of nanoscale optical transmission with a composite metascreen, *Physical Review Letters*, **110**(20), Art. No. 203903.
- MUHAMMAD-N., OUYANG-Z., LIU-Q., TANG-X., DENG-Z.-L., AND KHAN-A. D. (2019). Sensitive label-free sensor with high figure of merit based on plasmonic metasurface with unit cell of double two-split nanorings, *Journal of Materials Science*, **54**(8), pp. 6301–6309.
- NAFTALY-M., AND MILES-R. E. (2007). Terahertz time-domain spectroscopy for material characterization, *Proceedings of the IEEE*, **95**(8), pp. 1658–1665.
- NAGEL-M., HARING BOLIVAR-P., BRUCHERSEIFER-M., KURZ-H., BOSSERHOFF-A., AND BÜTTNER-R. (2002). Integrated THz technology for label-free genetic diagnostics, *Applied Physics Letters*, **80**(1), pp. 154–156.
- NAGEL-M., MARCHEWKA-A., AND KURZ-H. (2006). Low-index discontinuity terahertz waveguides, *Optics Express*, **14**(21), pp. 9944–9954.
- NAZAROV-M. M., SHILOV-A. V., BZHEUMIKHOV-K. A., MARGUSHEV-Z. C., SOKOLOV-V. I., SOTSKY-A. B., AND SHKURINOV-A. P. (2018). Eight-capillary cladding THz waveguide with low propagation losses and dispersion, *IEEE Transactions on Terahertz Science and Technology*, **8**(2), pp. 183–191.
- NELLEN-S., GLOBISCH-B., KOHLHAAS-R., STANZE-D., GÖBEL-T., BARRY-L., AND SCHELL-M. (2017). Fiber-coupled, photoconductive heterodyne receiver operating at frequencies up to 1 THz, *CLEO: Science and Innovations*, Optical Society of America, pp. SM3J–7.
- NGUYEN-T. T., AND LIM-S. (2017). Bandwidth-enhanced and wide-angle-of-incidence metamaterial absorber using a hybrid unit cell, *Scientific Reports*, **7**, Art. No. 14814.
- NIELSEN-K., RASMUSSEN-H. K., ADAM-A. J., PLANKEN-P. C., BANG-O., AND JEPSEN-P. U. (2009). Bendable, low-loss Topas fibers for the terahertz frequency range, *Optics Express*, **17**(10), pp. 8592–8601.

-
- NOVOSELOV-K. S., GEIM-A. K., MOROZOV-S. V., JIANG-D., ZHANG-Y., DUBONOS-S. V., GRIGORIEVA-I. V., AND FIRSOV-A. A. (2004). Electric field effect in atomically thin carbon films, *Science*, **306**(5696), pp. 666–669.
- OFFERMANS-P., SCHAAFSMA-M. C., RODRIGUEZ-S. R., ZHANG-Y., CREGO-CALAMA-M., BRONGERSMA-S. H., AND GOÉMEZ RIVAS-J. (2011). Universal scaling of the figure of merit of plasmonic sensors, *ACS Nano*, **5**(6), pp. 5151–5157.
- O'HARA-J. F., EKIN-S., CHOI-W., AND SONG-I. (2019). A perspective on terahertz next-generation wireless communications, *Technologies*, **7**(2), Art. No. 43.
- OSÓRIO-J. H., OLIVEIRA-R., ARISTILDE-S., CHESINI-G., FRANCO-M. A., NOGUEIRA-R. N., AND CORDEIRO-C. M. (2017). Bragg gratings in surface-core fibers: Refractive index and directional curvature sensing, *Optical Fiber Technology*, **34**, pp. 86–90.
- OTUPIRI-R., AKOWUAH-E. K., AND HAXHA-S. (2015). Multi-channel SPR biosensor based on PCF for multi-analyte sensing applications, *Optics Express*, **23**(12), pp. 15716–15727.
- PATRICK-H. J., KERSEY-A. D., AND BUCHOLTZ-F. (1998). Analysis of the response of long period fiber gratings to external index of refraction, *Journal of Lightwave Technology*, **16**(9), Art. No. 1606.
- PAUL-B. K., AHMED-K., ASADUZZAMAN-S., AND ISLAM-M. S. (2017a). Folded cladding porous shaped photonic crystal fiber with high sensitivity in optical sensing applications: design and analysis, *Sensing and Biosensing Research*, **12**, pp. 36–42.
- PAUL-B. K., ISLAM-M. S., AHMED-K., AND ASADUZZAMAN-S. (2017b). Alcohol sensing over O+ E+ S+ C+ L+ U transmission band based on porous cored octagonal photonic crystal fiber, *Photonic Sensors*, **7**(2), pp. 123–130.
- PAUL-B. K., ISLAM-M. S., SEN-S., AHMED-K., AND UDDIN-M. S. (2018). Low material loss and dispersion flattened fiber for single mode THz-wave transmission applications, *Results in Physics*, **11**, pp. 638–642.
- PAUL-D., AND BISWAS-R. (2018). Highly sensitive LSPR based photonic crystal fiber sensor with embodiment of nanospheres in different material domain, *Optics & Laser Technology*, **101**, pp. 379–387.
- PAVANELLO-F., GARET-F., KUPPAM-M.-B., PEYTAVIT-E., VANWOLLEGHEM-M., VAURETTE-F., COUTAZ-J.-L., AND LAMPIN-J.-F. (2013). Broadband ultra-low-loss mesh filters on flexible cyclic olefin copolymer films for terahertz applications, *Applied Physics Letters*, **102**(11), Art. No. 111114.
- PÉGARD-N. C., AND FLEISCHER-J. W. (2011). Optimizing holographic data storage using a fractional fourier transform, *Optics Letters*, **36**(13), pp. 2551–2553.
- PERETTI-R., BRAUD-F., PEYTAVIT-E., DUBOIS-E., AND LAMPIN-J.-F. (2018). Broadband terahertz light-matter interaction enhancement for precise spectroscopy of thin films and micro-samples, *Photonics*, **5**(2), Art. No. 11.
- PICKWELL-E., AND WALLACE-V. (2006). Biomedical applications of terahertz technology, *Journal of Physics D: Applied Physics*, **39**(17), Art. No. R301.
-

Bibliography

- PICKWELL-E., COLE-B. E., FITZGERALD-A. J., PEPPER-M., AND WALLACE-V. P. (2004). In vivo study of human skin using pulsed terahertz radiation, *Physics in Medicine & Biology*, **49**(9), Art. No. 1595.
- PINTO-A. M., AND LOPEZ-AMO-M. (2012). Photonic crystal fibers for sensing applications, *Journal of Sensors*, **2012**, Art. No. 598178.
- PODOBEDOV-V., PLUSQUELLIC-D., SIEGRIST-K., FRASER-G., MA-Q., AND TIPPING-R. (2008). New measurements of the water vapor continuum in the region from 0.3 to 2.7 THz, *Journal of Quantitative Spectroscopy and Radiative Transfer*, **109**(3), pp. 458–467.
- PODZOROV-A., AND GALLOT-G. (2008). Low-loss polymers for terahertz applications, *Applied Optics*, **47**(18), pp. 3254–3257.
- POLI-F., CUCINOTTA-A., AND SELLERI-S. (2007). *Photonic crystal fibers: properties and applications*, Vol. 102, Springer Science & Business Media.
- PONSECA JR-C. S., POBRE-R., ESTACIO-E., SARUKURA-N., ARGYROS-A., LARGE-M. C., AND VAN EIJKELENBORG-M. A. (2008). Transmission of terahertz radiation using a microstructured polymer optical fiber, *Optics Letters*, **33**(9), pp. 902–904.
- Product Data Sheet* (2015). *Zeonex 480R*, p. 2100.
- PU-M., FENG-Q., WANG-M., HU-C., HUANG-C., MA-X., ZHAO-Z., WANG-C., AND LUO-X. (2012). Ultrathin broadband nearly perfect absorber with symmetrical coherent illumination, *Optics Express*, **20**(3), pp. 2246–2254.
- QIN-F., DING-L., ZHANG-L., MONTICONE-F., CHUM-C. C., DENG-J., MEI-S., LI-Y., TENG-J., AND HONG-M. (2016). Hybrid bilayer plasmonic metasurface efficiently manipulates visible light, *Science Advances*, **2**(1), Art. No. e1501168.
- RAHMAN-A., RAHMAN-A. K., AND RAO-B. (2016). Early detection of skin cancer via terahertz spectral profiling and 3D imaging, *Biosensors and Bioelectronics*, **82**, pp. 64–70.
- RANA-S., ISLAM-M. S., FAISAL-M., ROY-K. C., ISLAM-R., AND KAIJAGE-S. F. (2016). Single-mode porous fiber for low-loss polarization maintaining terahertz transmission, *Optical Engineering*, **55**(7), Art. No. 076114.
- RANA-S., RAKIN-A. S., HASAN-M. R., REZA-M. S., LEONHARDT-R., ABBOTT-D., AND SUBBARAMAN-H. (2018). Low loss and flat dispersion kagome photonic crystal fiber in the terahertz regime, *Optics Communications*, **410**, pp. 452–456.
- RANA-S., RAKIN-A. S., SUBBARAMAN-H., LEONHARDT-R., AND ABBOTT-D. (2017). Low loss and low dispersion fiber for transmission applications in the terahertz regime, *IEEE Photonics Technology Letters*, **29**(10), pp. 830–833.
- RANDALL-C., AND RAWCLIFFE-R. (1967). Refractive indices of germanium, silicon, and fused quartz in the far infrared, *Applied Optics*, **6**(11), pp. 1889–1895.
- REYES-VERA-E., USUGA-RESTREPO-J., JIMENEZ-DURANGO-C., MONTOYA-CARDONA-J., AND GOMEZ-CARDONA-N. (2018). Design of low-loss and highly birefringent porous-core photonic crystal fiber and its application to terahertz polarization beam splitter, *IEEE Photonics Journal*, **10**(4), Art. No. 5900413.

- RIFAT-A. A., AHMED-R., MAHDIRAJI-G. A., AND ADIKAN-F. M. (2017). Highly sensitive D-shaped photonic crystal fiber-based plasmonic biosensor in visible to near-IR, *IEEE Sensors Journal*, **17**(9), pp. 2776–2783.
- RIFAT-A. A., HAIDER-F., AHMED-R., MAHDIRAJI-G. A., ADIKAN-F. M., AND MIROSHNICHENKO-A. E. (2018). Highly sensitive selectively coated photonic crystal fiber-based plasmonic sensor, *Optics Letters*, **43**(4), pp. 891–894.
- RIFAT-A. A., MAHDIRAJI-G. A., CHOW-D. M., SHEE-Y. G., AHMED-R., AND ADIKAN-F. R. M. (2015). Photonic crystal fiber-based surface plasmon resonance sensor with selective analyte channels and graphene-silver deposited core, *Sensors*, **15**(5), pp. 11499–11510.
- RIFAT-A. A., MAHDIRAJI-G. A., SUA-Y. M., AHMED-R., SHEE-Y., AND ADIKAN-F. M. (2016). Highly sensitive multi-core flat fiber surface plasmon resonance refractive index sensor, *Optics Express*, **24**(3), pp. 2485–2495.
- ROBERTS-P., COUNY-F., SABERT-H., MANGAN-B., WILLIAMS-D., FARR-L., MASON-M., TOMLINSON-A., BIRKS-T., AND KNIGHT-J. (2005). Ultimate low loss of hollow-core photonic crystal fibres, *Optics Express*, **13**(1), pp. 236–244.
- ROGALIN-V., KAPLUNOV-I., AND KROPOTOV-G. (2018). Optical materials for the THz range, *Optics and Spectroscopy*, **125**(6), pp. 1053–1064.
- RONNE-C., THRANE-L., ÅSTRAND-P.-O., WALLQVIST-A., MIKKELSEN-K. V., AND KEIDING-S. R. (1997). Investigation of the temperature dependence of dielectric relaxation in liquid water by THz reflection spectroscopy and molecular dynamics simulation, *The Journal of chemical physics*, **107**(14), pp. 5319–5331.
- RUSSELL-P. (2003). Photonic crystal fibers, *Science*, **299**(5605), pp. 358–362.
- RUSSELL-P. S. J., BERAVAT-R., AND WONG-G. (2017). Helically twisted photonic crystal fibres, *Philo. Trans. of the Royal Soc. A: Mathe. Phys. and Eng. Sciences*, **375**(2087), Art. No. 20150440.
- RYBIN-M., AND KIVSHAR-Y. (2017). Supercavity lasing, *Nature*, **541**(7636), pp. 164–165.
- SAKAI-K. (2005). *Terahertz Optoelectronics*, Vol. 6, Springer.
- SANJUAN-F., AND TOCHO-J. O. (2012). Optical properties of silicon, sapphire, silica and glass in the terahertz range, *Latin America Optics and Photonics Conference*, Optical Society of America, OSA., pp. LT4C–1. DOI: <https://doi.org/10.1364/LAOP.2012.LT4C.1>.
- SCHALL-M., WALTHER-M., AND JEPSEN-P. U. (2001). Fundamental and second-order phonon processes in CdTe and ZnTe, *Physical Review B*, **64**(9), Art. No. 094301.
- SCHARTNER-E. P., DOWLER-A., AND EBENDORFF-HEIDPRIEM-H. (2017). Fabrication of low-loss, small-core exposed core microstructured optical fibers, *Optical Materials Express*, **7**(5), pp. 1496–1502.
- SETTI-V., VINCETTI-L., AND ARGYROS-A. (2013). Flexible tube lattice fibers for terahertz applications, *Optics Express*, **21**(3), pp. 3388–3399.

Bibliography

- SHAFIEE-H., LIDSTONE-E. A., JAHANGIR-M., INCI-F., HANHAUSER-E., HENRICH-T. J., KURITZKES-D. R., CUNNINGHAM-B. T., AND DEMIRCI-U. (2014). Nanostructured optical photonic crystal biosensor for hiv viral load measurement, *Scientific Reports*, **4**, Art. No. 4116.
- SHARMA-M., BOROGOHAİN-N., AND KONAR-S. (2013). Index guiding photonic crystal fibers with large birefringence and walk-off, *Journal of Lightwave Technology*, **31**(21), pp. 3339–3344.
- SHEN-Y., LO-A. T., TADAY-P., COLE-B., TRIBE-W., AND KEMP-M. (2005). Detection and identification of explosives using terahertz pulsed spectroscopic imaging, *Applied Physics Letters*, **86**(24), Art. No. 241116.
- SHEPHARD-J., MACPHERSON-W., MAIER-R., JONES-J., HAND-D., MOHEBBI-M., GEORGE-A., ROBERTS-P., AND KNIGHT-J. (2005). Single-mode mid-ir guidance in a hollow-core photonic crystal fiber, *Optics Express*, **13**(18), pp. 7139–7144.
- SHIM-S., PARK-H.-Y., CHOI-G. J., SHIN-H.-C., AND KIM-S. J. (2019). A simply fabricated neural probe by laser machining of a thermally laminated gold thin film on transparent cyclic olefin polymer, *ACS Omega*, **4**(2), pp. 2590–2595.
- SHIN-W., AND FAN-S. (2012). Choice of the perfectly matched layer boundary condition for frequency-domain maxwell's equations solvers, *Journal of Computational Physics*, **231**(8), pp. 3406–3431.
- SHI-Z., SONG-L., AND ZHANG-T. (2019). Optical and electrical characterization of pure pmma for terahertz wide-band metamaterial absorbers, *Journal of Infrared, Millimeter, and Terahertz Waves*, **40**(1), pp. 80–91.
- SHUAI-B., XIA-L., AND LIU-D. (2012). Coexistence of positive and negative refractive index sensitivity in the liquid-core photonic crystal fiber based plasmonic sensor, *Optics Express*, **20**(23), pp. 25858–25866.
- SIEGEL-P. H. (2002). Terahertz technology, *IEEE Transactions on Microwave Theory and Techniques*, **50**(3), pp. 910–928.
- SIEGEL-P. H. (2004). Terahertz technology in biology and medicine, *IEEE Transactions on Microwave Theory and Techniques*, **52**(10), pp. 2438–2447.
- SIMA-B., MOMENI HASAN ABADI-S. M. A., AND BEHDAD-N. (2017). A reflective-type, quasi-optical metasurface filter, *Journal of Applied Physics*, **122**(6), Art. No. 064901.
- SINGH-R., CAO-W., AL-NAIB-I., CONG-L., WITHAYACHUMNANKUL-W., AND ZHANG-W. (2014). Ultrasensitive terahertz sensing with high-Q fano resonances in metasurfaces, *Applied Physics Letters*, **105**(17), Art. No. 171101.
- SMITH-D., VIER-D., KOSCHNY-T., AND SOUKOULIS-C. (2005). Electromagnetic parameter retrieval from inhomogeneous metamaterials, *Physical Review E*, **71**(3), Art. No. 036617.
- SMYE-S., CHAMBERLAIN-J., FITZGERALD-A., AND BERRY-E. (2001). The interaction between terahertz radiation and biological tissue, *Physics in Medicine & Biology*, **46**(9), Art. No. R101.
- ŠPAČKOVÁ-B., WROBEL-P., BOCKOVÁ-M., AND HOMOLA-J. (2016). Optical biosensors based on plasmonic nanostructures: a review, *Proceedings of the IEEE*, **104**(12), pp. 2380–2408.

- SRIVASTAVA-T., DAS-R., AND JHA-R. (2013). Highly sensitive plasmonic temperature sensor based on photonic crystal surface plasmon waveguide, *Plasmonics*, **8**(2), pp. 515–521.
- SRIVASTAVA-Y. K., MANJAPPA-M., CONG-L., CAO-W., AL-NAIB-I., ZHANG-W., AND SINGH-R. (2016). Ultrahigh-Q fano resonances in terahertz metasurfaces: Strong influence of metallic conductivity at extremely low asymmetry, *Advanced Optical Materials*, **4**(3), pp. 457–463.
- STEFANI-A., FLEMING-S. C., AND KUHLMEY-B. T. (2018). Terahertz orbital angular momentum modes with flexible twisted hollow core antiresonant fiber, *APL Photonics*, **3**(5), Art. No. 051708.
- SUI-C., LI-X., LANG-T., JING-X., LIU-J., AND HONG-Z. (2018). High Q-factor resonance in a symmetric array of all-dielectric bars, *Applied Sciences*, **8**(2), Art. No. 161.
- SULTANA-J., ISLAM-M., CORDEIRO-C., DINOVISER-A., KAUSHIK-M., NG-B. W.-H., AND ABBOTT-D. (2020). Terahertz hollow core antiresonant fiber with metamaterial cladding, *Fibers*, **8**(2), Art. No. 14.
- SULTANA-J., ISLAM-M., HABIB-M., CORDEIRO-C. M., CORDEIRO-M., DINOVISER-A., NG-B.-H., KOWSHIK-M., EBENDORFF-HEIDPRIEM-H., AND ABBOTT-D. (2019a). Novel hollow core antiresonant terahertz fiber with metamaterial cladding, *44th Int. Conf. on Infra., Milli.,and Tera. Waves (IRMMW-THz)*, IEEE. DOI: 10.1109/IRMMW-THz.2019.8873836.
- SULTANA-J., ISLAM-M. R., FAISAL-M., TALHA-K. M. A., AND ISLAM-M. S. (2019b). Design and analysis of a Zeonex based diamond-shaped core kagome lattice photonic crystal fiber for T-ray wave transmission, *Optical Fiber Technology*, **47**, pp. 55–60.
- SULTANA-J., ISLAM-M. S., AHMED-K., DINOVISER-A., NG-B. W.-H., AND ABBOTT-D. (2018a). Terahertz detection of alcohol using a photonic crystal fiber sensor, *Applied Optics*, **57**(10), pp. 2426–2433.
- SULTANA-J., ISLAM-M. S., ATAI-J., ISLAM-M. R., AND ABBOTT-D. (2017a). Near-zero dispersion flattened, low-loss porous-core waveguide design for terahertz signal transmission, *Optical Engineering*, **56**(7), Art. No. 076114.
- SULTANA-J., ISLAM-M. S., FAISAL-M., ISLAM-M. R., NG-B. W.-H., EBENDORFF-HEIDPRIEM-H., AND ABBOTT-D. (2018b). Highly birefringent elliptical core photonic crystal fiber for terahertz application, *Optics Communications*, **407**, pp. 92–96.
- SULTANA-J., ISLAM-M. S., ISLAM-M., AND ABBOTT-D. (2017b). High numerical aperture, highly birefringent novel photonic crystal fibre for medical imaging applications, *Electronics Letters*, **54**(2), pp. 61–62.
- SULTANA-J., SAIFUL-M., HABIB-M., CORDEIRO-C. M., DINOVISER-A., NG-B.-H., KAUSHIK-M., EBENDORFF-HEIDPRIEM-H., AND ABBOTT-D. (2019c). Five-capillary cladding terahertz fiber with low loss and single mode, *44th Int. Conf. on Infra. Milli. and Tera. Waves (IRMMW-THz)*, IEEE. DOI: 10.1109/IRMMW-THz.2019.8874476.
- TALATAISONG-W., ISMAEEL-R., BERESNA-M., AND BRAMBILLA-G. (2019). Suspended-core microstructured polymer optical fibers and potential applications in sensing, *Sensors*, **19**(16), Art. No. 3449.

Bibliography

- TALATAISONG-W., ISMAEEL-R., MARQUES-T. H., MOUSAVI-S. A., BERESNA-M., GOUVEIA-M., SANDOGHCHI-S. R., LEE-T., CORDEIRO-C. M., AND BRAMBILLA-G. (2018). Mid-IR hollow-core microstructured fiber drawn from a 3D printed PETG preform, *Scientific Reports*, **8**, Art. No. 8113.
- TANG-X.-L., SHI-Y.-W., MATSUURA-Y., IWAI-K., AND MIYAGI-M. (2009). Transmission characteristics of terahertz hollow fiber with an absorptive dielectric inner-coating film, *Optics Letters*, **34**(14), pp. 2231–2233.
- TATIAN-B. (1984). Fitting refractive-index data with the Sellmeier dispersion formula, *Applied Optics*, **23**(24), pp. 4477–4485.
- TIAN-J., LI-Q., BELOV-P. A., SINHA-R. K., QIAN-W., AND QIU-M. (2020). High-Q all-dielectric meta-surface: super and suppressed optical absorption, *ACS Photonics*, **7**(6), pp. 1436–1443.
- TIEN-C.-L., LIN-H.-Y., AND SU-S.-H. (2018). High sensitivity refractive index sensor by D-shaped fibers and titanium dioxide nanofilm, *Soft Matter Photonics*, **2018**, Art. No. 2303740.
- TONOUCHI-M. (2007). Cutting-edge terahertz technology, *Nature Photonics*, **1**(2), pp. 97–105.
- TSIMINIS-G., ROWLAND-K., SCHATNER-E., SPOONER-N., MONRO-T., AND EBENDORFF-HEIDPRIEM-H. (2016). Single-ring hollow core optical fibers made by glass billet extrusion for raman sensing, *Optics Express*, **24**(6), pp. 5911–5917.
- TSYDYNZHAPOV-G. E., GUSIKHIN-P. A., MURAVEV-V. M., ANDREEV-I. V., AND KUKUSHKIN-I. V. (2018). New terahertz security body scanner, *43rd Int. Conf. on In-fra. Milli. and Tera. Waves (IRMMW-THz)*, IEEE. 10.1109/IRMMW-THz.2018.8510513.
- TUNIZ-A., AND KUHLMEY-B. T. (2015). Two-dimensional imaging in hyperbolic media—the role of field components and ordinary waves, *Scientific Reports*, **5**, Art. No. 17690.
- TUNIZ-A., KALTENECKER-K. J., FISCHER-B. M., WALTHER-M., FLEMING-S. C., ARGYROS-A., AND KUHLMEY-B. T. (2013). Metamaterial fibres for subdiffraction imaging and focusing at terahertz frequencies over optically long distances, *Nature Communications*, **4**, Art. No. 2706.
- TUNIZ-A., LWIN-R., ARGYROS-A., FLEMING-S. C., AND KUHLMEY-B. T. (2012). Fabricating metamaterials using the fiber drawing method, *Journal of Visualized Experiments: JoVE*, (68), Art. No. 4299.
- VAN EXTER-M., FATTINGER-C., AND GRISCHKOWSKY-D. (1989). Terahertz time-domain spectroscopy of water vapor, *Optics Letters*, **14**(20), pp. 1128–1130.
- VAN PUTTEN-L., GORECKI-J., FOKOUA-E. N., APOSTOLOPOULOS-V., AND POLETTI-F. (2018). 3D-printed polymer antiresonant waveguides for short-reach terahertz applications, *Applied Optics*, **57**(14), pp. 3953–3958.
- VIAL-A., GRIMAULT-A.-S., MACÍAS-D., BARCHIESI-D., AND DE LA CHAPELLE-M. L. (2005). Improved analytical fit of gold dispersion: Application to the modeling of extinction spectra with a finite-difference time-domain method, *Physical Review B*, **71**(8), Art. No. 085416.
- VINCETTI-L. (2009a). Hollow core photonic band gap fiber for THz applications, *Microwave and Optical Technology Letters*, **51**(7), pp. 1711–1714.

- VINCETTI-L. (2009b). Numerical analysis of plastic hollow core microstructured fiber for terahertz applications, *Optical Fiber Technology*, **15**(4), pp. 398–401.
- VINCETTI-L., AND SETTI-V. (2010). Waveguiding mechanism in tube lattice fibers, *Optics Express*, **18**(22), pp. 23133–23146.
- VINCETTI-L., AND SETTI-V. (2013). Elliptical hollow core tube lattice fibers for terahertz applications, *Optical Fiber Technology*, **19**(1), pp. 31–34.
- WÄCHTER-M., NAGEL-M., AND KURZ-H. (2007). Metallic slit waveguide for dispersion-free low-loss terahertz signal transmission, *Applied Physics Letters*, **90**(6), Art. No. 061111.
- WALTHER-M., FISCHER-B. M., AND JEPSEN-P. U. (2003). Noncovalent intermolecular forces in polycrystalline and amorphous saccharides in the far infrared, *Chemical Physics*, **288**(3), pp. 261–268.
- WALTHER-M., FISCHER-B. M., ORTNER-A., BITZER-A., THOMAN-A., AND HELM-H. (2010). Chemical sensing and imaging with pulsed terahertz radiation, *Analytical and Bioanalytical Chemistry*, **397**(3), pp. 1009–1017.
- WANG-B.-X., WANG-G.-Z., SANG-T., AND WANG-L.-L. (2017a). Six-band terahertz metamaterial absorber based on the combination of multiple-order responses of metallic patches in a dual-layer stacked resonance structure, *Scientific Reports*, **7**, Art. No. 41373.
- WANG-D.-D., MU-C.-L., KONG-D.-P., AND GUO-C.-Y. (2019). High birefringence, low loss, and flattened dispersion photonic crystal fiber for terahertz application, *Chinese Physics B*, **28**(11), Art. No. 118701.
- WANG-H., ZHANG-H., DONG-J., HU-S., ZHU-W., QIU-W., LU-H., YU-J., GUAN-H., AND GAO-S. (2018). Sensitivity-enhanced surface plasmon resonance sensor utilizing a tungsten disulfide WS₂ nanosheets overlayer, *Photonics Research*, **6**(6), pp. 485–491.
- WANG-K., AND MITTLEMAN-D. M. (2004). Metal wires for terahertz wave guiding, *Nature*, **432**(7015), pp. 376–379.
- WANG-L., CHEN-Q.-D., CAO-X.-W., BUIVIDAS-R., WANG-X., JUODKAZIS-S., AND SUN-H.-B. (2017b). Plasmonic nano-printing: large-area nanoscale energy deposition for efficient surface texturing, *Light: Science and Applications*, **6**(12), Art. No. e17112.
- WANG-Y., WHEELER-N. V., COUNY-F., ROBERTS-P., AND BENABID-F. (2011). Low loss broadband transmission in hypocycloid-core kagome hollow-core photonic crystal fiber, *Optics Letters*, **36**(5), pp. 669–671.
- WAN-W., GAO-J., AND YANG-X. (2017). Metasurface holograms for holographic imaging, *Advanced Optical Materials*, **5**(21), Art. No. 1700541.
- WARREN-SMITH-S. C., EBENDORFF-HEIDPRIEM-H., FOO-T. C., MOORE-R., DAVIS-C., AND MONRO-T. M. (2009). Exposed-core microstructured optical fibers for real-time fluorescence sensing, *Optics Express*, **17**(21), pp. 18533–18542.

Bibliography

- WARREN-SMITH-S. C., SCHAARSCHMIDT-K., CHEMNITZ-M., SCHATNER-E. P., SCHNEIDEWIND-H., EBENDORFF-HEIDPRIEM-H., AND SCHMIDT-M. A. (2019). Tunable multi-wavelength third-harmonic generation using exposed-core microstructured optical fiber, *Optics Letters*, **44**(3), pp. 626–629.
- WEI-C., WEIBLEN-R. J., MENYUK-C. R., AND HU-J. (2017). Negative curvature fibers, *Advances in Optics and Photonics*, **9**(3), pp. 504–561.
- WEI-Q., HUANG-L., ZENTGRAF-T., AND WANG-Y. (2020). Optical wavefront shaping based on functional metasurfaces, *Nanophotonics*, **9**(5), pp. 987–1002.
- WEST-P. R., ISHII-S., NAIK-G. V., EMANI-N. K., SHALAEV-V. M., AND BOLTASSEVA-A. (2010). Searching for better plasmonic materials, *Laser & Photonics Reviews*, **4**(6), pp. 795–808.
- WHITE-I. M., AND FAN-X. (2008). On the performance quantification of resonant refractive index sensors, *Optics Express*, **16**(2), pp. 1020–1028.
- WHITMIRE-S., WOLPERT-D., MARKELZ-A., HILLEBRECHT-J., GALAN-J., AND BIRGE-R. (2003). Protein flexibility and conformational state: A comparison of collective vibrational modes of wild-type and D96N bacteriorhodopsin, *Biophysical Journal*, **85**(2), pp. 1269–1277.
- WILLIAMS-B. S. (2007). Terahertz quantum-cascade lasers, *Nature Photonics*, **1**(9), pp. 517–525.
- WITHAYACHUMNANKUL-W. (2009). Engineering aspects of terahertz time domain spectroscopy, *PhD Thesis*.
- WITHAYACHUMNANKUL-W., AND NAFTALY-M. (2014). Fundamentals of measurement in terahertz time-domain spectroscopy, *Journal of Infrared, Millimeter, and Terahertz Waves*, **35**(8), pp. 610–637.
- WITHAYACHUMNANKUL-W., FISCHER-B. M., AND ABBOTT-D. (2008). Material thickness optimization for transmission-mode terahertz time-domain spectroscopy, *Optics Express*, **16**(10), pp. 7382–7396.
- WITHAYACHUMNANKUL-W., FUJITA-M., AND NAGATSUMA-T. (2018). Integrated silicon photonic crystals toward terahertz communications, *Advanced Optical Materials*, **6**(16), Art. No. 1800401.
- WOLFBEIS-O. S., AND WEIDGANS-B. M. (2006). Fiber optic chemical sensors and biosensors: A view back, *Optical Chemical Sensors*, Springer, pp. 17–44.
- WOODWARD-R. M., WALLACE-V. P., COLE-B. E., PYE-R. J., ARNONE-D. D., LINFIELD-E. H., AND PEPPER-M. (2002). Terahertz pulse imaging in reflection geometry of skin tissue using time-domain analysis techniques, *Clinical Diagnostic Systems: Technologies and Instrumentation*, Vol. 4625, pp. 160–169.
- WOOLARD-D. L., BROWN-R., PEPPER-M., AND KEMP-M. (2005). Terahertz frequency sensing and imaging: A time of reckoning future applications?, *Proceedings of the IEEE*, **93**(10), pp. 1722–1743.
- WOYESSA-G., FASANO-A., MARKOS-C., STEFANI-A., RASMUSSEN-H. K., AND BANG-O. (2017). Zeonex microstructured polymer optical fiber: fabrication friendly fibers for high temperature and humidity insensitive bragg grating sensing, *Optical Materials Express*, **7**(1), pp. 286–295.

- WU-B., HU-Y., ZHAO-Y. T., LU-W. B., AND ZHANG-W. (2018). Large angle beam steering THz antenna using active frequency selective surface based on hybrid graphene-gold structure, *Optics Express*, **26**(12), pp. 15353–15361.
- WU-T., SHAO-Y., WANG-Y., CAO-S., CAO-W., ZHANG-F., LIAO-C., HE-J., HUANG-Y., AND HOU-M. (2017). Surface plasmon resonance biosensor based on gold-coated side-polished hexagonal structure photonic crystal fiber, *Optics Express*, **25**(17), pp. 20313–20322.
- WU-Z., KINAST-J., GEHM-M., AND XIN-H. (2008). Rapid and inexpensive fabrication of terahertz electromagnetic bandgap structures, *Optics Express*, **16**(21), pp. 16442–16451.
- WU-Z., NG-W.-R., GEHM-M. E., AND XIN-H. (2011). Terahertz electromagnetic crystal waveguide fabricated by polymer jetting rapid prototyping, *Optics Express*, **19**(5), pp. 3962–3972.
- WU-Z., SHI-Z., XIA-H., ZHOU-X., DENG-Q., HUANG-J., JIANG-X., AND WU-W. (2016). Design of highly birefringent and low-loss oligoporous-core THz photonic crystal fiber with single circular air-hole unit, *IEEE Photonics Journal*, **8**(6), Art. No. 4502711.
- XIAO-H., LI-H., WU-B., AND JIAN-S. (2018a). Polarization-maintaining terahertz bandgap fiber with a quasi-elliptical hollow-core, *Optics & Laser Technology*, **105**, pp. 276–280.
- XIAO-Y., QIAN-H., AND LIU-Z. (2018b). Nonlinear metasurface based on giant optical kerr response of gold quantum wells, *ACS Photonics*, **5**(5), pp. 1654–1659.
- XIE-Q., DONG-G.-X., WANG-B.-X., AND HUANG-W.-Q. (2018). High-Q fano resonance in terahertz frequency based on an asymmetric metamaterial resonator, *Nanoscale Research Letters*, **13**, Art. No. 294.
- XIN-X., ALTAN-H., SAINT-A., MATTEN-D., AND ALFANO-R. (2006). Terahertz absorption spectrum of para and ortho water vapors at different humidities at room temperature, *Journal of Applied Physics*, **100**(9), Art. No. 094905.
- XUE-J., LI-S., XIAO-Y., QIN-W., XIN-X., AND ZHU-X. (2013). Polarization filter characters of the gold-coated and the liquid filled photonic crystal fiber based on surface plasmon resonance, *Optics Express*, **21**(11), pp. 13733–13740.
- XU-Z., AND LAM-E. Y. (2010). Hyperspectral reconstruction in biomedical imaging using terahertz systems, *Proceedings of 2010 IEEE International Symposium on Circuits and Systems*, IEEE, pp. 2079–2082.
- YAHIAOUI-R., TAN-S., CONG-L., SINGH-R., YAN-F., AND ZHANG-W. (2015). Multispectral terahertz sensing with highly flexible ultrathin metamaterial absorber, *Journal of Applied Physics*, **118**(8), Art. No. 083103.
- YANG-J., ZHAO-J., GONG-C., TIAN-H., SUN-L., CHEN-P., LIN-L., AND LIU-W. (2016). 3D printed low-loss THz waveguide based on kagome photonic crystal structure, *Optics Express*, **24**(20), pp. 22454–22460.
- YANG-J., ZHU-Z., ZHANG-J., GUO-C., XU-W., LIU-K., YUAN-X., AND QIN-S. (2018a). Broadband terahertz absorber based on multi-band continuous plasmon resonances in geometrically gradient dielectric-loaded graphene plasmon structure, *Scientific Reports*, **8**, Art. No. 3239.

Bibliography

- YANG-L., HU-T., SHEN-A., PEI-C., YANG-B., DAI-T., YU-H., LI-Y., JIANG-X., AND YANG-J. (2014a). Ultracompact optical modulator based on graphene-silica metamaterial, *Optics Letters*, **39**(7), pp. 1909–1912.
- YANG-L., WU-D., LIU-Y., LIU-C., XU-Z., LI-H., YU-Z., YU-L., AND YE-H. (2018b). High-efficiency all-dielectric transmission metasurface for linearly polarized light in the visible region, *Photonics Research*, **6**(6), pp. 517–524.
- YAN-G., MARKOV-A., CHINIFOOROSHAN-Y., TRIPATHI-S. M., BOCK-W. J., AND SKOROBOGATIY-M. (2013). Resonant THz sensor for paper quality monitoring using THz fiber bragg gratings, *Optics Letters*, **38**(13), pp. 2200–2202.
- YANG-S., SHENG-X., ZHAO-G., AND LI-S. (2019a). Simple birefringent terahertz fiber based on elliptical hollow core, *Optical Fiber Technology*, **53**, Art. No. 102064.
- YANG-S., SHENG-X., ZHAO-G., LOU-S., AND GUO-J. (2020). Anti-deformation low loss double pentagon nested terahertz hollow core fiber, *Optical Fiber Technology*, **56**, Art. No. 102199.
- YANG-S., SHENG-X., ZHAO-G., WANG-Y., AND YU-Y. (2019b). Novel pentagram THz hollow core anti-resonant fiber using a 3D printer, *Journal of Infrared, Millimeter, and Terahertz Waves*, **40**(7), pp. 720–730.
- YANG-T., DING-C., ZIOLKOWSKI-R. W., AND GUO-Y. J. (2018c). A scalable THz photonic crystal fiber with partially-slotted core that exhibits improved birefringence and reduced loss, *Journal of Lightwave Technology*, **36**(16), pp. 3408–3417.
- YANG-X., ZHANG-D., WU-S., YIN-Y., LI-L., CAO-K., AND HUANG-K. (2017). Reconfigurable all-dielectric metasurface based on tunable chemical systems in aqueous solution, *Scientific Reports*, **7**, Art. No. 3190.
- YANG-Y., WANG-W., MOITRA-P., KRAVCHENKO-I. I., BRIGGS-D. P., AND VALENTINE-J. (2014b). Dielectric meta-reflectarray for broadband linear polarization conversion and optical vortex generation, *Nano Letters*, **14**(3), pp. 1394–1399.
- YAN-S., LOU-S., WANG-X., ZHAO-T., AND ZHANG-W. (2018). High-birefringence hollow-core anti-resonant THz fiber, *Optical and Quantum Electronics*, **50**, Art. No. 162.
- YAO-J., CHEN-Y., YE-L., LIU-N., CAI-G., AND LIU-Q. H. (2017). Multiple resonant excitations of surface plasmons in a graphene stratified slab by otto configuration and their independent tuning, *Photonics Research*, **5**(4), pp. 377–384.
- YETISEN-A. K., BUTT-H., MIKULCHYK-T., AHMED-R., MONTELONGO-Y., HUMAR-M., JIANG-N., MARTIN-S., NAYDENOVA-I., AND YUN-S. H. (2016). Color-selective 2.5D holograms on large-area flexible substrates for sensing and multilevel security, *Advanced Optical Materials*, **4**(10), pp. 1589–1600.
- YOU-B., LIU-T.-A., PENG-J.-L., PAN-C.-L., AND LU-J.-Y. (2009). A terahertz plastic wire based evanescent field sensor for high sensitivity liquid detection, *Optics Express*, **17**(23), pp. 20675–20683.

- YOU-B., LU-J.-Y., LIOU-J.-H., YU-C.-P., CHEN-H.-Z., LIU-T.-A., AND PENG-J.-L. (2010). Subwavelength film sensing based on terahertz anti-resonant reflecting hollow waveguides, *Optics Express*, **18**(18), pp. 19353–19360.
- YOU-B., LU-J.-Y., YU-C.-P., LIU-T.-A., AND PENG-J.-L. (2012). Terahertz refractive index sensors using dielectric pipe waveguides, *Optics Express*, **20**(6), pp. 5858–5866.
- YUDASARI-N., ANTHONY-J., AND LEONHARDT-R. (2014). Terahertz pulse propagation in 3D-printed waveguide with metal wires component, *Optics Express*, **22**(21), pp. 26042–26054.
- YU-F., AND KNIGHT-J. C. (2016). Negative curvature hollow-core optical fiber, *IEEE Journal of Selected Topics in Quantum Electron*, **22**(2), pp. 146–155.
- YU-L., HAO-L., MEIQIONG-T., JIAOQI-H., WEI-L., JINYING-D., XUEPING-C., WEILING-F., AND YANG-Z. (2019). The medical application of terahertz technology in non-invasive detection of cells and tissues: opportunities and challenges, *RSC Advances*, **9**(17), pp. 9354–9363.
- YU-N., GENEVET-P., KATS-M. A., AIETA-F., TETIENNE-J.-P., CAPASSO-F., AND GABURRO-Z. (2011). Light propagation with phase discontinuities: generalized laws of reflection and refraction, *Science*, **334**(6054), pp. 333–337.
- ZENG-S., SREEKANTH-K. V., SHANG-J., YU-T., CHEN-C.-K., YIN-F., BAILLARGEAT-D., COQUET-P., HO-H.-P., AND KABASHIN-A. V. (2015). Graphene–gold metasurface architectures for ultrasensitive plasmonic biosensing, *Advanced Materials*, **27**(40), pp. 6163–6169.
- ZENG-Y., HU-R., WANG-L., GU-D., HE-J., WU-S.-Y., HO-H.-P., LI-X., QU-J., AND GAO-B. Z. (2017). Recent advances in surface plasmon resonance imaging: detection speed, sensitivity, and portability, *Nanophotonics*, **6**(5), pp. 1017–1030.
- ZHANG-J., AND GRISCHKOWSKY-D. (2004). Waveguide terahertz time-domain spectroscopy of nanometer water layers, *Optics Letters*, **29**(14), pp. 1617–1619.
- ZHANG-L., MEI-S., HUANG-K., AND QIU-C.-W. (2016). Advances in full control of electromagnetic waves with metasurfaces, *Advanced Optical Materials*, **4**(6), pp. 818–833.
- ZHANG-X., WANG-R., COX-F., KUHLMMEY-B., AND LARGE-M. (2007). Selective coating of holes in microstructured optical fiber and its application to in-fiber absorptive polarizers, *Optics Express*, **15**(24), pp. 16270–16278.
- ZHANG-Y., LIANG-P., WANG-Y., ZHANG-Y., LIU-Z., WEI-Y., ZHU-Z., ZHAO-E., YANG-J., AND YUAN-L. (2017). Cascaded distributed multichannel fiber SPR sensor based on gold film thickness adjustment approach, *Sensors and Actuators A: Physical*, **267**, pp. 526–531.
- ZHANG-Y., LI-K., WANG-L., REN-L., ZHAO-W., MIAO-R., LARGE-M. C., AND VAN EIJKELNBORG-M. A. (2006). Casting preforms for microstructured polymer optical fibre fabrication, *Optics Express*, **14**(12), pp. 5541–5547.
- ZHAO-G., SAVINI-G., YU-Y., LI-S., ZHANG-J., AND ADE-P. (2019). A dual-port THz time domain spectroscopy system optimized for recovery of a sample's Jones matrix, *Scientific Reports*, **9**, Art. No. 2099.

-
- ZHAO-Y., DENG-Z.-Q., AND LI-J. (2014). Photonic crystal fiber based surface plasmon resonance chemical sensors, *Sensors and Actuators B: Chemical*, **202**, pp. 557–567.
- ZHENG-P., KASANI-S., AND WU-N. (2019). Converting plasmonic light scattering to confined light absorption and creating plexitons by coupling a gold nano-pyramid array onto a silica–gold film, *Nanoscale Horizons*, **4**(2), pp. 516–525.
- ZHENG-Z.-P., FAN-W.-H., AND YAN-H. (2012). Terahertz absorption spectra of benzene-1, 2-diol, benzene-1, 3-diol and benzene-1, 4-diol, *Chemical Physics Letters*, **525**, pp. 140–143.
- ZHOU-J., WANG-Y., LIAO-C., SUN-B., HE-J., YIN-G., LIU-S., LI-Z., WANG-G., AND ZHONG-X. (2015). Intensity modulated refractive index sensor based on optical fiber michelson interferometer, *Sensors and Actuators B: Chemical*, **208**, pp. 315–319.
- ZHU-B., REN-G., ZHENG-S., LIN-Z., AND JIAN-S. (2013). Nanoscale dielectric-graphene-dielectric tunable infrared waveguide with ultrahigh refractive indices, *Optics Express*, **21**(14), pp. 17089–17096.
- ZHU-Y.-F., CHEN-M.-Y., AND LIU-Y. (2019). Nested low-loss hollow core fiber, *IEEE Journal of Selected Topics in Quantum Electronics*, **26**(4), Art. No. 4500106.
- ZHU-Z., GUO-C., LIU-K., YE-W., YUAN-X., YANG-B., AND MA-T. (2012). Metallic nanofilm half-wave plate based on magnetic plasmon resonance, *Optics Letters*, **37**(4), pp. 698–700.
- ZIBAI-M., LATIFI-H., KARAMI-M., GHOLAMI-M., HOSSEINI-S., AND GHEZELAYAGH-M. (2010). Non-adiabatic tapered optical fiber sensor for measuring the interaction between α -amino acids in aqueous carbohydrate solution, *Measurement Science and Technology*, **21**(10), Art. No. 105801.

Glossary

The physical constants used in this thesis for generating material properties are in accordance with the recommendation of the Committee on Data for Science and Technology (Mohr et al. 2008).

Name of the constants	Symbol	Value
Speed of light at vacuum	c, c_0	2.99792458×10^8 m/s
Vacuum permittivity	ϵ	$8.854187817 \times 10^{-12}$ F/m
Vacuum permeability (magnetic constant)	μ_0	$4\pi \times 10^{-12}$ F/m
Electron charge	e	1.6×10^{-19} C
Electron mass	m_e	$9.1093837015 \times 10^{-31}$ kg
Graphene chemical potential	μ_c	0.1 eV
Graphene scattering rate	τ	0.1 ps
Boltzmann's constant	k_B	1.38064×10^{-23} m ² kg s ⁻² K ⁻¹
Reduced Planck's constant	$\hbar = \frac{h}{2\pi}$	1.055×10^{-34} Js
Zeonex permittivity	ϵ_z	2.3
Silicon permittivity	ϵ_s	11.68
Silicon plasma frequency	ω_{ps}	4.94×10^{13} rad·s ⁻¹
Silicon collision frequency	γ_s	1.117×10^{13} s ⁻¹
Gold collision frequency	γ_g	1.23×10^{13} s ⁻¹
Gold plasma frequency	ω_{pg}	1.38×10^{16} rad·s ⁻¹
Gold permittivity	$\epsilon_{\infty g}$	1.0

List of abbreviations

Au	gold
ABS	acrylonitrile butadiene styrene
ARC	australian research council
BIC	bound states in the continuum
CL	confinement loss
Cu	copper
CNC	computer numerical controlled
COC	cyclic-olefin copolymer
COP	cyclo-olefin polymer
CVD	chemical vapor deposition
CW	continuous wave
dB	decibel
DNA	deoxyribonucleic acid
DTG	derivative thermogravimetric
ECM	equivalent circuit model
EHF	extended high frequency
EML	effective material loss
EWFD	electromagnetic waves, frequency domain
FDM	fused deposition modelling
FEM	finite element method

List of abbreviations

FFT	fast Fourier transforms
FOM	figure of merit
F-P	febry perot
FTS	fourier transform spectroscopy
FIR	far infrared
FWHM	full width at half maxima
GA	genetic algorithm
GHz	gigahertz
GVD	group velocity dispersion
HC	hollow-core
HCF	hollow-core fibre
HDPE	high-density polyethylene
HIV	human immunodeficiency virus
HRS	high resistivity silicon
IC	inhibited coupling
ITO	indium tin oxide
IR	infrared
LOD	limit of detection
LSPR	localized surface plasmon resonance
MOF	microstructured optical fibre
MMA	methyl methacrylate
mTIR	modified total internal reflection
NA	numerical aperture
NDT	non-destructive testing
OAM	orbital angular momentum
PBG	photonic bandgap
PC	porous core
PCF	photonic crystal fibre
PLA	polylactic acid

PMD	polarization mode dispersion
PML	perfectly matched layer
PMMA	poly(methyl methacrylate)
PP	polypropylenes
PPO	polypyrrole-polyethylene oxide
QDs	quantum dots
RNA	ribonucleic acid
RI	refractive index
RIU	refractive index unit
SEM	scanning electron microscope
SiC	silicon carbide
SLA	stereolithography
SNR	signal to noise ratio
SPP	surface plasmon polaritons
SPR	surface plasmon resonance
SERS	surface-enhanced Raman scattering
Teflon	tetrafluoroethylene
TE	transverse electric
TEM	transverse electric and magnetic
TG	thermogravimetric
THF	tetrahydrofuran
TiN	titanium nitride
TIR	total internal reflection
TPX	polymethylpentene
THz	terahertz
THz-TDS	terahertz time-domain spectroscopy
TM	transverse magnetic
THz	terahertz
UV	ultraviolet
WS	wavelength sensitivity

Index

- 3D printer filaments, 97
- 3D printing, 15, 16, 29, 39, 96
- ABS, 51
- absorbers, 11, 153
- absorption (A), 159
- absorption coefficients, 24
- acidic, 28
- acidic (low pH), 25
- Advantest, 17
- Advantest TAS7400TS, 16, 100
- aluminium (Al), 124
- amplitude sensitivity (AS), 119
- antiresonant, 9
- antiresonant terahertz fibres, 31
- Appendix A, 7
- Appendix B, 7
- Appendix C, 7
- ARROW waveguide, 39
- asymmetrical, 82
- asymmetry, 187
- basic (high pH) NaOH, 25
- bending loss, 64
- BIC, 172, 173, 187
- bio-compatible, 124
- biosensing, 136, 137
- birefringence, 72, 82, 133
- birefringent PCF, 69
- BK7, 8, 22
- Bound States in the Continuum (BIC), 172
- Bragg fibres, 31
- capillary, 110
- characterization, 18
- chemical potential, 157, 164
- chemical stability, 14
- chemical vapor deposition (CVD), 126, 157
- coating, 9
- computer numerical controlled (CNC) drilling machine, 48
- COMSOL multiphysics, 6, 64, 109
- confinement loss, 64, 68, 82
- conjoined-tubes, 95
- continuous-wave (CW), 51
- copper (Cu), 124
- crystalline materials, 27
- CST microwave studio, 151
- deflection angle, 21
- derivative thermogravimetric (DTG), 25
- diamond suspension, 16
- dielectric loss, 20
- dielectric loss tangents, 24
- dispersion, 69, 72
- Drilling, 126
- dry nitrogen, 22
- Duran, 14, 22
- effective area, 68
- effective material loss (EML), 64, 68
- EHF, 3
- electromagnetic (EM), 137
- electron charge, 164
- equivalent circuit model (ECM), 158
- etched, 188
- EX2 Filabot, 97
- extinction coefficient, 21
- Extrusion, 50
- fabrication, 9, 51, 75, 114
- far-infrared, 12
- Fermi energy, 163
- Fermi velocity, 164
- Figure of Merit (FOM), 119
- Finite Element Method (FEM), 7, 64, 108, 151
- FIR, 3
- Floquet-port, 155

- FOM, 133
- Frequency domain solver, 155
- FS-300 silica, 22
- FTS, 13
- full width at half maxima (FWHM), 179
- fundamental mode, 31
- Fused Deposition Modelling (FDM), 15

- gas sensing, 93
- genetic algorithm (GA), 151, 155, 157, 171
- germanium, 13, 176
- glasses, 11
- gold (Au), 124
- graded-index, 56
- graphene, 7, 149, 151, 154, 155
- grit sizes, 16
- group velocity dispersion (GVD), 39
- guiding mechanism, 56
- GVD, 44, 46

- HDPE, 8, 22
- high-Q, 7, 183
- high-speed short-range optical communications, 94
- hollow hexagonal-core fibre (HCF), 93
- hollow waveguides, 93
- Hollow-core, 35, 38, 57
- horizontal extruder, 96

- indium tin oxide (ITO), 124
- internal sensing, 139

- kagome, 38, 39, 80

- lenses, 27
- limit of detection (LOD), 169
- lithography technique, 177
- localized, 9
- localized surface plasmon resonance (LSPR), 107, 108, 137
- LOD, 117
- LSPR, 108, 109, 112
- LSPR-PCF, 118
- MATLAB, 7

- Measurement, 13
- mechanical shaker, 25
- metal wire waveguide, 31
- metamaterials, 11
- metasurface, 7, 9, 151, 153, 154, 161
- microstructured optical fibres (MOF), 94
- microwaves, 12
- modified total internal reflection (mTIR), 32
- mTIR, 32
- multiband, 151, 160

- nitrogen, 18
- non-destructive testing (NDT), 30
- nozzle, 51, 98
- numerical aperture (NA), 66

- optical, 9
- optical constants, 18
- optimization, 157

- parabolic mirrors, 17
- PBG, 32, 33, 39, 95
- PCF, 77
- PCF-SPR, 135
- pellets, 8
- perfectly matched layer (PML), 67, 109, 125, 155
- permeability, 64
- permittivity, 64
- phase extrapolation, 19
- phase shift, 20
- photolithography, 177
- photonic bandgap (PBG), 87
- photonic crystal fibre (PCF), 108, 119
- picarin (tsurupica), 27
- Planck's constant, 164
- plasmonic, 138
- Plasmonic superabsorption, 152
- plasmonic metal, 109, 115, 116
- plasmonic metasurfaces, 172
- plasmons, 163
- PML, 86
- PMMA, 8, 14
- polarization, 67

- polarization mode dispersion (PMD), 67
polarization-maintaining, 73
polishing, 16
polyethylene alcohol, 56
polymers, 11, 14
polymethylpentene (TPX), 27
polypropylenes (PP), 27
polystyrene foams, 31
Porous-core, 36
power (dB), 17
power absorption coefficients, 13
power spectrum, 20
pump-probe, 12
- Q-factor, 10, 173
- reflection (R), 159
reflection coefficients, 27
reflectivity, 43
refractive index, 13, 20, 21, 67
relative permittivity, 164
resonance, 185
root mean square error (RMSE), 184
- saline NaCl, 25
salinic, 28
sandpaper, 16
scattering loss, 64
SEM, 189
semiconductors, 13
sensitivity, 115, 130, 133
sensor resolution, 133
SERS, 118
signal amplitude and phase, 13
signal to noise ratio (SNR), 18
Silica, 8
silicon, 13, 157, 188
silicon carbide (SiC), 16
silicon lens, 17
silver (Ag), 124
single-step, 96
solid core, 84
spectroscopy, 11, 12, 58
SPR, 112, 137
Stacking, 49
Stereolithography (SLA), 16
stylus profilometer (Dektak XT - Bruker), 177
sub-wavelength fibres, 31
superabsorber, 158
superabsorption, 151, 161
surface functionalization, 140
surface plasmon polaritons (SPPs), 153
surface plasmon resonance (SPR), 107, 108, 137
surface plasmon wave (SPW), 137
surface-enhanced Raman scattering (SERS), 108
- T-ray, 2, 3
TA Instruments, 25
TAS7400TS, 6
Teflon, 8, 14, 22
terahertz optical fibres, 35
terahertz power (dB), 22
terahertz transmission, 93
terahertz waveguide, 68
TGA, 28
thermal, 11, 14
thermal analyser, 25
thermogravimetric (TG), 25
THz-TDS, 7, 10, 12, 13, 28
time-domain spectroscopy, 77
TIR, 32, 56
titanium nitride (TiN), 124
Topas, 8, 14, 22
total internal reflection effect (TIR), 32
transfer function, 19
transmission, 11, 16, 106
transmission bandwidth, 22
transmission efficiency, 31
transmission spectroscopy, 14
transmittance, 11, 20
transparency, 15
transverse electric (TE), 160
transverse magnetic (TM), 160
tunable, 9
tuneability, 153
Two-wire waveguides, 31

unwrapping, 19

UV-resin, 14, 22

visible and infrared, 30

visible to mid-infrared, 106

waveguides, 6

wavelength sensitivity (WS), 108, 119

Zeon corporation, Japan, 16

Zeonex, 8, 14, 22

Biography

Md. Saiful Islam received the B.Sc. degree in Electronics & Telecommunication Engineering from Rajshahi University of Engineering & Technology (RUET), Rajshahi, Bangladesh. After his graduation he started working as a Lecturer in Electrical and Electronic Engineering of World University of Bangladesh. He worked there from 2012 to mid 2014.



Then he took up a post as a Senior Lecturer at Bangladesh University at 2014. Whilst simultaneously teaching, he carried out his M.Sc. degree in Electrical and Electronic Engineering at Islamic University of Technology (IUT), Gazipur, Bangladesh and finished in 2016 securing the highest possible CGPA 4.00 out of 4.00 with a number of high quality publications. He was then promoted to Assistant Professor at Bangladesh University in 2016.

In 2017 he joined the School of Electrical and Electronic Engineering of The University of Adelaide, Australia under a ECMS divisional Scholarship to study towards his PhD under the supervision of **Prof. Derek Abbott** and **A/Prof. Brian W.-H. Ng**. Mr. Islam also awarded the Research Travel Scholarship in 2019 and Frank Perry Travelling Scholarship in 2020.

Mr. Islam is a member of IEEE, IEEE Young Professionals, Optical Society of America (OSA), and Institute for Photonics & Advanced Sensing (IPAS). His research interests include optical fiber communication, terahertz waveguides, terahertz sensors, plasmonic biosensors, topological insulators, and metasurfaces for developing advanced electromagnetic devices. Mr. Islam has published 45 peer-reviewed articles and 11 conference papers. He actively reviews for *Scientific Reports*, *IEEE Access*, *Photonics Research*, *IEEE Journal of Lightwave Technology*, *IEEE Photonics Journal*, *IEEE Sensors Journal*, *IEEE Photonics Technology Letters*, *Optics Express*, *Optics Letters*, *Applied Optics*, *Optical Materials Express*, and *IEEE Transactions on Nanotechnology*, etc. A full detail of his reviewer profile can be found in the Publons profile. Mr. Islam is a top

Biography

peer reviewer in physics and cross-fields as awarded and recognized by Publons and Web of Science.

Md. Saiful Islam
mdsaiful.islam@adelaide.edu.au

Researcher Profile

Google Scholar

Researchgate

Publons

ORCiD

Linkedin

Scientific genealogy

Scientific Genealogy of Md. Saiful Islam



..... Mentoring relationship

— Formalised supervisor relationship

🏆 Nobel prize

2021-PhD, University of Adelaide, Md. Saiful Islam